THÈSE

En vue de l'obtention du

DOCTORAT DE L'UNIVERSITÉ DE TOULOUSE

Délivré par **l'Institut Supérieur de l'Aéronautique et de l'Espace**
Spécialité : Dynamique des fluides

Présentée et soutenue par **Benjamin DUDA**
le **19 septembre 2012**

Étude et analyse numérique d'un jet chaud débouchant dans un écoulement transverse en utilisant des simulations aux échelles résolues

---

JURY

M. Jean Piquet, président
M. Hervé Bézard
M. Sébastien Deck, co-directeur de thèse
Mme Marie-Josèphe Estève
M. Thomas Gatski, rapporteur
M. Charles Hirsch, rapporteur
M. Patrick Jenny
M. Florian Menter

École doctorale : **Mécanique, énergétique, génie civil et procédés**

Unité de recherche : **Équipe d'accueil ISAE-ONERA EDyF**

Directeur de thèse : **M. Pierre Millan**
Co-directeur de thèse : **M. Sébastien Deck**

Der Mensch muß bei dem Glauben verharren, daß das Unbegreifliche begreiflich sei; er würde sonst nicht forschen.

J. W. von Goethe

Acknowledgements

This doctoral thesis is the outcome of an extensive collaboration between Airbus Operations SAS, Ansys Germany GmbH as well as ONERA. At first, I would like to express my sincere gratitude to Dr Marie-Josèphe Estève, research engineer at the Department of Aerodynamic Methods & Tools at Airbus, for setting up such an excellent framework. In addition to my activities at Airbus, I had the great opportunity to work also at Ansys under the supervision of Dr Florian Menter, R & D fellow, and Thorsten Hansen, team leader Customer & Sales Support. From ONERA side, I had the pleasure to be supervised by Dr Sébastien Deck, research scientist at the Department of Applied Aerodynamics, who was also the co-director of this thesis as well as by Dr Hervé Bézard, research scientist at the Department of Aerodynamics and Energetics Modeling. Due to the large number of people directly involved, the input of ideas and the number of revealing discussions were equally large, which created an extremely fruitful atmosphere and an environment of rich exchange despite different geographical locations. This allowed me benefiting greatly from experience and expertise of my supervisors and I would like to thank all of them for their inspiration, support and kindness.

My sincere thanks go to Professor Tom Gatski and Professor Charles Hirsch for accepting the part of reporting on this thesis as well as to the invited members of the jury for their comments and remarks: Professor Jean Piquet, who chaired the jury as president, and Professor Patrick Jenny. Additional thanks go to Dr Pierre Millan, director of the Department of Aerodynamics and Energetics Modeling at ONERA, for being the director of this thesis.

Having spent one and a half years at Ansys in Otterfing, Germany and one and half years at Airbus in Toulouse, France I was welcomed cordially in two work environments where I encountered kind and highly skilled people. I had the opportunity to collaborate with many colleagues for whom I have great respect and I wish to extend my warmest thanks to all of those who have contributed directly or indirectly to this work.

Finally, I wish to thank everybody else who accompanied me along this way and I am especially grateful to the members of my family since it would have been impossible for me to reach this milestone without their encouragement and support.

Contents

List of Figures

Nomenclature

Latin Symbols

$\mathbf{A}$	solution matrix
A_f	surface area of cell face
c_p	specific heat capacity at constant pressure
c_v	specific heat capacity at constant volume
C	chord length
C_R	effective velocity ratio
d	characteristic thickness of ejector grid
D	characteristic length of ejector
e	specific energy
E	total energy, energy spectrum of turbulence
f	frequency, face
g	acceleration through gravity
G	filter kernel, power spectral density
$\widetilde{G}$	normalized power spectral density
h	specific enthalpy, heat transfer coefficient
H	total enthalpy, height
I	turbulence intensity
k	turbulence kinetic energy
L	characteristic length
L_{vK}	von Kármán length scale
$\dot{m}$	mass flow
M	number of sampling points
n	current time step
N	number of transient realizations of flow field
p	pressure
P_k	production term of turbulence kinetic energy
q_i	heat flux component
Q	source term, second invariant of velocity gradient tensor
R	momentum flux ratio, specific gas constant
R_{ij}	two-point velocity correlation tensor

S	source term
S_{ij}	shear rate tensor
t	time
T	temperature
u_i	i^{th} velocity component
u, v, w	velocity components
$\mathbf{U}$	unitary matrix containing temporal evolution of SVD modes
U, V, W	mean velocity components
V	cell volume
$\mathbf{V}$	unitary matrix containing SVD modes
V_R	velocity ratio
x_i	i^{th} Cartesian coordinate
X, Y, Z	Cartesian coordinates
y^+	non-dimensional wall distance
Z_w	wall distance

Greek Symbols

α	angle of attack
β_T	thermal expansion coefficient
Γ	diffusion coefficient
δ_1	boundary layer displacement thickness
δ_{ij}	Kronecker symbol
Δ, Δ_V, Δ_1	grid length scales
Δt	numerical time step
ΔT	temperature difference between jet and cross flow
ε	dissipation
η	thermal efficiency
$\eta_{\dot{m}}$	ratio of recirculating to jet mass flow
κ	wavenumber, von Kármán constant
λ	thermal conductivity
λ_t	turbulent thermal conductivity
Λ	aspect ratio
μ	dynamic viscosity
ν	kinematic viscosity
ρ	density
σ	singular value
σ^2	root mean square value
$\mathbf{\Sigma}$	matrix containing singular values
τ_{ij}	stress tensor
ϕ	generic flow variable

ω	specific dissipation rate, vorticity
Ω	flow domain

Indices and Superscripts

∞	free stream quantity
$_{cf}$	cross flow
$_{j}$	jet quantity
$_{ref}$	reference quantity
$_{t}$	turbulence quantity
$_{0}$	characteristic scale of geometry
*	characteristic scale of turbulence

Accents

$\overline{\phi}$	averaged part of Reynolds decomposition
ϕ'	fluctuating part of Reynolds decomposition
$\overline{\overline{\phi}}$	averaged part of Favre decomposition
ϕ''	fluctuating part of Favre decomposition
$\widetilde{\phi}$	filtered quantity
$\widehat{\phi}$	Favre-filtered quantity

Dimensionless Quantities

Ma	Mach number
Nu	Nusselt number
Pr	Prandtl number
Re	Reynolds number
Ri	Richardson number
St	Strouhal number

Frequent Acronyms

CRVP	Counter-Rotating Vortex Pair
(D)DES	(Delayed) Detached Eddy Simulation
(E)LES	(Embedded) Large Eddy Simulation
(M)JICF	(Multiple) Jet(s) in Cross Flow
SAS	Scale-Adaptive Simulation
SRS	Scale-Resolving Simulation
(U)RANS	(Unsteady) Reynolds-Averaged Navier-Stokes

Chapter 1

Introduction

1.1 Motivation

The aerothermal design of air system exhausts is of crucial interest to the aerospace industry in terms of certification, reduction of weight and overall aircraft performance. A special challenge in this context is the simulation of a hot jet in cross flow (JICF) as it appears for instance at discharge locations of the nacelle anti-icing system. Even though generic configurations have been studied both experimentally and numerically, basic similarity parameters like the Reynolds number or the effective velocity ratio differ strongly from those which occur at aircraft related problems. Additionally, the appearance of large-scale turbulent structures as well as the mixing of hot and cold fluid are not yet fully understood and still a subject of debate in the research community.

To give an illustrative example, a sketch of a generic nacelle anti-icing system is shown in figure 1.1. Hot air circulates inside the nacelle's leading edge in order to prevent the formation of ice on the outside of the engine's air intake. A part of this fluid is blown out through an ejector grid containing several orifices. On the outside, this fluid interacts with the external flow and forms multiple jets in cross flow. The main challenges can be summarized as follows. Firstly, hot fluid directly impacts the wall downstream of the orifice due to the low jet velocity compared to the main flow. Assuming an equal structural load, the use of carbon fiber reinforced plastics allows the reduction of weight compared to metallic structures. The downside of these components however lies in the increased sensitivity when exposed to high temperatures. For this reason a thermal shield is typically installed behind the exhaust and the knowledge of the surface temperature distribution is of major importance for a correct dimensioning. The current design process is based only on wind tunnel correlations of generic configurations since existing simulation techniques are not capable of capturing the lateral spreading of the thermal wake. Reliable computational methods are thus needed for improved accuracy. Secondly, any air system integration introduces parasitic drag. Since the illustrated anti-icing system is operated during the entire flight regime, the

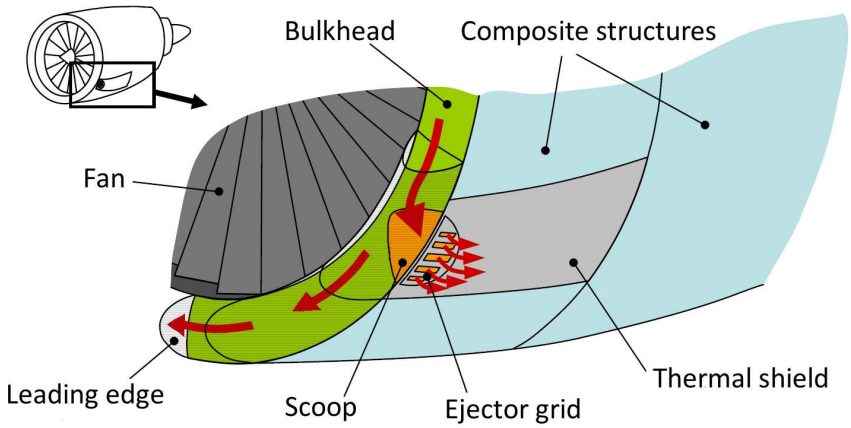

Figure 1.1: Generic nacelle anti-icing system with emergence of jets in cross flow at exhaust

impact on aircraft performance needs to be as low as possible. This shows the necessity to investigate and understand both flow physics and mixing phenomena of a jet in cross flow as well as the need to accurately simulate this type of flow. Thirdly, the integration of the air exhaust into the global aerodynamic design of the airplane leads to a classical multi-scale problem. The flow over large bodies in the order of 10^1m as the wing or the nacelle has to be handled at the same time as the jet in cross flow with typical geometrical dimensions of 10^{-2}m.

Finally, it shall be emphasized that apart from special aeronautical applications the simulation of a jet in cross flow is of great interest also in other industrial areas. An important example can be found in turbomachinery. In order to protect turbine blades from hot combustion gases film cooling is applied by injecting a coolant into the main stream, where a jet in cross flow forms. Due to its good mixing capability, jets in cross flow are frequently used in combustion chambers for fuel injections or in many areas of process engineering. The procedures developed in this work will therefore serve as a solid base to simulate also these types of applications.

1.2 Objectives and Rationale

The numerical simulation of this type of flow still poses a challenge to modern computational fluid dynamics (CFD) because of the emerging complex three-dimensional structures as well as their inherent transient and turbulent character. Additionally, the challenges of a heat transfer problem have to be coped with due to the temperature difference between jet and cross flow. Studies have shown that conventional approaches such as the application of statistical two equation turbulence models or even Reynolds Stress models fail when employed in a steady state calculation. On the other hand, Direct Numerical Simulations (DNS) and Large Eddy Simulations (LES) are capable of predicting this kind of flow. As high Reynolds number flows are going to

be encountered in jet in cross flow applications on aircraft, these types of simulations are out of question due to the need for excessively refined meshes and the correlating computational effort.

For this reason, the approach followed in this work is based on the assessment and validation of advanced turbulence models, which allow the resolution of at least a part of the turbulence spectrum in the area of interest and which will be here referred to as Scale-Resolving Simulations (SRS). The simplest SRS technique is the time-dependent solution of the Unsteady Reynolds-Averaged Navier-Stokes (URANS) equations in combination with a conventional statistical turbulence model, such as the various formulations of the $k-\omega$ model. A second approach is the use of the Scale-Adaptive Simulation (SAS), which is basically an improved URANS formulation. Within this framework the von Kármán length scale enters the turbulence model equations and serves as a sensor for resolvable structures. In contrast to SAS, whose local length scale is defined by the flow field, a different class of approaches known as Large Eddy Simulation (LES) obtains its length scale information for resolvable structures explicitly from the underlying numerical mesh. Since for the considered case the resolution of structures is only desired in critical flow regions, two approaches are investigated that combine LES with standard RANS capabilities. The first one is termed Embedded LES (ELES), where only within a user specified region an LES calculation is performed and the rest of the domain is treated with a RANS turbulence model. The other approach is known under the formulation Delayed Detached Eddy Simulations (DDES). Within this framework, a shielding function is employed to keep attached boundary layers in RANS mode and an LES formulation is enabled within regions of inherent flow instabilities.

The first main objective consists in the validation of the proposed turbulence modeling strategies against experimental data for a generic single jet in cross flow configuration. As this also includes higher order time statistics such as fluctuating quantities and spectral analysis, the transient flow solution is validated as well. This is of great importance because real-time flow simulations then serve as a basis for a profound flow analysis. This leads to the second main objective, which is to gain a better insight into the underlying dynamics of jets in cross flow at small momentum ratios and high Reynolds numbers by identifying transport and mixing phenomena. The third main objective consists in adapting the developed process in order to be applicable to industrial configurations by taking into account the associated challenges of high Reynolds numbers, increased geometrical complexity and multi-scale problems. This is achieved successively by passing on to a still generic but more complex configuration comprising multiple jets in cross flow. Subsequently, simulations for a real aircraft application are carried out and compared to available flight test data. The final step consists in applying the developed methodology to a second and more complex real aircraft system, showing its capability to be employed in the aerothermal design process for air system outlets.

1.3 Outline

The outline of this thesis is given in the following. A bibliographic research is conducted in chapter 2 in order to evaluate state of the art knowledge on flow dynamics and proposed mixing phenomena associated to jets in cross flow as well as on existing simulation strategies. Following this, the employed turbulence modeling approaches are introduced in chapter 3 as well as the numerical solution procedure. Simulations are carried out on a generic jet in cross flow configuration at high Reynolds numbers and results are compared to experimental data, which is described in chapter 4. The influence of the numerical time step size is studied and special attention is paid to the applicability of different meshing strategies in order to prepare the transition to industrial configurations where complex geometries are encountered. The second part of this chapter is devoted to an analysis in order to examine dominant flow features, mixing phenomena and flow dynamics. Extended investigations concerning thermal boundary conditions and a multiple jets in cross flow configuration are regarded as well. An adapted simulation strategy is presented in chapter 5 which allows the simulation of multiple jets in cross flow on aircraft by complying with the constraints encountered in industrial applications. To show its capabilities, simulations are carried out on a nacelle anti-icing system, whose design is based on the generic multiple jets in cross flow configuration and where numerical results can be compared to flight test data. The second part of this chapter deals with the simulation of another real aircraft application, which is the exhaust of the pre-cooling system located on the engine's pylon and which is chosen due to its challenging geometry and its interaction with a complex flow field. Finally, the results are summarized and an outlook for possible further investigations on this subject is presented in chapter 6.

Chapter 2

State of the Art

Since engineering applications comprising the jet in cross flow phenomenon are quite numerous, investigations on this subject date back to the 1930s and a vast body of literature exists. A general overview on the research activities until the 1990s is given by Margason [58]. This chapter begins with the general description of a jet in cross flow, including important similarity parameters and the influence of geometrical aspects. Flow dynamics, coherent structures and their origins are discussed. Focus is put on the thermal mixing behavior for jets with a temperature difference relative to the cross flow and different approaches for the numerical simulation are presented and discussed.

2.1 Description of a Jet in Cross Flow

A sketch of a generic jet in cross flow is presented in figure 2.1. The jet issues from a round orifice into the cross flow, where it is deflected and deformed due to the cross flow forces acting on its boundaries. The Cartesian coordinate system is placed in the symmetry plane at the windward side with the X-axis in cross flow direction and the Z-axis in jet flow direction. This convention will also hold for the generic test case considered later in this work. A jet trajectory can be defined as the line connecting the points of maximum velocity for every cross section. Alternative definitions of the jet path can be related to the maximum vorticity or to the streamline emanating from the center of the circular orifice. In the case of a hot jet, the trajectory of the local maximum temperature is of interest as well. While the derivation of an analytical expression for this path is rather complex, empirical formulations were developed to match experimental findings. Fearn & Weston [33] showed that the trajectory can be detected up to 15 jet diameters downstream along its path. The most robust formulation according to Margason is given by

$$\frac{Z}{D} = \left(\frac{U_\infty}{W_j}\right)^{2.6} \left(\frac{X}{D} - \frac{1}{2}\right)^3, \tag{2.1}$$

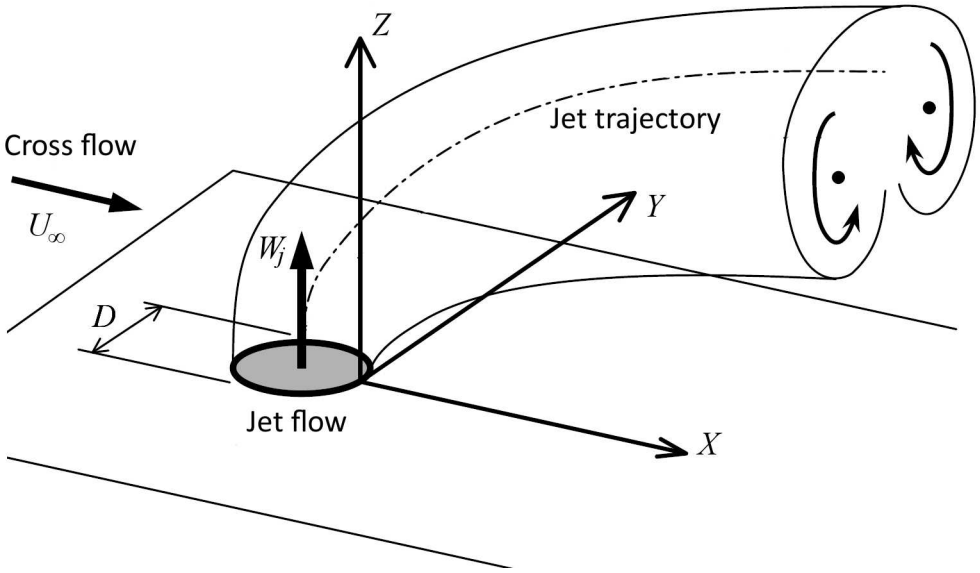

Figure 2.1: Generic jet in cross flow with jet trajectory and kidney shaped cross section

with the diameter D of the jet orifice and the velocities U_∞ and W_j of the cross flow and the jet respectively. Even though studies exist for supersonic jets and/or cross flows, investigations are limited to subsonic flows throughout this work since the considered aircraft related configurations also operate in this regime.

A simplified explanation of the cross sectional deformation can be obtained by regarding a circular jet with a boundary pressure distribution similar to that obtained from a potential flow around a rigid cylinder. Due to the pressure minima at the lateral sides the originally circular cross section of the jet becomes elliptical. Additionally, the entrainment by the cross flow leads to a kidney shaped contour.

2.1.1 Similarity Parameters

Depending on fluid parameters and geometrical aspects, very different flow regimes can be distinguished. For this reason similarity parameters are defined which allow their classification. The most important influence on the establishing flow is given through the velocity ratio V_R between the jet velocity W_j and the cross flow velocity U_∞:

$$V_R = \frac{W_j}{U_\infty}. \tag{2.2}$$

This velocity ratio is meaningful for configurations where jet and cross flow fluid have the same properties. If however fluids of different densities or temperatures, as in this work, are considered, this similarity parameter is insufficient. For that reason Callaghan & Ruggeri [16] extended the velocity ratio by their corresponding den-

sities ρ_j and ρ_∞, yielding the effective velocity or momentum ratio C_R:

$$C_R = \frac{\rho_j W_j}{\rho_\infty U_\infty}. \tag{2.3}$$

In order to account for strong density and temperature differences, Williams & Wood [105] in turn proposed another parameter, which relies on the momentum flux ratio R given by

$$R = \sqrt{\frac{\rho_j W_j^2}{\rho_\infty U_\infty^2}}. \tag{2.4}$$

In the case of vanishing differences in density all three expressions become identical. With the help of this parameter a division into different flow regimes can be established. For $R < 2$ the jet momentum is very small and the jet is not able to penetrate deeply into the main flow. In this case the jet rather attaches to the downstream wall and represents only a small obstacle to the cross flow. These ratios are typically found in turbomachinery applications such as film cooling, where the wall of turbine blades have to be protected from the hot cross flow. Other industrial applications such as fuel injection exhibit momentum flux ratios in the interval of 2 to 10. In this case the jet penetrates deeply into the cross flow and the jet interaction with the downstream wall decreases. The upper limit is reached as $R \to \infty$, which is known as a free jet in literature. It already becomes obvious from these findings that flow dynamics and coherent structures depend substantially on this ratio.

Furthermore, the development and characteristics of turbulent structures in the interaction region strongly depend on the Reynolds number. It is therefore useful to build the cross flow Reynolds number Re_{cf} based on a characteristic length scale of the orifice, which in the case of a circular jet with the diameter D can be written as

$$Re_{cf} = \frac{U_\infty D}{\nu_\infty}, \tag{2.5}$$

with the kinematic viscosity ν_∞ of the free stream. In an early study by Callaghan & Ruggeri [15] the Reynolds number showed only a negligible influence on the jet trajectory. However, for large cross flow Reynolds numbers in the order of 10^5, which are usually encountered at aircraft related problems, the size range of turbulent structures, which appear in the interaction region, is wide and their influence on thermal mixing behavior is rather strong.

Another similarity parameter is of interest for hot jets with a temperature difference ΔT relative to the cross flow. The cross flow Richardson number Ri_{cf} can then be defined as

$$Ri_{cf} = \frac{g\beta_T \Delta T D}{U_\infty^2}, \tag{2.6}$$

with acceleration through gravity g and thermal expansion coefficient β_T. This parameter provides information about the ratio of free to forced convection. In cases where $Ri_{cf} \ll 1$, buoyancy effects are negligible.

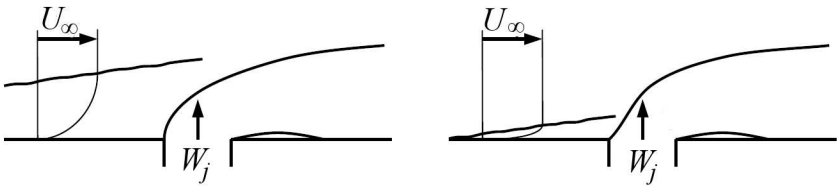

Figure 2.2: Influence of the cross flow boundary layer [7]

Beside these parameters, the displacement thickness of the cross flow boundary layer δ_1 influences the development of the jet in cross flow. Taking this effect into account, ANDREOPOULOS [7] refers to the aspect ratio of the boundary layer thickness over the diameter of the round jet as another similarity parameter:

$$\Lambda_{\delta_1} = \frac{\delta_1}{D}. \tag{2.7}$$

Figure 2.2 shows two different flow configurations where the influence of this length ratio becomes discernible. For the case on the left hand side, the jet turbulence will diffuse rather quickly inside the larger structures of the cross flow boundary layer, whereas opposite developments hold for the case depicted on the right hand side. As reported by FRÖHLICH ET AL. in [26], even if the initial boundary layers of both the cross flow and the supporting jet flow are laminar, a fully turbulent flow develops in the interaction region after a short transition.

2.1.2 Geometrical Considerations

The shape of the ejector has an important impact on the jet trajectory, i.e. the jet's penetration into the cross flow. HAVEN ET AL. [39] as well as RUGGERI ET AL. [80] examined rectangular and elliptical ejectors with different aspect ratios in wind tunnel experiments. The main result is that the larger the distance between the two counter-rotating vortices the smaller the penetration, which is depicted in figure 2.3 with the term *lift-off* corresponding to penetration. This was confirmed more recently by wind tunnel experiments and complementing LES of SALEWSKI ET AL. [83]. Additionally, the use of sharp-edged ejectors facilitates flow separation and with this the formation of vortices, which finally leads to an enhanced mixing behavior but also to increased drag.

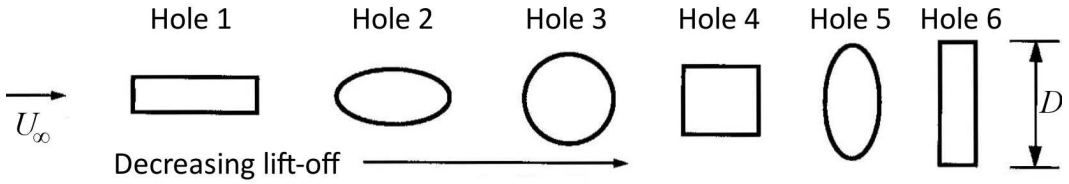

Figure 2.3: Effect of the ejector shape on the jet penetration [39]

Weston & Thames [102] examined in their wind tunnel studies the same ejector installed on a flat plate and on a faired body respectively. It showed that these two installations produce quantitatively and qualitatively different results. This highlights the fact that installation effects have to be taken into account for numerical simulations. Almost all investigations found in literature deal with jets in cross flow on flat plates except Albugues' experimental studies [4], where the ejector is installed on a three-dimensional wing profile under an adverse pressure gradient.

From a series of wind tunnel tests Andreopoulos [5] presents measurements inside the supporting pipe and its interaction with the upstream flow. It was shown that the pipe boundary layer can separate at the upstream part near the exit and that flow from the main stream enters the pipe. This was recently confirmed by a Direct Numerical Simulation conducted by Muppidi et al. [68]. Additionally, the range of influence of the pipe flow extends up to three diameters upstream the orifice. This emphasizes that for numerical simulations as much as possible of the supporting pipe should be included to obtain representative results.

In many engineering applications a jet in cross does not appear individually but rather multiple jets are aligned in a row. Experimental studies of these types of configuration have been carried out by Kamotami & Greber [48] as well as by Sugiyama & Usami [96]. One important observation was that each jet develops individually before it merges with its neighboring jets in the mid and far field. This led to the fact that research was focused primarily on single jets in cross flow.

2.2 Dynamics and Coherent Structures

Basically, the injection of a jet into a cross flow constitutes a free turbulent shear flow. As it already became obvious in the previous sections, flow dynamics as well as appearance of vortices and other coherent structures will strongly depend on the mentioned similarity parameters. Foremost, the question of global stability of the flow arises. Blanchard, Brunet & Merlen [13] carried out a number of experiments and constituted that stable jets in cross flow can indeed exist for small values of C_R and Re_{cf} as presented in figure 2.4. In recent investigations, Bagheri et al. [10] carried out a global stability analysis of a jet in cross flow based on DNS data for a small cross

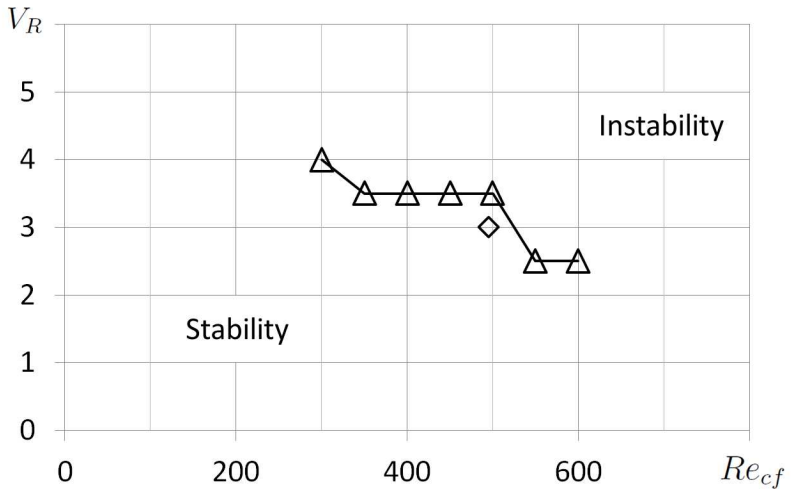

Figure 2.4: Stability study by Blanchard, Brunet & Merlen [13] with △ indicating experiment and ⋄ the stability analysis by Bagheri et al. [10]

flow Reynolds number revealing its globally unstable character. As the configurations investigated in this work will all feature very large cross flow Reynolds numbers, the following discussion is limited to unstable jets in cross flow.

Even if a large number of experimental and numerical investigations have been conducted, the range in examined similarity parameters is equally wide spread, which leads to very different flow characteristics. The starting point for the following description is a phenomenological view of the main vortical structures associated with the jet in cross flow. Figure 2.5 shows the most common illustration proposed by Fric & Roshko [34] containing four principal types of dynamics:

- Shear layer vortices
- Counter-rotating vortex pair
- Horseshoe vortex
- Wake vortices

It has to be emphasized at this point that the conclusions were drawn from experiments with velocity ratios between 2 and 10 as well as cross flow Reynolds numbers in the range from 3 800 up to 11 400. In the related literature a general consensus exists on this view. However, the origin and interaction between the vortices are controversially debated and the extension to low velocity ratios and/or high cross flow Reynolds numbers is questionable.

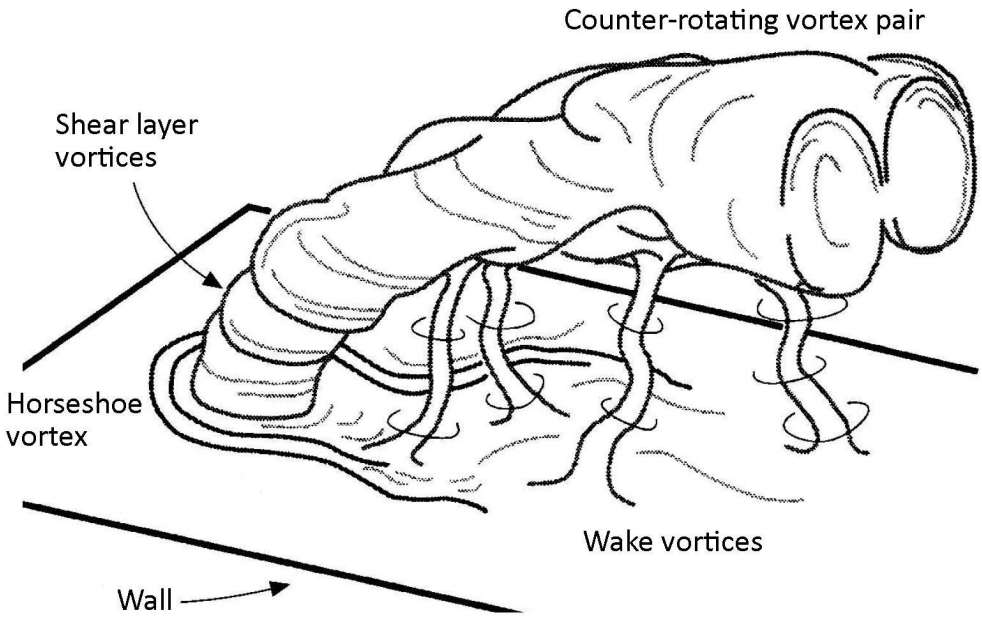

Figure 2.5: Main vortical structures as proposed by Fric & Roshko [34]

2.2.1 Shear Layer Vortices

An important aspect for the formation of coherent structures in a JICF is the existence of a shear layer, which is created by the difference in length and in orientation of the velocity vectors of jet and cross flow respectively. Due to its relation, some researchers tried to transfer the results obtained from free jets to jets in cross flow. It is well known that free round jets form closed ring vortices in the shear layer between the jet and the surrounding fluid at rest, which are caused by Kelvin-Helmholtz instabilities, cf. for instance Danaila et al. [21]. In a free round jet however, the shear layer characteristics are independent of the circumferential position whereas for a JICF the shear layer strongly differs whether the upstream, the downstream or the lateral shear layers are regarded.

To gain more insight into the development of the pipe shear layer inside the cross flow, a simulation method based on vortex elements can be used, which was first employed by Cortelezzi & Karagozian [19]. In this method vorticity is introduced at the boundaries. With the help of the Biot-Savart law the velocity can be calculated at every point of the flow field, leading to the convection of the vorticity filaments. As it can be seen in figure 2.6 a) for an effective velocity ratio of 5.4, the emanating vortex sheet remains cylindrical and the formation of a vortex ring clearly becomes obvious. In figure 2.6 b) the vortex ring tilts due to the cross flow and it is much tighter

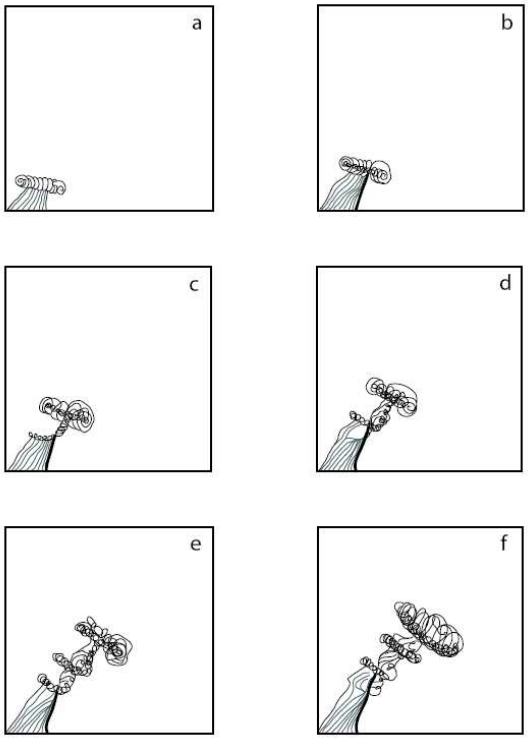

Figure 2.6: Development of jet shear layer using vortex method [19]

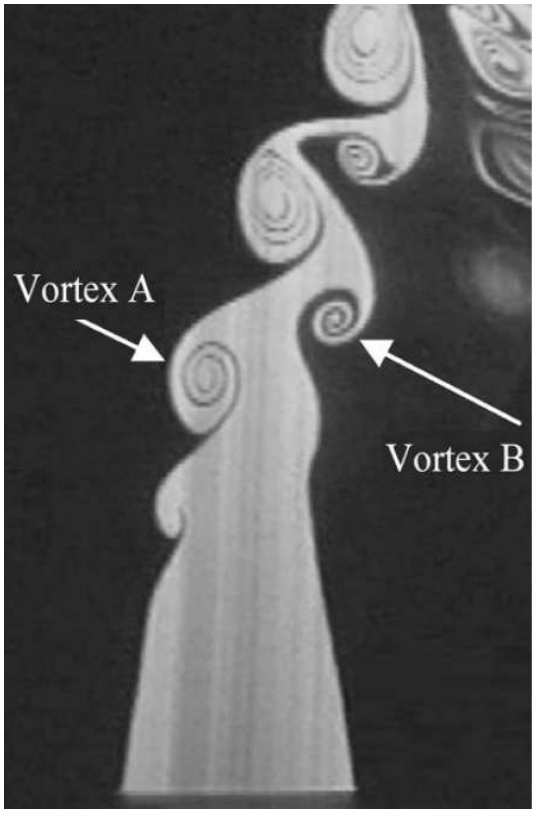

Figure 2.7: Two independent vortices forming in upstream and downstream shear layer [56]

packed at the windward side. In figures 2.6 c) and d) a secondary vortex evolves with its downstream part aligned with the jet trajectory, which can be associated to the formation of the counter-rotating vortex pair as will be discussed in section 2.2.2. The last two pictures of this sequence show the periodic behavior of the mechanism. More recent simulations based on vortex methods were carried out by Marzouk et al. [59, 60] and support these results.

On the other side, Lim et al. [56] showed in water tunnel experiments with an effective velocity ratio of 4.6 that no evidence for closed ring vortices exists. They rather observed that spanwise vortices form on the upstream and the downstream side of the jet, which are not connected. This is illustrated in figure 2.7. These experimental findings were confirmed by LES and DNS conducted by Yuan et al. [106], Kali et al. [47] and Sau et al. [84, 85] respectively. The LES of a round jet shows the development of Kelvin-Helmholtz rollers at the lee and the windward side, which are not connected. Additionally, the formation of these structures on the upstream side is much more regular and begins earlier than on the lee side. This is due to the presence of a favorable pressure gradient on the lee side, stabilizing the shear layer. The DNS computed for a square jet in cross flow shows comparable results. However, the Kelvin-

Helmholtz rollers are only visible on the upstream side. A possible explanation could be the different cross section of the orifice (square vs. circle) and the different cross flow Reynolds numbers.

2.2.2 Counter-Rotating Vortex Pair

As the jet is deflected by the cross flow a complex and highly transient flow field develops. The most dominant feature however is the formation of a counter-rotating vortex pair (CRVP) as depicted in figure 2.5. Its existence dominates the far field and experiments by Pratte & Baines [74] showed its presence up to $100D$ downstream the orifice. Due to its transient behavior the CRVP interacts and overlaps with the shear layer vortices. Nonetheless, despite the large number of experiments and numerical simulations the origin of the vortex pair is still subject to debate and no final answer has been agreed on yet.

Broadwell & Breidenthal [14] see the basic reason for its formation in the presence of the jet momentum, which is orientated perpendicularly to the main flow momentum. This assumption is supported by Muppidi & Mahesh [69], who proposed a two-dimensional model problem. According to their studies, the origination of the counter-rotating vortex pair is due to the formation and redistribution of vortices caused by the Kelvin-Helmholtz instability, which are created in the shear layer between jet and cross flow. Regarding the temporal evolution of this problem, its results can be transferred to the spatial development within a three-dimensional jet in cross flow. It is interesting to notice that in this model problem the supporting pipe and with it the corresponding boundary layer vorticity has not been accounted for.

Andreopolous [7] and Coelho & Hunt [18] see the origin in the shear layer exiting from the supporting pipe. In their view the vortex sheet, i.e. the vorticity containing boundary layer emanating from the pipe, realigns to form the CRVP. Figure 2.8 portrays the reorientation of the vortex rings proposed by Kelso, Lim & Perry [49]. These rings fold in such a way that the plane of the upstream part becomes normal to the mean curvature of the jet, whereas the plane of the downstream part aligns tangentially with the jet trajectory and contribute vorticity to the CRVP. This mechanism is supported by the simulation based on the vortex method carried out by Cortelezzi & Karagozian [19] as depicted in figure 2.6.

Experimental studies conducted by Lim, New & Luo [56] show that the jet shear layer does not develop closed annular vortices, cf. also figure 2.7 in the previous section. The authors therefore propose a different origin for the formation of the CRVP, which is depicted in figure 2.9. In their view, the side arms of the lateral vortices align with the jet trajectory and form the CRVP as it becomes visible in section B-B.

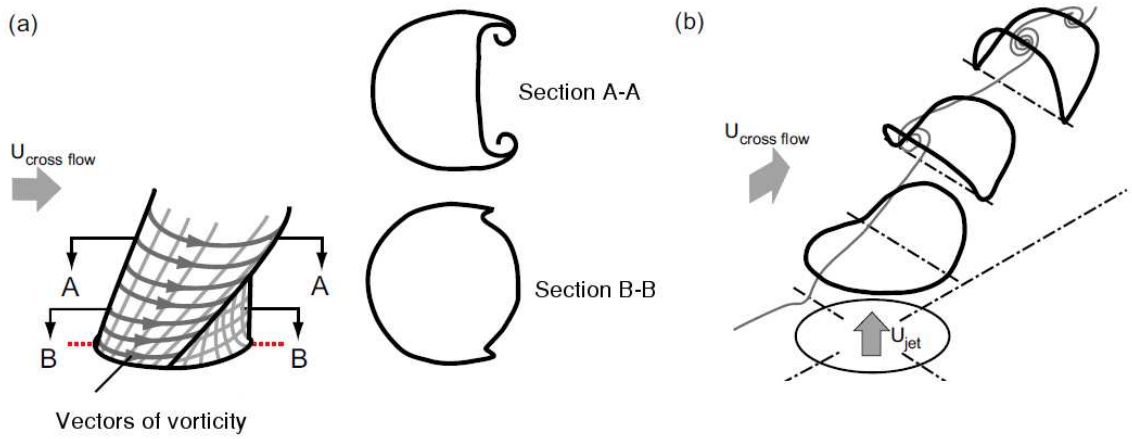

Figure 2.8: a) Interpretation of the folding of the cylindrical vortex sheet and b) Entrainment and tilting of vortex rings as proposed by Kelso, Lim & Perry [49]

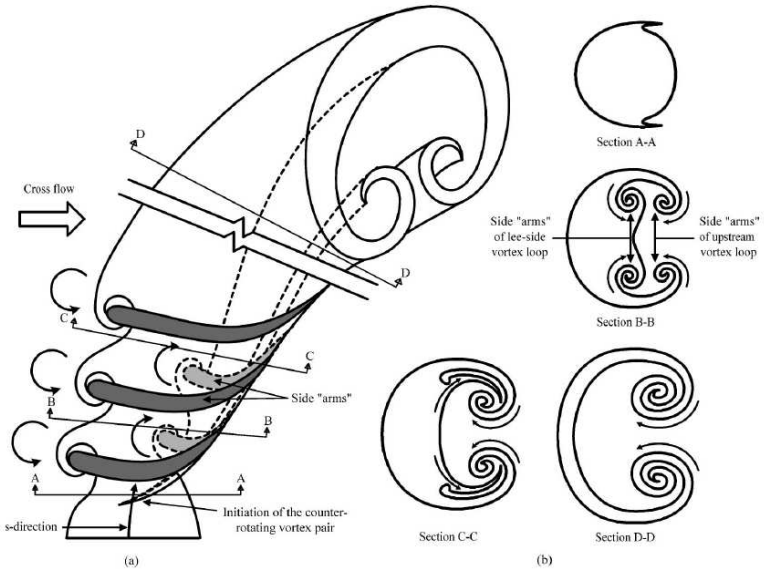

Figure 2.9: Interpretation of the originating of the CRVP by Lim, New & Luo [56]

LES computations by Yuan et al. [106] relate the very origin of the CRVP to hanging vortices at the lateral edges of the jet close to the wall. In these regions the high velocities of both the cross flow and the jet create skewed mixing layers. Within these areas quasi-steady vortices are observed. Vortical fluid from the supporting pipe passes through these vortices and is transported to the back of the jet. The breakup of the hanging vortices finally leads to the origin of the weaker CRVP. More recently, Sau, Sheu, Hwang et al. support this hypothesis in a series of publications [84, 85]

Figure 2.10: DNS of a square jet in cross flow with the origin of the CRVP inside the jet boundary layer [84]

on a square jet in cross flow computation employing DNS. They clearly see the origin of the CRVP in the lateral jet pipe boundary layer as illustrated by figure 2.10.

As a concluding remark it has to be mentioned that the shear layer vortices and the CRVP interfere quite strongly with each other. The question whether the very origin of the CRVP lies in the skewed mixing layer as proposed by Yuan et al. or in the folding and stretching of the shear layer ring vortices proposed by Kelso et al. remains still unanswered.

2.2.3 Horseshoe Vortex System

The origin of the horseshoe vortex can be attributed to the adverse pressure gradient present at the wall upstream of the jet. Similar flow fields are identified for any wall-mounted blunt body, which might lead to the assumption that the horseshoe vortex resulting from a round jet in cross flow is identical to that of a rigid cylinder.

Kelso & Smits [50] however refer to the entraining vortex sheet, the formation of vortex rings and the flow separations inside the supporting pipe as differences, which lead to an unsteady behavior of the horseshoe vortex and cannot be compared to the flow around a wall-mounted cylinder. From water tunnel test campaigns the authors were able to classify the dynamical behavior of the horseshoe vortex into three regimes depending on velocity ratio and Reynolds number; i.e. steady, oscillating and coalescing. The steady regime is characterized by two vortices with the same sign in vorticity as the wall boundary layer, while the other cases show a third vortex. In the first unsteady regime the vortices oscillate in direction of the main stream, while for the

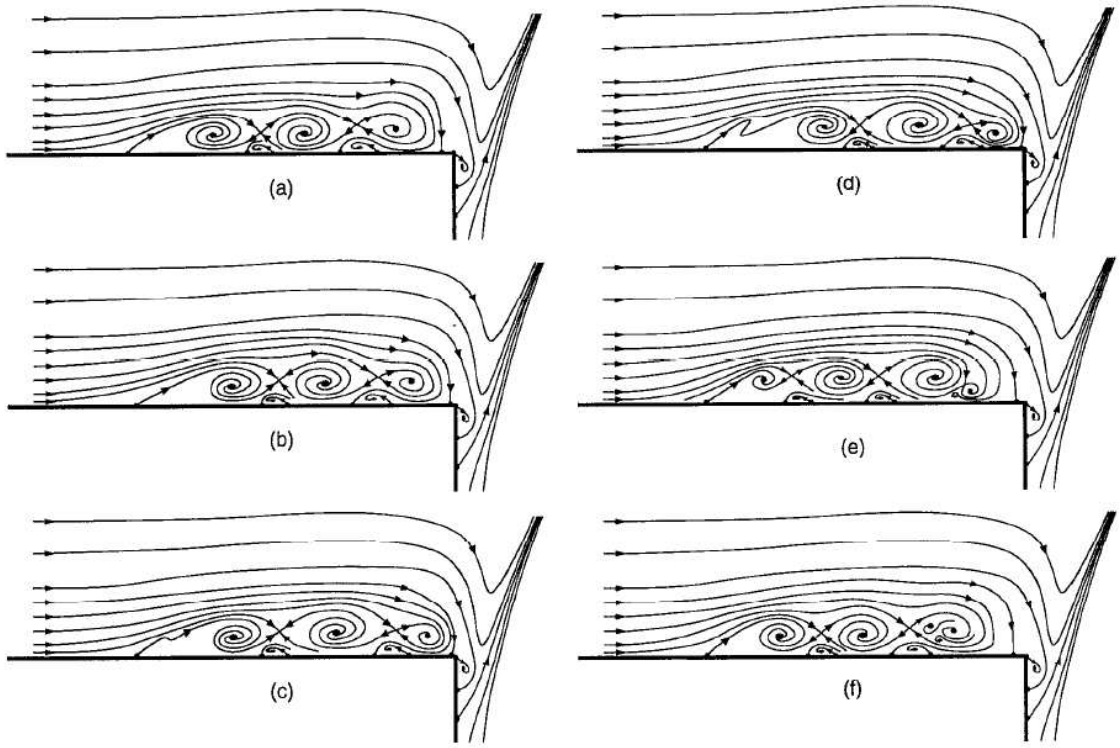

Figure 2.11: Evolution of horseshoe vortices in coalescing flow regime [50]

second unsteady regime (coalescing) the vortices advect downstream and merge with each other as a new vortex is formed upstream. This pattern is depicted in figure 2.11

Additionally to this, a small oscillation is found for all three regimes due to the periodic formation of the shear layer vortices. The free ends of the horseshoe vortex can play an important role in the wake, which will be discussed in the following subsection. Since Sau [84, 85] reported only one vortex in their DNS of a square jet, the question remains whether Kelso's and Smit's classification is limited to round jets and a specific range of Reynolds numbers or effective velocity ratios.

2.2.4 Wake Vortices

The existence of shear layer vortices, a CRVP and a horseshoe vortex can be expected for a JICF even if the effective velocity ratio is small. Considering however the wake region, the development of coherent structures will strongly depend whether the jet remains attached to the wall or whether it is lifted up. Furthermore, turbulent interaction between the structures will be more important for small velocity ratios. From experimental investigations Gopalan et al. [38] distinguish two different regimes with the demarcating velocity ratio around two.

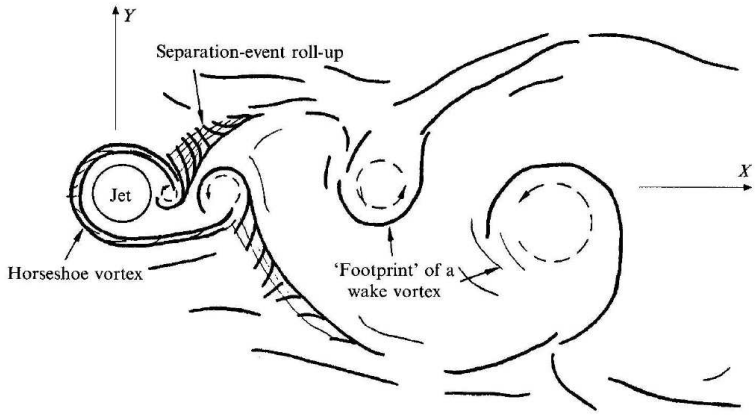

Figure 2.12: Boundary layer roll-up and footprints of wake vortices [34]

High Velocity Ratios

Equivalent to the formation of the horseshoe vortex, a similarity might be expected between the wake structures of a JICF and those of a flow around a rigid cylinder. This analogy was examined by Fric & Roshko [34]. Height H of the cylinder and penetration of the JICF should be of the same order to obtain comparable flow fields. In the studied case, the velocity ratio $C_R = 4$ for the JICF corresponds to a cylinder with an aspect ratio $\Lambda = H/D = 6$. The experiments showed however that the cross flow wraps around the jet, whereas the flow around the solid cylinder separates and forms an open wake. Additionally, an early formation of vortical structures is observed for the jet wake.

As illustrated in figure 2.5 upright vortical structures develop, resembling the vortices behind a cylinder caused by the shedding of vorticity, which is generated at the wall of the cylinder. If one considers the transport equation for vorticity ω in incompressible flows

$$\frac{D\omega}{Dt} = \omega \cdot \nabla u + \nu \nabla^2 \omega, \tag{2.8}$$

no explicit source term is visible, which means that vorticity can only be generated at wall boundaries [67]. Indeed, Fric & Roshko showed in their experiments that upright structures contain vorticity from the cross flow boundary layer. This is important to notice and additionally completely different to the vortex shedding observed from rigid cylinders. The authors propose an interpretation of the formation as illustrated in figure 2.12.

Due to an adverse pressure gradient, the boundary layer separates and vorticity is tilted and stretched to form upright vortices. If an alternate and periodic separation of the boundary layer takes place on each side of the jet, a structure very similar to the von Kármán vortex street appears. Kelso et al. [49] mentioned however that

this has not to be necessarily the case. A recent LES by Komuro & Tsukiji [53] supports this statement as illustrated in figure 2.13, where no periodic pattern is visible regarding the orientation of the vortices. Finally, for very high momentum ratios, i.e. above $C_R = 8$, the entrainment of the jet does not reach the wall anymore to produce well developed structures.

Additionally, as it already becomes obvious in figure 2.12, the arms of the horseshoe vortex play a role in the wake of the jet since they might also be entrained by the CRVP. The DNS of Sau et al. confirms this behavior for low cross flow Reynolds numbers. Figure 2.14 shows the entrainment of the horseshoe vortex (yellow streamlines) and the formation of two pairs of upright vortices (red and blue streamlines) from the boundary layer.

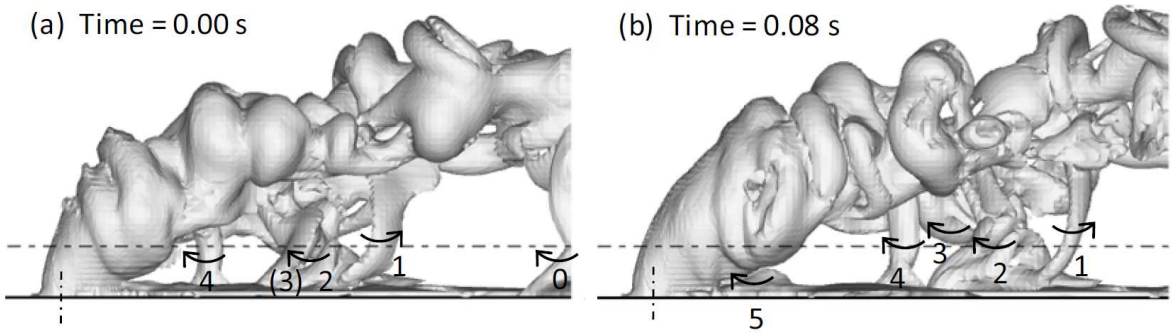

Figure 2.13: Development of wake vortices including rotational direction as computed in a Large Eddy Simulation at $Re_{cf} = 3\,800$ and $C_R = 4$ [53]

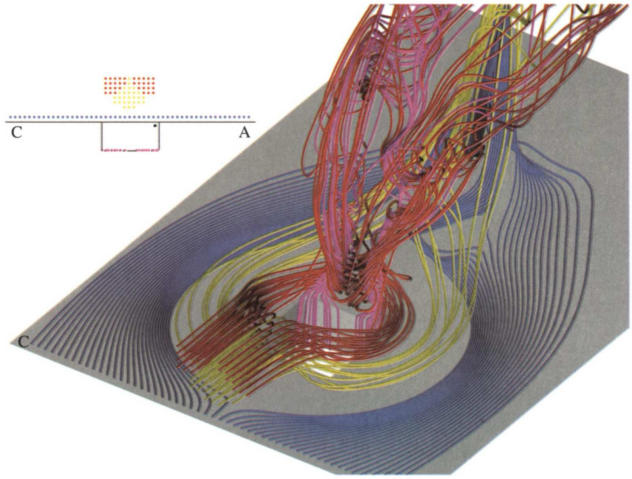

Figure 2.14: The entrainment of the horseshoe vortex (yellow streamlines) and the formation of two pairs of upright vortices (red and blue streamlines) from the boundary layer [84]

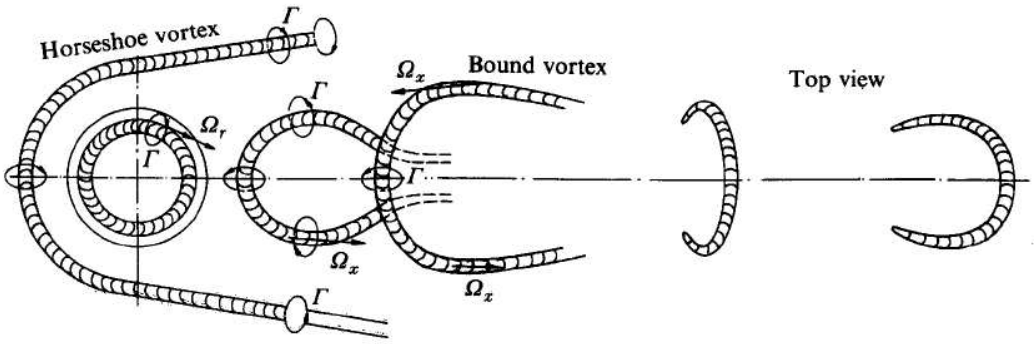

Figure 2.15: Formation of archlike vortices proposed by ANDREOPOULOS [7]

Low Velocity Ratios

In contrast to high effective velocity ratios, the formation of upright vortices is not observed for values smaller than two. In this case, the cross flow acts as a partial cover of the jet and bends it over rather strongly in such a way that the jet remains attached to the downstream wall. However, experiments conducted by ANDREOPOULOS [7] for a JICF with an effective velocity ratio of 0.5 show that large-scale structures exist in the jet wake. They exit from the supporting pipe with a vorticity of the same sign as the pipe boundary layer and decay within 6-10 diameters downstream of the orifice. A Strouhal number $St_D = fD/U_\infty$ with the characteristic frequency f is found to be equal to 0.4. However, the regularity of the appearance decreases with growing cross flow Reynolds numbers and the size of the structures varies over a wide range.

An illustration of the proposed formation of these structures is depicted in figure 2.15. As the vortex ring exits the supporting pipe, the downstream part is stretched, breaks up and two legs are forming. After being advected some distances behind the orifice, the upper part is also accelerated by the cross flow. Even if this model is based on experiments with a laminar jet boundary layer, the author emphasizes its valid extension to turbulent jet boundary layers.

Results from a Large Eddy Simulation conducted by TYAGI [99] with $C_R = 0.5$ and $Re_{cf} = 4\,700$ are depicted in figure 2.16. An isosurface of the Laplacian of pressure is used to identify vortex core regions and three archlike vortices become visible in this instantaneous view. Even if these structures are consistent with those described by ANDREOPOULOS, their origin and dynamics are not yet clear.

Concerning the velocity field directly downstream of the jet, ANDREOPOULOS & RODI [8] identify a region of reversed flow for low effective velocity ratios. Large Eddy Simulations conducted by IOUROKINA & LELE [42] as well as experimental studies by GOPALAN ET AL. [38] support these findings but the connection with the development of archlike vortices is not examined.

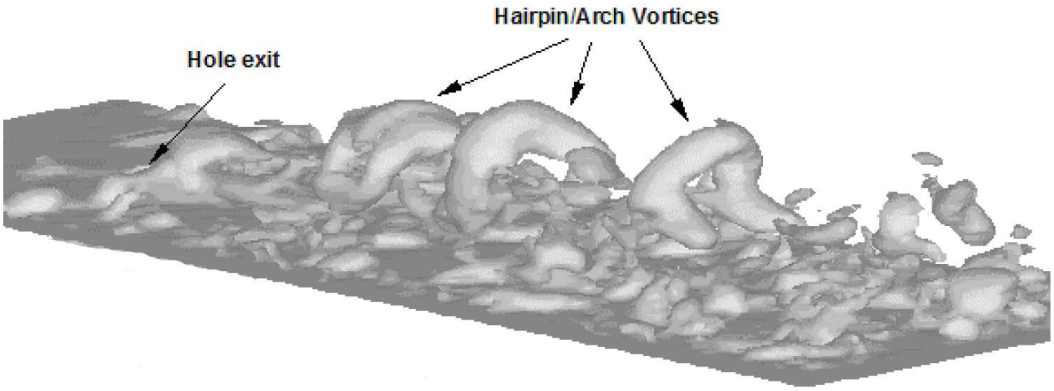

Figure 2.16: Coherent structures obtained from an LES at $C_R = 0.5$ and $Re_{cf} = 4\,700$ indicating hairpin vortices [99]

2.3 Thermal Mixing Aspects

Due to the highly turbulent flow field and the existence of coherent structures in the wake of the jet, the energy transfer caused by thermal mixing between the jet and the cross flow is quite distinctive. However, the identification and description of mixing phenomena which are responsible for heat transfer other than the CRVP are not reported and the available literature is limited.

For the considered configurations, the temperature distribution behind the jet is of special interest. Therefore, the local thermal efficiency η is defined as

$$\eta = \frac{T - T_\infty}{T_j - T_\infty}, \tag{2.9}$$

with the static temperature T, the free stream temperature T_∞ and the jet temperature T_j. This definition was originally introduced for film cooling application but holds for the inverse case, i.e. a hot jet in a cold cross flow, as well. If instead of the temperature T the adiabatic wall temperature T_{aw} is used, the thermal footprint of the jet is obtained at the wall.

Clearly, the similarity parameters introduced in section 2.1.1 have a strong influence on the wall temperature distribution. Recalling the effective velocity ratio C_R, a higher jet momentum will lead to a deeper penetration of the jet into the cross flow and therefore to a smaller thermal footprint. A high cross flow Reynolds number Re_{cf} on the other side leads to the formation of smaller structures, which will result in an enhanced thermal mixing behavior. The ratio of cross flow boundary layer thickness to jet diameter Λ_δ also has a strong influence on the thermal footprint. In the case of a thick boundary layer, the jet will not be able to penetrate it and the thermal impact on the wall will be rather strong. Depending on the application, different characteristics

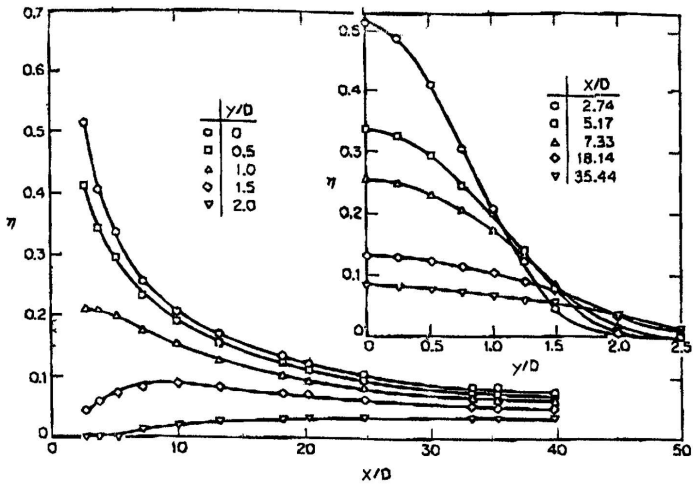

Figure 2.17: Wall thermal efficiency η in streamwise X/D and spanwise Y/D direction for $C_R = 0.469$ and $Re_{cf} = 87\,000$ [30]

are desirable. Eriksen [30] measured the time-averaged wall temperature distribution behind the jet and an example evolution is illustrated in figure 2.17 with the spanwise coordinate Y/D and the streamwise coordinate X/D. In the near and mid field of the jet, i.e. X/D up to 10, the jet has a strong impact on the wall temperature. This is caused by the small momentum ratio which characterizes an attached jet wake. Even if a strong gradient can be seen for the centre line $Y/D = 0$ in streamwise direction, the influence on the wall temperature is still perceivable even in the very far field. The lateral influence is also rather important and extends up to $2.5D$ to each side of the symmetry plane. As shown by experimental investigations of Andreopoulos [6], thermal efficiency on the symmetry plane scales with the square root of the distance to the ejector for velocity ratios smaller than two, i.e. $\eta\,(Y/D = 0) \sim (X/D)^{-1/2}$.

In another experimental study, Ramsey and Goldstein [75] obtained the averaged temperature distribution on lateral planes downstream of the orifice for two different effective velocity ratios as depicted in figure 2.18. For both ratios, kidney shaped temperature contours become apparent on the first plane, which are a result of the counter-rotating vortex pair. This study also points out the influence of the effective velocity ratio. For the case of the lower jet momentum, the maximal temperature on the lateral planes is obtained at the wall. Considering the higher jet momentum, the temperature contours form circles and the maximal temperature of the plane is found above the surface.

The influence of small effective velocity ratios as well as the shape of the ejector on the thermal footprint was examined experimentally by Albugues in his thesis [4]. It was shown that the impact of the velocity ratio is superior over the impact of the shape. Actually all thermal traces almost collapsed for the smallest value of $C_R = 0.37$,

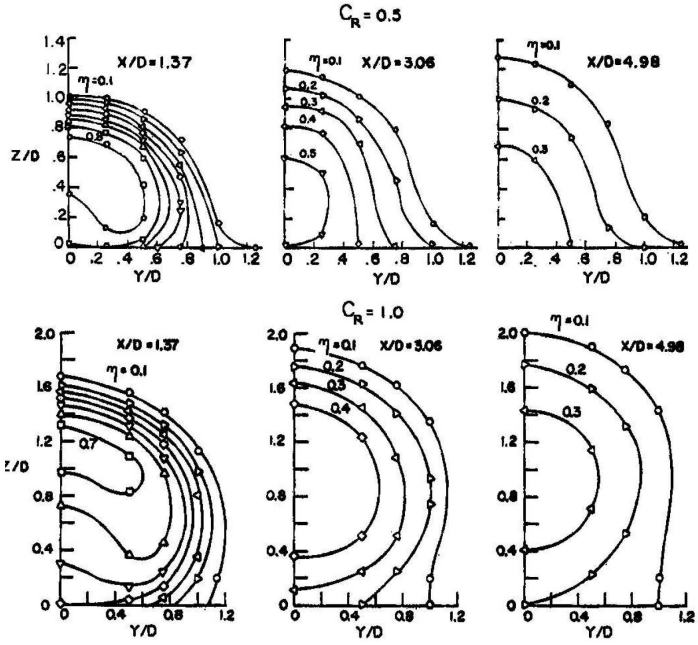

Figure 2.18: Thermal efficiency η on lateral planes downstream of the ejector for $C_R = 0.5$ and $C_R = 1.0$ as well as $Re_{cf} = 87\,000$ [75]

irrespective the ejector shape. Additionally, the maximal thermal efficiency decreases if multiple ejectors are employed with the same accumulated cross sectional area as a single ejector.

As jets in cross flow are frequently used for film cooling applications, the heat transfer coefficient h and with this the Nusselt number $Nu = hL/\lambda$ are also of interest. In an experimental study by Carlomagno et al. [17], convective heat transfer measurements were performed for a round jet in cross flow with velocity ratios ranging from 1 to 5 at a constant cross flow Reynolds number of 8 000. For all configurations a region of large Nusselt numbers were found in front of the jet. The authors contribute this to a suction effect, which the jet has on the oncoming boundary layer. The behavior of the Nusselt number in the wake is governed by the forming of the counter-rotating vortex pair, which is strongly dependent on the velocity ratio. In general, the Nusselt number distribution enlarges in lateral direction for increasing velocity ratio but its maximal value decreases.

If the cross flow Richardson number is small, the variable temperature can be regarded as a passive scalar. This analogy allows the transfer of results from scalar mixing in a JICF to cases where a moderate temperature difference between jet and cross flow fluid exists. An experimental study was carried out by Smith & Mungal [90] for velocity ratios between 5 and 25 with corresponding cross flow Reynolds numbers between 8 400 and 41 500. Planar images of concentration show that free stream fluid deeply penetrates the upper edge of the jet leading to strong mixing in the wake and

that small regions with high concentrations exist. Transferring the latter observation to a hot jet in cross flow indicates that spots with a high temperature appear in the wake, which can impact on the wall for cases with smaller velocity ratios. Ensemble-averaged images allow the investigation on concentration decay along the jet path and the possibility of self-similarity is discussed. Focussing on one specific configuration, i.e. $C_R = 5.7$ and $Re_{cf} = 5\,000$, Su and co-workers [94, 95] study jet trajectory, concentration fields and its decay along the jet path. Additional attention is paid to the measurement of shear stresses, scalar flux components and averaged scalar variance. A main observation was that maximal mixing takes initially place in the upstream shear layer but as the jet is bent into the direction of the cross flow the mixing of the downstream shear layer becomes eventually more important.

An interesting approach in enhancing the mixing behavior consists in unsteady forcing of the jet flow. Narayanan, Barooah & Cohen [70] employed a flow control mechanism and studied the influence of high and low frequency forcing. On the one hand, they found that high frequency forcing has an impact on Kelvin-Helmholtz instabilities but the effect on mixing behavior is small. On the other hand, low frequency forcing in the range of $St_D = 0.2 - 0.4$ has a strong influence on the counter-rotating vortex pair and the associated dynamics in the jet wake leading to an enhanced mixing behavior.

2.4 Numerical Simulations

Apart from empirical models, the first elaborate numerical methods applied to predict jet in cross flow characteristics were integral models as described in [24]. Due to the increase in computational power and the advancements in turbulence modeling over the last two decades, the possibility of three-dimensional simulations for a jet in cross flow arose. To keep simulation costs manageable, steady state solutions of the RANS equations in combination with eddy viscosity turbulence models were investigated first. The definition of this approach implies that neither temporal nor spatial fluctuations are resolved; instead all effects arising from turbulent mixing and heat transfer have to be modeled. The simulation of a jet in cross flow poses therefore a major challenge for turbulence modeling since the influence of large and small scale dynamics on the time-averaged flow field needs to be accounted for.

RANS simulations carried out by Roth et al. [76],[77] and Li et al. [55] show that qualitatively reasonable agreement with experimental data can be obtained for the jet trajectory. Additionally, the counter-rotating vortex pair can be captured as well due to its steady behavior. The capabilities of different eddy viscosity turbulence models were investigated by Demuren [23], Acharya et al. [1] and Dai et al. [20]. The main findings were that RANS turbulence models within both the $k - \varepsilon$ and $k - \omega$ framework fail in predicting the correct velocity distribution and turbulence

kinetic energy. In order to obtain enhanced RANS simulations for a jet in cross flow, Lischer [57] focused on a special modification of existing turbulence models. By introducing an additional transport equation for eddy viscosity, an improved agreement with experimental data was obtained. Demuren [25] as well as Acharya et al. [2] investigated turbulence models based on second order closures, which can account for anisotropic effects of the flow. Even if this anisotropy is prevalent for the considered case, no noteworthy amelioration of the flow prediction became evident.

As steady RANS calculation did not show satisfying results, attention shifted towards transient simulations. The first unsteady RANS calculation based on a $k-\varepsilon$ turbulence model was carried out by Hsu, He & Gu [40]. More recently, this approach was applied to a buoyant jet in cross flow showing good agreement with experimental data [81]. In a series of publications, Ivanova and co-workers present numerical studies for scalar mixing in transverse jets for a very high velocity ratio of 26 and a cross flow Reynolds number of 20 000 [43, 44, 45]. In addition to an unsteady RANS simulation using a $k-\omega$ turbulence model, the Scale-Adaptive Simulation was applied and results compare well with experimental data for the mean and fluctuating velocity field. However, the high velocity ratio leads to a deep penetration into the cross flow and the interaction of the jet with the wall is small, which is contrary to the cases considered in this work. Complementing unsteady RANS simulations, Lagrangian simulations for jets in cross flow are proposed in [59] and [60], which do not rely on numerical grids. Even though characteristic structures for a jet in cross flow are observed, no comparison with experimental data was presented for validation of this method.

With further development in computational sciences, the focus of numerical simulations shifted towards LES and DNS computations. These types of simulations resolve either a part or the entire turbulence spectrum, which allows reproducing flow features and gaining insight into flow dynamics. The LES carried out by Ziefle & Kleiser [107] and Fröhlich et al. [35] for a jet in cross flow at a momentum ratio of 3.3 and a cross flow Reynolds number of 2 100 revealed all typical flow structures and is in good agreement with experimental data. More recently, Jouhaud et al. [46] performed an LES for a hot jet in cross flow at a very high cross flow Reynolds number of Re_{cf}=93 900, which compares well with experimental data for both the flow and temperature field. Due to high costs, simulations of multiple jets in cross flow however are not common and only one LES of this type of configuration is mentioned casually in [86]. On the DNS side, a detailed JICF study can be found in a series of publications by Denev et al [26], [27] and [28]. On the one hand, the agreement of flow statistics with experimental data is greatly enhanced by LES and DNS computations compared to simulations relying on statistical turbulence models. On the other hand, grid resolution requirements are extremely high and long simulation times are needed.

It remains therefore to say that a major drawback of these types of simulations is their limitation to small Reynolds numbers. As a matter of fact, almost all available LES in literature deal with cross flow Reynolds numbers in the order of 10^3 and

the use of DNS is restricted to even smaller values. Assuming constant growth in computational power, SPALART [91] estimated that LES of an aircraft at high Reynolds numbers will not be feasible before the year 2045. Even if the focus of this work concerns only a subsystem of the aircraft, fully resolved LES for wall-bounded jets in cross flow at Reynolds numbers in the range of $Re_{cf} = 10^4 - 10^6$ will not be possible in the near future. This shall be exemplified by the size estimation of a hexahedral mesh for the exhaust type shown in figure 1.1 installed on a flat plate (1m x 2m) at a Reynolds number of $5 \cdot 10^7$ based on the plate length. Wall adjacent mesh resolution requires a non-dimensional cell height in the order of 1 and a growing ratio in wall-normal direction of 1.15 inside the boundary layer. Outside the boundary layer the cell size in wall-normal direction is maintained in the zone of jet penetration. Spanwise and streamwise resolution for wall-bounded LES usually requires 40 and 20 non-dimensional wall units respectively. A total number of about $40 \cdot 10^9$ cells would then be necessary to discretize a block-shaped volume of 2m^3. As this is out of reach, advanced turbulence models with the capability to efficiently treat boundary layers and to locally resolve turbulent fluctuations need to be applied and their capabilities need to be explored.

Summarizing this chapter, the fundamental flow phenomenon of a jet in cross flow was described and corresponding similarity parameters such as velocity ratio and cross flow Reynolds number were introduced. State of the art knowledge on related dynamics and appearing coherent structures was presented, highlighting the inherent unsteady and turbulent character of this flow as well as the ongoing discussion about their origins. Special focus was put on thermal mixing between jet and cross flow but mixing phenomena other than the counter-rotating vortex pair are not reported in literature. Finally, existing approaches for numerical simulations were regarded, emphasizing the need for new strategies in order to cope with the aerothermal prediction of jets in cross flow at high Reynolds numbers.

Chapter 3

Turbulence Modeling

As it became apparent in the previous section, there is a lack of simulation capabilities for jets in cross flow at high Reynolds numbers, necessitating the investigation of new approaches based on scale-resolving turbulence models. Therefore, this chapter starts with a review of the need for turbulence modeling, followed by an elaboration and categorization of the models considered in this work. Finally, the strategy for the numerical solution of the resulting system of equations is outlined.

3.1 Governing Equations

Starting point for a numerical simulation are the conservation equations for mass, momentum and energy for compressible flows without source terms in differential notation using the Einstein summation convention

$$\frac{\partial \rho}{\partial t} + \frac{\partial}{\partial x_i}\left(\rho u_i\right) = 0 \tag{3.1}$$

$$\frac{\partial}{\partial t}\left(\rho u_i\right) + \frac{\partial}{\partial x_j}\left(\rho u_j u_i\right) = -\frac{\partial p}{\partial x_i} + \frac{\partial}{\partial x_j}\left(\tau_{ij}\right) \tag{3.2}$$

$$\frac{\partial}{\partial t}\left(\rho E\right) + \frac{\partial}{\partial x_j}\left(\rho u_j H\right) = \frac{\partial}{\partial x_j}\left(u_i \tau_{ij}\right) - \frac{\partial}{\partial x_j}\left(q_i\right), \tag{3.3}$$

with fluid density ρ, time t and velocity components u_i in the direction of the Cartesian coordinates x_i. Considering a Newtonian fluid and Stokes' Law, the viscous stress tensor τ_{ij} can be expressed as

$$\tau_{ij} = 2\mu\left(S_{ij} - \frac{1}{3}\frac{\partial u_k}{\partial x_k}\delta_{ij}\right), \tag{3.4}$$

with the dynamic viscosity μ and the strain rate S_{ij} defined as the symmetrical part of the velocity gradient tensor:

$$S_{ij} = \frac{1}{2}\left(\frac{\partial u_i}{\partial x_j} + \frac{\partial u_j}{\partial x_i}\right). \tag{3.5}$$

The heat flux q_j can be related to the temperature gradient using Fourier's Law

$$q_j = -\lambda \frac{\partial T}{\partial x_j} \tag{3.6}$$

by specifying the thermal conductivity λ of the fluid. Assuming an ideal gas, the pressure p can be obtained from the state equation

$$p = \rho R T, \tag{3.7}$$

with the specific gas constant R. Specific internal energy e and specific enthalpy h can then be related to temperature via

$$e = c_v T \quad \text{and} \quad h = c_p T \tag{3.8}$$

using the specific heat capacities c_v and c_p at constant volume and constant pressure respectively. This allows the definition of the total energy E and total enthalpy H:

$$E = e + \frac{u_i u_i}{2} \quad \text{and} \quad H = h + \frac{u_i u_i}{2}. \tag{3.9}$$

Specifying fluid dependent values for the constants μ, λ and $R = c_p - c_v$, the resulting set of equations is closed and can be solved numerically when appropriate initial and boundary conditions are imposed.

3.1.1 Reynolds-Averaging

As no assumption has been made concerning a laminar or a turbulent flow, these equations equally hold for both cases. However, the direct numerical solution for highly turbulent wall bounded flows is practically not feasible since a very fine spatial and temporal resolution is needed, leading to extremely high or even unattainable computational costs. Additionally, the impact of small scale turbulence motion on the mean flow is in most cases of more interest than the resolution of these fluctuations itself. For these reasons, the set of equations is treated statistically by using Reynolds' decomposition. Considering the temporal evolution of a flow variable $\phi(\vec{x}, t)$, it can be separated into a mean part $\bar{\phi}(\vec{x})$ and a fluctuating part $\phi'(\vec{x}, t)$, such as

$$\phi(\vec{x}, t) = \bar{\phi}(\vec{x}) + \phi'(\vec{x}, t), \tag{3.10}$$

with

$$\bar{\phi}(\vec{x}) = \lim_{\Delta t \to \infty} \frac{1}{\Delta t} \int_t^{t+\Delta t} \phi(\vec{x}, t) \mathrm{d}t \tag{3.11}$$

over a discrete time step Δt. As the compressible Navier-Stokes equations need to be considered, it is more convenient to use a mass-weighted Reynolds-Average as introduced by Favre [31, 32]

$$\tilde{\phi} = \frac{\overline{\rho \phi}}{\overline{\rho}}, \tag{3.12}$$

which leads to the decomposition

$$\phi(\vec{x},t) = \tilde{\phi}(\vec{x}) + \phi''(\vec{x},t). \tag{3.13}$$

Introducing the original Reynolds decomposition for pressure and density, applying the mass-weighted Reynolds decomposition for all other dependent flow variables and exercising once again the averaging procedure described, the compressible Reynolds-Averaged Navier-Stokes Equations are obtained

$$\frac{\partial \overline{\rho}}{\partial t} + \frac{\partial}{\partial x_i}\left(\overline{\rho}\tilde{u}_i\right) = 0 \tag{3.14}$$

$$\frac{\partial}{\partial t}\left(\overline{\rho}\tilde{u}_i\right) + \frac{\partial}{\partial x_j}\left(\overline{\rho}\tilde{u}_j\tilde{u}_i\right) = -\frac{\partial \overline{p}}{\partial x_i} + \frac{\partial}{\partial x_j}\left(\tilde{\tau}_{ij} - \widetilde{\overline{\rho}u_i''u_j''}\right) \tag{3.15}$$

$$\begin{aligned}\frac{\partial}{\partial t}\left(\overline{\rho}\tilde{E}\right) + \frac{\partial}{\partial x_j}\left(\overline{\rho}\tilde{u}_j\tilde{H}\right) &= \frac{\partial}{\partial x_j}\left[\tilde{u}_i\left(\tilde{\tau}_{ij} - \widetilde{\overline{\rho}u_i''u_j''}\right)\right] \\ &\quad - \frac{\partial}{\partial x_j}\left(\tilde{q}_j + \widetilde{\overline{\rho}u_j''h''} - \widetilde{\tau_{ij}u_i''} + \widetilde{\overline{\rho}u_j''k}\right),\end{aligned} \tag{3.16}$$

with the turbulence kinetic energy $k = \frac{1}{2}u_i''u_i''$. Due to the nonlinear convection terms $\frac{\partial}{\partial x_j}(\rho u_j u_i)$ and $\frac{\partial}{\partial x_j}(\rho u_j H)$ in the momentum and energy conservation equations, unknown correlations of fluctuating quantities enter the equations respectively, i.e. $\widetilde{u_i''u_j''}$, $\widetilde{u_i''h''}$, $\widetilde{\tau_{ij}u_i''}$ and $\widetilde{u_j''k}$. Their appearance can be explained physically since turbulent fluctuations do not cancel each other out and need to be accounted for in time-averaged solutions.

An important assumption in order to close this extended set of equations is to make use of the Boussinesq hypothesis, which states in analogy to molecular shear stresses that turbulent shear stresses can be related to the mean velocity gradient via a turbulent viscosity μ_t:

$$\tilde{\tau}_{ij}^{turb} = -\widetilde{\overline{\rho}u_i''u_j''} = 2\mu_t\left(\tilde{S}_{ij} - \frac{1}{3}\frac{\partial \tilde{u}_k}{\partial x_k}\delta_{ij}\right) - \frac{2}{3}\bar{\rho}\tilde{k}\delta_{ij}. \tag{3.17}$$

The last term has been added to ensure that the trace of the Reynolds stress tensor $\tilde{\tau}_{ij}^{turb}$ satisfies the definition of the turbulence kinetic energy. Similarly to this, the turbulent heat flux $\tilde{q}_j^{turb}$ can be approximated by applying Fourier's law to the mean temperature gradient

$$\tilde{q}_j^{turb} = \bar{\rho}\widetilde{v_j''h''} = -\lambda_t\frac{\partial \tilde{T}}{\partial x_j} \tag{3.18}$$

and by introducing a turbulent thermal conductivity λ_t. The last two terms in equation (3.16), signifying molecular diffusion of k and turbulent transport of k, can be neglected

for transonic and supersonic flows. This finally allows rewriting the set of equations as

$$\frac{\partial \overline{\rho}}{\partial t} + \frac{\partial}{\partial x_i}\left(\overline{\rho}\tilde{u}_i\right) = 0 \tag{3.19}$$

$$\frac{\partial}{\partial t}\left(\overline{\rho}\tilde{u}_i\right) + \frac{\partial}{\partial x_j}\left(\overline{\rho}\tilde{u}_j\tilde{u}_i\right) = -\frac{\partial \bar{p}}{\partial x_i} + \frac{\partial}{\partial x_j}\left(\tilde{\tau}_{ij} + \tilde{\tau}_{ij}^{turb}\right) \tag{3.20}$$

$$\frac{\partial}{\partial t}\left(\overline{\rho}\tilde{E}\right) + \frac{\partial}{\partial x_j}\left(\overline{\rho}\tilde{u}_j\tilde{H}\right) = \frac{\partial}{\partial x_j}\left[\tilde{u}_i\left(\tilde{\tau}_{ij} + \tilde{\tau}_{ij}^{turb}\right)\right] - \frac{\partial}{\partial x_j}\left(\tilde{q}_j + \tilde{q}_j^{turb}\right), \tag{3.21}$$

which has formally the same structure as the instantaneous equations (3.1)-(3.3). By defining a turbulent Prandtl number $Pr_t = c_p\frac{\mu_t}{\lambda_t}$, which can be assumed to be constant in most flows, the modeling of the unknown correlations, which have been introduced by the averaging procedure, is reduced to assess a turbulent viscosity μ_t. This is the task of the statistical turbulence model.

3.1.2 Spatial Filtering

Another method to cope with turbulent flows at moderate Reynolds numbers is to apply a filtering technique to the Navier-Stokes equations. The idea is to use a low pass filter in order to eliminate small scale turbulent fluctuations. As large-scale turbulent motion of the fluid is preserved, this approach is referred to as Large Eddy Simulation. The operation for a flow variable ϕ reads

$$\overline{\overline{\phi}}(\vec{x},t) = \int_\Omega \phi(\vec{x},t)G(\vec{x}_0,\vec{x})\mathrm{d}\vec{x}, \tag{3.22}$$

with the filter kernel G and the flow domain Ω. Different definitions exist, with the simplest approach being the filter over the volume V of a computational cell:

$$G(\vec{x},\vec{x}_0) = \begin{cases} 1/V, & \text{if } \vec{x}_0 \in \Omega \\ 0, & \text{otherwise.} \end{cases} \tag{3.23}$$

As the compressible Navier-Stokes equations need to be considered, a density weighted filtering similar to the Favre-averaging is applied:

$$\widehat{\phi} = \frac{\overline{\overline{\rho\phi}}}{\overline{\overline{\rho}}}. \tag{3.24}$$

Introducing spatial filtering for density and pressure as well as the density weighted filtering for all other flow variables, the filtered Navier-Stokes equations are obtained:

$$\frac{\partial \overline{\overline{\rho}}}{\partial t} + \frac{\partial}{\partial x_i}\left(\overline{\overline{\rho}}\widehat{u}_i\right) = 0 \tag{3.25}$$

$$\frac{\partial}{\partial t}\left(\overline{\overline{\rho}}\widehat{u}_i\right) + \frac{\partial}{\partial x_j}\left(\overline{\overline{\rho}}\widehat{u}_j\widehat{u}_i\right) = -\frac{\partial \overline{\overline{p}}}{\partial x_i} + \frac{\partial}{\partial x_j}\left(\widehat{\tau}_{ij} + \tau_{ij}^{SGS} + \mathcal{A}\right) \tag{3.26}$$

$$\frac{\partial}{\partial t}\left(\overline{\overline{\rho}}\widehat{E}\right) + \frac{\partial}{\partial x_j}\left(\overline{\overline{\rho}}\widehat{u}_j\widehat{H}\right) = \frac{\partial}{\partial x_j}\left(\widehat{u}_i\widehat{\tau}_{ij} - \widehat{q}_j + q_j^{SGS} + \mathcal{B} + \mathcal{C} + \mathcal{D}\right). \tag{3.27}$$

The assumption has been made that the filtering operation and the differentiation operation commute. This is in general not the case but the introduced errors are usually negligible. Again, due to the nonlinear convective terms $\frac{\partial}{\partial x_j}(\rho u_j u_i)$ and $\frac{\partial}{\partial x_j}(\rho u_j H)$ in the momentum and energy conservation equations, unknown correlations defined as

$$\tau_{ij}^{SGS} = -\overline{\overline{\rho}}\left(\widehat{u_i u_j} - \widehat{u}_i \widehat{u}_j\right) \tag{3.28}$$

$$q_j^{SGS} = c_p \overline{\overline{\rho}}\left(\widehat{u_j T} - \widehat{u}_j \widehat{T}\right) \tag{3.29}$$

$$\mathcal{A} = \overline{\overline{\tau}}_{ij} - \widehat{\tau}_{ij} \tag{3.30}$$

$$\mathcal{B} = \overline{\overline{\rho}}\left(\widehat{u_j k} - \widehat{u}_j \widehat{k}\right) \tag{3.31}$$

$$\mathcal{C} = \overline{\overline{q}}_j - \widehat{q}_j \tag{3.32}$$

$$\mathcal{D} = \overline{\overline{u_j \tau_{ij}}} - \widehat{u}_j \widehat{\tau}_{ij} \tag{3.33}$$

are introduced. The first correlation term τ_{ij}^{SGS} representing the subgrid-scale shear stresses is expanded by the isotropic part $\frac{1}{3}\tau_{kk}^{SGS}\delta_{ij}$:

$$\tau_{ij}^{SGS} = \tau_{ij}^{SGS} - \frac{1}{3}\tau_{kk}^{SGS}\delta_{ij} + \frac{1}{3}\tau_{kk}^{SGS}\delta_{ij}. \tag{3.34}$$

The deviatoric part can be modeled following the Boussinesq hypothesis as

$$\tau_{ij}^{SGS} - \frac{1}{3}\tau_{kk}^{SGS}\delta_{ij} = 2\mu_t\left(\widehat{S}_{ij} - \frac{1}{3}\frac{\partial \widehat{u}_k}{\partial x_k}\delta_{ij}\right). \tag{3.35}$$

The second correlation term representing the subgrid-scale energy flux q_j^{SGS} can be modeled as

$$q_j^{SGS} = -\lambda_t \frac{\partial \widehat{T}}{\partial x_j}. \tag{3.36}$$

The viscous stress term $\mathcal{A}$ as well as the heat flux term $\mathcal{C}$ are usually neglected. According to KNIGHT [52], the correlation term $\mathcal{B}$ signifying subgrid-scale turbulent diffusion can be modeled as

$$\overline{\overline{\rho}}\left(\widehat{u_j k} - \widehat{u}_j \widehat{k}\right) = \widehat{u}_j \tau_{ij}^{SGS}. \tag{3.37}$$

Due to the small contribution to the energy equation, the viscous diffusion term $\mathcal{D}$ is not taken into account. Using these simplifications and modeling assumptions, the Favre-filtered Navier-Stokes equations can now be rewritten as

$$\frac{\partial \overline{\overline{\rho}}}{\partial t} + \frac{\partial}{\partial x_i}\left(\overline{\overline{\rho}}\widehat{u}_i\right) = 0 \tag{3.38}$$

$$\frac{\partial}{\partial t}\left(\overline{\overline{\rho}}\widehat{u}_i\right) + \frac{\partial}{\partial x_j}\left(\overline{\overline{\rho}}\widehat{u}_j\widehat{u}_i\right) = -\frac{\partial \overline{\overline{p}}}{\partial x_i} + \frac{\partial}{\partial x_j}\left(\widehat{\tau}_{ij} - \tau_{ij}^{SGS}\right) \tag{3.39}$$

$$\frac{\partial}{\partial t}\left(\overline{\overline{\rho}}\widehat{E}\right) + \frac{\partial}{\partial x_j}\left(\overline{\overline{\rho}}\widehat{u}_j\widehat{H}\right) = \frac{\partial}{\partial x_j}\left[\widehat{u}_i\left(\widehat{\tau}_{ij} + \tau_{ij}^{SGS}\right) - \left(\widehat{q}_j + q_j^{SGS}\right)\right] \tag{3.40}$$

and be solved by specifying a turbulent viscosity μ_t and a turbulent thermal conductivity λ_t with the help of a subgrid-scale model. Even though the physical concept between Reynolds averaging and spatial filtering is different, the resulting set of equations bears a remarkable resemblance to the RANS equations. This will be further discussed in subsection 3.3.5.

3.2 Scale-Resolving Simulations

A standard statistical turbulence model, which is generally used to close the steady state RANS equations by providing a turbulent viscosity, accounts for turbulent fluctuations only by modeling their statistical impact on the mean flow. This approach is well suited for attached boundary layers as well as shear layers and is also able to predict pressure induced boundary layer separation. However, as it is not possible to cover all turbulence related phenomena by one universal model and due to the advent of high performance computations, simulation strategies emerged, in which at least a portion of turbulent fluctuations is resolved in space and in time. All approaches satisfying this definition are summarized under the generalizing term Scale-Resolving Simulation (SRS). To illustrate this, the spectral function $E(\kappa)$ of turbulence kinetic energy is defined, which contains all kinetic energy of the turbulent fluctuations as a function of the wavenumber κ, allowing writing

$$k = \int_0^\infty E(\kappa)\mathrm{d}\kappa. \tag{3.41}$$

Due to the relation $\kappa = 2\pi/l$, with l being a length scale of turbulence motion, the energy spectrum function $E(\kappa)$ can be interpreted as a measure for the contribution of a turbulent eddy of size l to the total turbulence kinetic energy. For sufficiently high Reynolds numbers, the concept of the turbulence energy spectrum is governed by the idea of an energy cascade. This means that, generated by the mean shear rate, turbulence kinetic energy enters the process through large-scale motions, which are in the order of the characteristic length scale of the flow and are thus problem respectively geometry dependent. Due to instabilities of the large eddies, they subsequently break up into smaller and smaller vortices determined by a constant transfer rate of energy. The corresponding wavenumber spectrum is referred to as the inertial subrange since this process is not affected by viscous phenomena. However, as the velocity gradient for smaller eddies becomes more and more important, dissipation plays an increasingly more dominant role. The local Reynolds number based on the characteristic scales of the smallest velocities tending towards unity, dissipation of the smallest scales takes place. This means that the transfer rate of energy has to be equal to the dissipation rate at the end of the cascade.

An idealized spectrum for homogeneous and isotropic turbulence at high Reynolds numbers is illustrated in figure 3.1. Following the above explanation, this spectrum can

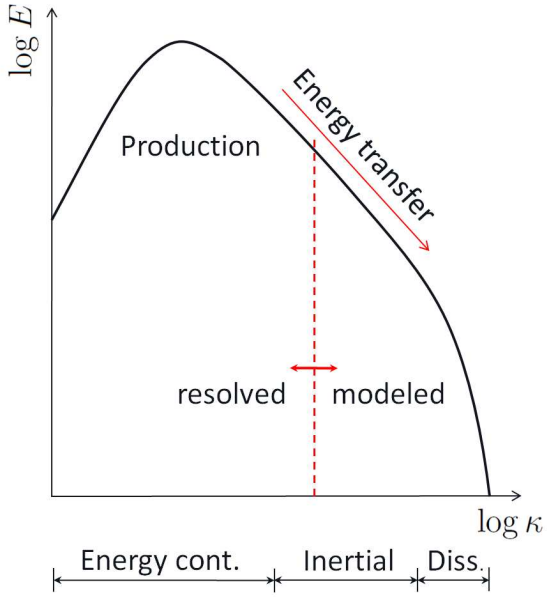

Figure 3.1: Idealized spectrum of homogeneous and isotropic turbulence

be divided into the energy containing part, the inertial subrange and the dissipation range depending on the length scale. For turbulence modeling, the most important aspect of the concept of the energy cascade arises from the increasingly more universal character for smaller scales. The idea of a Scale-Resolving Simulation now is to resolve the large, energy containing and geometry dependent vortices and to model the impact of the smaller and more universal ones. An example demarcation line between resolved and modeled turbulence scales has been placed inside the spectrum for illustration. Ideally, this line should lie within the inertial subrange since on the one hand, the resolution of geometry dependent vortices has to be ensured and on the other hand, the resolution of the dissipative scales is computationally not feasible.

The concept of SRS can be extended to only a local resolution of scales. Considering the air system exhaust shown in figure 1.1, it would be desirable to resolve turbulent fluctuations in the vicinity of the jet and cross flow interaction region and its wake. On the other side, the calculation of the global flow including boundary layers around the remaining parts of the nacelle or even the entire aircraft can in many cases be efficiently treated by employing steady state RANS turbulence models. In principle, two possibilities exist to achieve this: the *integrated* and the *sequential* approach.

3.3 Integrated Approaches

The integrated SRS approach can be defined as a simulation strategy, which allows the *local* resolution of scales in an area of interest, whereas at the same time (almost)

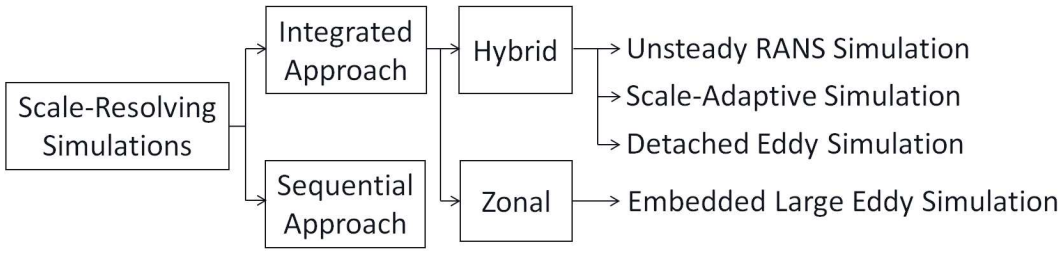

Figure 3.2: Categorization of Scale-Resolving Simulations

no turbulent fluctuations are resolved in the remaining parts of the computational domain. Again, two different possibilities exist to achieve this, which are referred to as the *hybrid* and the *zonal* approach. The hybrid integrated approach depends on one single turbulence model, which determines resolvable scale either via the underlying numerical mesh or via inherent flow instabilities. The zonal integrated approach on the other side relies on the definition of an a priori fixed fluid zone inside the domain of computation. A turbulence model that allows the resolution of scales is employed inside this fluid zone, whereas a standard RANS turbulence model is employed in the rest of the domain. Figure 3.2 illustrates this categorization and assigns the turbulence modeling approaches investigated throughout this work. They will be presented in the following sections while the model constants are listed in appendix A. The four designated strategies considered here are of course not exhaustive and many different but still related techniques exist like the Zonal Detached Eddy Simulation (ZDES) [22]. The final choice was based on maturity and on availability of the models in the CFD solver as well on their applicability on unstructured meshes in the prospect of the complex geometries envisaged.

3.3.1 Unsteady RANS Simulation

The simplest SRS approach originates from the idea of solving the unsteady Reynolds-Averaged Navier-Stokes equations with the help of a standard statistical turbulence model. As the simulation of a transient problem needs a finite numerical time step Δt, the averaging procedure as described in equation (3.11) is not strictly obeyed anymore. Instead, the assumption is made that Δt is large enough for averaging small turbulent fluctuations and yet small enough for resolving large-scale motion.

From dimensional reasoning, the dynamic eddy viscosity $\nu_t = \mu_t/\rho$, which is required to close the RANS equations, can be expressed via two variables, e.g. a velocity u^* and a length scale l^* of turbulent motion. To account for production, convection and historical effects of turbulence, transport equations are considered for these quantities.

In practical turbulence modeling it is very common to relate the turbulence kinetic energy k to the turbulent velocity scale as $u^* \sim \sqrt{k}$. This stems from the fact that a transport equation can be derived from the exact correlation of the Navier-Stokes equations with little modeling effort. The choice of the second transport equation is not as straightforward and many formulations for different variables have been proposed over the years. A common choice however is the specific dissipation rate ω, whose transport equation is modeled in analogy to the one of k. The specific dissipation rate ω having the dimension [1/s], a turbulence length scale can be expressed with $l^* \sim \sqrt{k}/\omega$, which finally allows writing the relation:

$$\nu_t \sim u^* l^* \sim \frac{k}{\omega}. \tag{3.42}$$

Several modifications and ameliorations of the original $k-\omega$ model have been developed throughout the years. The Shear Stress Transport (SST) turbulence model [62] is employed in the course of this work as it is optimized for turbulent boundary layers under adverse pressure gradients, commonly encountered in external aircraft aerodynamics. The two transport equations read

$$\frac{\partial}{\partial t}(\bar{\rho}k) + \frac{\partial}{\partial x_j}(\bar{\rho}\tilde{u}_j k) = \hat{P}_k - \beta^* \bar{\rho} k \omega + \frac{\partial}{\partial x_j}\left[\left(\mu + \frac{\mu_t}{\sigma_k}\right)\frac{\partial k}{\partial x_j}\right] \tag{3.43}$$

$$\begin{aligned}\frac{\partial}{\partial t}(\bar{\rho}\omega) + \frac{\partial}{\partial x_j}(\bar{\rho}\tilde{u}_j \omega) = {} & \alpha \frac{1}{\nu_t}\hat{P}_k - \beta \bar{\rho}\omega^2 + \frac{\partial}{\partial x_j}\left[\left(\mu + \frac{\mu_t}{\sigma_\omega}\right)\frac{\partial \omega}{\partial x_j}\right] \\ & + 2(1-F_1)\bar{\rho}\sigma_{w2}\frac{1}{\omega}\frac{\partial k}{\partial x_j}\frac{\partial \omega}{\partial x_j},\end{aligned} \tag{3.44}$$

with the constants $\alpha, \beta, \beta^*, \sigma_k, \sigma_\omega$ and $\sigma_{\omega 2}$, the blending function F_1 as well as the production terms $\hat{P}_k$ and P_k respectively:

$$\hat{P}_k = \min(P_k, 10 \cdot \beta^* \rho k \omega), \quad P_k = \mu_t \frac{\partial u_i}{\partial x_j}\left(\frac{\partial u_i}{\partial x_j} + \frac{\partial u_j}{\partial x_i}\right). \tag{3.45}$$

The dynamic eddy viscosity is finally calculated by

$$\nu_t = \frac{a_1 k}{\max(a_1 \omega, S F_2)}, \tag{3.46}$$

with the constants a_1 and the blending function F_2. This definition limits the shear stress in non-equilibrium flows such as adverse pressure gradient boundary layers, where production and dissipation of k do not cancel each other out. This in turn ensures the Bradshaw relation, which states that in these areas turbulent shear stresses are proportional to the turbulence kinetic energy. Finally, in combination with the time dependent RANS equations (3.19)-(3.21) a complete set of equations is available, which can be solved numerically.

3.3.2 Scale-Adaptive Simulation

Due to the fact that simple URANS approaches do not deliver satisfying results for flows comprising mixing phenomena, advanced statistical turbulence models have been developed. The Scale-Adaptive Simulation (SAS) by MENTER and co-workers [29, 63] being one of them, it is taken into consideration for the current flow problem.

One of the flaws of the common standard statistical turbulence model is the turbulence scale equation. As it became apparent in the previous section on the SST turbulence model, the ω-equation is a pure model equation relying on empiricism, dimensional analysis and assuming a conventional transport equation. Statistical turbulence models relying on a transport equation for the dissipation rate ε do not exhibit increased physical rigor. Even though an exact transport equation for

$$\varepsilon = \nu \overline{\frac{\partial u_i'}{\partial x_k} \frac{\partial u_i'}{\partial x_k}} \tag{3.47}$$

can be derived by taking the respective correlation of the Navier-Stokes equations (see for instance [104]), the resulting expression contains numerous unknown correlation terms which require modeling in a quite drastic way with little hope for experimental proof.

However, a physically better founded starting point for the scale equation is the two-point velocity correlation tensor $R_{ij}(\vec{x}, t, \vec{r}) = \overline{u_i'(\vec{x}, t) u_j'(\vec{x} + \vec{r}, t)}$. An exact transport equation can be derived for

$$kL = \frac{3}{16} \int_{-\infty}^{\infty} R_{ij}(\vec{x}, t, r) \mathrm{d}r, \tag{3.48}$$

with $r = |\vec{r}|$, cf. [79]. ROTTA introduced modeling assumptions to derive a $k - kL$ turbulence model [78], whose scale equation reads in boundary layer formulation with wall-normal distance y

$$\frac{\partial}{\partial t}(kL) + u_j \frac{\partial}{\partial x_j}(kL) = -\overline{u'v'} \left(\tilde{\zeta}_1 L \frac{\partial U}{\partial y} + \tilde{\zeta}_2 L^3 \frac{\partial^3 U}{\partial y^3} \right) - \tilde{\zeta}_3 \cdot k^{3/2} + \frac{\partial}{\partial y} \left[\frac{\nu_t}{\sigma_\Phi} \frac{\partial}{\partial y}(kL) \right]. \tag{3.49}$$

Contrary to conventional scale equations, the production term features a second term containing a higher order derivative of the flow field. This is due to the assumption made by ROTTA, who expanded the following correlation of the exact kL transport equation with the help of a Taylor's series

$$\begin{aligned} \int_{-\infty}^{\infty} \frac{\partial U(\vec{x} + r_y)}{\partial y} R_{12} \mathrm{d}r_y = \frac{\partial U(\vec{x})}{\partial y} \int_{-\infty}^{\infty} R_{12} \mathrm{d}r_y + \frac{\partial^2 U(\vec{x})}{\partial y^2} \int_{-\infty}^{\infty} R_{12} r_y \mathrm{d}r_y \\ + \frac{1}{2} \frac{\partial^3 U(\vec{x})}{\partial y^3} \int_{-\infty}^{\infty} R_{12} r_y^2 \mathrm{d}r_y + \cdots \end{aligned} \tag{3.50}$$

and, by supposing a homogeneous shear flow, argued that the second integral of the expansion is zero. Modeling the third integral finally introduces the third derivative of

velocity into the scale equation (3.49). MENTER & EGOROV recall however that for this case the second velocity gradient is zero anyway, which leads them to the argument that the second integral should be conserved for inhomogeneous shear flow and should be modeled using the second velocity gradient as

$$\int_{-\infty}^{\infty} R_{12} r_y \mathrm{d}r_y \sim -\overline{u'v'} \frac{L}{L_{vK}} L^2, \tag{3.51}$$

with the von Kármán length scale

$$L_{vK} = \kappa \left| \frac{\partial U/\partial y}{\partial^2 U/\partial y^2} \right|. \tag{3.52}$$

The turbulence scale equation can now be rewritten as

$$\begin{aligned} \frac{\partial}{\partial t}(kL) + u_j \frac{\partial}{\partial x_j}(kL) = -\overline{u'v'} L \frac{\partial U}{\partial y} \left[\tilde{\zeta}_1 - \tilde{\zeta}_2^* \left(\frac{L}{L_{vK}} \right)^2 \right] - \tilde{\zeta}_3 \cdot k^{3/2} \\ + \frac{\partial}{\partial y} \left[\frac{\nu_t}{\sigma_\Phi} \frac{\partial}{\partial y}(kL) \right]. \end{aligned} \tag{3.53}$$

As it is desirable to introduce this modeling approach to already existing turbulence models, the new model has been generalized for three-dimensional, compressible flow. A transformation of the turbulence scale quantity kL to ω leads to two additional source terms in the transport equation:

$$Q_{SAS} = \overline{\rho} \zeta_2 S^2 \left(\frac{L_t}{L_{vK}} \right)^2 - C_{SAS} \frac{2\overline{\rho} k}{\sigma_\Phi} \cdot \frac{1}{\omega^2} \frac{\partial \omega}{\partial x_j} \frac{\partial \omega}{\partial x_j}, \tag{3.54}$$

where the three dimensional generalization of the von Kármán length scale reads

$$L_{vK} = \kappa \left| \frac{U'}{U''} \right| \quad \text{with} \quad U' = \sqrt{2 \cdot S_{ij} S_{ij}} \quad \text{and} \quad U'' = \sqrt{\frac{\partial^2 U_i}{\partial x_k^2} \frac{\partial^2 U_i}{\partial x_j^2}}. \tag{3.55}$$

In order to preserve the standard capabilities in RANS areas, where the first and second term are of the same order, the expression is modified with the help of maximum functions, yielding:

$$Q_{SAS} = \max \left[\overline{\rho} \zeta_2 S^2 \left(\frac{L_t}{L_{vK}} \right)^2 - C_{SAS} \frac{2\overline{\rho} k}{\sigma_\Phi} \max \left(\frac{1}{k^2} \frac{\partial k}{\partial x_j} \frac{\partial k}{\partial x_j}, \frac{1}{\omega^2} \frac{\partial \omega}{\partial x_j} \frac{\partial \omega}{\partial x_j} \right), 0 \right]. \tag{3.56}$$

Introducing this source term into the turbulence scale equation (3.44) of the SST model, the treatment of stable flow regimes remains unchanged as $Q_{SAS} = 0$. In areas with inherent flow instabilities however, the expression containing the von Kármán length scale dominates the other terms. The modeled turbulence length scale L_t can be obtained from the turbulence kinetic energy and specific dissipation ratio via

$$L_t = \frac{\sqrt{k}}{\beta^* \omega}. \tag{3.57}$$

The resulting model was termed SST-SAS and will be used throughout this work. The effect of this source term shall be discussed in the following. For inherently unsteady flows, the second derivative of velocity plays an important role as the von Kármán length scale decreases for already resolved turbulence content. This decrease activates the production term of the specific dissipation rate and eventually results in a decrease of eddy viscosity ν_t, which enters the conservation equations. This is an important characteristic and different to standard statistical turbulence model, where resolved fluctuations are not accounted for and thus are damped by an overestimation of eddy viscosity. However, the flow to be simulated has to be inherently unstable for the process of scale-adaption to be triggered. Intrinsic to this formulation is that there exists no explicit numerical grid dependency. However, as a finer mesh does obviously allow a better estimation of the second derivative of velocity more turbulence content is actually resolved.

3.3.3 Detached Eddy Simulation

Due to the fact that a pure Large Eddy Simulation of the entire flow domain is too expensive for the considered problem, a hybrid RANS/LES technique is taken into account. The first approach was introduced by Spalart et al. [92], who used a blending of the Spalart-Allmaras turbulence model and an LES model. As this technique can be extended to any other RANS turbulence model employing a turbulence length scale, Strelets [93] adopted this methodology for the $k-\omega$ SST model.

The transport equation of turbulence kinetic energy from the $k-\omega$ SST model is rewritten using equation (3.57) in order to introduce the turbulence length scale into the dissipation term, yielding:

$$\frac{\partial}{\partial t}(\bar{\rho}k) + \frac{\partial}{\partial x_j}(\bar{\rho}\tilde{u}_j k) = \hat{P}_k - \bar{\rho}\frac{k^{3/2}}{L_t} + \frac{\partial}{\partial x_j}\left[\left(\mu + \frac{\mu_t}{\sigma_k}\right)\frac{\partial k}{\partial x_j}\right]. \tag{3.58}$$

The underlying turbulence model for the LES formulation is the Dynamic Kinetic Energy Subgrid-Scale Model by Kim & Menon [51]. The subgrid-scale kinetic energy is defined as

$$k_{SGS} = \frac{1}{2}\left(\widehat{u_k u_k} - \widehat{u}_k\widehat{u}_k\right) \tag{3.59}$$

and its transport equation can be written as

$$\frac{\partial}{\partial t}(\bar{\rho}k_{SGS}) + \frac{\partial}{\partial x_j}(\bar{\rho}\tilde{u}_j k_{SGS}) = \hat{P}_k - C_\varepsilon\bar{\rho}\frac{k_{SGS}^{3/2}}{\Delta} + \frac{\partial}{\partial x_j}\left[\left(\mu + \frac{\mu_t}{\sigma_k}\right)\frac{\partial k_{SGS}}{\partial x_j}\right], \tag{3.60}$$

where the explicit grid length scale $\Delta = \max(\Delta x, \Delta y, \Delta z)$ is defined as the maximal element length in Cartesian coordinates. The subgrid-scale eddy viscosity μ_t is obtained from the characteristic subgrid-scale velocity $\sqrt{k_{SGS}}$ and from the subgrid length scale $\Delta_V = \sqrt[3]{V}$:

$$\mu_t = C_k\sqrt{k_{SGS}}\Delta_V. \tag{3.61}$$

The subgrid-scale shear stresses τ_{ij}^{SGS} can then be estimated as

$$\tau_{ij}^{SGS} - \frac{2}{3} k_{SGS} \delta_{ij} = -2 C_k \sqrt{k_{SGS}} \Delta_V \widehat{S}_{ij} \tag{3.62}$$

by omitting the last term in equation (3.35). A simple blending function is employed in order to hybridize LES and RANS formulation. If the turbulent length scale is larger than the characteristic grid spacing, turbulent fluctuations are spatially resolvable and the LES formulation is employed. If the turbulent length scale is smaller than the characteristic grid spacing, turbulent fluctuations cannot be resolved by the underlying mesh and the RANS formulation is applied. The blending function reads

$$\min\left(L_t, C_{DES}\Delta\right) = \begin{cases} \text{LES}, & \text{if } L_t > C_{DES}\Delta \\ \text{RANS}, & \text{if } L_t < C_{DES}\Delta \end{cases} \tag{3.63}$$

with the model constant C_{DES}. It was however shown in [65] that problems in boundary layers can arise caused by the definition of the grid length scale Δ. When the usually highly anisotropic hexahedral elements close to solid boundaries are refined in streamwise direction, the LES formulation can be activated too early in the boundary layer without a sufficient spatial resolution to compensate the decrease of modeled turbulence. For this reason, the minimum function is extended by the F_2 blending function stemming from the SST turbulence model. This allows protecting the boundary layers from an under-resolved LES since they are forced to RANS regime. The model is referred to as Delayed Detached Eddy Simulation (DDES) and the transport equation for turbulence kinetic energy thus finally reads [66]:

$$\frac{\partial}{\partial t}(\bar{\rho}k) + \frac{\partial}{\partial x_j}(\bar{\rho}\tilde{u}_j k) = \hat{P}_k - \bar{\rho}\frac{k^{3/2}}{\min\left[L_t(1-F_2), C_{DES}\Delta\right]} + \frac{\partial}{\partial x_j}\left[\left(\mu + \frac{\mu_t}{\sigma_k}\right)\frac{\partial k}{\partial x_j}\right]. \tag{3.64}$$

The eddy viscosity μ_t is then provided by definition (3.46) in RANS zones and by definition (3.61) in LES zones, allowing closure of the governing equations.

3.3.4 Embedded Large Eddy Simulation

The last integrated approach considered in this work consists in a local resolution of turbulence scales by employing a conventional LES inside a spatially fixed subdomain embedded in a larger fluid zone, which in contrast is treated using a conventional RANS formulation. This concept is illustrated in figure 3.3, following a basic jet in cross flow configuration. The entire fluid zone, framed by red lines, is divided into zones *I* and *II*, separated by dashed black lines. As zone *I* essentially comprises the jet and cross flow interaction region, necessary turbulent fluctuations can be resolved using an LES approach. Consisting of stable flow regimes and large areas of attached boundary layers, zone *II* is favorably treated by a RANS approach in combination with a standard statistical turbulence model.

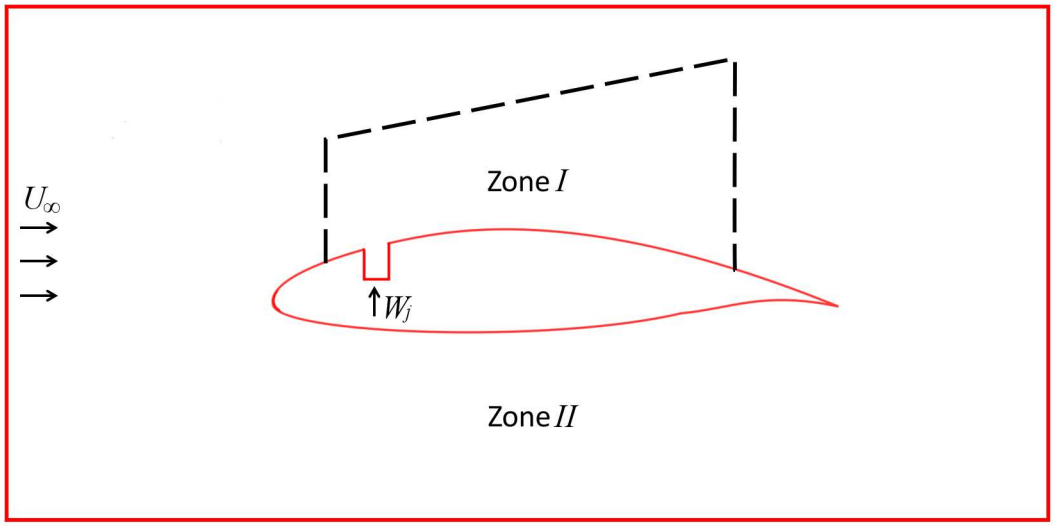

Figure 3.3: Division of fluid domain into two zones, with zone I using an LES turbulence model and zone II a standard RANS turbulence model

In order to close the filtered Navier-Stokes equation in zone I, the subgrid-scale turbulence model by Smagorinsky [89] in its formulation including the wall damping function of Piomelli et al [72] is considered here. The subgrid-scale eddy viscosity is obtained from

$$\mu_t = \overline{\overline{\rho}} \left(C_S \Delta\right)^2 \|\widehat{S}\| \left\{1 - \exp\left[-\left(\frac{y^+}{A}\right)^3\right]\right\}, \tag{3.65}$$

allowing the modeling of the subgrid-scale stresses defined in equation (3.35) by omitting the last term. Even if the extent of zone I is already substantially reduced compared to the overall domain, a fully resolved LES of wall bounded flows at high Reynolds numbers is not feasible as numerical grid resolution requirements tend towards those needed for Direct Numerical Simulations. In order to avoid this, a Wall Modeled Large Eddy Simulation proposed by Shur et al. [88] is employed, which allows the treatment of the viscous sublayer with the help of the simple but efficient Prandtl mixing length approach, yielding:

$$\mu_t = \overline{\overline{\rho}} \min\left[\left(\kappa d_w\right)^2, \left(C_S \Delta_1\right)^2\right] \|\widehat{S}\| \left\{1 - \exp\left[-\left(\frac{y^+}{A}\right)^3\right]\right\}. \tag{3.66}$$

The grid spacing has been modified to include information about the wall distance d_w and is given by $\Delta_1 = \min\left[\max\left(C_w d_w, C_w \Delta, h_{wn}\right), \Delta\right]$ with the empirical constant C_w and the element size h_{wn} in wall-normal direction. Regarding the treatment of turbulence in zone II, the standard $k-\omega$ SST turbulence model is employed as already introduced in section 3.3.1.

By embedding a zone of scale-resolution, interfaces between modeled and resolved turbulence kinetic energy appear, which require special treatment. A correct conver-

sion of modeled turbulence kinetic energy to resolved velocity fluctuations has to be ensured across the RANS→LES interfaces, i.e. the inflow condition for zone *I*. This can be achieved by using a Vortex Method as SERGENT [87] proposed for ideally plane RANS→LES interfaces normal to the mean flow. A specified number of point vortices is randomly distributed on the interface with their circulation being calculated from the vorticity obtained from the RANS solution. The characteristic size of each vortex depends on the local turbulence kinetic energy as well as on the local dissipation and the spatial resolution imposed by the grid has to be respected. Applying the Biot-Savart Law an instantaneous velocity field is calculated to obtain in-plane fluctuations. The point vortices are randomly convected inside the plane and the sign of circulation changes arbitrarily as well. In order to construct proper velocity fluctuations in streamwise direction, their magnitude is considered equal to the projection of in-plane fluctuations onto the mean velocity gradient. Finally, the treatment of LES→RANS interfaces has to be considered as well. The simplest approach consists of freezing an initial global RANS simulation of the entire domain and imposing this solution as inflow boundary condition at the LES→RANS interfaces. Obviously, a treatment of this kind requires the interfaces to be placed far downstream the region of interest.

3.3.5 Structural Similarities and Discussion

As it became already apparent in the derivation and simplification of the Favre-averaged Navier-Stokes equations (3.19)-(3.21) and the Favre-filtered Navier-Stokes equations (3.38)-(3.40), both resulting sets of equations are mathematically identical, disregarding the physical interpretation. If the turbulent Prandtl number Pr_t is assumed to be constant, which indeed is in many cases a justified simplification, the only way in which turbulence modeling strategies affect these equations and influence the solution behavior is via the eddy viscosity μ_t. A standard RANS turbulence model leads to large levels of eddy viscosity as these models attempt to account for all turbulent fluctuations. In contrast to this, a pure Large Eddy Simulation will resolve by definition the bulk of the turbulence spectrum and only model small scales, leading to eddy viscosity levels orders of magnitude smaller. The mathematical identity in combination with the Boussinesq hypothesis is thus the foundation for hybrid formulations that blend RANS and LES turbulence models.

Beyond this, the practical implementation in order to solve the resulting transport equation leads to additional mathematical manipulation. For a time dependent problem, the temporal derivative of a variable ϕ is usually approximated using finite differences. Employing the common forward differencing scheme, the approximation yields

$$\frac{\partial \phi}{\partial t} \approx \frac{\phi\left(t+\Delta t\right)-\phi\left(t\right)}{\Delta t}. \tag{3.67}$$

This finite difference can be re-approximated with the help of an integral, allowing writing

$$\frac{\phi\left(t+\Delta t\right)-\phi\left(t\right)}{\Delta t} \approx \frac{1}{\Delta t}\int_{t}^{t+\Delta t}\frac{\partial\phi}{\partial t}\mathrm{d}t = \frac{\partial}{\partial t}\left[\frac{1}{\Delta t}\int_{t}^{t+\Delta t}\phi\mathrm{d}t\right] = \frac{\partial\overline{\phi}}{\partial t}. \tag{3.68}$$

The temporal discretization can thus be physically interpreted as a temporal averaging over the numerical time step size Δt, cf. equation (3.11). This is reasonable as a numerical simulation with a time step size Δt does not allow the resolution of turbulent structures with a characteristic time smaller than Δt. Similarly, the use of a finite volume scheme for spatial discretization leads to spatial averaging, i.e. filtering over the computational cell volume Ω. This is also reasonable as no turbulent structures can be resolved by the numerical mesh, which are smaller than the local mesh size. Therefore, by numerically solving the Reynolds-Averaged Navier-Stokes equations (3.19)-(3.21) and the Favre-filtered Navier-Stokes equations (3.38)-(3.40) with the help of temporal and spatial discretization, the set of equations are filtered/averaged again. In a transient flow simulation, the discretized equations can be interpreted as also being physically identical and the solution-behavior is only determined by the underlying turbulence model.

Indeed, as demonstrated by the SAS turbulence model, which is derived on the RANS rationale, and by works of Travin et al. [98] or Fröhlich & von Terzi [36], unsteady RANS simulations exist that allow the resolution of turbulent scales, highlighting that this capability is not a unique LES feature. A classical LES shall rather not be defined by its capability to resolve turbulent fluctuations but as a turbulence modeling strategy, where eddy viscosity is a function of the underlying numerical grid, i.e. $\nu_t = f\left(\Delta\right)$. Only the application to highly resolved meshes leads to small levels of eddy viscosity and thus to the resolution of turbulent scales.

Due to the different levels of eddy viscosity, important issues arise when considering simulation techniques that allow within the same calculation the statistical treatment of turbulence and the resolution of turbulence. Deck [22] refers to two major points as illustrated in figure 3.4. The first one concerns grey areas of the flow, where the resolution of turbulent content is triggered but the decrease in eddy viscosity is insufficiently compensated by turbulent fluctuations. Since this behavior has the most important impact on boundary layers (region II), it can be remedied by shielding areas close to the wall as realized in the SAS and DDES approaches. The second issue concerns the transition from modeled to resolved turbulence as shown in region III. Independent of being triggered or not, transition is not instantaneous and can thus delay the formation of instabilities by advecting high levels of eddy viscosity and affecting downstream regions of the flow.

All strategies presented here aim at the resolution of turbulence scales and are therefore basically suitable for the simulation of jets in cross flow. However, the global stability of the flow type plays an important role, which might favor one approach over

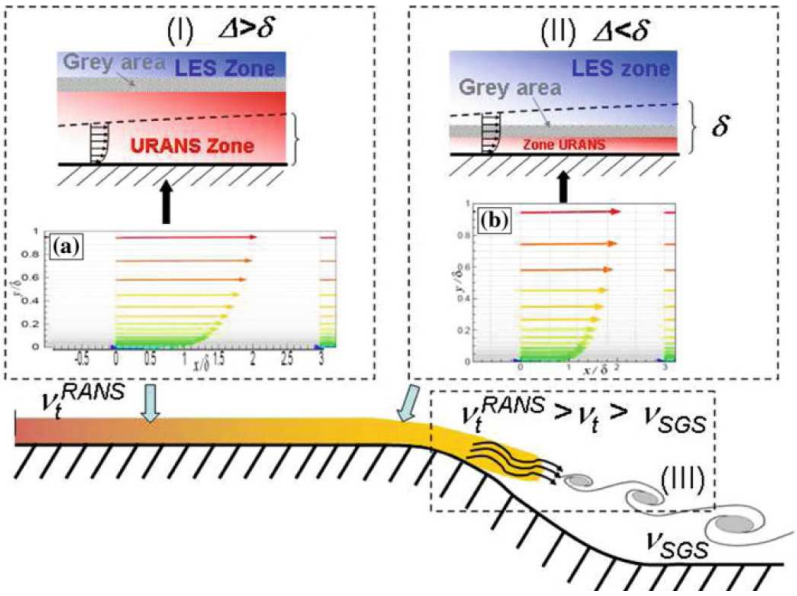

Figure 3.4: Issues arising from combining simulation techniques allowing the statistical treatment of turbulence and the resolution of turbulence in the same calculation [22]

the other. Leaving the conventional URANS approach aside, the hybrid integrated strategies SAS and DDES rely on inherent flow instabilities, which allow the transition from RANS areas to areas with LES-like behavior, i.e. to areas with resolution of turbulent fluctuations. If instabilities are not strong enough to activate the transition, a RANS-like solution will be obtained instead. Recalling the envisioned application for air system outlets, jets in cross flow can appear on the wing or the fuselage in combination with thick oncoming boundary layers and consequently high levels of eddy viscosity, with the possibility to delay instabilities as discussed above or even to prohibit transition. The zonal approach of the Embedded Large Eddy Simulation represents a significant advantage in this case since a conversion of modeled to resolved turbulent fluctuations is imposed at the RANS→LES interfaces. Even though this method forces transition, its effectiveness will strongly depend on the efficiency of the underlying vortex generation method.

3.4 Sequential Approach

Even though the turbulence modeling strategies presented above allow the resolution of turbulence fluctuations in the jet and cross flow interaction region, the overall computational cost of these types of simulations can become prohibitively expensive for aircraft applications at realistic flight conditions. Recalling the example presented in section 1.1, a simulation of the entire aircraft geometry with only a local area of

scale-resolution is up to now not feasible. Even the use of an Embedded Large Eddy Simulation with a rather coarse mesh in the RANS zone would lead to high computational costs: A typical RANS mesh of a semi-aircraft has a physical dimension in the order of 10^2m containing about 100 million computational cells. Introducing a spatially refined subdomain adapted for scale-resolution into the underlying RANS mesh, additional 25 - 50 million cells would be needed depending on the exhaust type and its location. Even though the increase in mesh size is moderate, an unsteady calculation has to be carried out in the entire domain leading to very long computing times. As the associated transient treatment of the RANS area does not offer any considerable advantage, the additional effort would thus not be justified.

In this work, a sequential approach is thus proposed for the solution of this problem and is depicted in figure 3.5. A basic jet in cross flow configuration is considered with the entire flow field framed by red lines, as shown in the top illustration 3.5(a). In a first step, a conventional RANS approach is employed on a for this purpose suited numerical grid in order to obtain a global estimation of the flow field, even if the solution in the jet and cross flow interaction region will show an underestimated mixing behavior. The second step consists in defining a spatially fixed domain of interest, where a scale-resolving simulation should be applied. The extents of this zone are shown as dashed black lines in the middle figure 3.5(b) and the RANS solution is then extracted on these surfaces. By providing a second numerical mesh adapted for spatial resolution of turbulent fluctuations in this domain of interest, a scale-resolving simulation is carried out using the extracted RANS solution as fixed boundary conditions at inlet and outlet surfaces, which is illustrated in the bottom figure 3.5(c). This approach thus allows a significant reduction of the number of computational cells, providing a feasible strategy for large computational domains with a very local resolution of turbulent scales. To allow the biggest flexibility of this strategy as well its application to complex geometries, all meshing constraints have to be eliminated. In an ideal way, the RANS and the SRS mesh are decoupled as well, allowing for instance highly anisotropic hexahedral meshes adapted for the RANS simulation and isotropic hybrid prismatic and tetrahedral meshes in the area of scale-resolution.

The drawbacks of this approach need to be considered as well. Firstly, the extraction of the RANS solution and its imposing as boundary conditions introduces interpolation errors. They can be reduced by already including the extents of the domain of interest into the RANS mesh by means of interior faces. Secondly, there exists only a one way coupling between the RANS Simulation and the Scale-Resolving Simulation. As the boundary conditions are kept fixed for the transient simulation, possible changes in the upstream flow topology due to the presence of jets remain unconsidered. However, the effect of the jet on the oncoming cross flow as well as interpolation errors can be reduced by enlarging the domain of interest such as its boundaries lie in the undisturbed free flow.

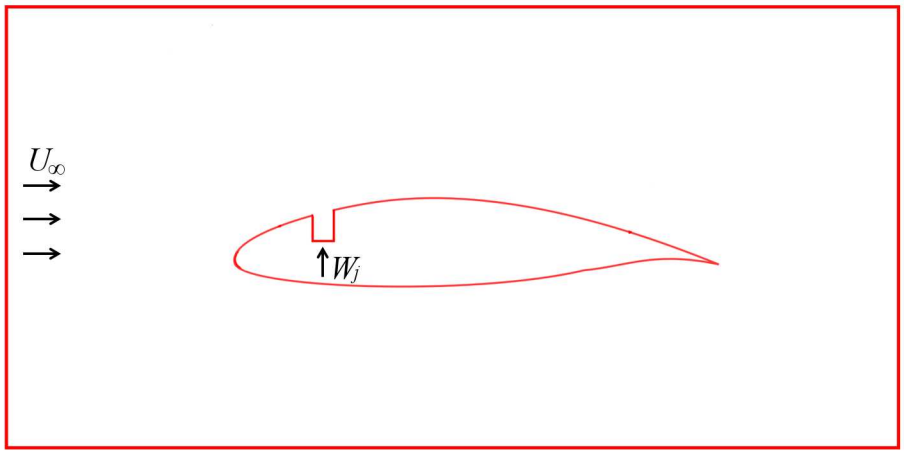

(a) RANS simulation of entire configuration

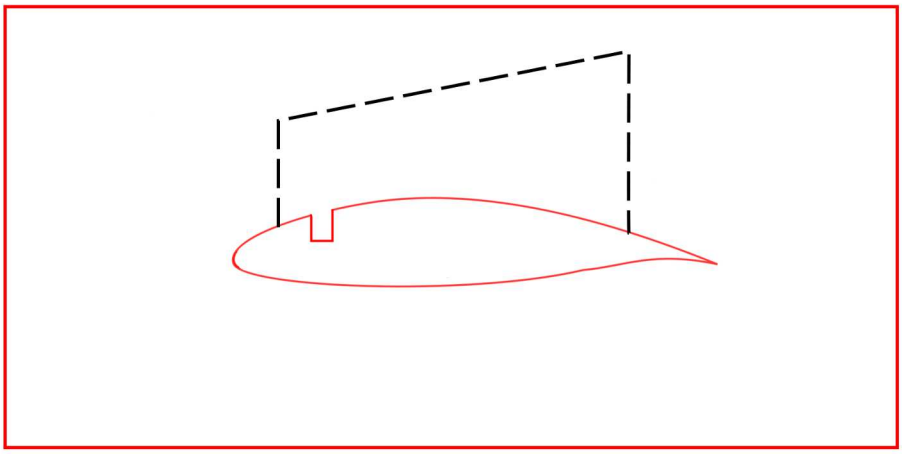

(b) Definition of subdomain and extraction of solution on its boundaries

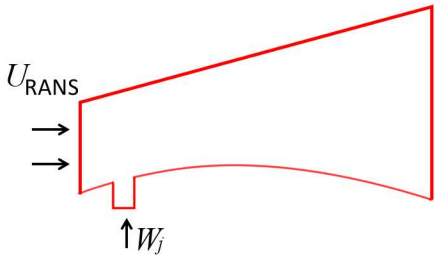

(c) Sacle-Resolving Simulation only in subdomain

Figure 3.5: The sequential approach

3.5 Solution Strategy

The conservation equations for mass, momentum and energy in combination with the turbulence model form a closed set of partial differential equations, which need to be solved numerically. The CFD solver Ansys Fluent [9] is used throughout this work, which employs the finite volume method outlined in the following. Meshing strategies, boundary conditions and numerical set-up will be described in more detail and separately in chapters 4 and 5 for the configurations considered.

Spatial Discretization

The first step consists in dividing the computational domain into a finite number of control volumes with the help of an unstructured numerical mesh. A cell-centered approach is used, where the flow variables are stored at the center of each element. The transport equation for momentum, energy and turbulence quantities are rewritten in integral form and applied to every computational cell, yielding a spatially discrete equation of the form

$$\frac{\partial \rho\phi}{\partial t}\Omega + \sum_f \rho_f \vec{v}_f \phi_f \cdot \vec{A}_f = \sum_f \Gamma_\phi \vec{\nabla}\phi_f \cdot \vec{A}_f + S_\phi \Omega, \tag{3.69}$$

with the diffusion coefficient Γ_ϕ and the source term S_ϕ. The sum is taken over all the faces f enclosing the cell with the surface vector $\vec{A}_f$ describing area and orientation of each face. As the value of the variable itself has to be known at the faces to evaluate convective fluxes, they have to be reconstructed. Depending on transport quantity and turbulence modeling approach, either a second order upwind [11] or a bounded central differencing scheme following [54] is chosen. The discretization of the diffusion terms is always second order accurate and achieved by a central differencing scheme. In order to estimate the diffusion term on the right hand side of the equation the gradient $\vec{\nabla}\phi$ has to be evaluated too. This is achieved by assuming a linear variation of ϕ between the considered and the neighboring cells. The resulting overdetermined system is then solved with the help of the method of least squares.

Time Discretization

As Scale-Resolving Simulations are transient by definition, the first term in equation (3.69) needs to be discretized as well. A second-order accurate discretization is given by

$$\frac{\partial \rho\phi}{\partial t} = \frac{3\rho\phi^{n+1} - 4\rho\phi^n + \rho\phi^{n-1}}{2\Delta t}, \tag{3.70}$$

with the superscripts n, $n+1$ and $n-1$ referring to the value at the current time t, the next time step $t + \Delta t$ and the previous time step $t - \Delta t$ respectively. For the cases considered here, a fixed time step Δt is sufficient. Implicit time integration is

employed, which means that all remaining terms in equation (3.69) are evaluated at time step $n + 1$. This requires on the one hand an iterative solution procedure but allows on the other hand larger time steps because this approach is unconditionally stable.

Pressure-Velocity Coupling

A pressure-based approach is used to solve the resulting algebraic set of equations. Even though this method was originally intended for problems at low-speed and incompressible flows, modifications and extensions have been introduced that allow its application also to high speed compressible aerodynamics [64], which need to be considered in this work as well. Starting point are the discretized transport equations for momentum, which are obtained by setting $\phi = u, v$ and w in equation (3.69), and an additional relation for pressure (correction), which is obtained by taking the divergence of the momentum equation and which ensures mass conservation. These equations can either be solved in a segregated, i.e. one after another, or in a coupled manner.

For the segregated approach, the momentum equations can be solved with the help of an initial pressure field but the resulting velocities will generally not satisfy the continuity equation inside the control volume. Solving the pressure correction equation to ensure mass conservation, the initial pressure field as well as the velocities are updated with the help of the obtained correction as proposed by VAN DOORMAAL & RAITHBY [100] within the SIMPLEC framework. Subsequently, transport equations for energy and turbulence quantities are solved with the obtained pressure and velocity field. As the new velocity field does not satisfy the momentum equation anymore, they have to be solved again with the updated pressure field. This iterative procedure has to be repeated until the applied corrections are sufficiently small.

The coupled method relies on the fully implicit discretization of the pressure gradient term in the momentum equation, which leads to a system of equations that has to be solved simultaneously. This is achieved with the help of an iterative procedure. Even if memory requirements are higher for the coupled approach, this method can be advantageous for complex flows due to its increased robustness.

In summary, the basic equations governing fluid flow have been presented as well as an averaging and a filtering procedure in order to cope with turbulent flows. As the resolution of at least a part of the turbulence spectrum is necessary for the proper aerothermal prediction of a jet in cross flow, different *integrated* approaches have been introduced. These are the Unsteady RANS simulation, the Scale-Adaptive Simulation, the Delayed Detached Eddy Simulation and the Embedded Large Eddy Simulation, which allow the simultaneous solution of the global flow domain and, to some degree, the resolution of scales in the jet in cross flow interaction region. As only a local resolution of scales is desired, a *sequential* approach has been introduced

as well, which is based on a global steady state RANS solution of the flow field with a subsequent Scale-Resolving Simulation in a subdomain, containing the jet in cross flow.

Chapter 4

Validation and Flow Analysis

The simulation approaches introduced in the previous chapter will now be applied to a generic jet in cross flow configuration and numerical results will be compared to experimental data for validation. In a further step, these unsteady simulations are analyzed in order to identify important flow and thermal mixing phenomena.

The chapter starts with a description of the generic configuration and the different meshing strategies in order to discretize the fluid domain. Simulations are carried out according to a validation matrix representing the three most important parameters: turbulence model, meshing strategy and time step size. Following this, a detailed flow analysis is carried out revealing stationary and transient flow phenomena as well as their importance for thermal mixing. A Proper Orthogonal Decomposition is employed to gain deeper insight into the inherent dynamics. Finally, the influence of thermal boundary conditions is examined as well as the applicability of the SAS turbulence model to multiple jets in cross flow.

4.1 Test Case Description

Simulations are carried out for the experimental set-up investigated during the MAEVA[1] project [4], which was realized by a cooperation of ONERA and Airbus Operations SAS. The configuration is illustrated in figure 4.1 in an exploded assembly view. It basically consists of a three-dimensional airfoil with an integrated air system exhaust on its suction side. Since the mock-up was designed to resemble a nacelle anti-icing system exhaust, the clean airfoil yields a pressure distribution similar to that of a nacelle and the exhaust grid is located close to the leading edge (cf. figure 1.1), which ensures the correct ratio of boundary layer height to characteristic jet diameter. The air system is composed of two pipes supplying hot air symmetrically into a plenum. As the hot fluid exits through an exchangeable ejector grid with different

[1] Modélisation Aérothermique des Écoulements en Ventilation Avion (French for Aerothermal Modeling of Flows for Aircraft Ventilation)

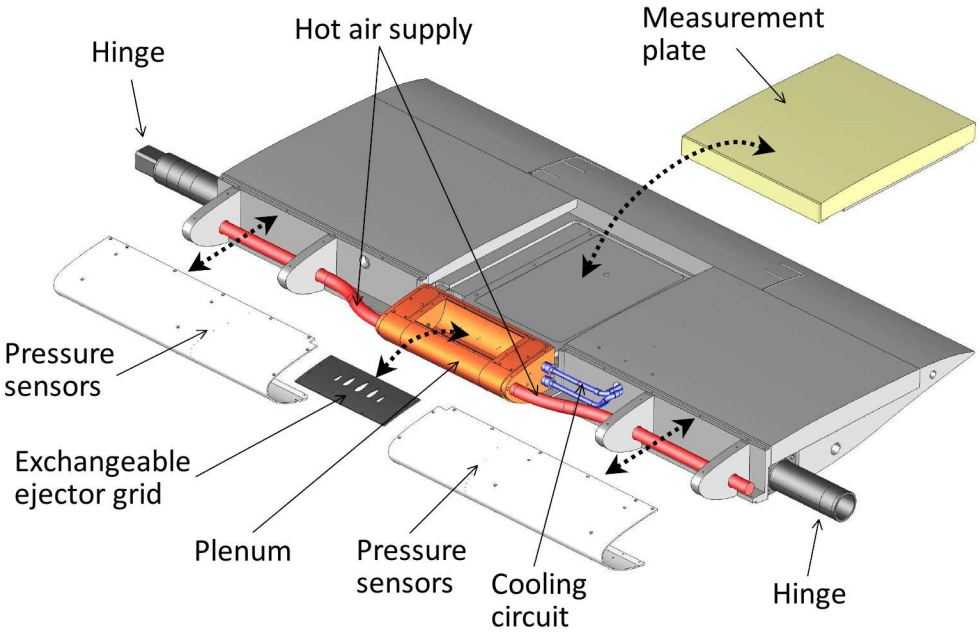

Figure 4.1: Generic jet in cross flow configuration for experimental investigation [4]

designs of orifices, the jet in cross flow forms. The plenum is cooled by a refrigerating circuit in order to minimize thermal conductance inside the mock-up. The configuration has been mounted in the rectangular test section of the low speed ONERA wind tunnel F2 [3]. The test section diverges with a small angle to compensate the thickening of the boundary layer. The wing has a chord length $C = 700$mm and a span of 1 400mm, corresponding to the width of the test section. The hinge allows pitching the model but only a fixed angle of attack, i.e. $\alpha = 1°$, is considered here.

Among the different grid designs experimentally investigated, two are chosen for numerical studies and are depicted in figure 4.2. The square shaped ejector grid on the left hand side represents the more academic test case and the multiple droplet shaped ejectors on the right hand side resemble a grid used in industrial applications. Different measurement techniques have been applied to extract relevant information in the jet in cross flow interaction region depending on the investigated grid. As small momentum ratios shall be analyzed, the thermal impact on the wall downstream of the ejector is important and of prime interest. For this reason, Infrared Thermography (IRT) has been used to quantify the surface temperature on the measurement plate indicated in figure 4.1, which is available for both ejector grids. More detailed information is available for the velocity field of the single jet in cross flow, where Particle Image Velocimetry (PIV) and Laser Doppler Anemometry (LDA) have been carried out in several planes with streamwise and lateral orientation. These types of measurements also allow the determination of fluctuating quantities of velocity. Finally, power spectral

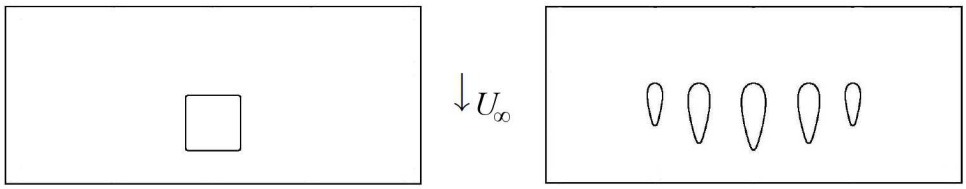

Figure 4.2: The two grid designs investigated

densities are obtained from Hot Wire Anemometry (HWA) at probes located in the jet wake to gain insight into the transient character of the flow.

4.2 Meshing Strategies

The spatial discretization of the fluid zone plays a crucial role for a proper flow simulation. As numerical studies shall represent the experimental set-up in the most accurate way, the overall extents of the domain are chosen to be equivalent to the non-divergent wind tunnel test section, which enables to account for pressure effects of wind tunnel walls on the mock-up. Additionally, the interior parts of the air system, i.e. the plenum and the pipes for hot air supply, are included for consistency. This allows taking into account the development of boundary layers inside the pipes and a mixing of the impinging jets within the plenum. Even though the cooling circuit has an influence on heat conduction, it is neglected for simplicity. Figure 4.3 presents the position of the mock-up and the overall computational domain.

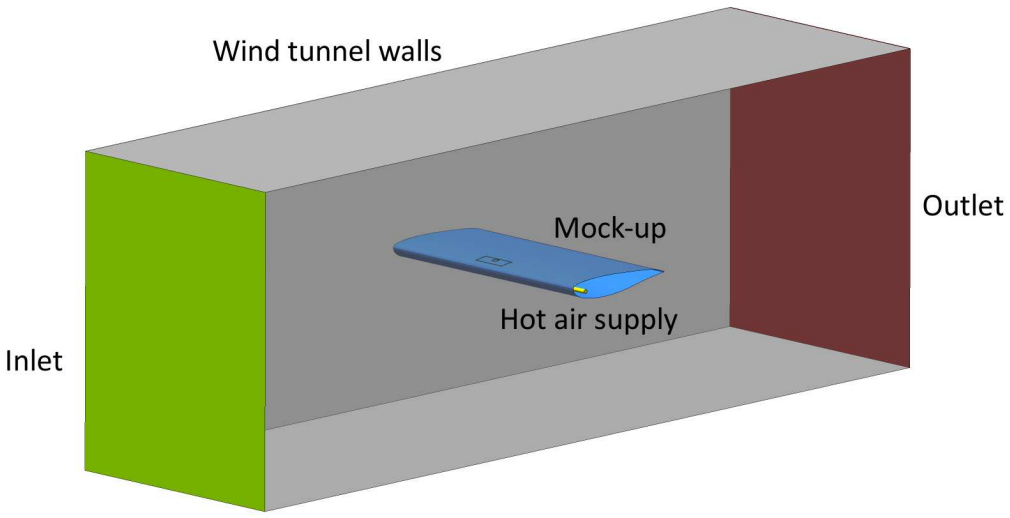

Figure 4.3: Computational domain comprising wind tunnel test section, mock-up and hot air supply

In general, different strategies allow the creation of the underlying numerical grid because the utilized CFD solver supports unstructured as well as non-coincident meshes and no restriction exists concerning element types. The appearance of wall bounded turbulence and the desired accuracy require the resolution of the viscous sublayer. Additionally, a sufficient mesh refinement is needed in the jet in cross flow interaction region. This region ideally consists of isotropic elements as the orientation of the turbulent structures to be resolved is random. Three approaches, fulfilling the above-mentioned criteria, are investigated throughout this work:

- Mesh a) hexahedral mesh based on a structured multi-block approach
- Mesh b) hybrid tetrahedral mesh with prismatic inflation layers
- Mesh c) hybrid Cartesian mesh with hexahedral and prismatic inflation layers

All of these approaches will be applied to the single ejector test case in order to validate their applicability in the context of Scale-Resolving Simulations. This is of importance in order to prepare the simulation of complex industrial applications, where hybrid meshing strategies might become inevitable.

Hexahedral Mesh

The first mesh is based on a structured multi-block approach. Due to highly anisotropic cells near walls, the wall-normal direction can be sufficiently resolved in order to accurately capture the boundary layer. Additionally, a smooth transition of cell sizes throughout the volume can be achieved. The downside however is the substantial manual effort, which increases drastically for complex geometric configurations. In addition to this, mesh refinement cannot be kept locally leading to an increase in the number of cells in areas where it is superfluous.

The hexahedral mesh generated for the single ejector configuration is illustrated in the top part of figure 4.4. A non-dimensional wall distance $y^+ = u^* y/\nu$ smaller than one is enforced on the exterior wing surfaces. The growing rate in wall-normal direction is restricted to a maximal ratio of 1.2. As the inclined wind tunnel walls are not respected in the simulation, the thickening of the boundary layer should neither be taken into account. For this reason, no mesh refinement is required for wind tunnel walls. The ejector and the area downstream are sufficiently refined to allow the resolution of turbulent structures, which is shown in the top part of figure 4.5. Due to the underlying topology this refinement passes through the entire flow domain.

Hybrid Tetrahedral Mesh

The second approach is a hybrid strategy combining prismatic and tetrahedral cells. An automatic mesh generation for complex geometries can easily be achieved with the help of tetrahedra and local mesh refinements can be integrated into the volume.

Furthermore, there is almost no influence of these areas on other parts of the mesh, leading to a locally confined reduction of cell size. On the other side, tetrahedral elements are not appropriate for boundary layer resolution as they cannot be aligned with the flow direction at the wall. For this reason, prismatic elements are employed in the vicinity of rigid boundaries. This retains the flexibility for mesh generation of complex geometries, while allowing highly anisotropic cells in wall-normal direction. The total number of elements, which is not a quality criteria but an indicator for the computational effort, is strongly increased compared to the first approach.

The realized mesh for this strategy is shown in the middle part figure 4.4. For the sake of comparability of the meshes, the height of the first prismatic cell layer at the wall is identical to that of the hexahedral mesh. A total number of twenty layers are used on all walls of the configuration and in the area of interest a growing ratio of 1.2 is respected. For the same reason as for the hexahedral mesh, neither a mesh refinement nor prism layers are employed on the wind tunnel walls. In order to augment the mesh density in the jet in cross flow interaction region, two geometric sources have been introduced to the meshing algorithm. Within these bodies of influence, an element size is specified and an isotropic mesh is generated, which is highlighted in the middle part of figure 4.5.

Hybrid Cartesian Mesh

The last approach is also a hybrid strategy, which employs hexahedral, prismatic, pyramidal and tetrahedral cells. The Cartesian volume mesh is generated by an octree approach, which is easily automatable and also applicable to complex geometries. Mesh refinement is achieved through the use of hanging nodes with the ratio 2:1. This allows a local increase of elements without affecting other parts of the mesh. As a Cartesian volume grid is not appropriate for boundary layer resolution, highly anisotropic prismatic and hexahedral elements are applied near rigid boundaries in order to resolve the large wall-normal flow gradient. To achieve a transition from near wall regions to the Cartesian volume mesh, pyramids and tetrahedra are employed.

The Cartesian mesh is depicted in the bottom part of figure 4.4. In order to allow comparison with the other two approaches, the characteristics of the inflation layers are identical, i.e. height of wall-adjacent cells and growing ratio with a total number of twenty layers. Again no mesh refinement is applied near wind tunnel walls as a resolution of boundary layers is not anticipated. Local mesh refinement is enforced within the same bodies of influence as shown in the bottom part of figure 4.5. Additionally, the edge length of the Cartesian cells in these areas is identical to the edge length of the tetrahedral elements.

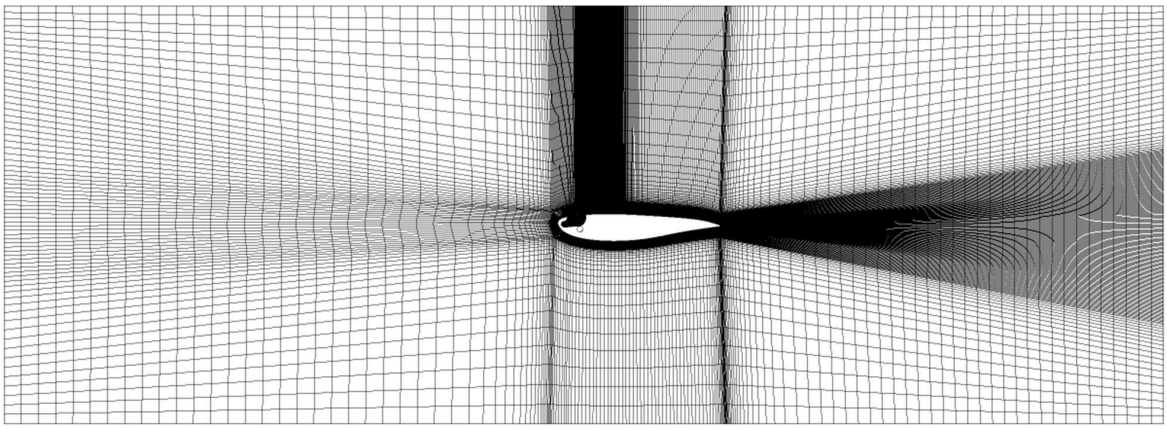

(a) Mesh a) hexahedral mesh based on structured multi-block approach

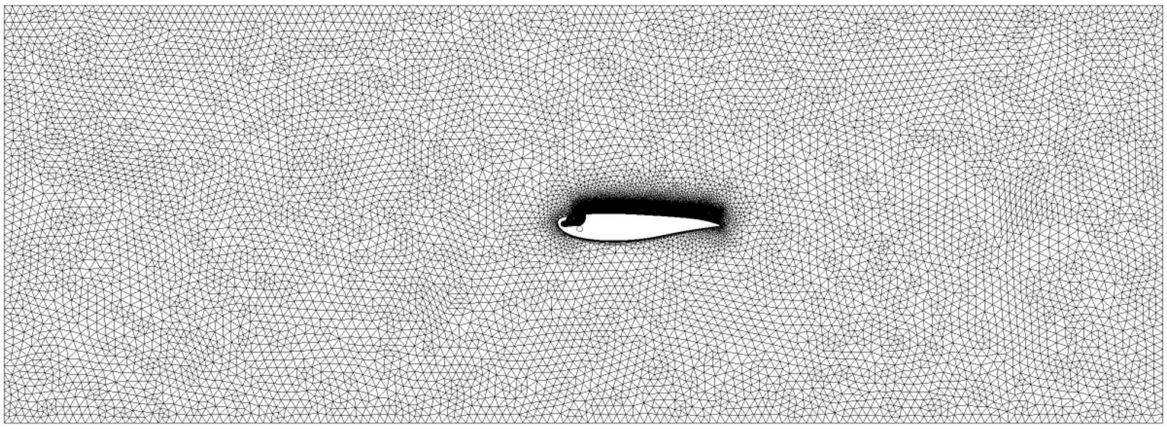

(b) Mesh b) hybrid tetrahedral mesh with prismatic inflation layers

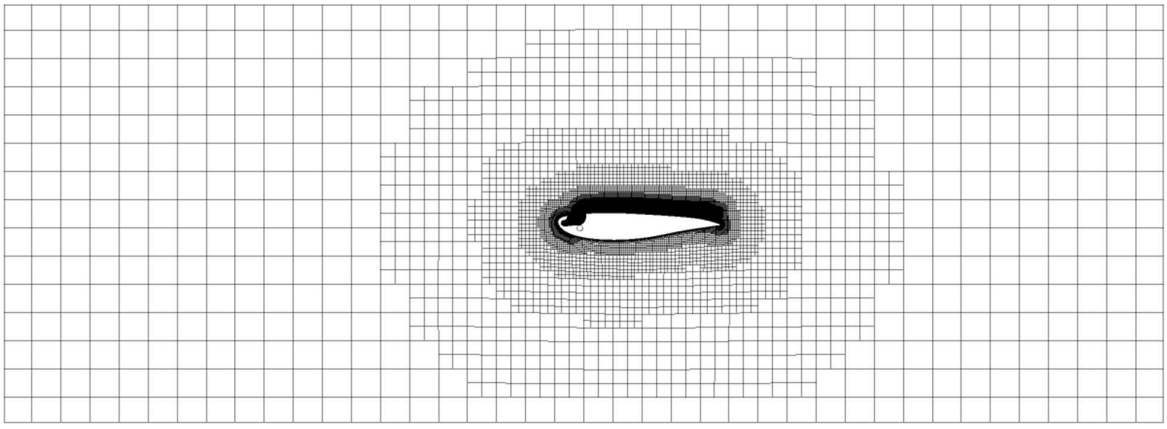

(c) Mesh c) hybrid Cartesian mesh with hexahedral and prismatic inflation layers

Figure 4.4: View of the global flow domain discretized by three different meshing strategies

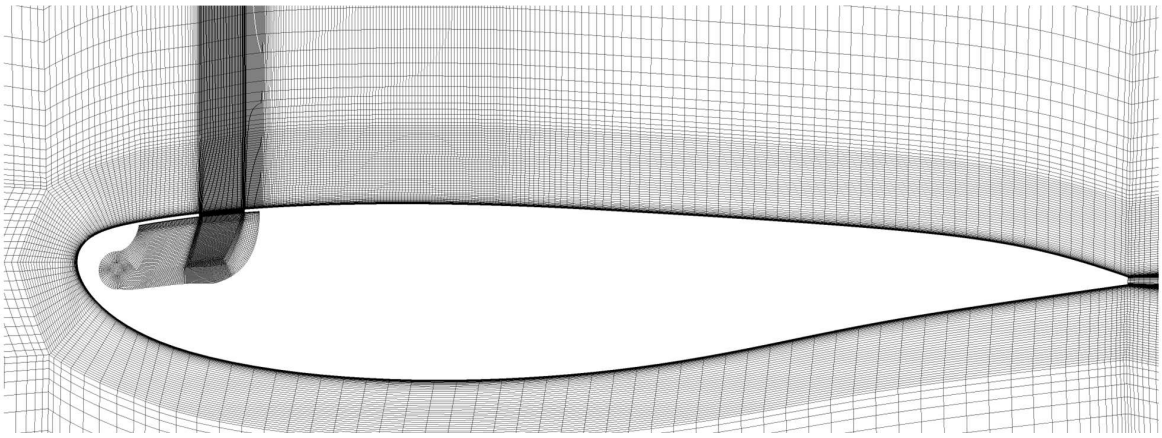

(a) Mesh a) hexahedral mesh based on structured multi-block approach

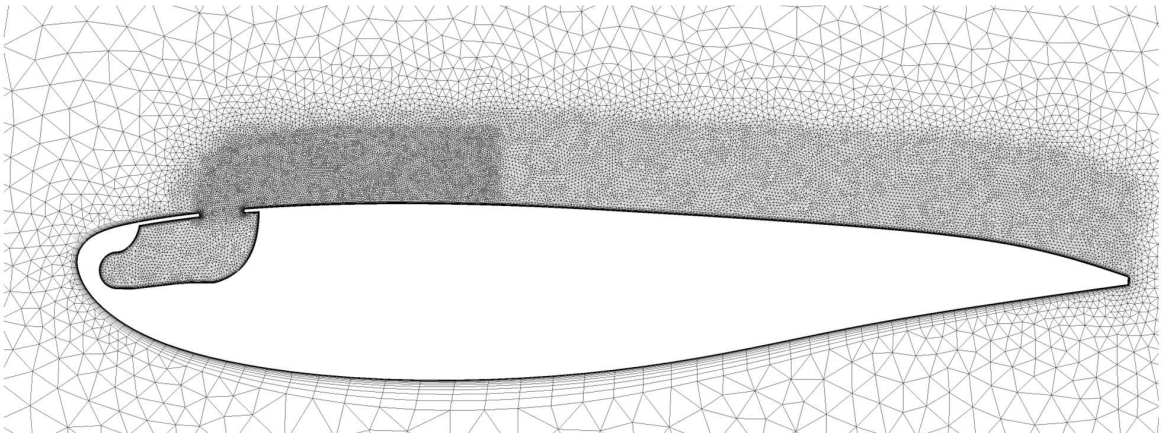

(b) Mesh b) hybrid tetrahedral mesh with prismatic inflation layers

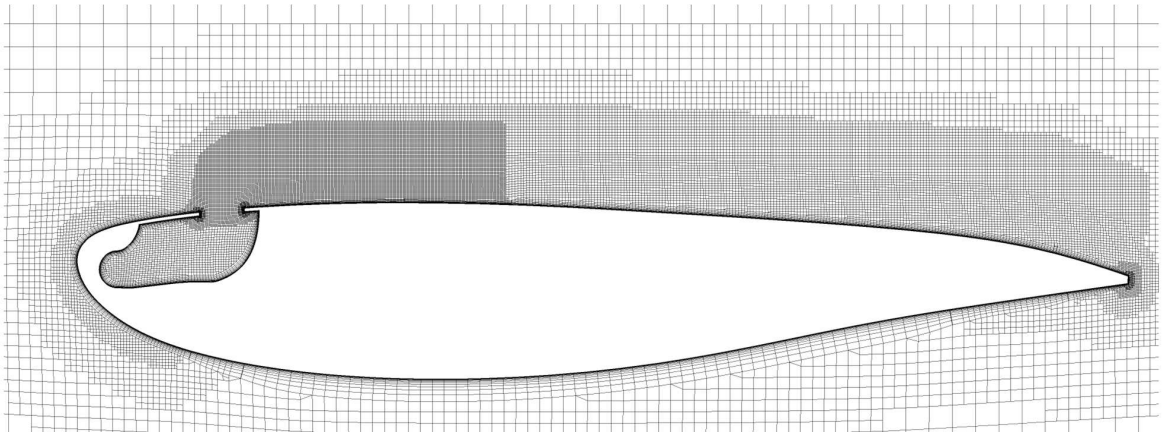

(c) Mesh c) hybrid Cartesian mesh with hexahedral and prismatic inflation layers

Figure 4.5: Detailed view of the areas refined for the resolution of turbulent scales

Table 4.1: Mesh statistics for generic single ejector configuration

	Elements	Min. cell angle	Max. aspect ratio	Max. volume change
Mesh a)	$12.9 \cdot 10^6$	28.1°	3 500	10
Mesh b)	$21.0 \cdot 10^6$	20.0°	7 600	8
Mesh c)	$13.1 \cdot 10^6$	6.0°	6 000	16

Mesh characteristics and quality criteria are summarized in table 4.1. The total number of elements is increased when the hybrid tetrahedral mesh is employed. As the element edge length is identical for both hybrid approaches in the refined areas, the number of elements decreases in turn for the third approach. The angle between two adjacent faces of a computational cell can be regarded as a quality measure. As the face angle decreases, the quality of the cell decreases as well. Mesh a) and b) have comparable minimum values, whereas Mesh c) exhibits a smaller angle due to the need of pyramidal elements in the transition area between the volume mesh and the inflation layers. Due to the large maximal aspect ratios of the wall adjacent cells, special care has to be taken to avoid numerical errors. This can be achieved by increasing the machine accuracy with the help of a double precision format. Another mesh metric is the volume change, which describes the volume ratio of a computational cell to its smaller neighbor. Values close to one describe a smooth transition in cell size. The large value of 16 for the hybrid Cartesian mesh is caused by the intrinsic refinement method of hanging nodes with a ratio of 2:1 in three dimensions.

Special Considerations for the Sequential Approach

Even if for the sake of consistency an identical mesh is desirable, the hexahedral mesh needs slight modifications in order to be applied to the sequential approach. The main constraint stems from the need to impose the RANS solution on the reduced SRS domain. As basically either inlet or outlet boundary conditions are available, the extents of this domain have to be surfaces that are uniquely inflow respectively outflow surfaces. Ambiguously orientated surfaces are not desirable as no unique boundary condition can be imposed. For this reason, the SRS domain diverges in main flow direction in order to avoid surfaces that are tangential to the flow. The angle defined by the arctangent of $(H_2 - H_1)/L$ yields about 20° which is found to constitute a sufficient inlet boundary condition. Because of this, the underlying mesh topology has to be adapted accordingly but in the crucial jet in cross flow interaction region the numerical grid remains unchanged. The modified mesh contains only $5.49 \cdot 10^6$ computational cells and is presented in figure 4.6.

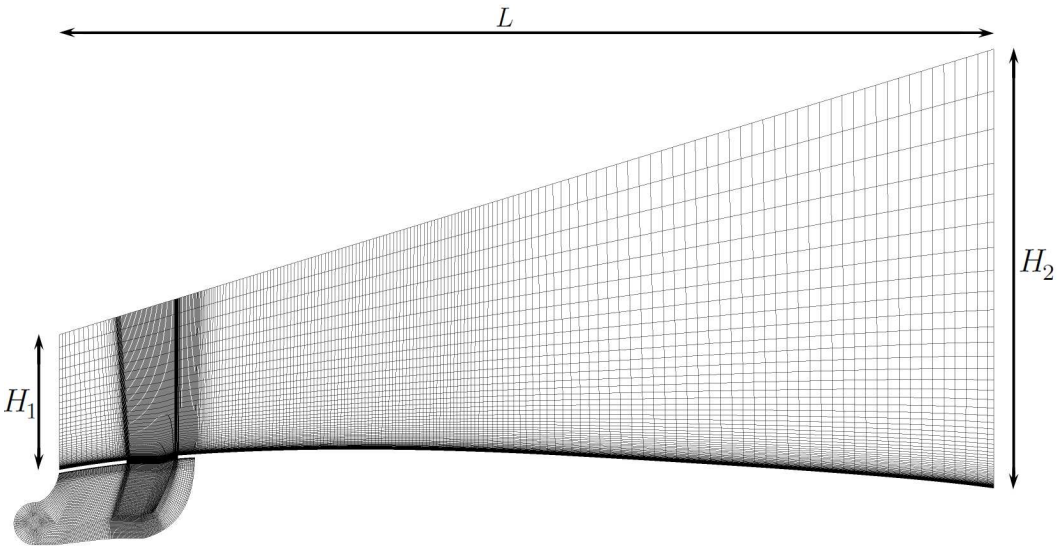

Figure 4.6: Adapted mesh for the sequential approach

Mesh Adaption for Multiple Ejector Grid

Due to the modular design of the MAEVA configuration, the adaption of the hexahedral mesh for the multiple ejector grid consists only in changing the local block topology around the orifices. The in-line configuration of the droplet shaped ejectors considerably enlarges the overall width of the jet wakes. As scale-resolution has to be ensured in this zone, the total number of hexahedral elements also increases considerably to $25.5 \cdot 10^6$ cells. Figure 4.7 illustrates a detailed view of the surface mesh in the vicinity of the ejectors. Minimum face angle, aspect ratio and maximum volume ratio remain unchanged.

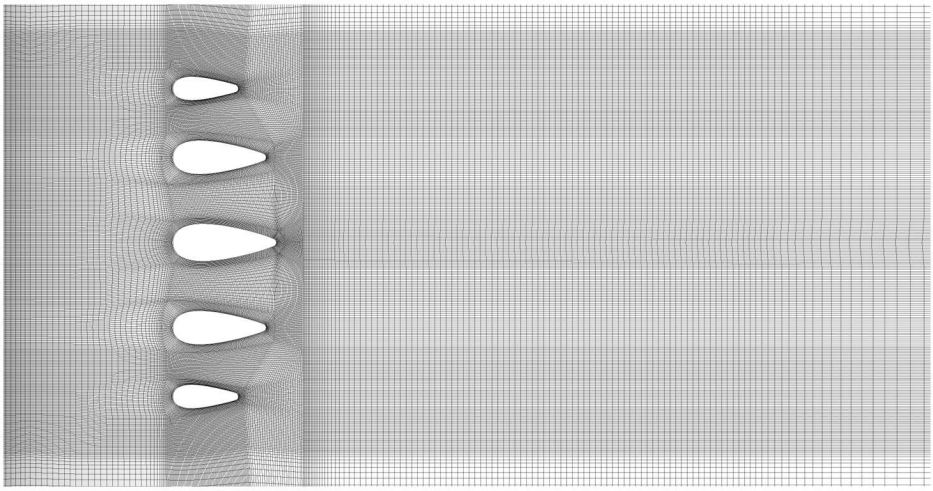

Figure 4.7: View of the surface mesh for the multiple ejector grid

4.3 Numerical Set-Up

The flow case considered for validation is equivalent to the one studied by ALBUGUES [4] and is characterized by the following parameters: The experiment was conducted at an ambient pressure of 101 325 Pa and at an ambient temperature of $T_\infty = 291\text{K}$. The free stream Mach number yields $Ma_\infty = 0.14$ and the mass flow for hot air alimentation corresponds to $\dot{m} = 17.71\text{g/s}$ for each pipe. The total temperature of the hot fluid is assumed to be equal to the jet temperature, which then yields $T_{t,j} = 353\text{K}$. This allows constructing the similarity parameters introduced in section 2.1.1 with the values shown in table 4.2. The small value of C_R characterizes an attached jet wake with strong thermal impact on the wall due to the absolute temperature difference of $\Delta T = 62\text{K}$. The high cross flow Reynolds number implies the broad range of turbulent structures that will appear and the vanishing cross flow Richardson number justifies the negligence of buoyancy effects.

Table 4.2: Similarity parameters for the generic single jet in cross flow configuration

C_R	Re_{cf}	Ri_{cf}	$\Delta T/T_{ref,1}$
0.69	$9.30 \cdot 10^4$	$\ll 1$	0.21

The numerical boundary conditions are chosen to match the experimental ones. The wind tunnel inlet of the computational domain is modeled with the help of a velocity inlet. A block profile with an X-velocity $U_\infty = 47.18\text{m/s}$ as well as a uniform temperature distribution of $T_\infty = 291\text{K}$ are prescribed. The outflow boundary of the domain is represented by a pressure outlet with a constant value equal to an ambient pressure of 101 325Pa. As explained in section 4.2, no boundary layers shall be resolved at the wind tunnel walls which leads to the use of a symmetry boundary condition to model slip walls. In contrast to this, the no-slip boundary condition is enforced on all walls of the mock-up. At each supporting pipe a mass flow equal to $\dot{m} = 17.71\text{g/s}$ is prescribed together with a total jet temperature of $T_{t,j} = 353\text{K}$. As transport equations for turbulence quantities are solved, appropriate inflow boundary conditions have to be applied as well. Rather than directly specifying values for turbulence kinetic energy k and specific dissipation rate ω, the more tangible quantities turbulence intensity $I = 0.5\%$ and turbulent viscosity ratio $\mu_t/\mu = 10$ are prescribed. For simplification and in order to facilitate the subsequent analysis of thermal mixing phenomena, all walls are treated adiabatically. This assumption is however revisited in section 4.6.1.

The basic numerical settings are mostly identical for all simulations carried out in this section and only the segregated flow solver is used. As described in section 3.5, two possibilities for the discretization of convective fluxes are taken into consideration. The first one, the second order accurate upwind scheme, is employed for all convective

fluxes in the URANS simulation, whereas the second option, the bounded central differencing scheme, is used to discretize convective fluxes for momentum and energy in the three remaining Scale-Resolving Simulations: SAS, DDES and ELES. The reason for applying this scheme lies in its lesser numerical diffusion, which is needed in order to capture strong flow gradients caused by the resolution of turbulent fluctuations.

Due to the confined computational domain, non-physical pressure fluctuations can appear. In order to avoid this and due to the small cross flow Mach number a weakly compressible fluid is considered. Instead of the state equation 3.7, the following expression is used

$$\rho = \frac{p_{op}}{RT}, \tag{4.1}$$

where the operating pressure p_{op} is kept constant and equivalent to ambient pressure. This formulation still allows taking into account density variations caused by the temperature difference between the hot jet fluid and the cold cross flow fluid.

As already stated in section 2.1.1, the aspect ratio Λ_{δ_1} has an impact on the development of the jet and especially on the upstream shear layer. On the one hand, a turbulent boundary layer has been enforced in the experimental configuration in order to resemble the real aircraft application by a tripping device at a relative chord length of $X/C = 3.54\%$, which leads to an aspect ratio Λ_{δ_1} between 1.0 and $1.8{\cdot}10^{-2}$. On the other hand, all simulations carried out feature a fully turbulent boundary layer developing from the leading edge. It was however confirmed by an additional steady state calculation with forced transition that this systematic error is negligible.

The choice of the numerical time step size Δt is crucial for a transient calculation since it directly affects scale-resolvability. On the one hand, the time step has to be small enough to allow temporal resolution of turbulent fluctuations, which are of importance for the considered problem. On the other hand, the time step should not be too small since this would lead to unnecessary high computational costs. Ideally, the chosen time step size should correspond to the mesh as temporal and spatial resolution correlate. For a jet in cross flow, the size l_0 of large eddies is in the same order of magnitude as the jet diameter D and their characteristic velocity u_0 is in the order of U_∞. As stated by Pope [73], the demarcation size l_d between geometry dependent vortices and those within the inertial subrange can be estimated to be $l_d = 1/6 l_0$. The corresponding characteristic time t_d can be calculated and the numerical time step size should be smaller, yielding the requirement

$$\Delta t < t_d \sim \frac{l_0}{u_0} \left(\frac{l_d}{l_0} \right)^{2/3}. \tag{4.2}$$

For the considered case, the baseline time step is thus chosen to be $\Delta t = 5 \cdot 10^{-}5\text{s}$. In order to investigate the influence on the obtained solution, additional calculations are carried out with a doubled and a halved baseline time step.

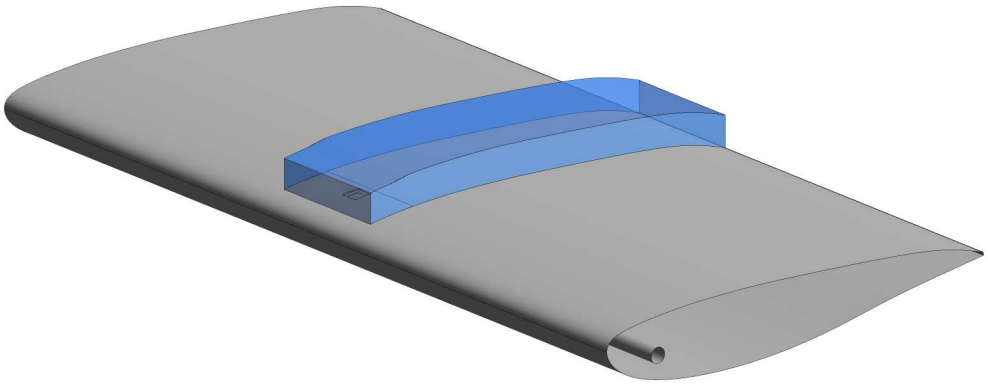

Figure 4.8: View of the Embedded LES zone inside the global RANS domain

Special Considerations for the Embedded Large Eddy Simulation

In contrast to the other approaches, a spatially and temporally fixed fluid domain has to be defined for the ELES. The most straightforward method is to use the hexahedral mesh as it is based on a structured multi-block topology. This efficiently allows using the already existing topology and the resulting numerical grid will be identical with the only difference being addressable interior faces, where the vortex generation method described in section 3.3.4 has to be applied. The resulting LES zone is shown in figure 4.8. On the one hand, the extents of the LES domain have to be large enough to cover the jet in cross flow interaction region. On the other hand, the supporting pipes and the plenum shall not be included to the LES domain to save computational costs. As existing studies showed that the ejector itself has an impact on the flow evolution, the LES domain is extended just below the orifice, which thus leads to additional RANS→LES interfaces. For the numerical set-up, the number of vortices at each interface is estimated to be equivalent to 25% of the total number of surface elements of the corresponding interface.

Transient Flow Initialization

Basically two possibilities exist for transient flow initialization. In the first case, the transient simulation is directly started from an initial solution at rest. For large computational domains and small time steps however, this procedure is impracticable. The second option consists in running a steady state RANS simulation and switching to an unsteady calculation after a sufficient number of iterations, once a reasonable flow solution is obtained. In this context, the adjective reasonable describes a solution that exhibits the global phenomena characteristic for the considered flow and does not signify a converged solution. The unsteady calculation has then to be run for a sufficient number of time steps before the solution can be processed or time statistics can be collected. This is due to the fact that the initially steady flow has to pass through a

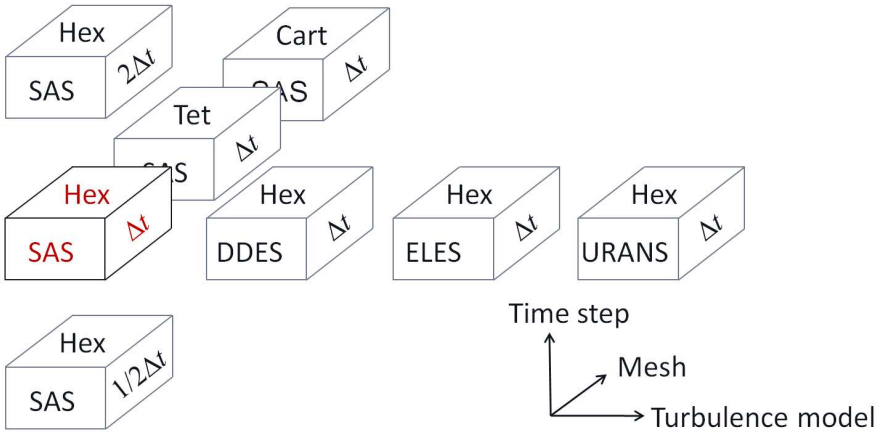

Figure 4.9: Validation matrix for the integrated approaches of Scale-Resolving Simulations

transition period in order to become fully transient and to be independent of the initial flow field. The length of this transition period can be expressed by a characteristic convective time, which describes the time necessary for the mean flow to pass over the characteristic length of the problem. Usually, 2-5 characteristic convective times are adequate to evacuate the domain of unphysical remainders of the stationary flow initialization before starting the flow analysis.

The following procedure has been applied for the considered case: After a uniform initialization of the field with values obtained from the wind tunnel inlet but with a more moderate velocity, a full multi-grid initialization is run. Following this, a steady state RANS calculation either using the SST or the SAS turbulence model is carried out for a total number of 150 iterations. After switching to an unsteady calculation, 1 000 time steps are simulated. This is done independently of the time step size, which means that the effective convective times based on the chord length are 1.7, 3.4 and 5.1 respectively. It is however found that in every case the transition period is sufficiently long.

4.3.1 Validation Matrix

The three most important parameters turbulence model, meshing strategy and numerical time step size are used to construct a validation matrix. Due to the large amount of simulations to be conducted for all possible combinations, the matrix is reduced to the one illustrated in figure 4.9. Each simulation is represented by a cube and its three visible sides show the value of the corresponding parameter. The front of the cube displays the utilized turbulence model, the top the underlying numerical grid and the side the time step size. The SAS calculation on the hexahedral mesh with the time step size Δt is considered to be the baseline simulation and is displayed in red. The sequential approach is not included in this overview since it is regarded separately.

4.4 Validation

Transient simulations contain a detailed description of turbulence and of the unsteady flow field. Even if primarily mean quantities are of final interest, the temporal evolution of the flow has to be validated as well if flow dynamics are to be analyzed. For this reason, the procedure proposed by Sagaut & Deck [82] is followed, which defines different levels of increasing validation depth: After considering first order time statistics such as the time-averaged surface temperature and velocity field, attention is turned to second order time statistics, i.e. root mean square values of the velocity field, giving information about the magnitude of fluctuating quantities and Reynolds stresses. Finally one-point spectral analyses are carried out in order to obtain information about the frequency contribution to the fluctuating quantities, which is achieved by normalizing power spectral densities of the velocity signal.

In contrast to steady flow simulations, the judgment of convergence is complicated by the fact that two aspects have to be taken into consideration. The first one concerns convergence within every numerical time step, i.e. inner convergence. As time integration is implicit, the equations have to be solved iteratively. An iteration error is then introduced because the solution procedure is interrupted before reaching the exact solution for the discretized equations. On the one hand, the evolution of the flow field can be monitored over the subiterations and convergence is achieved once the field does not change anymore or only within a defined tolerance. On the other hand, the residuals can be regarded as a function of subiterations. If within every time integration the value of each residual decreases by one to two orders of magnitude, the number of subiterations is sufficient. The second aspect concerns convergence of time statistics, i.e. outer convergence. Every realistic flow is physically bounded, which means that first and second order time statistics approach a constant value as time reaches infinity. Transferring this to numerical calculations, enough time integration steps are carried out when time statistics do not change anymore or only within a defined tolerance.

Two aspects are of major importance in this context: Firstly, the capability of the underlying model to resolve turbulent fluctuations and secondly, the mean temperature distribution on the wing surface behind the orifice. They are presented qualitatively and separately for all cases in the following devoted sections. Subsequently, temperature and velocity profiles of first and second time statistics in combination with spectral analysis allow a more quantitative view and a general discussion.

4.4.1 Turbulence Model Impact

In this section, the influence of the different turbulence models is discussed in the following order: Scale-Adaptive Simulation, Delayed Detached Eddy Simulation, Embedded Large Eddy Simulation and finally Unsteady RANS Simulation.

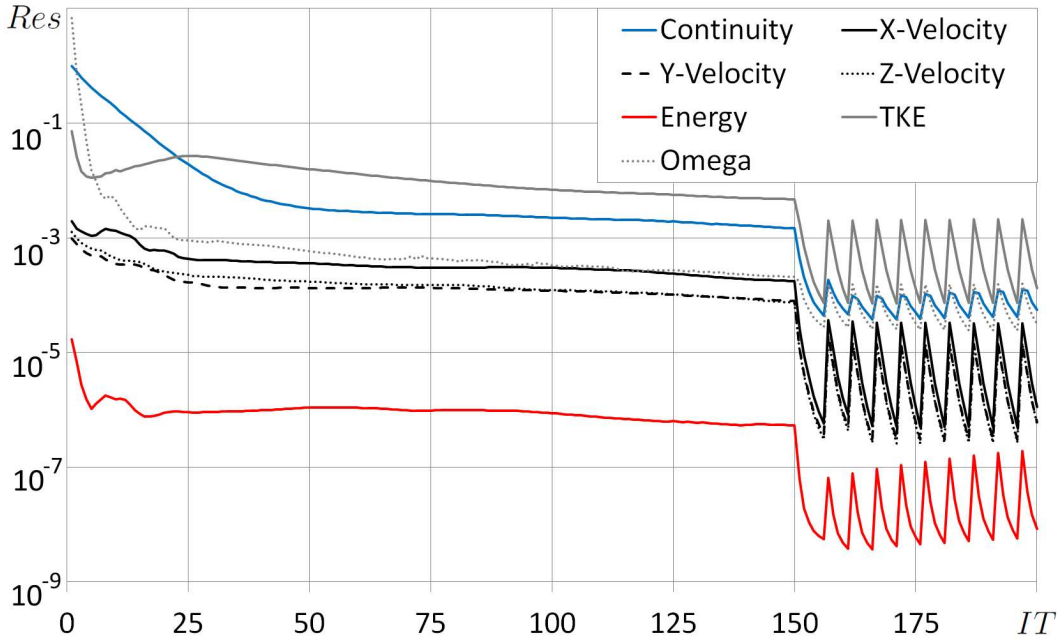

Figure 4.10: Evolution of residuals

Scale-Adaptive Simulation

Evolution of residuals for all transport equations are presented in figure 4.10. After 150 steady state iterations, the simulation is switched to unsteady mode which is clearly visible in the different behavior. Within every time step n, the residuals decrease about one to two orders of magnitude. The termination condition for inner iterations is defined by a maximal residual. Once all residuals are smaller than 10^{-4} (10^{-7} for the energy equation), the next time step will be calculated. The required number of subiterations to achieve this criterion yields 6 at the beginning of the transient simulation and increases steadily to 10 for the fully developed transient flow. When the solution is updated to the new time step $n+1$, the residuals grow abruptly as the old solution does not satisfy the current equation anymore. In order to judge inner convergence, a monitor point inside the jet wake is exemplarily considered and velocity magnitude and static temperature are plotted as a function of subiterations in figure 4.11. It can be stated that at the end of each time step the shown values only vary within small tolerances and inner convergence can be considered to be achieved.

For outer convergence, first order time statistics of temperature for an exemplarily chosen monitor point in the jet wake are presented in figure 4.12 as a function of accumulated sampling time Δt_{acc}. It can be seen that the values approach a limit as the number of time steps increases. Only very small oscillations are discernible at the end of the simulation which shows that outer convergence is achieved as well. The time-averaged data presented in the following has thus been averaged for a total

sampling time of $\Delta t_{acc} = 0.35$s after flow initialization, i.e. 7 000 time steps. An additional indicator for outer convergence in this special case is symmetry, which is also sufficiently respected as will be seen in the following.

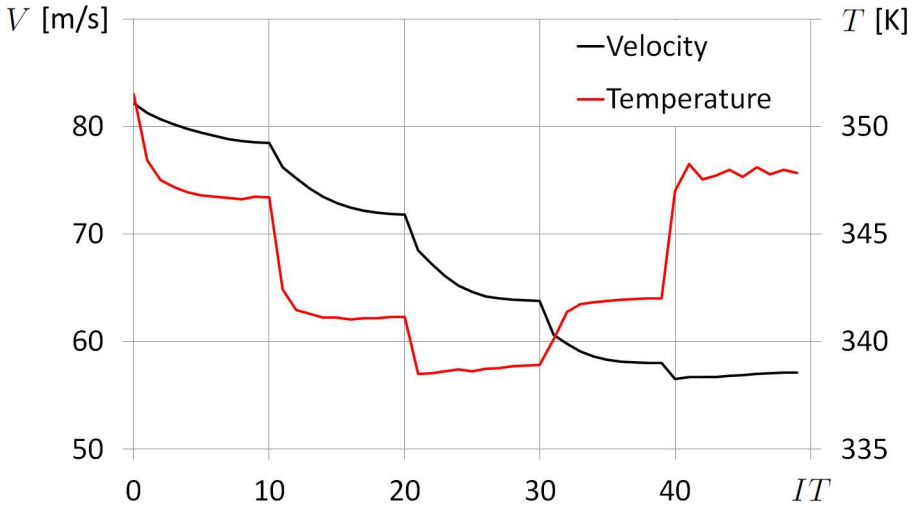

Figure 4.11: Inner convergence

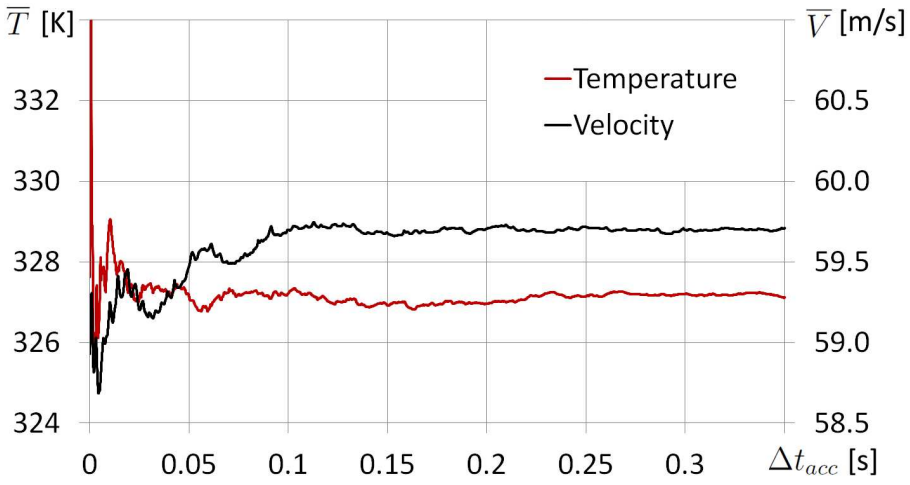

Figure 4.12: Outer convergence

In order to judge scale-resolvability of the Scale-Adaptive Simulation, the Q-criterion [41] is plotted in figure 4.13(a) for a normalized isovalue $Q^* = QD^2/U_\infty^2 = 1.0$. The isosurface is colored by temperature, ranging from red to blue, i.e. hot to cold. Clearly, turbulent structures of different size and nature are visible in the jet in cross flow interaction region. The coarsening mesh leads to the dissipation of these structures at about 50% of the chord, which is however acceptable as the main share of

thermal mixing is generated in the near field. A finer resolution of the wake in the far field would not justify the additional computational effort, which is especially true if aircraft applications are considered. Due to the behavior of the SAS turbulence model, which relies on inherent flow instabilities in order to transition from modeled to resolved turbulence fluctuations, the considered jet is thus globally unstable. Character and influence of these fluctuations on thermal mixing will be discussed in section 4.5. As a cut through the wing is presented, it remains worth mentioning that turbulent structures are also observable inside the plenum.

For the validation of the obtained solution, the time-averaged thermal efficiency distribution $\bar{\eta}$ is compared to experimental data. Contour plots on the wing surface downstream of the ejector are shown in figure 4.13(b). In general, a good agreement is obtained in the mid and far field for lateral thermal spreading and the decrease in temperature along the symmetry line is accurately captured as well. However, the lateral spreading in the very near field remains underestimated. This is due to the fact that heat conduction through the ejector grid affects the cross flow boundary layer leading to the development of a thermal boundary layer as well. This phenomenon and its influence on the global temperature distribution is discussed in section 4.6.1. Finally it can be said that the contours are fairly symmetrical, highlighting sufficient outer convergence.

Delayed Detached Eddy Simulation

As the same procedure is followed for flow initialization, the evolution of residuals is very similar to the ones presented in figure 4.10 with a decrease of one to two orders of magnitudes within every time step. Convergence criteria are set identical and sufficient inner and outer convergence is achieved during 8 subiterations. The same value of $Q^* = 1.0$ is used for the Q-criterion of instantaneous isosurfaces, which are shown in figure 4.14(a). This approach also clearly allows the resolution of similar coherent structures in the jet in cross flow interaction region before their dissipation takes place in the far field. In contrast to the SAS computations however, fewer scales are resolved, which is also observable inside the plenum. Concerning the thermal efficiency illustrated in figure 4.14(b), a satisfying agreement between numerical and experimental data is obtained. Lateral spreading is very well estimated in the mid and far field, whereas the near field remains again underestimated. Directly behind the orifice an area of increased temperature becomes apparent, which was less pronounced in the SAS computation. A possible explanation stems from the fact that fewer structures are resolved in the plenum and subsequently in the vicinity of the orifice leading to a reduced thermal mixing prediction.

Embedded Large Eddy Simulation

Also for this approach, evolution of residuals show the same behavior as the ones already presented in figure 4.10. Sufficient inner convergence is achieved within the same number of iterations as the DDES approach, where residuals decrease by one or two orders of magnitude and values at monitor points reach a limit. Additionally, the intended 7 000 time steps also suffice for outer convergence. Isosurfaces of the Q-criterion for the value of $Q^* = 1.0$ are presented in figure 4.15(a). This approach also resolves turbulent content in the near and mid field of the jet, which is however not surprising as this method does not rely on inherent flow instabilities and scale-resolution is triggered by the RANS→LES interfaces below the orifice. Compared to the hybrid approaches, more structures are apparent before their dissipation at about half the chord length. Due to the definition of the LES zone, the plenum is treated with a URANS formulation leading to almost no resolved turbulent content in the internal part. The corresponding surface temperature distribution is illustrated in figure 4.15(b). Downstream extent of the thermal trace in the mid and far field corresponds well with experimental data as well as the lateral spreading. Directly behind the orifice however, a large zone with high temperatures is visible which is neither as pronounced in experimental data nor predicted by the DDES and SAS approach.

Unsteady RANS Simulation

Finally, scale-resolvability of the URANS approach is investigated. Very similar to the other methods already presented, the evolution of residuals are qualitatively the same as shown in figure 4.10. Convergence criteria are identical, necessitating only six subiterations for inner convergence with a decrease of residuals between one to two orders of magnitudes. Outer convergence is achieved within a total of 7 000 time steps after transient flow initialization. For this case, the isosurfaces of the Q-criterion have to be plotted at a smaller value, i.e. $Q^* = 0.5$, in order to visualize any flow structures in figure 4.16(a). Major differences are observable when comparing this to the previous results. Only large-scale structures appear in the near and mid field and no resolution of smaller turbulent fluctuations is visible at all. This behavior is also discernible inside the plenum, which corresponds to the observations made for the ELES approach. The thermal trace predicted by the URANS approach is plotted in figure 4.16(b), which also shows major discrepancies when compared to experimental data. The most striking aspect is the underestimation of lateral spreading in the mid and far field. On the other hand, an overestimation becomes obvious along the symmetry line. This poor thermal mixing prediction has to be attributed to the incapability of the URANS approach to sufficiently resolve turbulent fluctuations. This is even more highlighted by the fact that underlying numerical mesh and time step size are identical for all the investigated turbulence modeling approaches. The major conclusion of this comparison is thus the

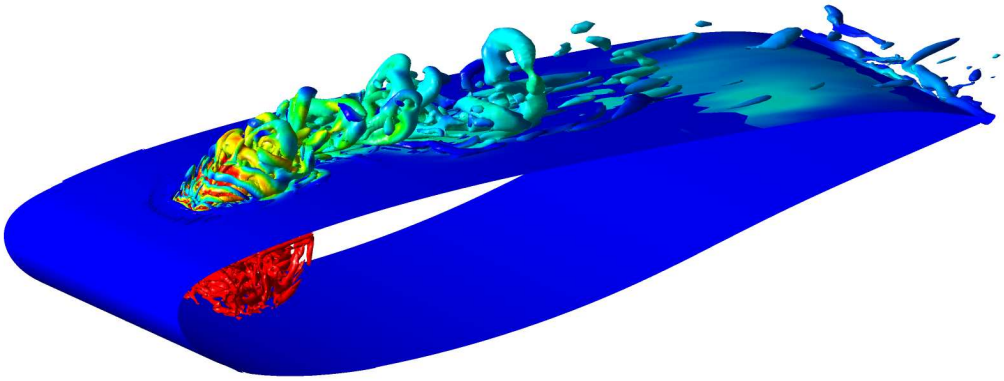

(a) Q-criterion for $Q^* = 1.0$

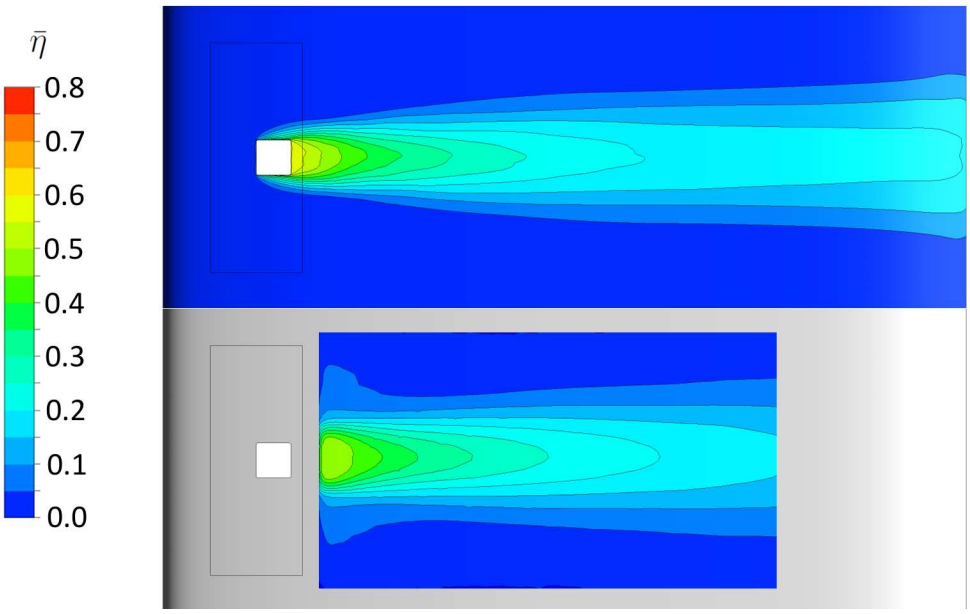

(b) Comparison of time-averaged thermal efficiency $\bar{\eta}$ against experimental data

Figure 4.13: Results obtained from the SAS approach on the hexahedral mesh utilizing the baseline time step Δt

necessity of scale-resolution for the proper aerothermal prediction of jets in cross flow, which is provided by the SAS, the DDES and the ELES approach. Even if dissipation of resolved turbulence content takes place at about 50% of the chord due to the coarsening mesh, sufficient scale-resolution in the near and mid field has been achieved for a proper prediction.

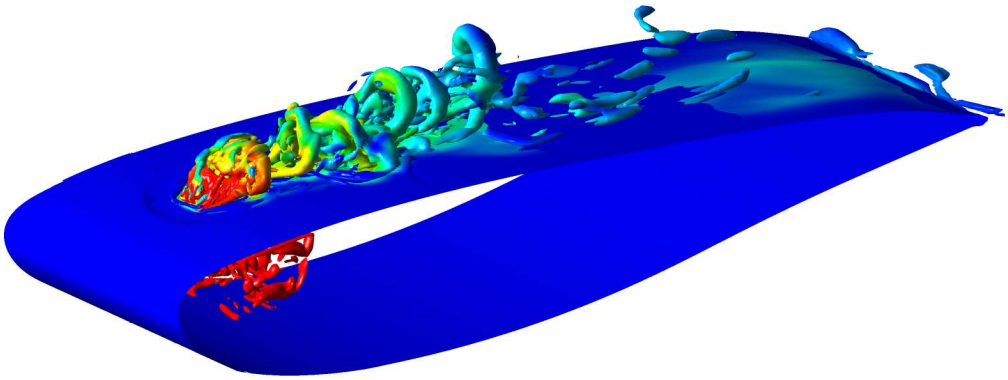

(a) Q-criterion for $Q^* = 1.0$

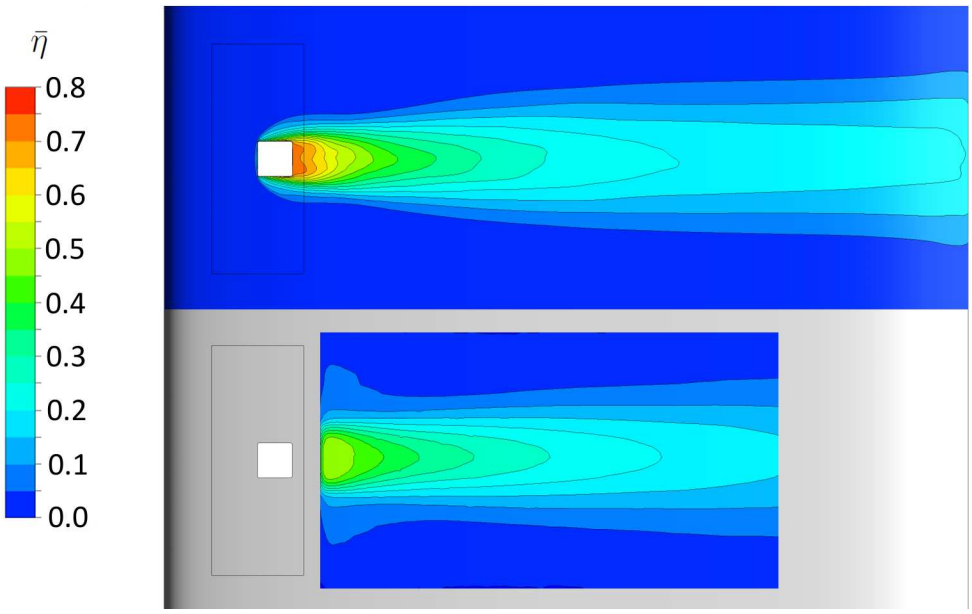

(b) Comparison of time-averaged thermal efficiency $\bar{\eta}$ against experimental data

Figure 4.14: Results obtained from the DDES approach on the hexahedral mesh utilizing the baseline time step Δt

4.4.2 Mesh Influence

Having shown the general scale-resolving capabilities of the SAS turbulence model, the influence of the underlying meshing strategy is discussed in this section. First the hybrid tetrahedral mesh, presented in section 4.2, is considered. No qualitative differences are discernible in the evolution of residuals, which resemble those presented in figure 4.10. As convergence criteria are identical, i.e. all residuals have to be smaller

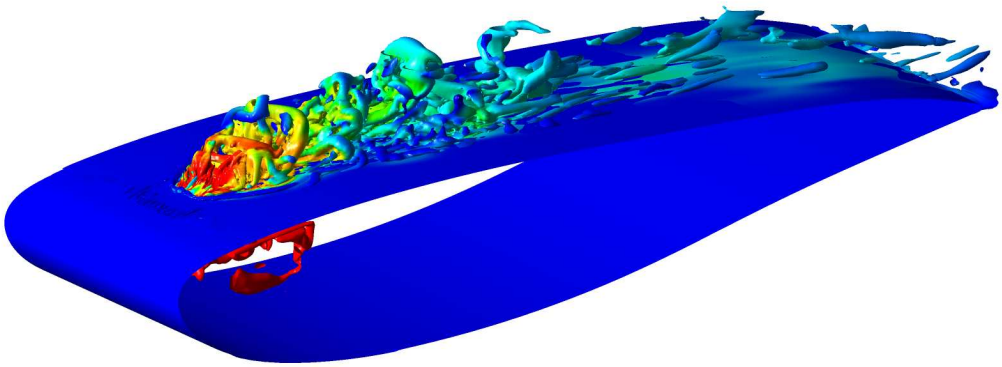

(a) Q-criterion for $Q^* = 1.0$

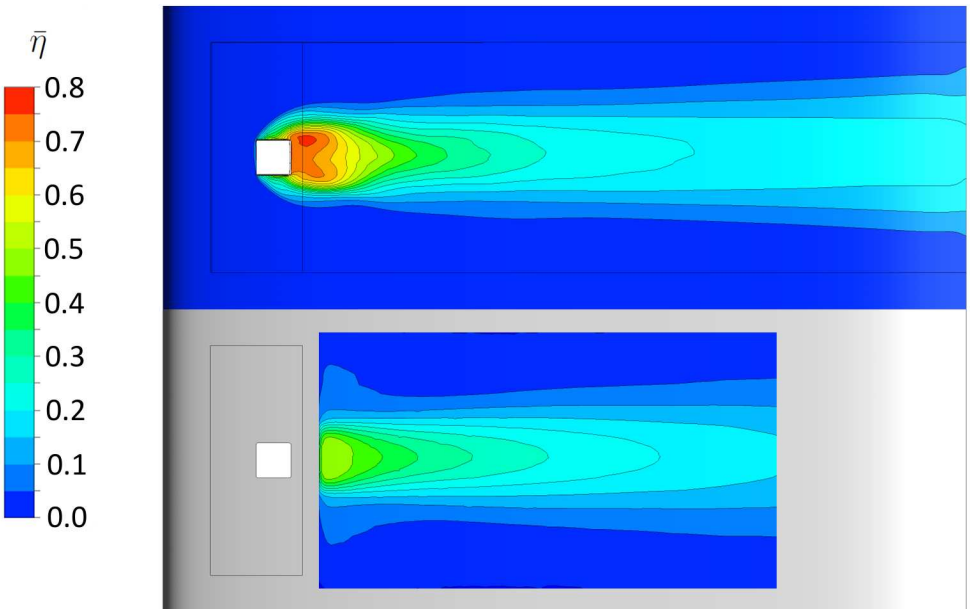

(b) Comparison of time-averaged thermal efficiency $\bar{\eta}$ against experimental data

Figure 4.15: Results obtained from the ELES approach on the hexahedral mesh utilizing the baseline time step Δt

than 10^{-4} (10^{-7} for the energy equation), the only quantitative difference is the number of necessary inner iteration to achieve these criteria, which increases to 12. Once inner convergence and transient flow initialization are ensured, the same number of time steps suffices for outer convergence. The instantaneous vortex topology is depicted in figure 4.17(a) for the ordinary value of $Q^* = 1.0$. Spatial resolution is achieved in the jet in cross flow interaction region also for this meshing strategy. Coherent structures of different size and nature are visible inside the plenum, the near and mid field of the jet in cross flow as well as in the far field. The latter is in contrast to the calculation

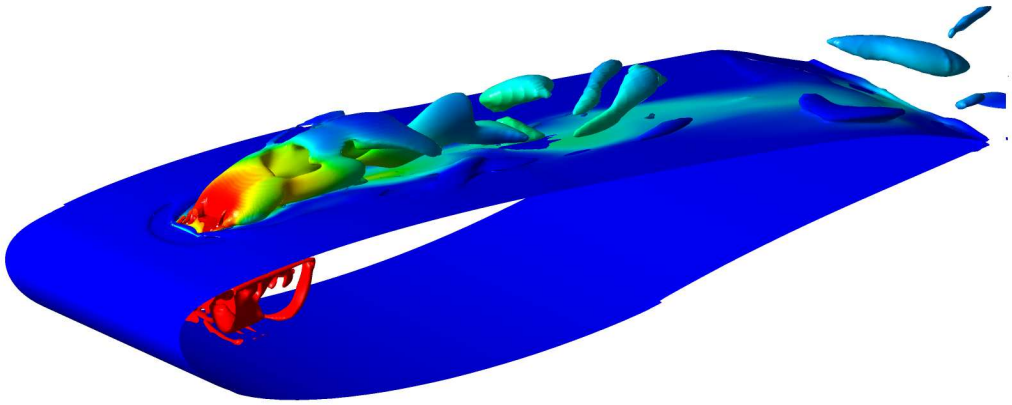

(a) Q-criterion for $Q^* = 0.5$

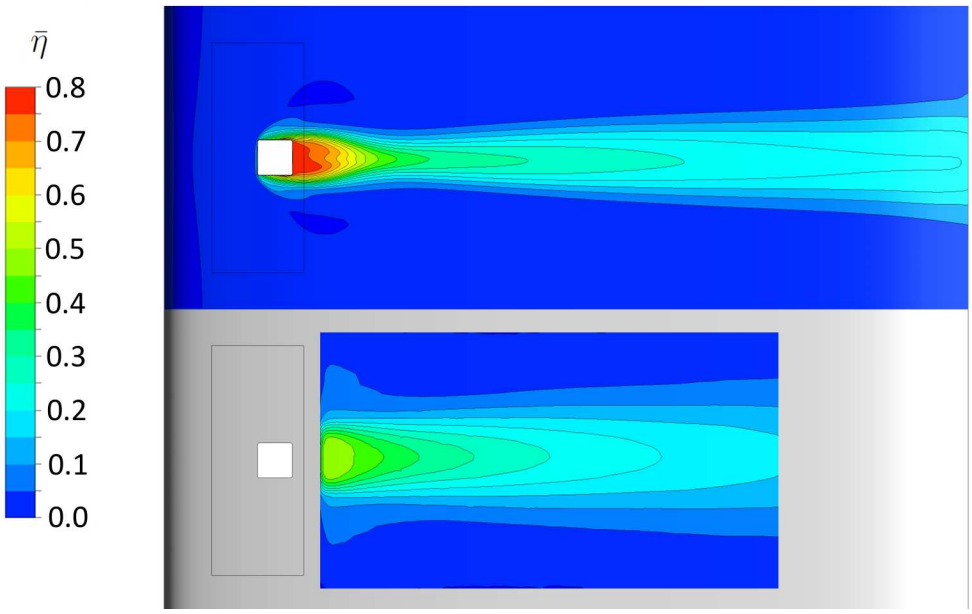

(b) Comparison of time-averaged thermal efficiency $\bar{\eta}$ against experimental data

Figure 4.16: Results obtained from the URANS approach on the hexahedral mesh utilizing the baseline time step Δt

on the hexahedral mesh, cf. figure 4.13(a), where the spatial resolution is not fine enough for resolving turbulent fluctuations anymore. This is inherent to the hybrid meshing strategy, where local and isotropic refinement is achieved in the jet in cross flow interaction region with the help of bodies of influence. The comparison of numerical and experimental data for thermal efficiency is shown in figure 4.17(b). Like the SAS computation on the hexahedral mesh, a comparable level of agreement is achieved in the mid and far field. Lateral spreading of temperature and downstream propagation are slightly larger, which can be attributed to the increased resolution of turbulent

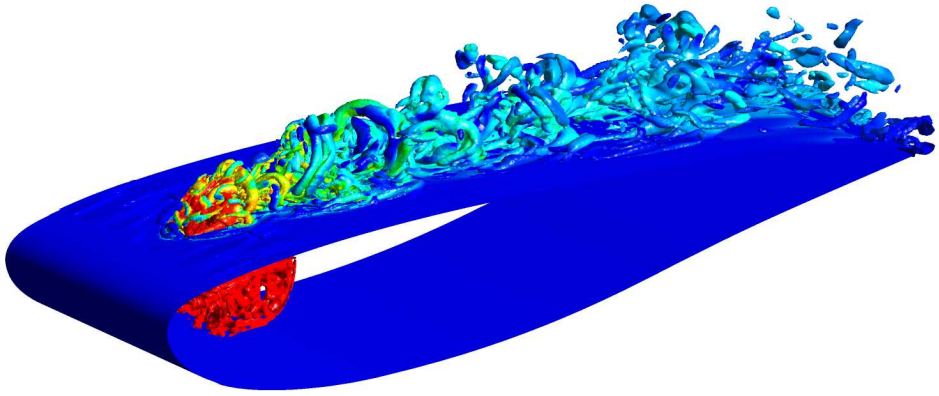

(a) Q-criterion for $Q^* = 1.0$

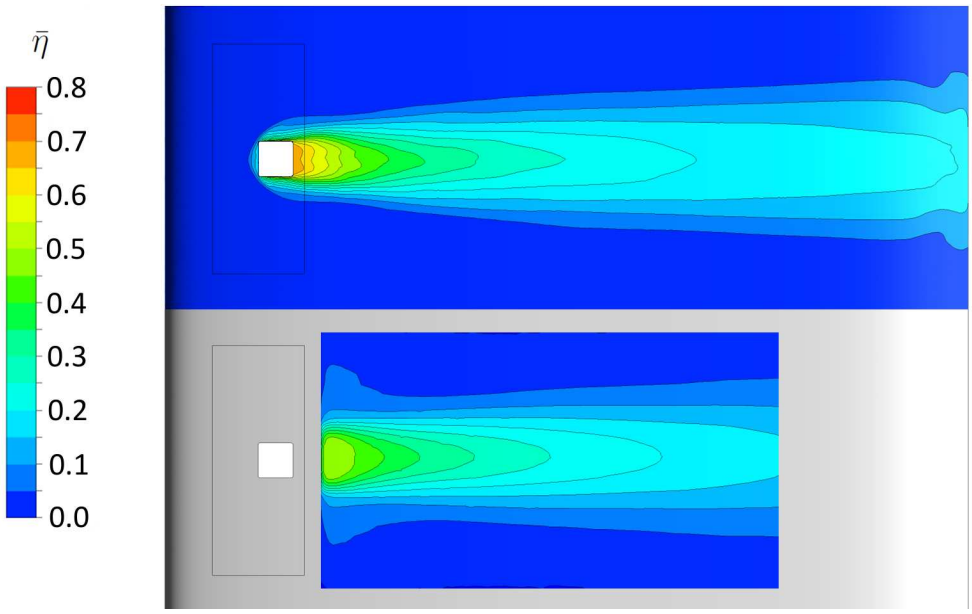

(b) Comparison of time-averaged thermal efficiency $\bar{\eta}$ against experimental data

Figure 4.17: Results obtained from the SAS approach on the hybrid tetrahedral mesh utilizing the baseline time step Δt

fluctuations and thus to an enhanced prediction of thermal mixing. Attention is now turned towards the SAS computation on the hybrid Cartesian mesh, which was presented in section 4.2. Once again, residuals evolve in a similar manner as shown in figure 4.10, with the only difference consisting in inner convergence. Contrary to the SAS calculation on the hexahedral and the hybrid tetrahedral mesh, convergence criteria are not entirely met. In order to avoid excessive computational time and for consistency, the number of inner iterations are limited to 12, which corresponds to the number needed to meet the standard convergence criteria on the hybrid tetrahedral

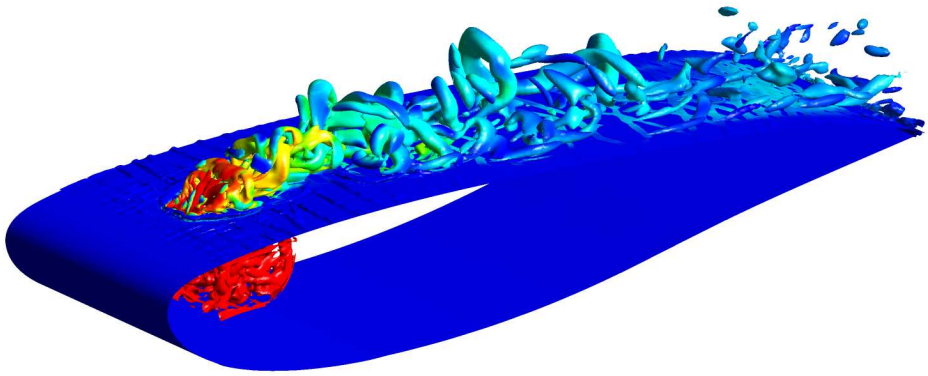

(a) Q-criterion for $Q^* = 1.0$

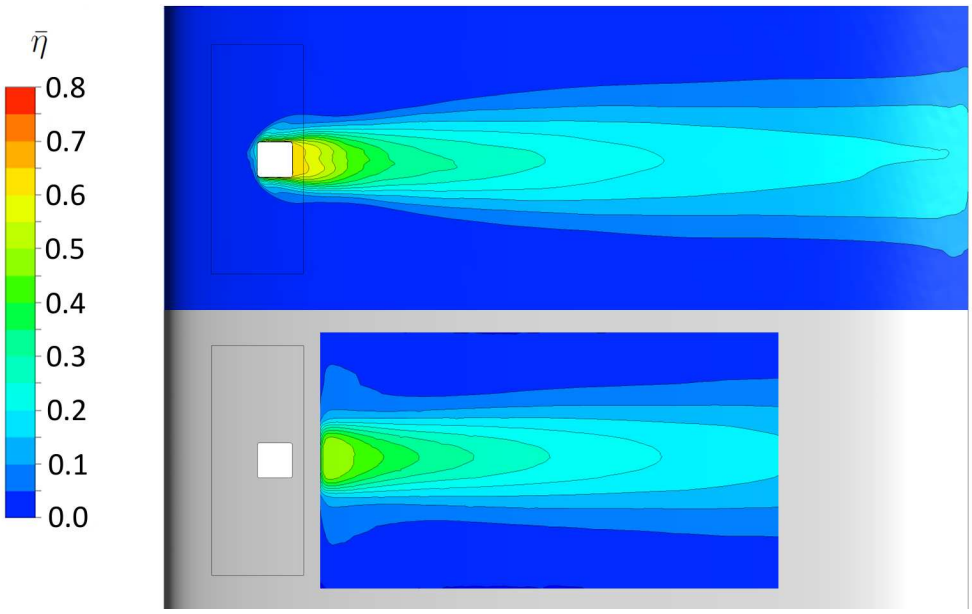

(b) Comparison of time-averaged thermal efficiency $\bar{\eta}$ against experimental data

Figure 4.18: Results obtained from the SAS approach on the hybrid Cartesian mesh utilizing the baseline time step Δt

mesh. Investigation of monitor points inside the jet, similar to the ones presented in figure 4.11, still shows a sufficiently converged solution at the end of the subiterations. This behavior can be attributed to the existence of computational cells with a decreased quality, which locally constrain convergence. The illustration of the Q-criterion with isosurfaces at a value of $Q^* = 1.0$ point out the capability of the underlying numerical mesh to resolve turbulent fluctuations in the same areas of inherent flow instabilities, i.e. plenum and entire jet in cross flow interaction region. Similar to the other hybrid mesh and different to the hexahedral approach, coherent structures are also visible in

the far field. This is also caused by the use of bodies of influence for mesh generation, which allows a locally refined and an isotropic mesh throughout the entire jet wake. In difference to the hybrid tetrahedral mesh however, fewer structures are discernible here. For the sake of comparability between the hybrid approaches, the element edge length for the Cartesian mesh and the tetrahedral mesh in the area of scale-resolution has been kept identically. This eventually leads to larger hexahedral elements allowing lesser scale-resolution. Concerning the contour plot of thermal efficiency illustrated in figure 4.18(b), a satisfying agreement with experimental data is achieved in the mid and far field, where lateral spreading is correctly predicted. The main difference for the three proposed meshing strategies arises directly downstream of the orifice, where the highest values of thermal efficiency are predicted on the hybrid tetrahedral mesh.

Concluding this, it can be stated that the SAS turbulence model is applicable to a jet in cross flow independently of the underlying meshing strategy. The only requirements are the proper resolution of boundary layers and a sufficient spatial refinement in the area of interest, ideally consisting of isotropic cells. This is important for the application to the more complex geometries, which will be encountered and where one meshing strategy might be favored over another. As the hexahedral meshing strategy allows a better control of transition from boundary to volume cells, this approach will be followed throughout the remaining part of this work whenever geometrical complexity allows its application.

4.4.3 Time Step Study

Finally, the impact of the numerical time step size on scale-resolvability of the SAS turbulence model and subsequently its influence on thermal mixing prediction is discussed in this section. Choice of the time step size is crucial as it presents a parameter, which is usually fixed a priori and directly influences the resolution of turbulent scales. Indeed, an implicit time advancement scheme is unconditionally stable, also allowing large time steps. As spatial and temporal resolution of coherent structures correlate, a sufficiently small time step is however necessary.

The SAS computation utilizing the small time step $0.5\Delta t$ is considered first. Evolution of residuals is qualitatively identical to the ones presented in figure 4.10. Quantitatively, a strong difference is however perceivable. Due to small advancement in time, inner convergence is achieved much faster compared to the baseline time step Δt, i.e. after only 5 subiterations. As already mentioned above, accumulated times for transient flow initialization and outer convergence are different since the number of time steps are kept constant. Nonetheless, outer convergence is achieved within 7 000 time steps. Following the procedure above, isosurfaces of the Q-criterion at a value of $Q^* = 1.0$ are illustrated in figure 4.19(a). Comparing this to the corresponding simulation at the baseline time step Δt in figure 4.13(a), more and smaller turbulent

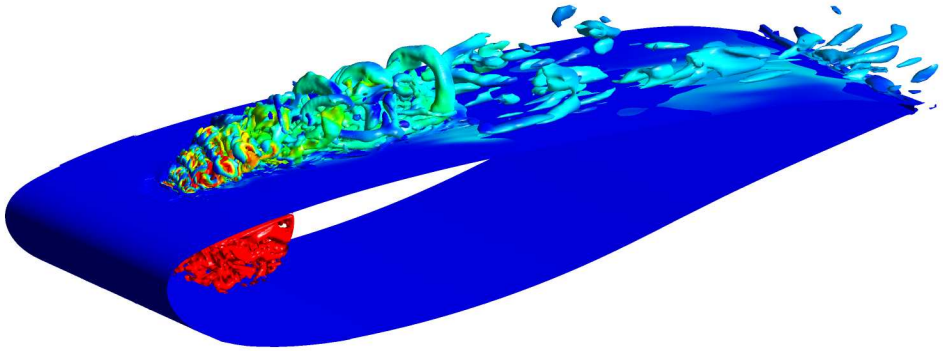

(a) Q-criterion for $Q^* = 1.0$

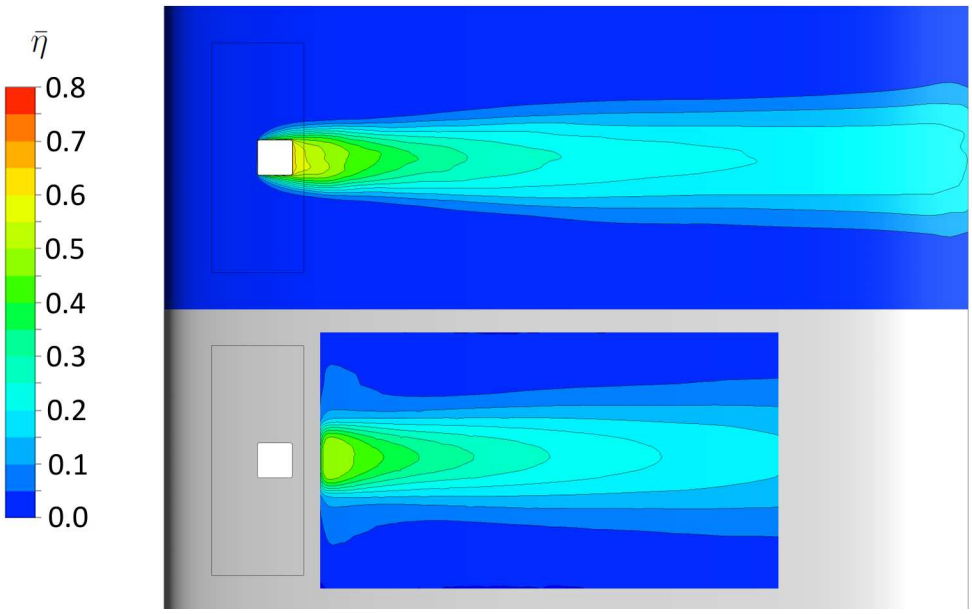

(b) Comparison of time-averaged thermal efficiency $\bar{\eta}$ against experimental data

Figure 4.19: Results obtained from the SAS approach on the hexahedral mesh utilizing half the baseline time step $0.5\Delta t$

structures are discernible in the jet in cross flow interaction region and inside the plenum. Contrary to this, no noticeable difference appears in the far field. This is a consistent behavior since an increased temporal refinement will not allow the resolution of turbulent fluctuations in areas with insufficient spatial refinement, which the jet far field of the hexahedral mesh has shown to be. On the other side, more and finer structures will be resolved in areas with high spatial refinement as the near and mid field of the jet. This points out that the mesh refinement in these areas are too strict for the calculation with the baseline time step Δt. The influence on the surface tem-

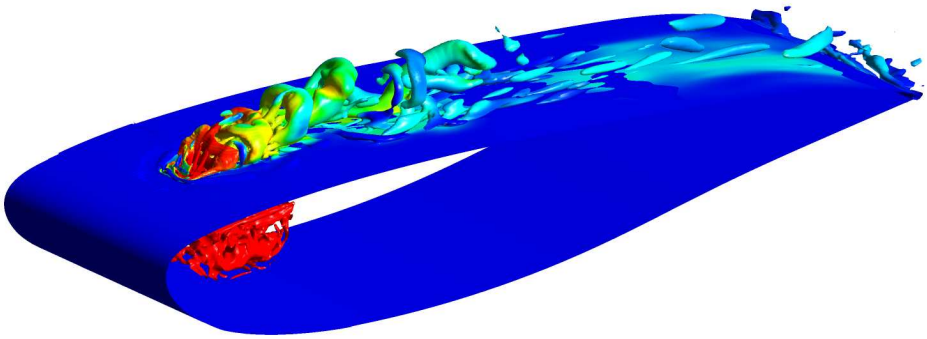

(a) Q-criterion for $Q^* = 1.0$

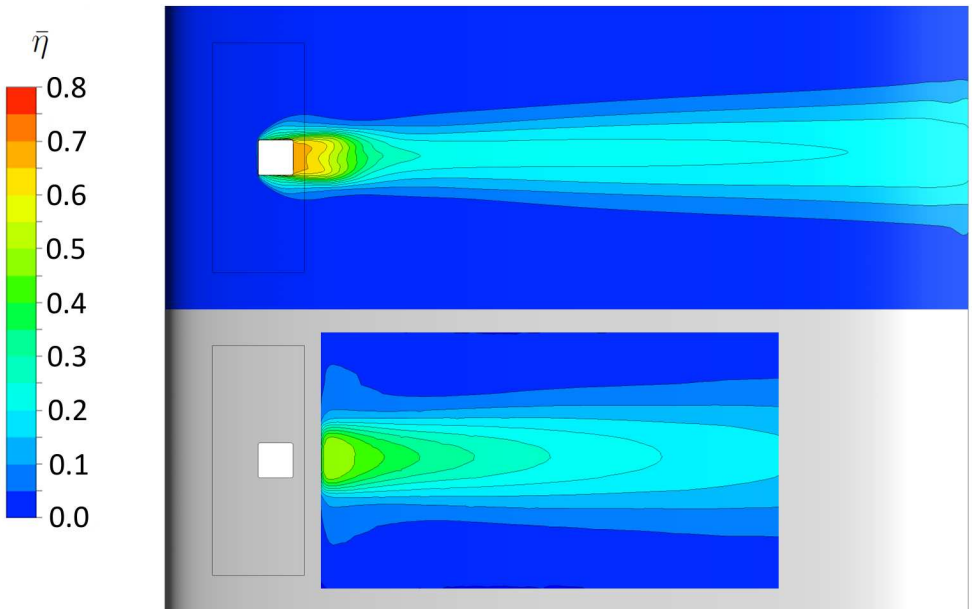

(b) Comparison of time-averaged thermal efficiency $\bar{\eta}$ against experimental data

Figure 4.20: Results obtained from the SAS approach on the hexahedral mesh utilizing double the baseline time step $2\Delta t$

perature distribution is presented in figure 4.19(b). Only small difference compared to the computation with the larger time step are discernible and lateral spreading remains underestimated in the near field. Due to the increased resolution of turbulent content in the near and mid field, thermal mixing prediction is enhanced leading to an elongated thermal trace.

Secondly, the SAS computation with the larger time step $2\Delta t$ is presented. Concerning the evolution of residuals, the tendency observed before remains. The qualitative behavior is identical but again a strong quantitative difference exists. This

time caused by the large advancement in time, standard inner convergence criteria are met only within 20 subiterations. Indeed, the number is quite high but for the sake of consistency necessary. Accumulated time for transient flow initialization and outer convergence is now increased by a factor of two compared to the baseline time step Δt by keeping the required 1 000 time steps for initialization and 7 000 time steps for outer convergence. The isosurfaces for a value of $Q^* = 1.0$ show the instantaneous vortex topology in figure 4.20(a). As expected fewer and larger structures appear inside the plenum and the jet in cross flow interaction region, which is nonetheless still more as seen for the URANS approach, cf. figure 4.16(a). The comparison of the resulting temperature distribution shown in figure 4.20(b) with the experimental one now becomes insufficient. Even if a tendency for lateral spreading is observable in the mid and far field, it remains underestimated. This plot has actually similar features as the URANS computation, which was shown in figure 4.16(b). This is also consistent since an insufficient temporal resolution does not properly activate the source term Q_{SAS}, cf. equation (3.54), resulting in a more URANS-like behavior of the SAS model. The dependence on the physical time step is pointed out by these results. Ideally, spatial and temporal resolution should correlate in the region of interest to save computational resources. This is however not feasible as a different mesh would be needed every time step to account for the changes in local flow topology. An interesting feature of the SAS turbulence model is revealed as time step size and number of subiterations are inversely proportional. In combination with the fact that the same number of time steps is needed for outer convergence, a smaller time step is beneficial if the mesh still allows additional spatial resolution.

4.4.4 Detailed Examination

Having shown a qualitative validation of the proposed integrated turbulence modeling approaches, a more quantitative view is presented in the following section. In order to distinguish between the different simulations carried out, table 4.3 provides the nomenclature used for clarity. Also included in this table is the ratio of CFL number, defined as CFL=$U\Delta t/\Delta_V$, over the number of iterations necessary to obtain inner convergence. As an implicit time-advancement scheme is employed, very large CFL numbers can be encountered locally. This is indeed the case for the hexahedral mesh, where the boundary layer refinement of the external wing surface traverses the orifice due to the underlying blocking topology. This leads to an overly refined mesh and thus to large values of the CFL number. The average CFL number in the region of scale-resolution is however close to 3 for the baseline time step. Since this refinement is not encountered for the meshes based on the hybrid strategies, the ratios are significantly smaller. As already pointed out by the time step study, a reciprocal relation between time step size and number of inner iterations exists, which leads to the identical ratio encountered in cases 1, 7 and 8.

Table 4.3: Nomenclature of integrated simulation approaches carried out for validation of the single ejector configuration

	Turbulence model	Meshing strategy	Numerical time step	CFL/N_{inner}
Case 1	SAS	hexahedral	Δt	75
Case 2	DDES	hexahedral	Δt	94
Case 3	ELES	hexahedral	Δt	94
Case 4	URANS	hexahedral	Δt	125
Case 5	SAS	hybrid tetrahedral	Δt	9
Case 6	SAS	hybrid Cartesian	Δt	4
Case 7	SAS	hexahedral	$0.5\Delta t$	75
Case 8	SAS	hexahedral	$2\Delta t$	75

Profiles of time-averaged thermal efficiency $\bar{\eta}$ along the symmetry line $Y/D = 0$ on the surface are shown in figures 4.21(a) and 4.22(a). Two aspects are striking. The first one concerns the strong scattering of numerical results in the near field up to $X/D = 3$ and the second one the convergence in the mid and far field towards experimental data. Even though the deficiency of the URANS simulation is not as drastically seen here, an overestimation remains visible in the far field. Except the simulation with the largest time step, all results obtained from the SAS turbulence model compare very well with experimental data. The best agreement is achieved on the hybrid tetrahedral mesh, which can be attributed to the enhanced scale-resolution due to the refined mesh in the wake.

The lateral spreading in the vicinity of the ejector, i.e. $X/D = 1$, is presented in figure 4.21(b) and 4.22(b), where rather strong differences become perceivable. Consistently with the previous observation, the ELES and the URANS approach strongly overestimate the temperature between $Y/D = \pm 0.5$. However, all simulations accurately capture the width of the thermal trace and the corresponding temperature gradient. Additionally, the two symmetric maxima found in experimental investigations are confirmed. The fact that thermal impact is still perceivable outside $Y/D \pm 1.5$ for experimental data is due to internal heat conduction inside the mock-up and will be discussed in section 4.6.1. Results presented for the mid field, i.e. $X/D = 3$ and 8, in figures 4.21(c), 4.22(c), 4.21(d) and 4.22(d) exhibit a smaller scattering and in general a very good agreement with experimental data. As already discussed in the previous section, the URANS approach strongly underestimates lateral spreading. This behavior persists also in the far field, which becomes apparent in figures 4.21(e) and 4.22(e). It can be summarized that the SAS and DDES approach yield very satisfying results and only small influences of the meshing strategy and time step size becomes noticeable.

For validation of the flow field, time statistics of velocity components will be considered next. Profiles for X-velocity components are plotted for wall-normal lines in the symmetry plane at locations $X/D = 1$ and X/D=2 in figures 4.23(a), 4.24(a), 4.23(b) and 4.24(b). Qualitatively, all simulations agree well with experimental data and the recirculation zone at X/D=1 for $Z_w/D < 0.7$ is confirmed. Due to this, hot air accumulates behind the orifice leading to the strong thermal impact in the near field as seen previously. The ELES approach yields the strongest recirculation zone, which is moreover in best agreement with experimental values. This explains the high temperature predicted in the near field, which is however contradictory to experimental data for temperature. The influence of the jet is discernible up to $1D$ away from the wall, where numerical and experimental velocity profiles merge. The zone of velocity deficit extends up to $1.5D$ at the location of the second profile but the recirculation zone has disappeared. Only the URANS approach predicts a small area with a negative X-velocity component. Concerning the Z-velocity components plotted in figures 4.23(c), 4.24(c), 4.23(d) and 4.24(d) a satisfying agreement with experimental data is obtained. In contrast to the temperature field, the deficiency of the URANS approach becomes not as drastically visible for the mean velocity field. The scattering of results caused by the different meshing strategies is small as well, highlighting the general applicability of the SAS approach. Additional contour plots of the mean velocity field on planes with streamwise and lateral orientations show also a very good agreement with experimental data and are presented in appendix B.

As second order time statistics are important for the validation of the transient flow field, the root mean square values are presented for all three velocity components on the same wall-normal lines in figures 4.25 and 4.26. In general, a very good agreement with experimental data is obtained from all simulations except the URANS approach. Indeed, profiles obtained from this type of calculation show also a qualitative agreement but the magnitude is drastically underestimated. They will therefore be left aside for the following discussion. For X-velocity components, results compare rather well with experimental data and the location of maximal fluctuations at $0.75Z_w/D$ is predicted correctly at $X/D = 1$ in figures 4.25(a) and 4.26(a). The high value of $0.5\sqrt{\overline{u'^2}}/U_\infty$ emphasizes the strong dynamics in this area. Moving downstream to X/D=2 in figures 4.25(b) and 4.26(b), the peak diminishes and moves further away from the wall. At the first location shown in figures 4.25(c) and 4.26(c), results for the Y-velocity component exhibit a peak close to the wall, which is stronger than the one seen in the experiment. In contrast to this, the second maximum at $Z_w/D = 0.6$ shown by experimental data remains underestimated by the simulations. For the second location presented in figures 4.25(d) and 4.26(d), the peak for the Y-velocity component approaches the wall, which is consistent with experimental findings. Finally, profiles for the Z-velocity components are shown in figures 4.25(e), 4.26(e), 4.25(f) and 4.26(f). For the first one, the location of the maximum is accurately predicted at $Z_w/D = 0.7$ with a slightly underestimated maximal value. The profiles flatten as they reach the second location, which is also in

sufficient agreement with experimental findings. Once again, the overall characteristics for the SAS calculations remain the same and vary only slightly with respect to mesh and time step size. Complementing contour plots of second order time statistics of the velocity field also compare very well with experimental data and are presented in appendix B.

For the last level of validation, spectral analysis is carried out for time signals of velocity components in the jet wake. Signals have been collected every time step for a total number of 5 000 physical time steps at several points, which corresponds to those also investigated experimentally. After dividing the time signal into 12 blocks overlapping by 50%, the Hann window function is applied to the each of these data segments. The one-sided power spectral density G (PSD) is subsequently estimated using Welch's method [101] with a spectral resolution Δf of 25Hz. Due to the different sampling frequencies for the simulations with double and half the baseline time step, spectral resolution double and halve as well. As the contribution of a frequency band to the overall fluctuation is of interest, the normalized spectrum $\tilde{G} = f \cdot G/\sigma^2$ with $\sigma^2 = \int G(f)\mathrm{df}$ being the root mean square value of the considered quantity is calculated instead. The Strouhal number can then be calculated via $St_D = f \cdot D/U_\infty$ with the characteristic quantities of the jet in cross flow D and U_∞.

The presentation of spectra is reduced to five as only those will be considered here that exhibit a strong spectral peak and are located in zones with a turbulent intensity greater than %5. The location of the monitor points and the investigated quantity are given in table B.1 of appendix B and the corresponding spectra are plotted in figures 4.27 and 4.28. Indeed, due to the strong discrepancies in sampling time and sampling frequency of several orders of magnitudes, the evolution of spectra are much smoother for experimental than for numerical data. Nonetheless, the strong spectral peak around $St_D = 0.14$, which is encountered in experiments, is also accurately captured by the simulations with exception of the URANS approach, which predicts a spectral peak around $St_D = 0.095$ at the points $\mathrm{P_{JICF,1}}$, $\mathrm{P_{JICF,2}}$ and at $\mathrm{P_{JICF,4}}$. This can be attributed to the incapability of the URANS approach to properly resolve turbulent fluctuations as already seen in the previous section. This is also reflected by the fact that the power spectral density obtained from the URANS calculation shows no high frequency contributions at all.

Concerning the influence of time step size and meshing strategy it can be stated that the SAS calculations employing the large time step $2\Delta t$ and the Cartesian mesh respectively tend to overestimate the intensity of the spectral peak, indicating an overly coherent motion. In general, results obtained from the SAS calculation with the small time step $0.5\Delta t$ and the ELES computation predict an amplitude consistent with experiments. Interestingly, only the SAS computation with the small time step is able to predict the spectral peak for the X-velocity component in figure 4.28(c). The physical meaning of the spectral peak almost solely encountered for the Y-velocity component will be discussed in section 4.5.

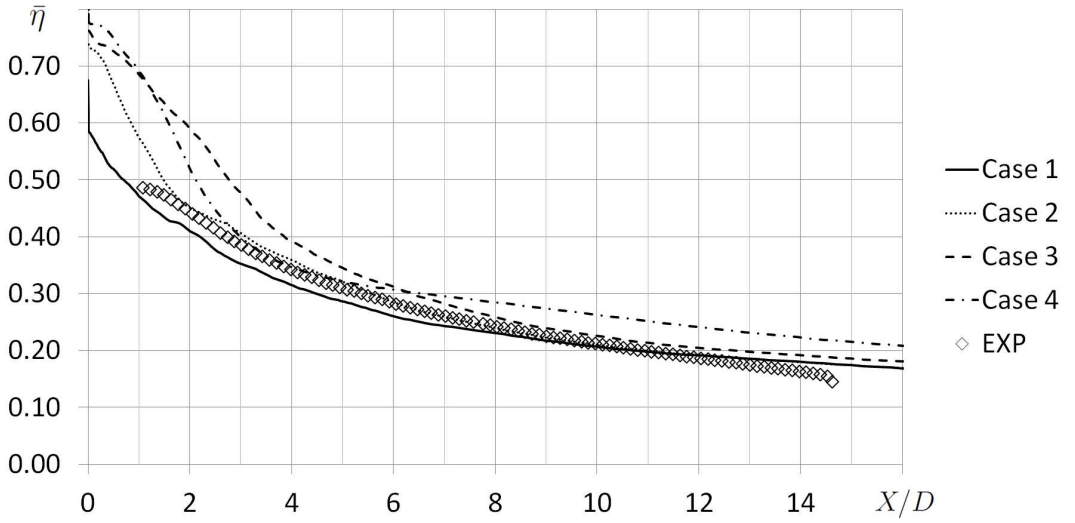

(a) Symmetry line $Y/D = 0$

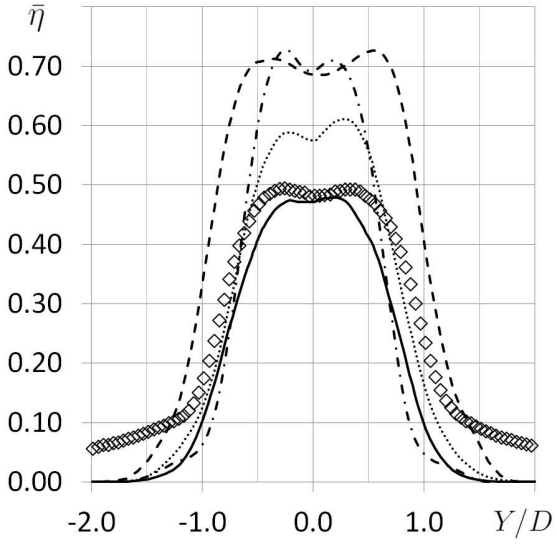

(b) Lateral distribution at $X/D = 1$

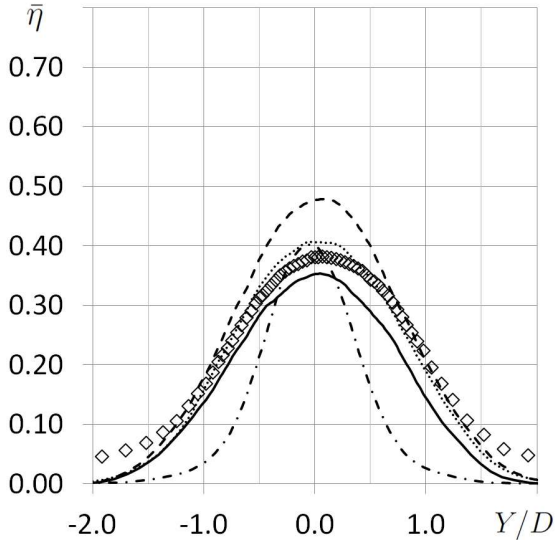

(c) Lateral distribution at $X/D = 3$

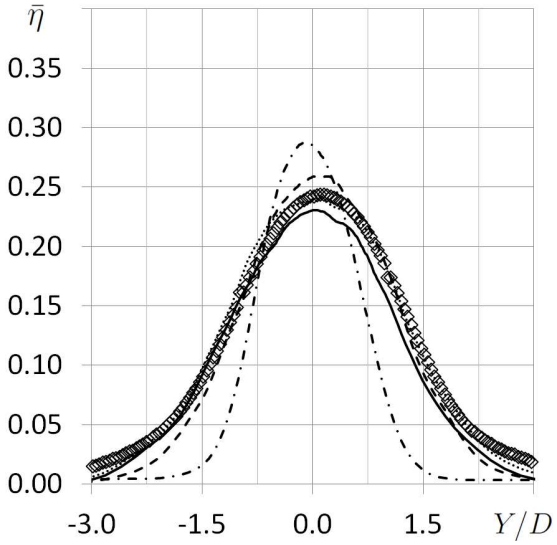

(d) Lateral distribution at $X/D = 8$

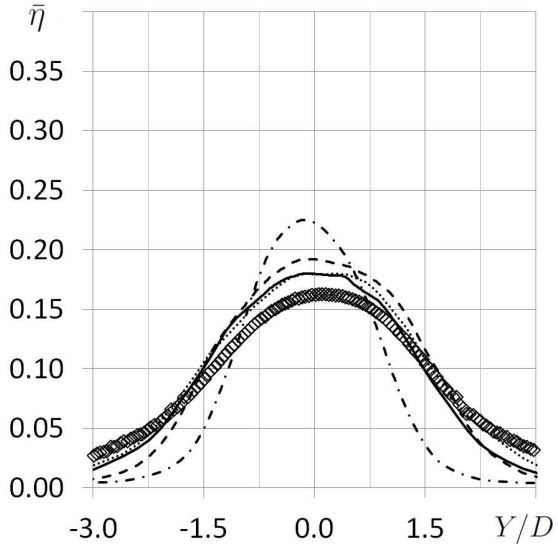

(e) Lateral distribution at $X/D = 14$

Figure 4.21: Profiles of time-averaged thermal efficiency, nomenclature given in table 4.3

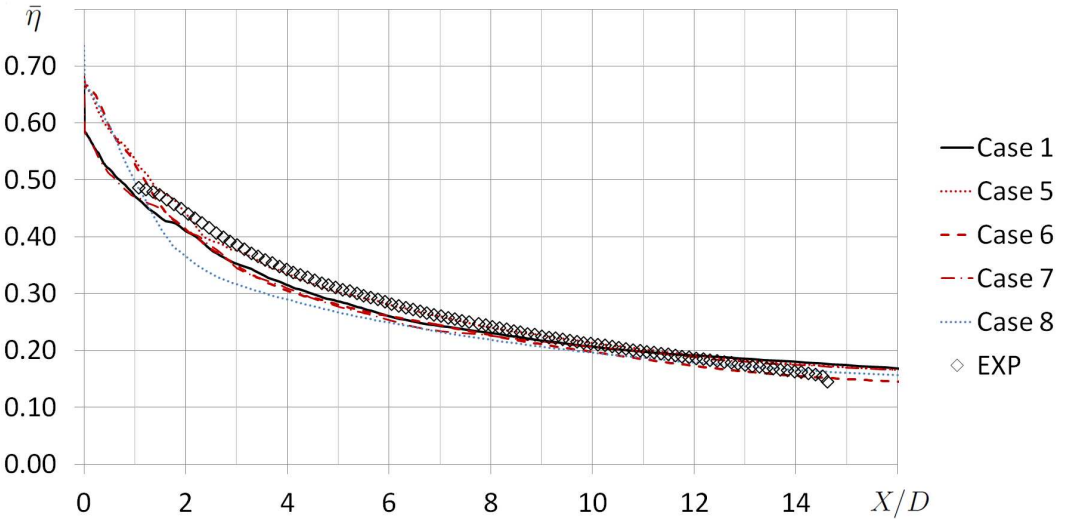

(a) Symmetry line $Y/D = 0$

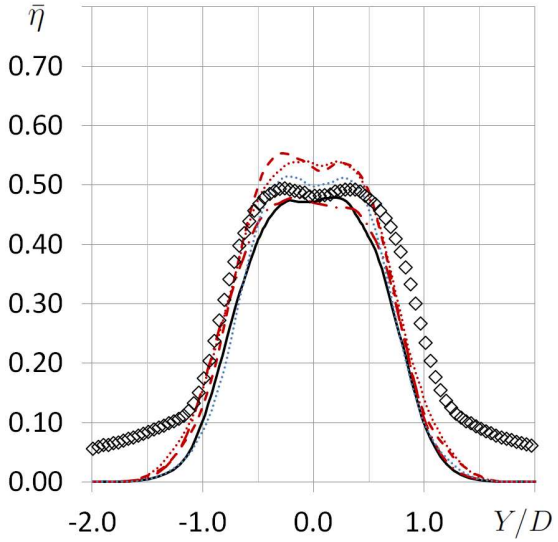

(b) Lateral distribution at $X/D = 1$

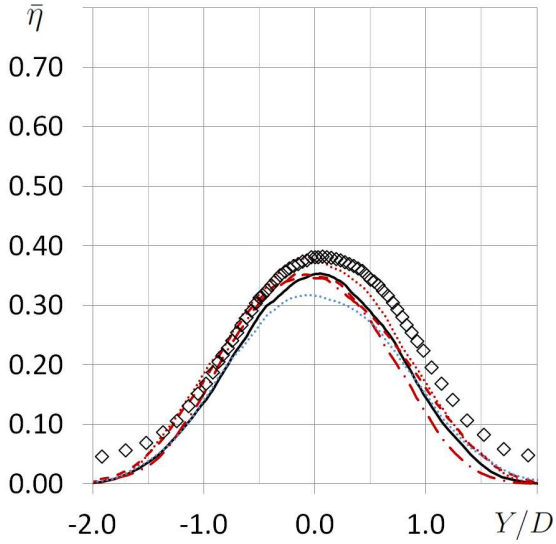

(c) Lateral distribution at $X/D = 3$

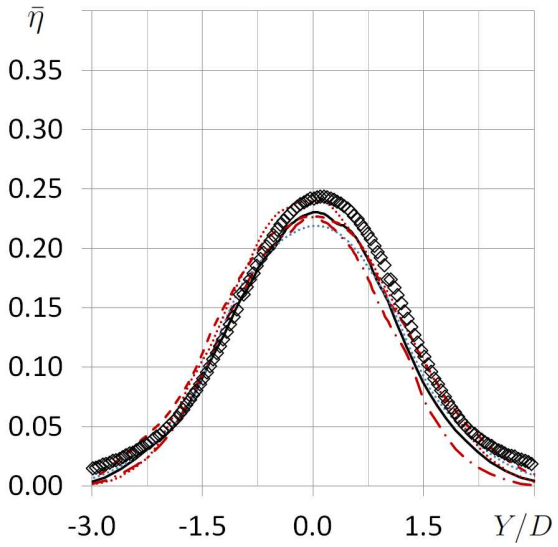

(d) Lateral distribution at $X/D = 8$

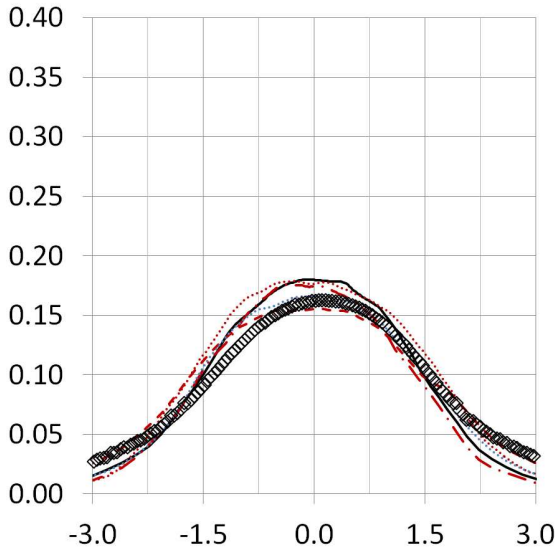

(e) Lateral distribution at $X/D = 14$

Figure 4.22: Profiles of time-averaged thermal efficiency, nomenclature given in table 4.3

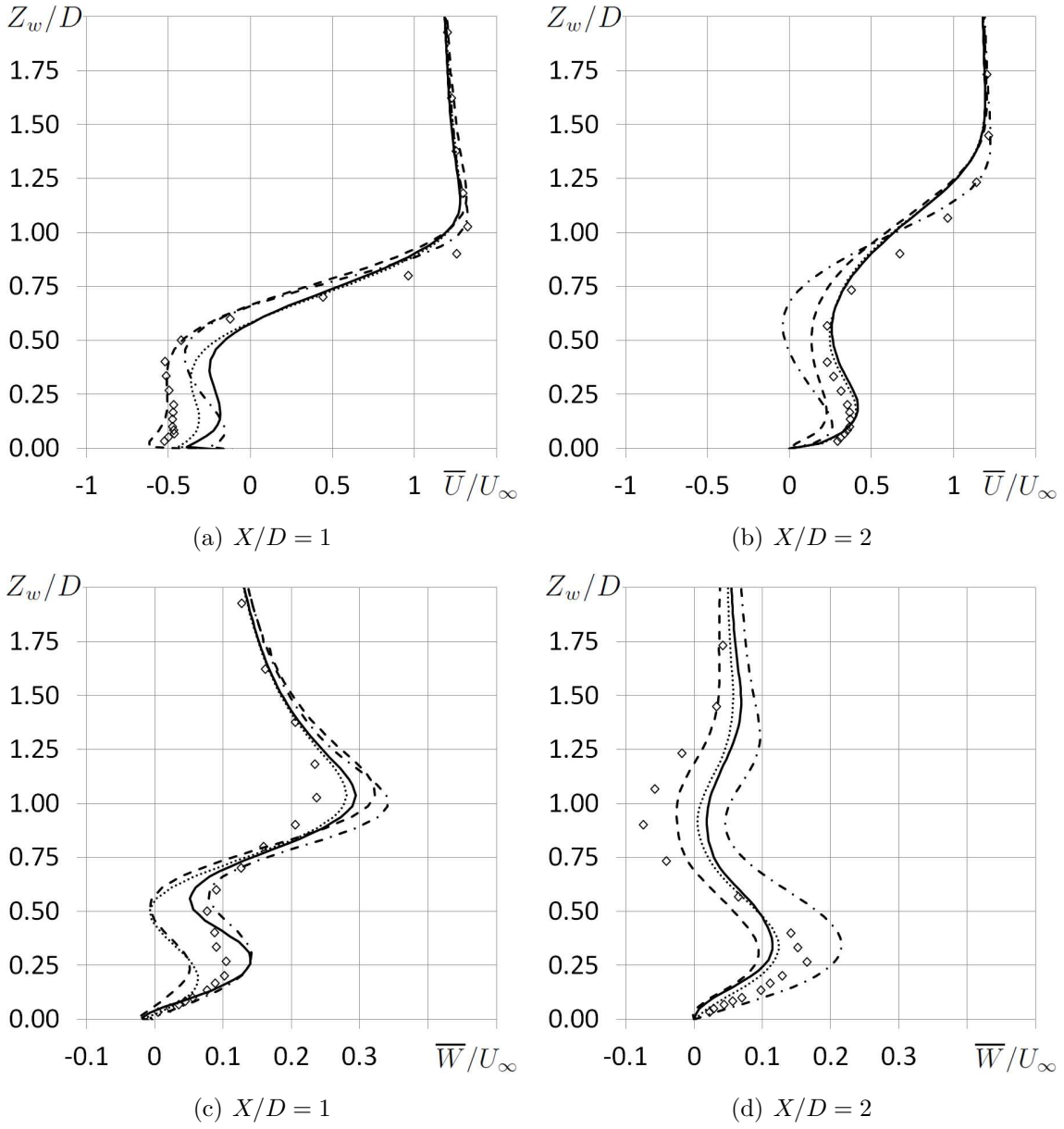

(a) $X/D = 1$ (b) $X/D = 2$

(c) $X/D = 1$ (d) $X/D = 2$

Figure 4.23: Profiles of mean velocity; symbols as given in figure 4.21

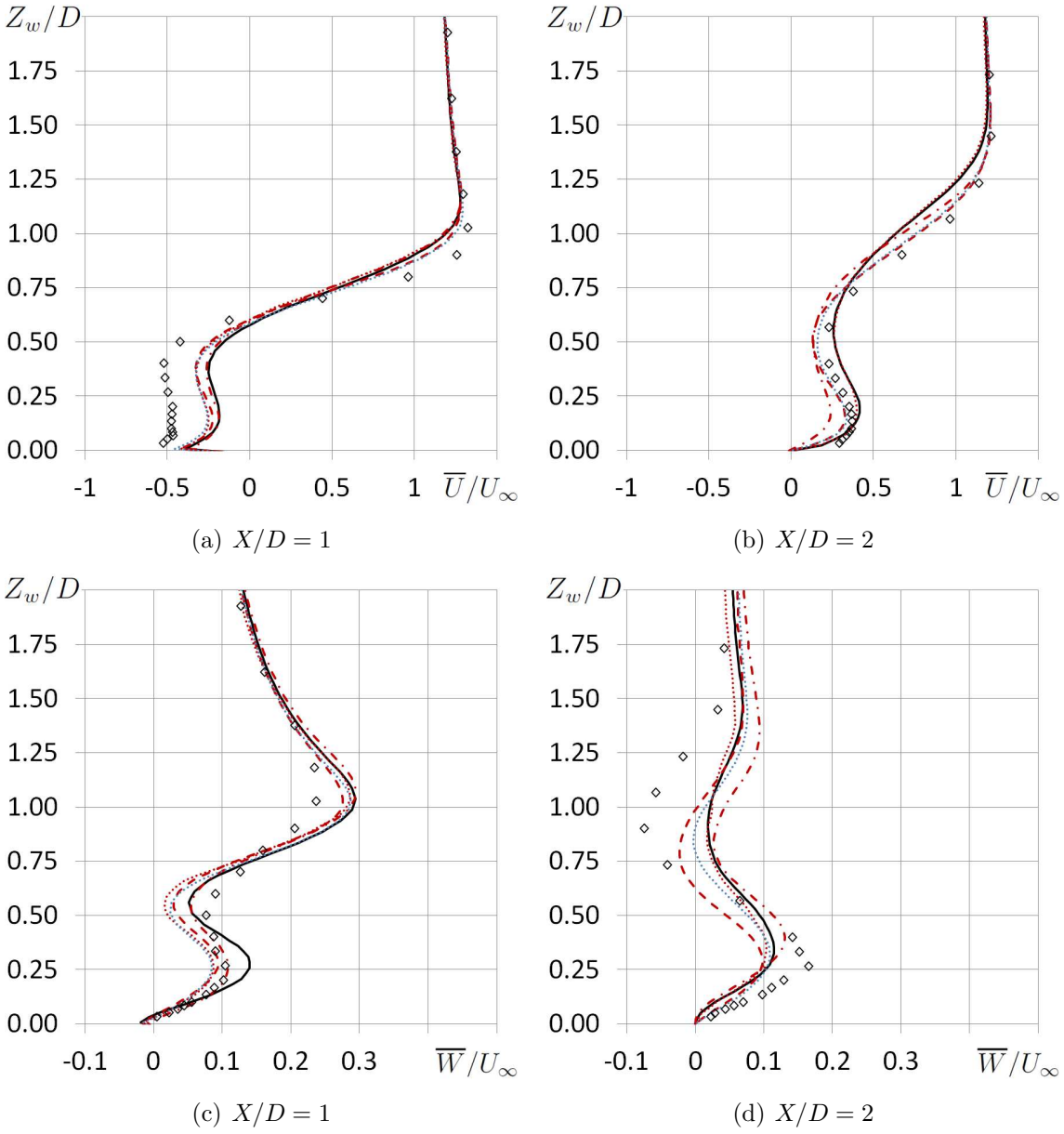

(a) $X/D = 1$ (b) $X/D = 2$

(c) $X/D = 1$ (d) $X/D = 2$

Figure 4.24: Profiles of mean velocity; symbols as given in figure 4.22

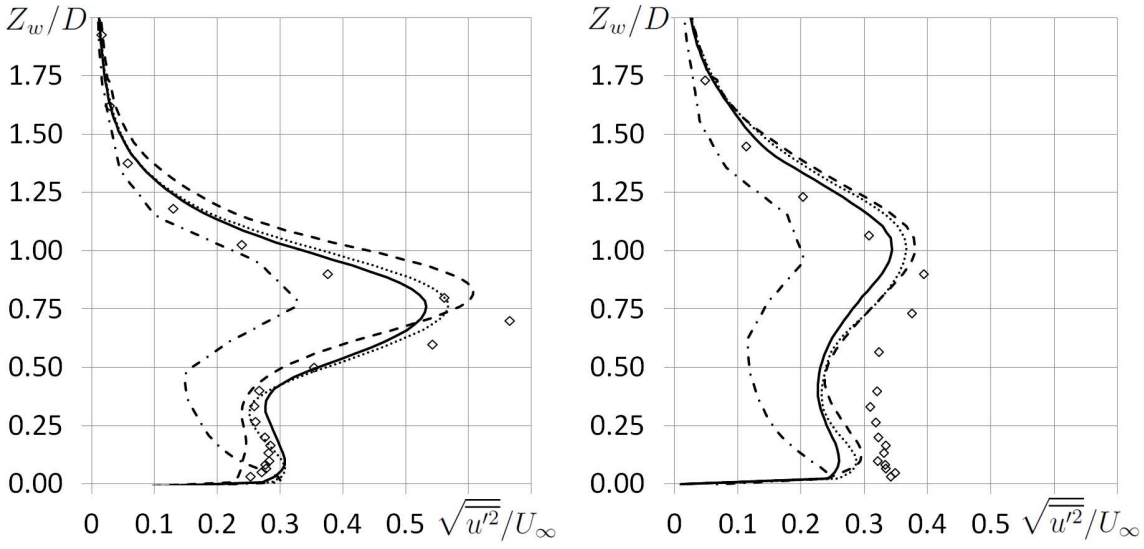

(a) $X/D = 1$

(b) $X/D = 2$

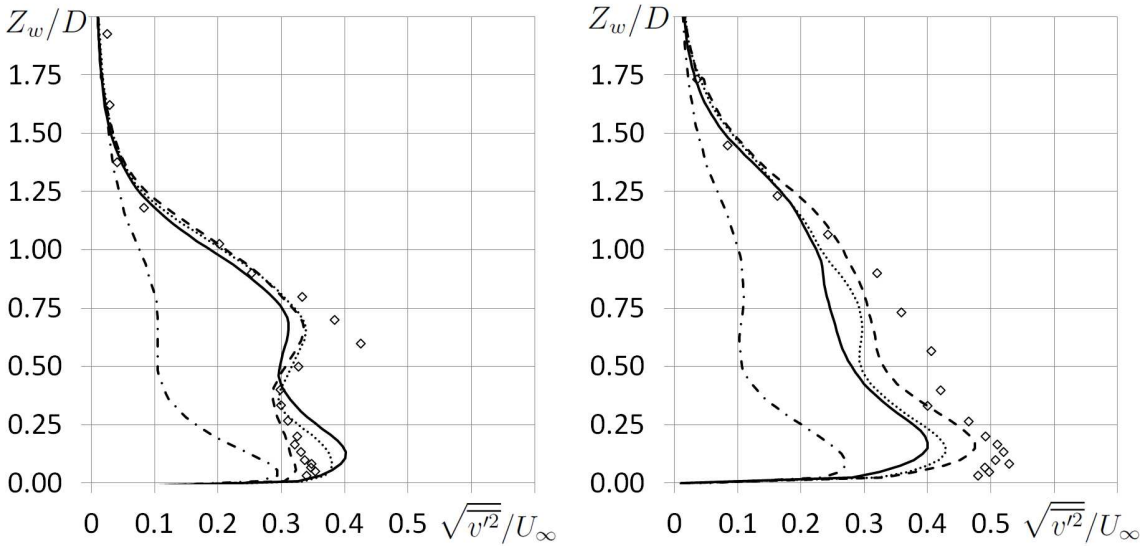

(c) $X/D = 1$

(d) $X/D = 2$

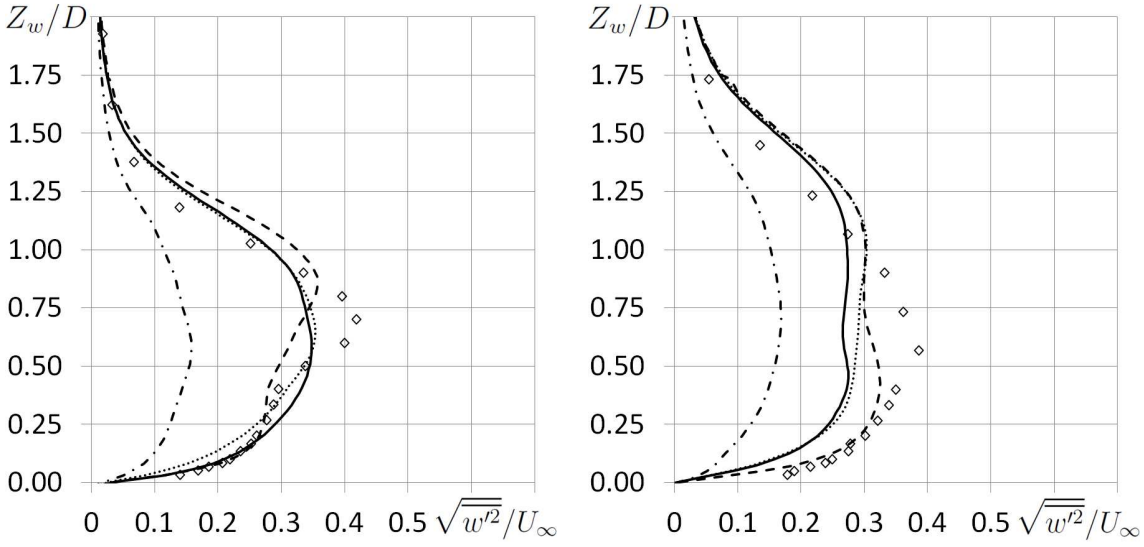

(e) $X/D = 1$

(f) $X/D = 2$

Figure 4.25: Profiles of fluctuating quantities; symbols as given in figure 4.21

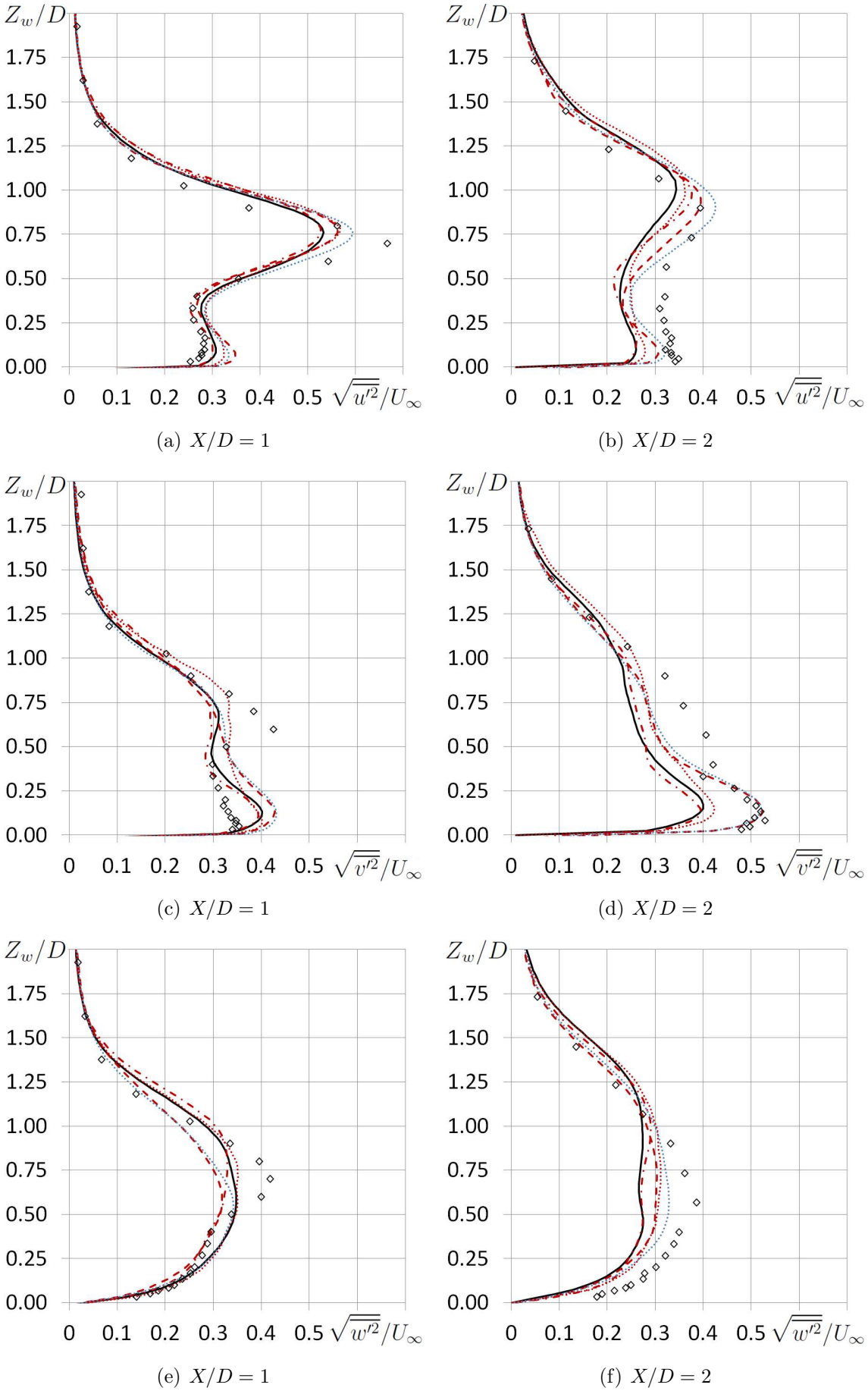

(a) $X/D = 1$ (b) $X/D = 2$

(c) $X/D = 1$ (d) $X/D = 2$

(e) $X/D = 1$ (f) $X/D = 2$

Figure 4.26: Profiles of fluctuating quantities; symbols as given in figure 4.22

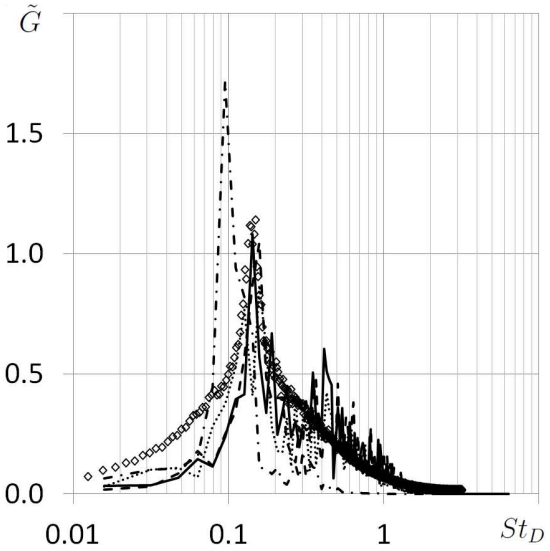

(a) PSD for Y-velocity component at $\mathrm{P}_{\mathrm{JICF},1}$

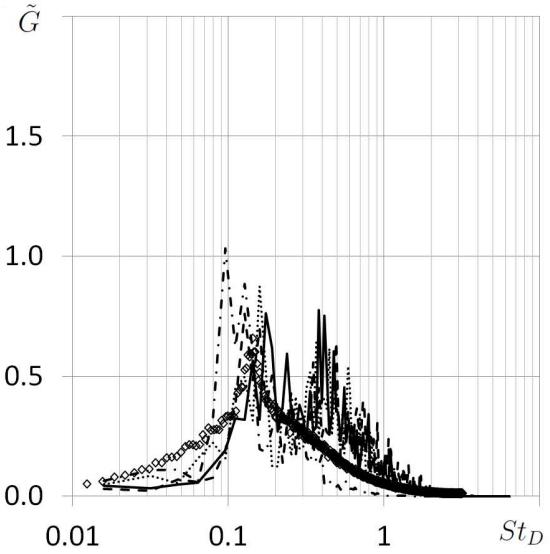

(b) PSD for Y-velocity component at $\mathrm{P}_{\mathrm{JICF},2}$

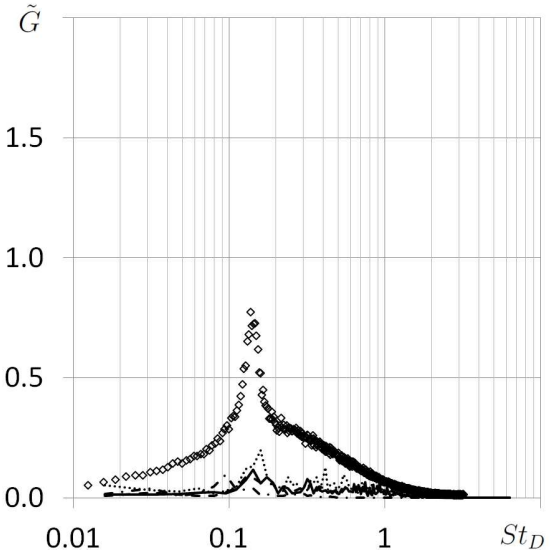

(c) PSD for X-velocity component at $\mathrm{P}_{\mathrm{JICF},3}$

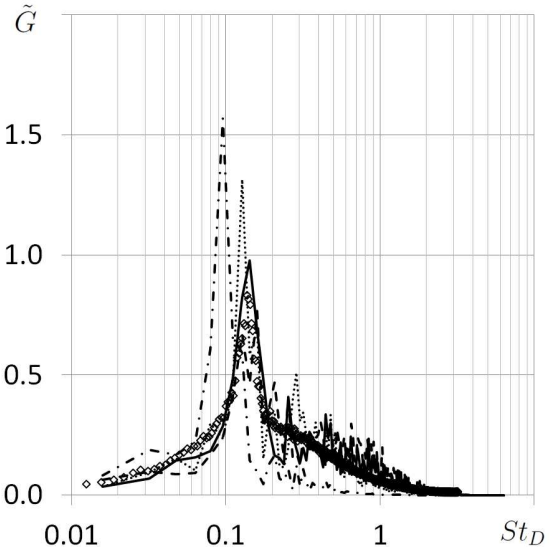

(d) PSD for Y-velocity component at $\mathrm{P}_{\mathrm{JICF},4}$

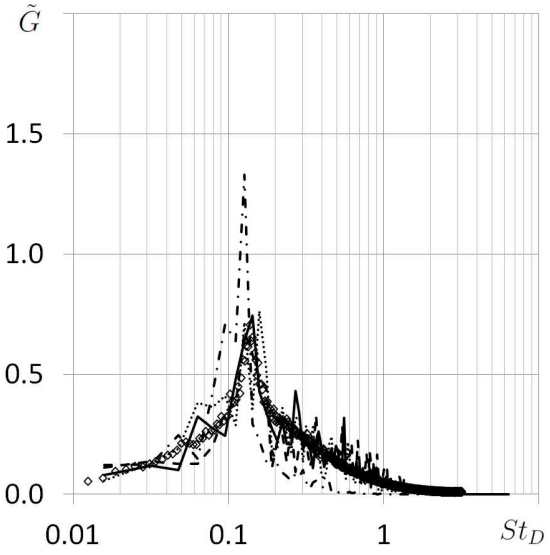

(e) PSD for Y-velocity component at $\mathrm{P}_{\mathrm{JICF},5}$

Figure 4.27: Estimates of power spectral density; symbols as given in figure 4.21

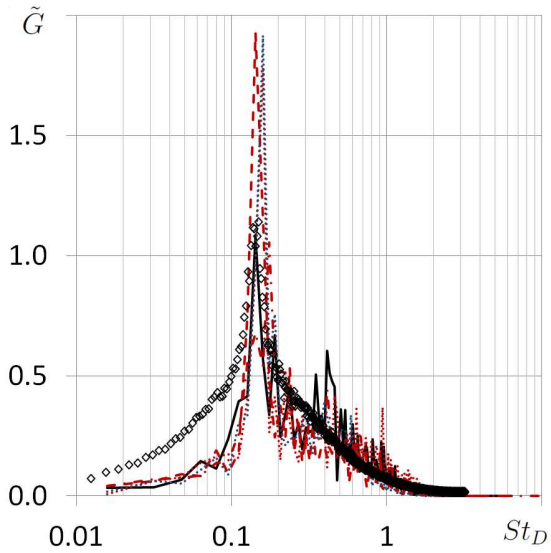

(a) PSD for Y-velocity component at $\mathrm{P}_{\mathrm{JICF},1}$

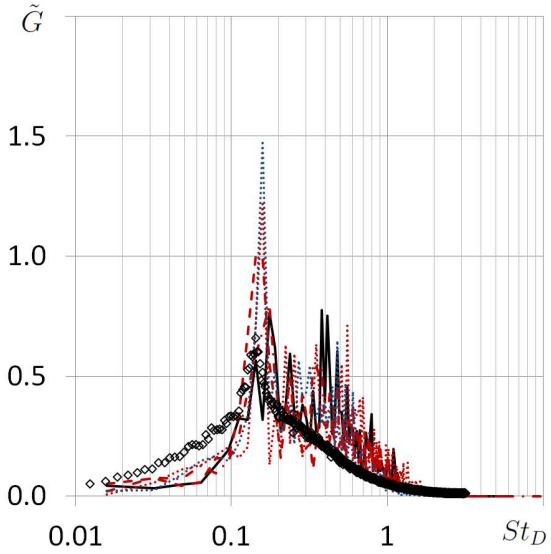

(b) PSD for Y-velocity component at $\mathrm{P}_{\mathrm{JICF},2}$

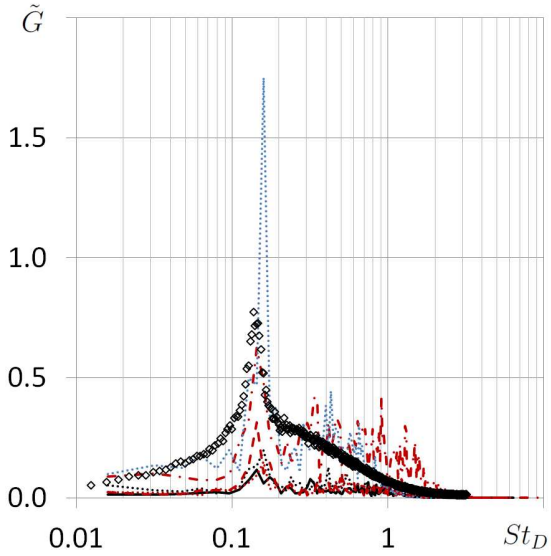

(c) PSD for X-velocity component at $\mathrm{P}_{\mathrm{JICF},3}$

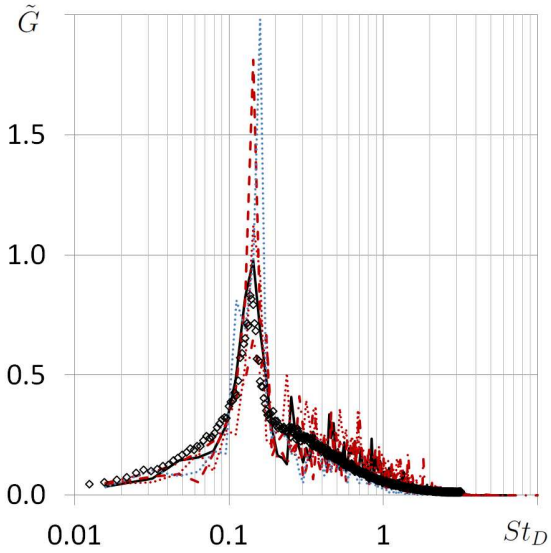

(d) PSD for Y-velocity component at $\mathrm{P}_{\mathrm{JICF},4}$

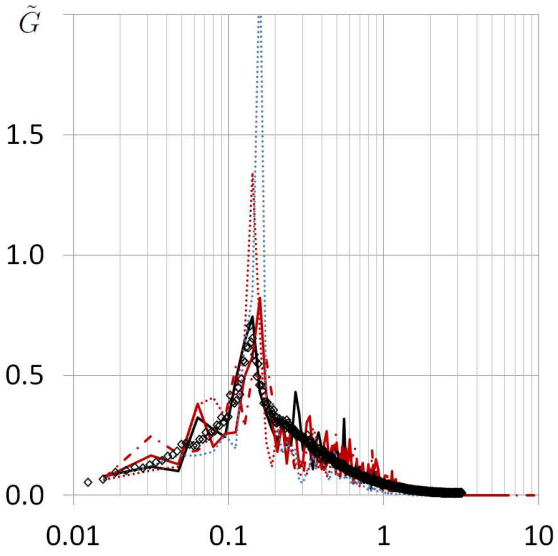

(e) PSD for Y-velocity component at $\mathrm{P}_{\mathrm{JICF},5}$

Figure 4.28: Estimates of power spectral density; symbols as given in figure 4.22

4.4.5 Sequential Approach

Attention is now turned towards the capability of the last methodology proposed. Starting point for the sequential approach is a steady state solution of the entire configuration. Even though three meshes are already available to compute an appropriate RANS solution, a further but coarser mesh is preferable for the following reason. In a standard process, one would also begin with a steady state computation on a coarse mesh before conducting a Scale-Resolving Simulation in a truncated but spatially refined subdomain. As interpolation is necessary for the extraction of RANS solution data, its quality will also depend on the spatial refinement of the global domain. It is therefore more practical to start from a poor quality interpolation as this could easily be encountered in the everyday process. The hexahedral mesh is thus locally coarsened but a boundary layer resolution of y^+ in the order of one is still maintained. As only half of the domain needs to be considered for the RANS computation, the total number of computational cells is reduced significantly, yielding now only $2.4 \cdot 10^6$.

The flow field is uniformly initialized and only 1 000 steady state iterations are calculated using the SST turbulence model. Obviously, the obtained solution is not converged in the jet in cross flow interaction region as well as in the jet wake. Nonetheless, all inflow surfaces where solution data needs to be extracted lie in a sufficient distance to the orifice with only a small impact of the locally non-converged solution. Values for velocity components, pressure, temperature as well as turbulence kinetic energy and specific dissipation rate are then extracted on all exterior cell faces of the SRS domain with the help of a first order interpolation scheme. Once these values are specified as velocity inlet and pressure outlet boundary conditions for the small domain, another initialization has to be carried out in analogy to the other approaches. Uniform values are thus prescribed first and 150 steady state iterations are carried out using the SAS turbulence model. Finally, 1 000 time steps are computed for transient flow initialization. From the experience obtained from the integrated approaches, a fixed number of 10 subiterations per time step are employed, which lead to a decrease of residuals of one to two orders of magnitude. Identically to the integrated approaches, a total number of 7 000 time steps are calculated for outer convergence.

In order to show the local scale-resolvability of this approach, the Q-criterion is shown in figure 4.29(a) at the standard isovalue of $Q^* = 1.0$. The wing surface shown in blue highlights the small extents of the subdomain. As already seen from the other simulations employing the SAS model, resolution of turbulent fluctuations of different size and nature is achieved in the area of interest. As internal parts of the air system are identical to the integrated approaches, no difference is visible inside the plenum. Compared to the results obtained from the integrated SAS approach presented in figure 4.13(a) no major differences are discernible. Being of crucial interest, the thermal efficiency is plotted in the top part of figure 4.29(b), which also compares sufficiently well with the experimental data presented in the bottom part of this figure. Lateral

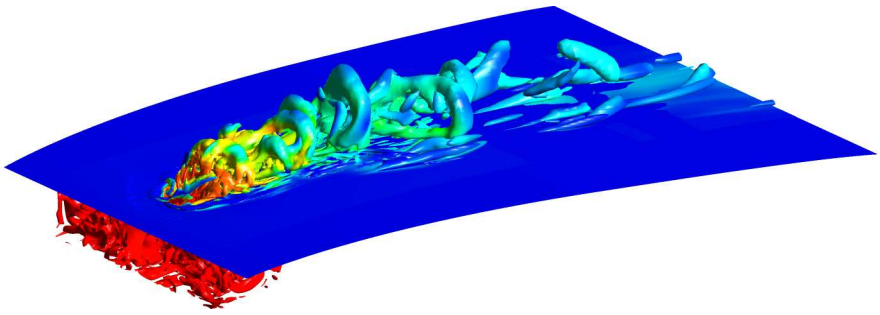

(a) Q-criterion for $Q^* = 1.0$

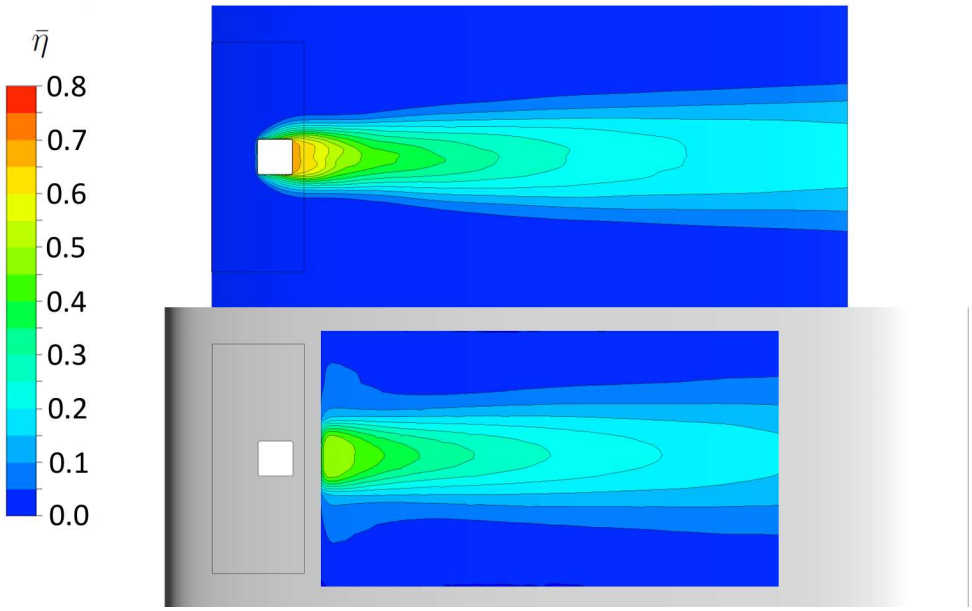

(b) Comparison of time-averaged thermal efficiency $\bar{\eta}$ against experimental data

Figure 4.29: Results obtained from the sequential approach using the SAS turbulence model and the baseline time step Δt

spreading in the near field is underestimated as seen for all other approaches but correctly predicted in the mid and far field. Only small differences compared to the results obtained from the integrated SAS approach in figure 4.13(b) are visible behind the ejector, where a slightly higher temperature distribution is observable leading to an elongated thermal trace. For the quantification of the these differences, time-averaged thermal efficiency of both the integrated and the sequential approach are compared to experimental data in figure 4.30. Despite the minor discrepancy in the near field, the sequential approach yields results, which are very similar to the ones obtained from the integrated approach. Installation effects are thus taken into account and the surface temperature distribution can still be accurately predicted with a reduction of computational costs by roughly 50%.

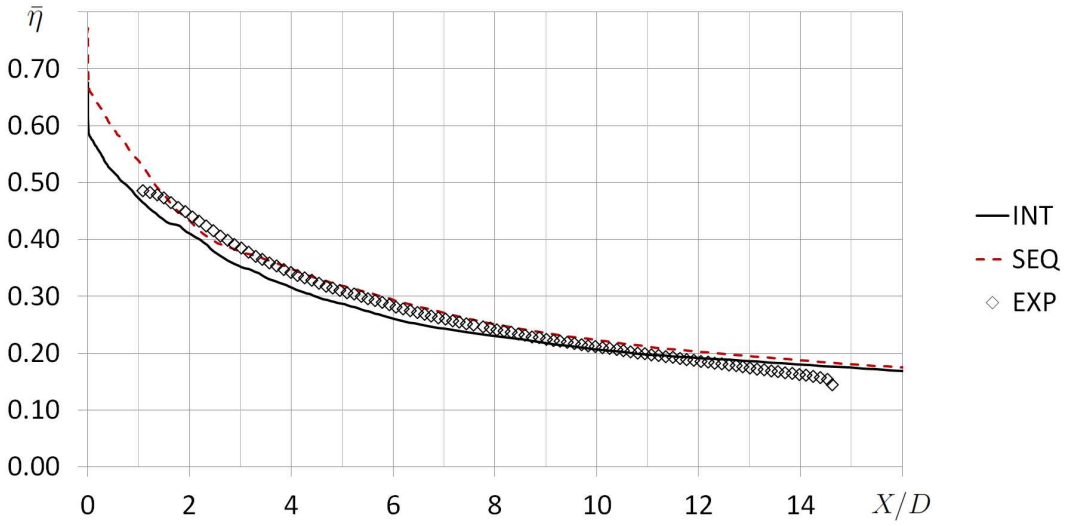

(a) Symmetry line $Y/D = 0$

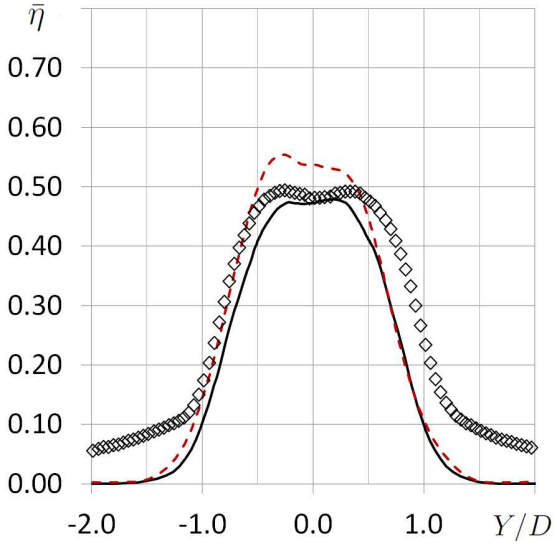

(b) Lateral distribution at $X/D = 1$

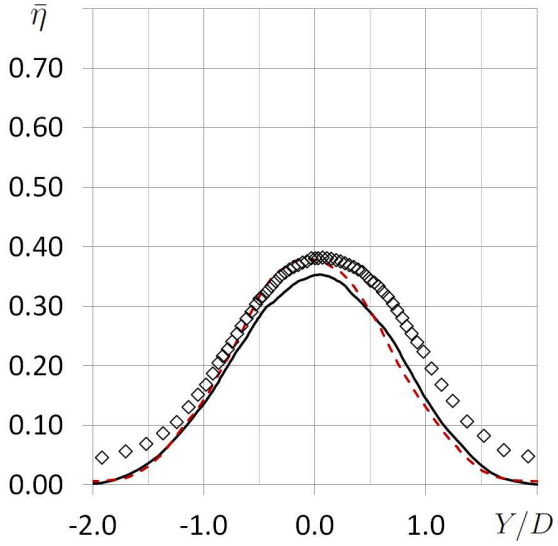

(c) Lateral distribution at $X/D = 3$

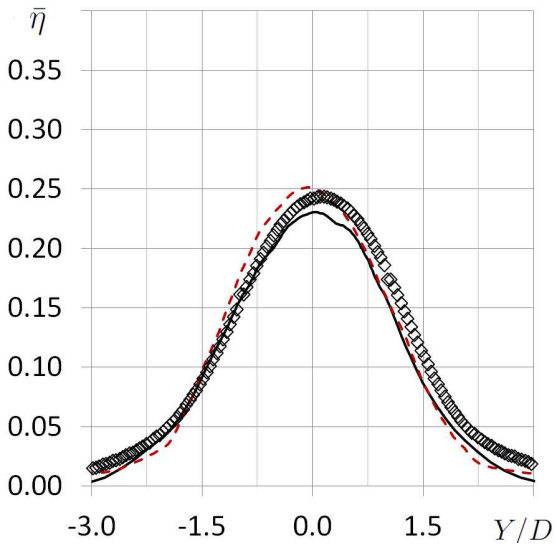

(d) Lateral distribution at $X/D = 8$

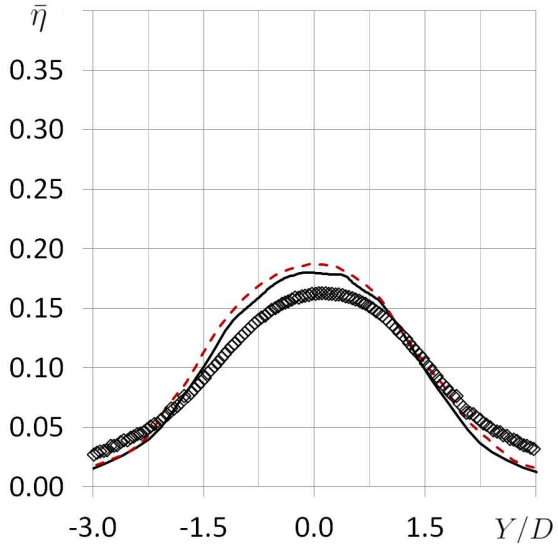

(e) Lateral distribution at $X/D = 14$

Figure 4.30: Profiles of time-averaged thermal efficiency comparing integrated and sequential SAS approach

4.5 Flow Analysis

After validation of the simulations, focus is now turned towards the physical analysis of the flow, which constitutes the second main objective of this work. It shall be highlighted at this point that reasonable conclusions can be drawn only from simulations with a sufficient depth of validation, which is the case here. Results obtained from the SAS calculation utilizing the baseline time step Δt on the hexahedral mesh are presented, which are consistent with the results of the DDES and ELES approach except if otherwise stated. As the URANS approach did not yield satisfying results, it will not be included into the general discussion except for the final aspect concerning the wake meandering.

4.5.1 Stationary Flow Topology

Starting point are the time-averaged solutions, which allow an investigation of the stationary flow topology. Being the most dominant feature, the counter-rotating vortex pair is discussed first. As shown in figure 4.31(a), the vortex pair develops as the jet flow wraps around the lateral edges of the ejector. Recalling the controversial discussion about the origin of the counter-rotating vortex pair, one explanation is based on the vorticity of the jet's boundary layer. However, the current case does not include any jet boundary layer and the origin is solely related to the sharp edges of the ejector leading to a flow separation as the jet is deflected by the cross flow. In addition to the vortex pair, an isosurface of the Q-criterion for the steady flow field is included in this visualization showing a single horseshoe vortex lying in front of the jet. The side arms are oriented at angle of about 30° relative to the cross flow and extend to the level of the downstream ejector edge.

The influence on thermal mixing of these two flow phenomena is quite distinctive. As the isosurface in figure 4.31(a) is also colored by time-averaged thermal efficiency $\bar{\eta}$, showing a uniform value close to zero, the horseshoe vortex contains only cross flow fluid and has thus no direct influence on thermal mixing. In contrast to this, the counter-rotating vortex pair has a strong impact on thermal mixing. The contours of thermal efficiency in figure 4.31(a) display the characteristic kidney shape of the jet cross section. The tangentially projected velocity vectors show that hot jet fluid is transported away from the core on the upper side whereas cold cross flow fluid is entrained towards the jet's center on the lower side. Additional contours of thermal efficiency are plotted in figure 4.31(b) to illustrate the thermal distribution inside the wake with a maximal thermal penetration of $5/3D$ at $X/D = 5$. While the influence of the counter-rotating vortex pair is clearly discernible on the second and third cut, its impact vanishes for locations further downstream. It finally remains worth mentioning that in the near and mid field of the jet the maximal temperature is obtained in the upper part of the jet while in the far field the hot core approaches the wall.

Pseudo streamlines of the stationary flow are illustrated in a top view on the left-hand side of figure 4.32. Due to the low momentum ratio, the jet constitutes only a small obstacle to the main flow, which leads to a strong recirculation area behind the orifice. This zone consists of two symmetric vortices with a maximal velocity up to $-1/2\,U_\infty$. On the right-hand side of this figure, velocity vectors are plotted on the symmetry plane and a contour of the recirculation area (grey) is included. In order to quantify this zone, a characteristic height $H/D = 0.63$, length $L/D = 1.26$ and width $W/D = 1.60$ are defined. As hot air accumulates in this zone, the thermal impact on the wall is rather strong. Depending on the simulation approach, the recirculation domain differs in strength and size and with this the thermal wall efficiency.

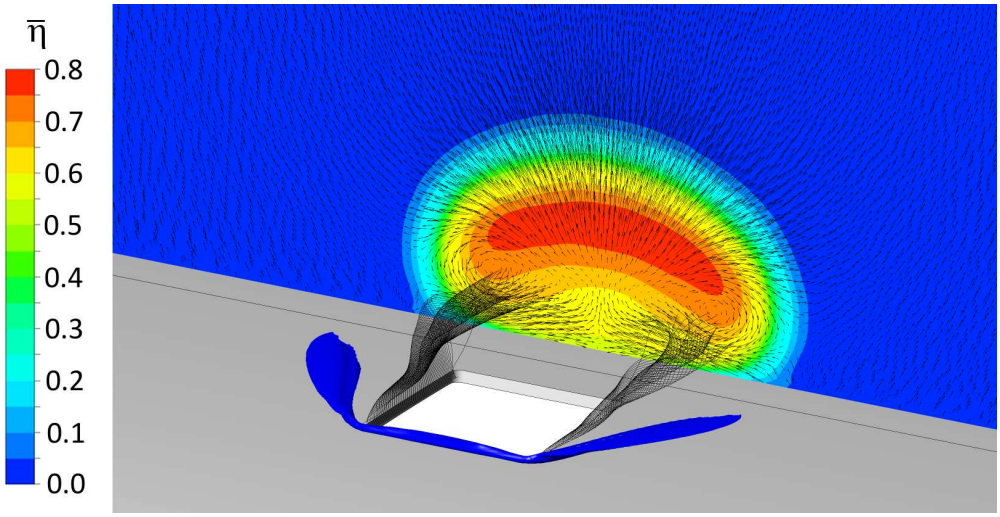

(a) Counter-rotating vortex pair originating at lateral ejector edges and horseshoe vortex forming in front of orifice

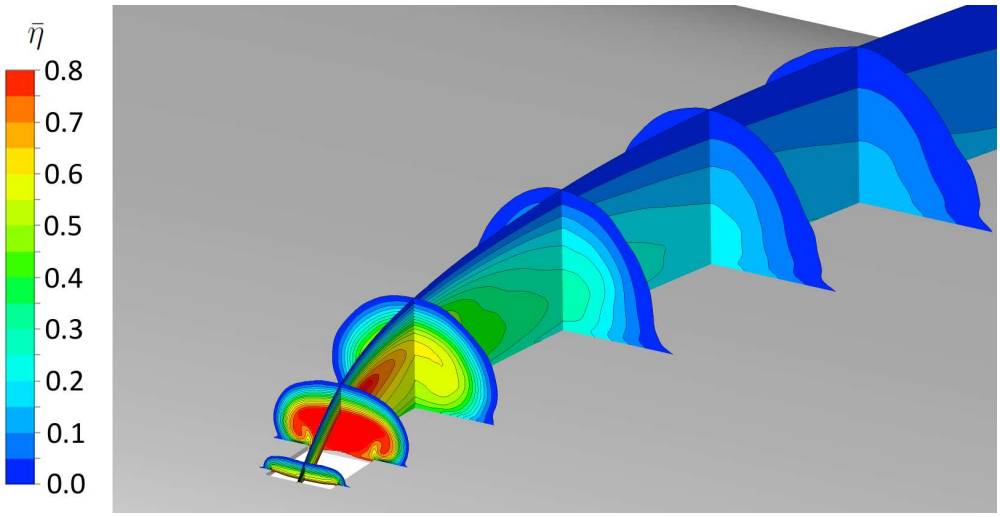

(b) Thermal wake showing mixing induced by counter-rotating vortex pair

Figure 4.31: Stationary flow topology and influence on thermal mixing

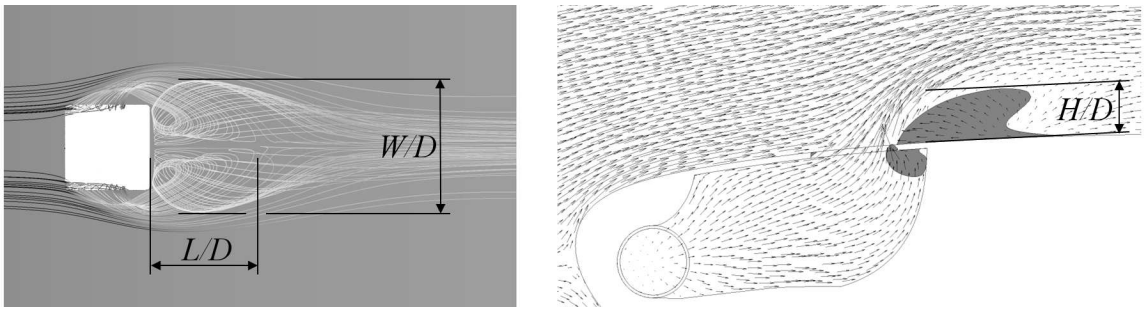

Figure 4.32: Top view (left) of pseudo streamlines and lateral view (right) of velocity vectors with contour of recirculation zone

Finally, the lateral thermal distribution is regarded. Recalling the surface temperature plots of $\bar{\eta}$, the observation of a spreading rate suggests a possible self similarity of the lateral temperature profiles. Indeed, if thermal efficiency $\bar{\eta}$ and Y-coordinate are scaled with the square root of the dimensionless distance to the ejector X/D such as

$$\hat{\bar{\eta}} = \bar{\eta} \left(\frac{X}{D} \right)^{-1/2} \quad \text{and} \quad \hat{y} = \frac{Y}{D} \left(\frac{X}{D} \right)^{1/2}, \tag{4.3}$$

all profiles between $X/D = 4$ and 12 collapse reasonably to a single curve, which is shown in figure 4.33.

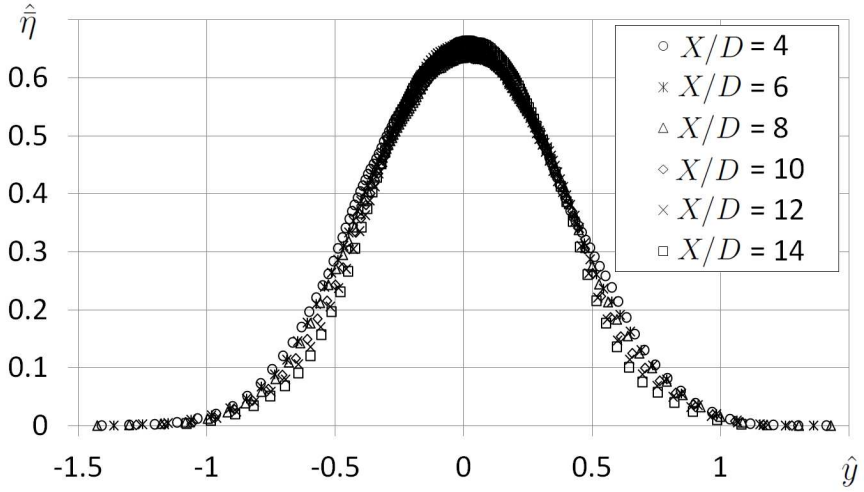

Figure 4.33: Self similarity of lateral temperature distributions when scaled with $\sqrt{X/D}$

4.5.2 Wake Vortices

After investigation of steady flow features, attention is now turned towards unsteady phenomena. A closer inspection of the instantaneous isosurface of the Q-criterion re-

veals periodic coherent structures in the jet wake, which are also referred to as hairpin vortices and are shown in figure 4.34. Their existence is thus in agreement with results from literature as already presented in section 2.2.4 for low effective velocity ratios. ANDREOPOULOS's hypothesis for their origin is however arguable as it relies on vortex rings emanating from the supporting pipe of jet fluid. Since neither vortex rings nor a supporting pipe exists for this configuration, another hypothesis is presented, which explains the development of archlike structures as a result of the recirculation zone establishing behind the orifice. As jet and main stream fluid pass around this obstacle, archlike vortices form, which are advected downstream but experience quick deformation due to strong dynamics inside the wake. In the present simulations these structures decay after a distance equal to $5-6D$ downstream of the ejector. Even if the increasingly coarsening numerical mesh dissipates these structures, a similar distance was recorded by ANDREOPOULOS.

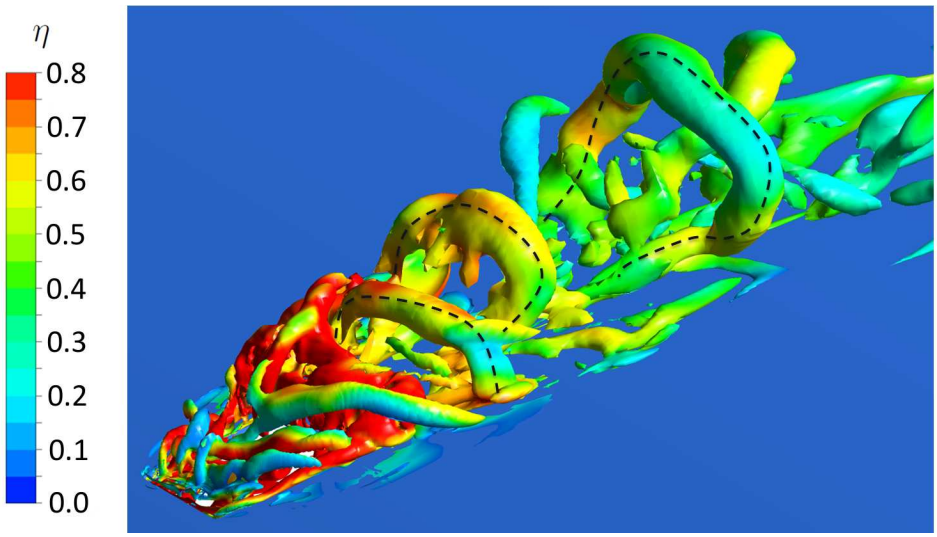

Figure 4.34: Instantaneous isosurface of Q-criterion show hairpin vortices in jet wake

In order to analyze temporal behavior, a spectral analysis is carried out for the points $P_{JICF,6}$ and $P_{JICF,7}$ indicated in figure 4.35 (cf. table B.1 in appendix B) and corresponding dominant Strouhal numbers are given in table 4.4 for different approaches. While SAS and DDES clearly show a spectral peak for St_D between 0.37 and 0.4, the results obtained from ELES show a stronger variation. Even if no experimental data for this configuration is available, a Strouhal number $St_D = 0.41$ has been reported by ANDREOPOULOS [7]. Finally, the influence on thermal mixing is important as well. As visible in the instantaneous thermal efficiency plot in figure 4.35, the vortex core contains high temperature fluid which is advected with the cross flow. These structures entrain cold cross flow fluid deeply into the wake leading to a strong impact on thermal mixing.

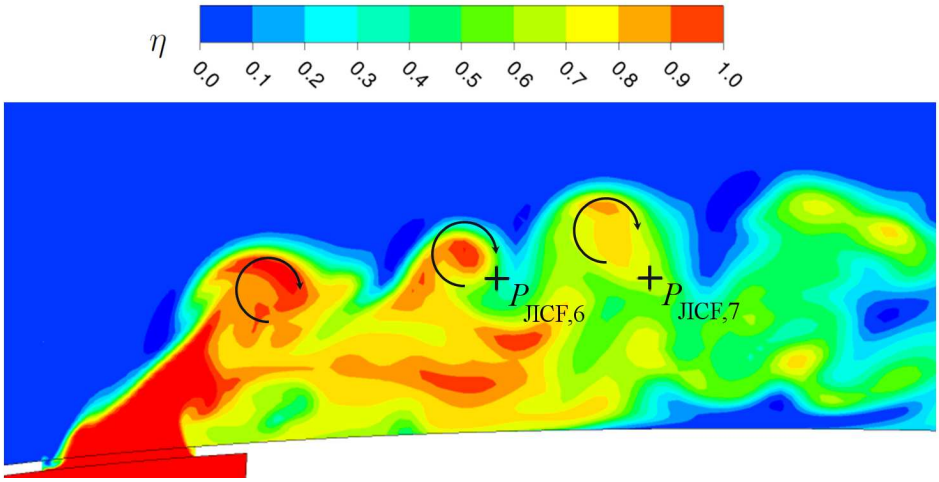

Figure 4.35: Instantaneous temperature distribution on symmetry plane with location of monitor points $P_{JICF,6}$ and $P_{JICF,7}$

Table 4.4: Strouhal numbers observed for hairpin vortices

Monitor	Quantity	SAS	DDES	ELES
$P_{JICF,6}$	X-velocity	0.38	0.37	0.28, 0.42
$P_{JICF,6}$	Z-velocity	0.40	0.37	0.50
$P_{JICF,7}$	X-velocity	0.40	0.38	0.28
$P_{JICF,7}$	Z-velocity	0.40	0.38	0.50

4.5.3 Shear Layer Vortices

Due to the ejector shape and the small momentum ratio, the two lateral shear layers do not develop freely since they are incorporated immediately by the counter-rotating vortex pair. Only the upstream shear layer is regarded in this section because the downstream shear layer between jet and recirculation zone is related to the dynamics of the wake vortices described in the previous section. This already points out that no evidence for closed vortex rings exists, which highlights the difference to a free jet.

The dynamics of the upstream shear layer are intrinsically connected to the turbulence modeling approach. The oncoming cross flow boundary is either treated entirely by a RANS approach, as in the case for SAS and DDES, or by the wall modeled LES approach for the ELES. In any case, parts of the turbulent boundary layer are modeled leading to an increased value of eddy viscosity. As this has a damping effect on the transition from modeled to resolved turbulent fluctuations, the dynamics of the upstream shear layer are susceptible to this.

Indeed, the contour plots of the instantaneous thermal efficiency on the symmetry plane at the upstream ejector, illustrated on the left hand side of figure 4.36, show a different behavior for every turbulence modeling strategy. The plot obtained from SAS results show a strong instability of the shear layer, leading to an oscillation that is similar to the von Kármán vortex street. The characteristic frequency obtained from the temperature history of a monitor point $P_{JICF,8}$ (cf. figure 4.36(a) and table B.1 in appendix B) inside this area yields a large Strouhal number of $St_D = 1.30$. As the characteristic length is rather the thickness of the ejector plate d, the corresponding Strouhal number now yields $St_d = 0.09$. Contrary to this, the plot for the DDES simulation shows a much lesser pronounced vortex street with a characteristic Strouhal number of $St_D = 0.57$ or $St_d = 0.04$ respectively. Even though instability is visible directly behind the ejector edge, its amplitude is however damped. Finally, the plot obtained from ELES result shows almost no oscillations at all. Again, the instability is visible directly in the vicinity of the upstream ejector edge but this time it is damped entirely and no characteristic Strouhal number can be obtained from spectral analysis.

No experimental data is available to confirm any of these behaviors and the Strouhal numbers found in literature [61], ranging between 0.6 and 1.0, are obtained for cross flow Reynolds numbers only in the order of 2 000. To explore its origin, the eddy viscosity ratio μ_t/μ is plotted at the same location on the right hand side of figure 4.36. Starting with the SAS calculation, very low levels of eddy viscosity are discernible in the upstream shear layer explaining the rapid growth of oscillations. Additionally, almost no eddy viscosity is transported across the ejector even though spots of high values exist inside the scoop, which could damp the instability. The presumable discontinuity is in fact a rather strong gradient caused by the activation of the SAS source term Q_{SAS} in this area: The necessity to resolve the wing's boundary layer leads to extremely fine cells crossing the ejector due to the underlying topology of the hexahedral mesh. The turbulence model of the DDES approach shows another behavior. Spots of high eddy viscosity levels are visible inside the scoop, which traverse the ejector and consequently lead to higher levels inside the jet. In combination with the oncoming boundary layer, which also transports eddy viscosity into the jet, the instability of the upstream shear layer is damped. Again, an alleged discontinuity can be observed in the same mesh region. As the LES formulation is activated here, eddy viscosity is proportional to the cell size leading to a strong local reduction. Even if the instability is damped as well for the ELES approach, the reason is not the same. Stemming from the methodology, the high levels of eddy viscosity are reduced as the fluid enters the Embedded LES domain and turbulent fluctuations are resolved in return. Due to the high shear rate in the upstream shear layer, higher levels of eddy viscosity are predicted from the LES turbulence model. As this behavior is visible already from the lower corner of the upstream ejector edge, the instability is entirely damped.

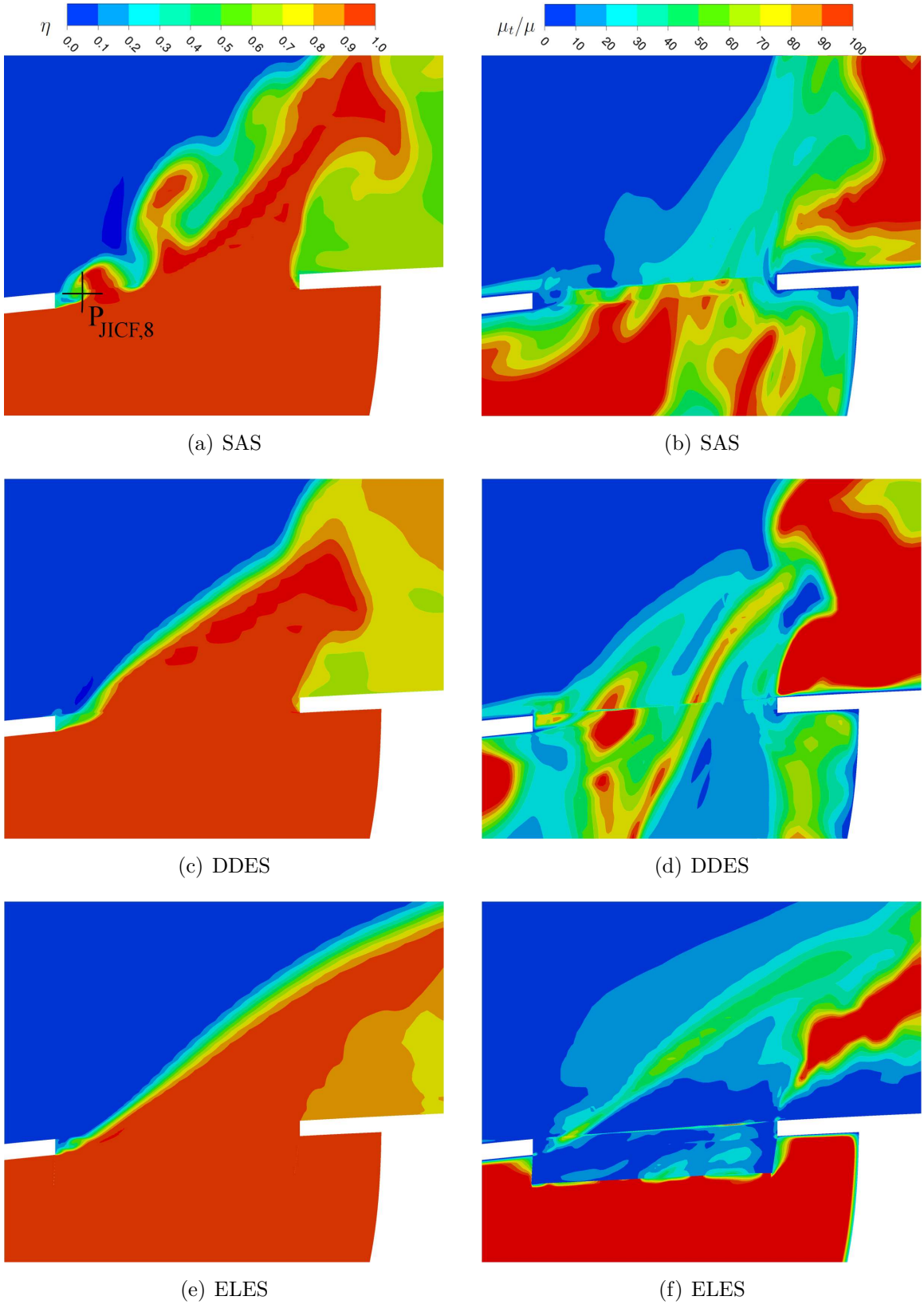

(a) SAS (b) SAS

(c) DDES (d) DDES

(e) ELES (f) ELES

Figure 4.36: Instantaneous eddy viscosity ratio μ_t/μ (right) impacting dynamics of upstream shear layer indicated by thermal efficiency η (left)

4.5.4 Wake Meandering

When comparing results obtained from the URANS simulation to the three remaining SRS approaches and to experimental data, the heavily underestimated thermal spreading in lateral direction is striking. A strong dynamic has thus to be connected to this phenomenon, which is correctly resolved by SAS, DDES and ELES. Recalling the spectral peaks observed for $St_D = 0.14$ throughout the jet wake, a first evidence of this dynamical behavior arises. However, the character of this flow phenomenon is not yet clear and needs to be investigated. Even if the analysis of time statistics and the visualization of coherent structures give a deeper understanding of the underlying flow dynamics, the amount of data to be analyzed can become very large and unclear for turbulent flows at high Reynolds numbers. For this reason, further statistical treatment of the transient solution data can help in extracting coherent structures and flow dynamics. A common technique is the Proper Orthogonal Decomposition (POD) as described by Berkooz, Holmes & Lumley [12].

Proper Orthogonal Decomposition

Starting point is the solution matrix $\mathbf{A}\,(N \times m)$, containing N transient realizations of the velocity field on m sampling points, i.e. computational cells. As thermal mixing is of interest in this case, a solution matrix containing the temperature field is regarded as well. Considering the discrete character of numerical data, the Singular Value Decomposition (SVD) [37] of the solution matrix is employed for POD analysis. The solution matrix $\mathbf{A}$ can then be decomposed into

$$\mathbf{A} = \mathbf{U}\mathbf{\Sigma}\mathbf{V}^T, \tag{4.4}$$

with the two unitary matrices $\mathbf{U}\,(N \times N)$ and $\mathbf{V}\,(m \times m)$. The particularity of this decomposition consists in matrix $\mathbf{\Sigma}\,(N \times m)$, which is a diagonal matrix of the form

$$\mathbf{\Sigma} = \left(\begin{array}{ccc|ccc} \sigma_1 & & & & \vdots & \\ & \ddots & & \cdots & 0 & \cdots \\ & & \sigma_r & & \vdots & \\ \hline & \vdots & & & \vdots & \\ \cdots & 0 & \cdots & \cdots & 0 & \cdots \\ & \vdots & & & \vdots & \end{array}\right). \tag{4.5}$$

Its entries σ_i are referred to as singular values of $\mathbf{A}$, which are all real valued and usually arranged such that

$$\sigma_1 \geq \cdots \geq \sigma_i \geq \cdots \geq \sigma_r > 0. \tag{4.6}$$

The index r is equal to the rank of $\mathbf{A}$ and can be assumed to have the same value as the smaller dimension of $\mathbf{A}$, which in the case discussed here is the number of transient flow

realizations N. The singular values and with this the matrices $\mathbf{U}$ and $\mathbf{V}$ are uniquely determinable for every matrix $\mathbf{A}$.

As a consequence of this decomposition, the following relation holds:

$$\sqrt{\sum_{i}^{N}\sum_{j}^{m} a_{ij}^2} = \sqrt{\sum_{i}^{N} \sigma_i^2}, \tag{4.7}$$

which states that the energy content of matrix $\mathbf{A}$ with its entries a_{ij} is uniquely describable by matrix $\mathbf{\Sigma}$ and its singular values. Due to the diagonal form of $\mathbf{\Sigma}$, equation (4.4) can be rewritten as an outer product

$$\mathbf{A} = \sum_{i}^{N} \sigma_i \vec{U}_i \otimes \vec{V}_i^T, \tag{4.8}$$

with $\vec{U}_i$ and $\vec{V}_i$ being the i^{th} column vectors of the corresponding matrices. As this leads to the separation of coordinates, i.e. $\mathbf{A}(i,j) = U(i)V(j)$, the column vector $\vec{U}_i$ contains the temporal evolution of the flow field, whereas the column vector $\vec{V}_i$ contains the spatial representation corresponding to the singular value σ_i. Since the values of σ_i decrease rapidly and due to relation (4.7), the spatial representation with its temporal evolution corresponding to large values of σ_i are considered to be high energy modes of the flow.

Before applying this procedure to the test case, computational requirements need to be considered. Starting from the SAS calculation on the hexahedral mesh with the baseline time step Δt, the entire solution matrix is dense and has a size of $7\,000 \times 12,9 \cdot 10^6$ entries, which indeed leads to an unfeasible decomposition, thus necessitating spatial and temporal truncation. As known from prior spectral analysis, the lowest frequency component appearing in this study yields a Strouhal number of around $St_D = 0.14$. Reducing the number of flow realizations to $N = 300$ for the baseline time step Δt, the period of the corresponding flow phenomenon is still covered 3.5 times. Subsequently, the SVD does not need to be carried out in the entire flow domain but only in the region of interest, which is illustrated in figure 4.37. As discernible from its discretization, this domain does not need clustering in wall-normal direction as dynamics inside the boundary layer are of minor importance here. This finally allows the reduction to $m = 440\,000$ sampling points, which in combination with the likewise reduced number of flow realization yields a manageable problem size.

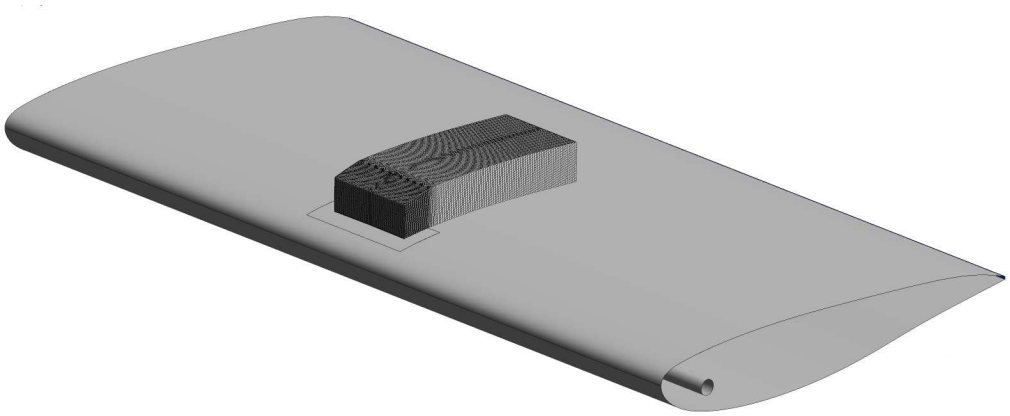

Figure 4.37: Reduced domain for POD analysis

The numerical solutions of 300 time steps are thus interpolated in order to reconstruct the values in this domain and the SVD is carried out for all three velocity components as well as for temperature. The corresponding normalized singular values $\sigma_i^* = \sigma_i / \sum \sigma_i$ are presented in figure 4.38, which show a first, very large singular value followed by an almost constant exponential decay of the values for $i > 1$. As the instantaneous and not the fluctuating quantities are considered, the first mode contains the temporal average of N flow realizations. This is shown in figure 4.39 for velocity vectors in a plane above the wing surface. The recirculation zone behind the ejector is visible and the deviation of the cross flow around the jet. Even if the number of flow realizations is rather small for a converged temporal average, the temporal evolution of the first mode is almost constant with a maximal deviation from the mean of 0.1%.

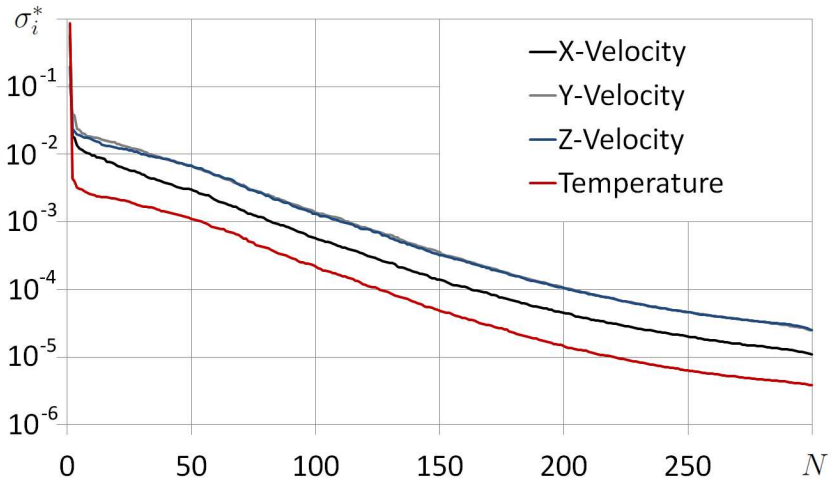

Figure 4.38: Singular values σ_i^* for the three velocity components and temperature

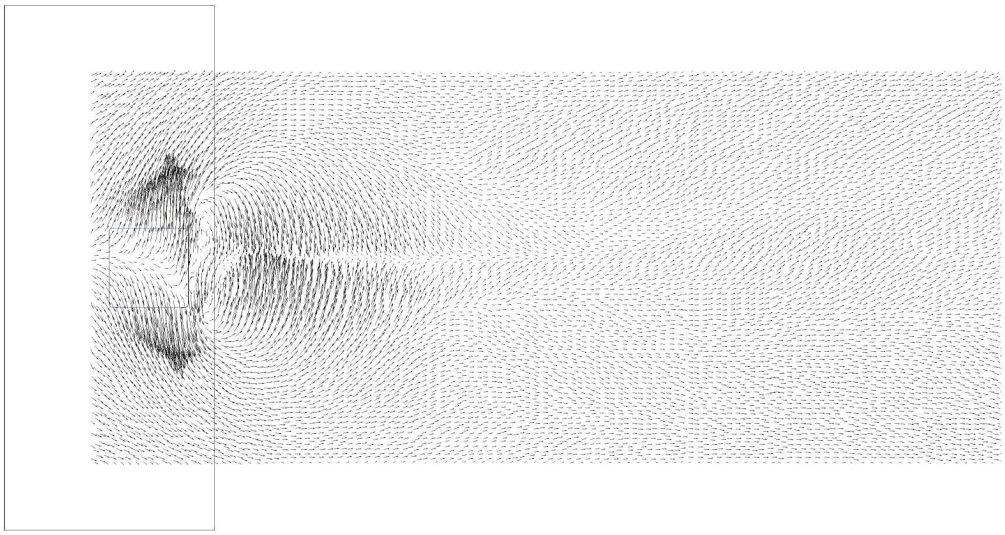

Figure 4.39: First mode of velocity components illustrated as vectors on a plane at $Z/D = 0.17$ above the wing surface

More interestingly is the discussion of higher order modes, as they can contain the representation of flow dynamics. For this reason, the temporal evolution of the second mode is shown in figure 4.40(a) and a clearly periodical behavior becomes obvious. If instead of the number of flow realizations N, the flow time $N\Delta t$ is regarded, a frequency can be attributed to this sinusoidal oscillation. The corresponding Strouhal number yields $St_D = 0.14$, which is exactly the same as the one obtained from spectral analysis of numerical results in section 4.4 and of experimental data.

In order to give a spatial description of this phenomenon, the second mode for the Y-velocity component is plotted on a plane above the wing surface in the bottom part of figure 4.40(b). Directly behind the jet local minima and maxima appear in a regular manner separated by a distance of about $2D$. In combination with the temporal coefficient this flow field representation changes periodically its algebraic sign at a frequency corresponding to the double of the characteristic Strouhal number. As indicated by the contour plot on the symmetry, which are shown in the top part of the figure, these oscillations are not oriented in wall-normal direction but are rather tilted by an angle of 45°. Transferring these results from the SVD mode to the physical flow leads to the conclusion of a meandering of the jet wake with a frequency of $St_D = 0.14$ and spatial period of $2D$.

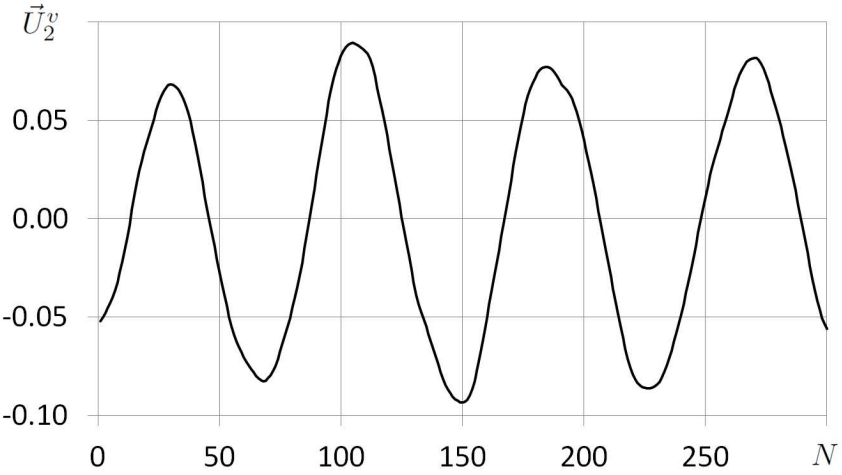

(a) Temporal evolution $\vec{U}_2^v$ of second mode

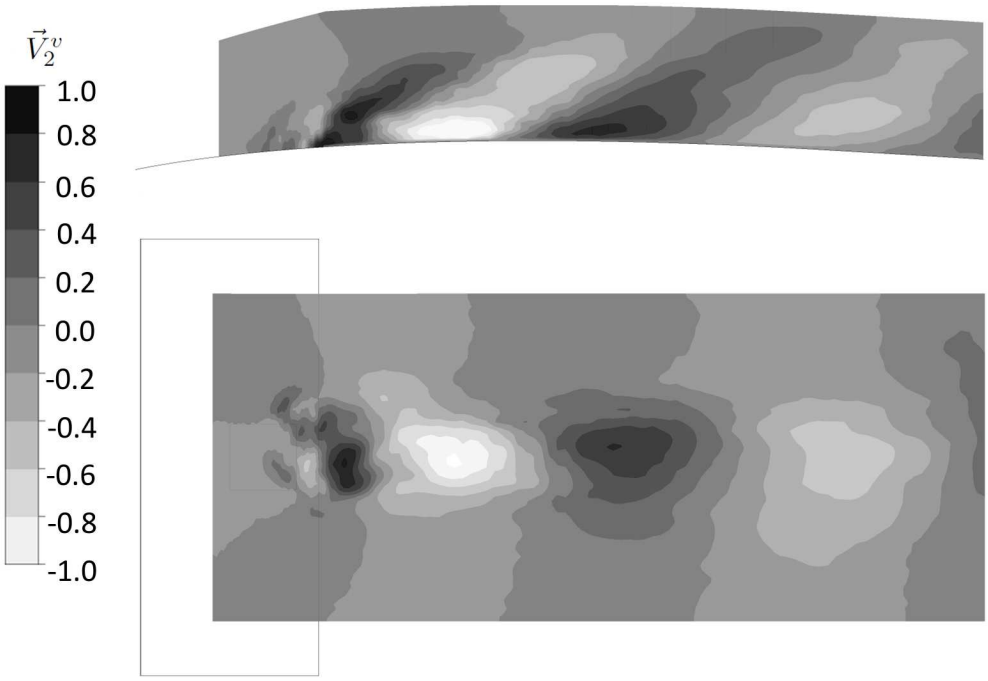

(b) Spatial representation $\vec{V}_2^v$ of second mode

Figure 4.40: Results of POD for Y-velocity component

A low rank approximation is carried out to support these findings. Recalling equation (4.8), solution matrix $\mathbf{A}$ can be rewritten as a weighted sum of submatrices $\tilde{\mathbf{A}}_i$ with the weighting factors σ_i:

$$\mathbf{A} = \sum_i^N \tilde{\mathbf{A}}_i = \sum_i^N \sigma_i \vec{U}_i \otimes \vec{V}_i^T. \tag{4.9}$$

Matrix $\mathbf{A}$ can thus be approximated by its submatrices $\tilde{\mathbf{A}}_i$ to any given degree of

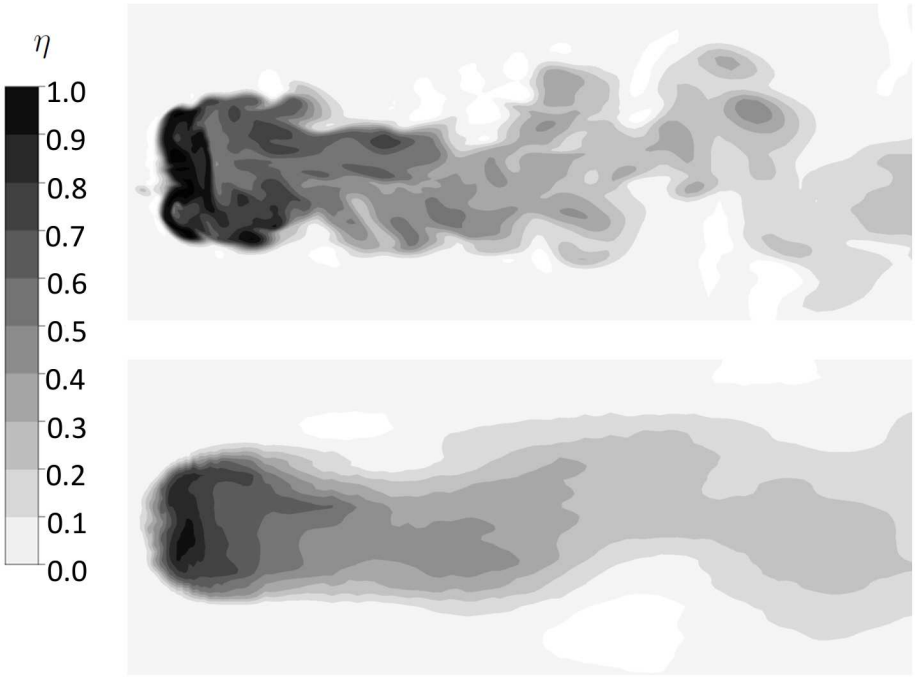

Figure 4.41: Low rank approximation of instantaneous temperature field showing wake meandering on a plane at $Z/D = 0.17$

completeness. If only the s first singular values are used, i.e. $\sigma_i = 0$ for all $i > s$, an approximation of rank s is obtained.

For the case considered here, matrix $\mathbf{A}$ of temperature shall be approximated only by the first two modes in order to illustrative the wake meandering. Figure 4.41 presents the instantaneous temperature distribution in the jet wake on a plane above the wing surface, which is clearly highly turbulent and hard to interpret in terms of large-scale dynamics of the jet. The low rank approximation of this field gives a clear view of the dynamics of the jet and show the wake meandering identified above. The importance for thermal mixing is not only qualitatively visible from the contour plot but is also revealed by the fact that a POD maximizes energy in its modes in descending order and that this dynamic is represented by the second mode, with the higher energy mode only being the mean flow.

The formation of the wake meandering can be explained recalling the stationary flow topology as depicted in figure 4.32. A top view of the ejector with jet and cross flow streamlines shows the existence of a recirculation zone behind the orifice as also pointed out by the velocity profiles in figure 4.23(a). In contrast to a rigid body in cross flow, where a well fixed boundary between obstacle and cross flow exists, the jet is an obstacle with a variable boundary with respect to the cross flow. In a transient flow, this leads to a recirculation zone with strong dynamics inducing the wake meandering as cross flow fluid is entrained alternately from the left and from the right after the

nodal point. This mechanism resembles indeed the development of the von Kármán Vortex Street but generally a Strouhal number of $St = 0.21$ is reported in literature for a (square) cylinder in cross flow. The question arises, if the ejector edge length D is the appropriate characteristic length scale for constructing the Strouhal number for a JICF. A physically more meaningful length scale would be the width W of the stationary recirculation zone, leading to a shift of the power spectra towards higher Strouhal numbers. The spectral peak now occurs at $St_W = 0.22$, which is remarkably close to the classical Strouhal number of the von Kármán vortex shedding.

Finally, the origin of the underestimation of lateral thermal spreading of the URANS calculation shall be discussed. The first reason is the appearance of only large-scale structures, which appear in the jet wake and are shown in figure 4.16(a). The more important aspect however is a damping of the wake meandering. Indeed, spectral analysis for the URANS approach yields also a dominant frequency, which is different though to the ones obtained from other turbulence modeling strategies and experimental data. This can be explained by a strong overestimation of turbulent viscosity, which hinders the lateral movement of the jet wake as the standard statistical turbulence model does not account for turbulent fluctuations already resolved. In a study by Wienken, Stiller & Keller [103] a similar behavior was observed. The authors investigated a flow around a square cylinder with a URANS and an LES approach, whereas the prior one did not yield the correct Strouhal number. Only large, two-dimensional turbulent structures appeared, which confirms the conclusions drawn here.

4.6 Extended Investigations

Following validation and analysis of flow dynamics, additional aspects are regarded in this part of the chapter. Firstly, the assumption of an adiabatic wall treatment is revisited and simulations with more appropriate thermal boundary conditions are conducted. Secondly, the multiple ejector grid is considered. Even if only limited data is available for validation, this successive procedure is necessary in order to proceed to real aircraft applications in chapter 5.

4.6.1 Improved Thermal Boundary Conditions

As already mentioned in the previous section, internal heat conduction plays an important role for this configuration. Especially the ejector grid, which has a thickness of only 2mm, is exposed to hot fluid on the internal side and to cold fluid on the external side. The plate is thus heated, which subsequently leads to the development of a thermal boundary layer of the oncoming cross flow with impact on thermal mixing and on downstream surface temperature distribution. This is confirmed by experimental data (cf. for instance figure 4.13(b)), where the isoline for $\bar{\eta} = 0.05$ forms two lateral pockets close to the ejector grid. In order to take heat conduction into account, a first and

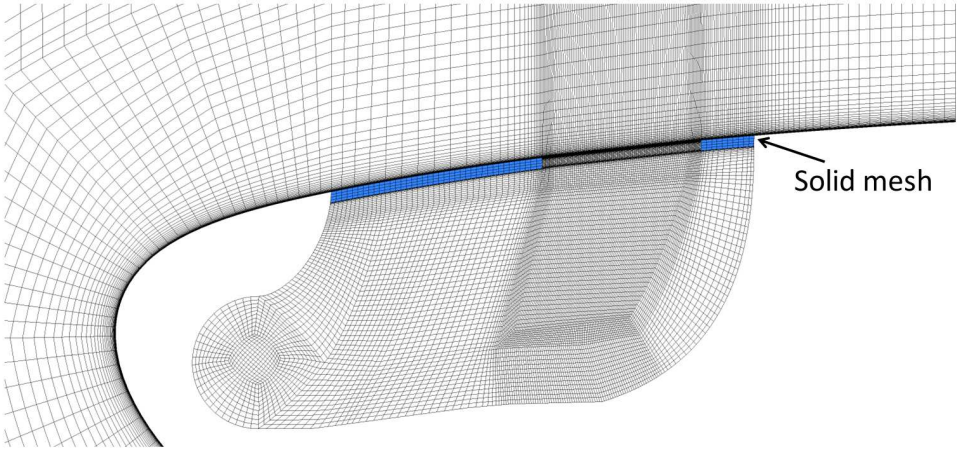

Figure 4.42: Solid mesh in ejector plate for a coupled fluid structure simulation

rather pragmatic approach as well as a second and more elaborate one are presented in the following. Nonetheless, it is important to notice that only the negligence of internal heat conduction allowed the proper identification of thermal mixing phenomena solely associated to a jet in cross flow in the previous sections.

The most straightforward approach consists in specifying a constant temperature T_1 on those surfaces of the ejector grid, which are in contact with fluid. These are the internal and external surfaces of the plate as well as the edges of the ejector. The value of T_1 is simply estimated to be the average of jet and cross flow temperature, i.e. $T_1 = 1/2\,(T_\infty + T_j) = 322\text{K}$. The more advanced approach is also based on an isothermal boundary condition for those surfaces in contact with fluid but rather a temperature distribution $T_2 = f(x, y, z)$ is prescribed than a single constant value. In order to take into account local flow characteristics, especially inside the plenum, and their impact on temperature distribution, a steady state CFD calculation is carried out, which contains a solid model of the ejector plate and allows thus the simulation of heat conduction. The set-up is illustrated in figure 4.42, showing the coarse and equidistant solid mesh, which is non-conformal with the fluid mesh. The plate consists of stainless steel and a thermal conductivity λ of 20W/(mK) has been assumed. As a steady RANS simulation is calculated, only the symmetrical part of the fluid domain needs to be considered, which facilitates convergence. The obtained temperature field is then symmetrized and used as a boundary condition for a transient calculation.

The convergence behavior is very similar to the adiabatic case and plots for inner and outer convergence are not shown repeatedly. Additionally, as the impact of the modification of thermal boundary conditions on the flow field is small, its presentation is redundant and only the time-averaged temperature distribution on the wing surface is of interest here. The results of the two approaches are shown in figure 4.43 together with experimental data. Both approaches clearly ameliorate the lateral thermal spreading

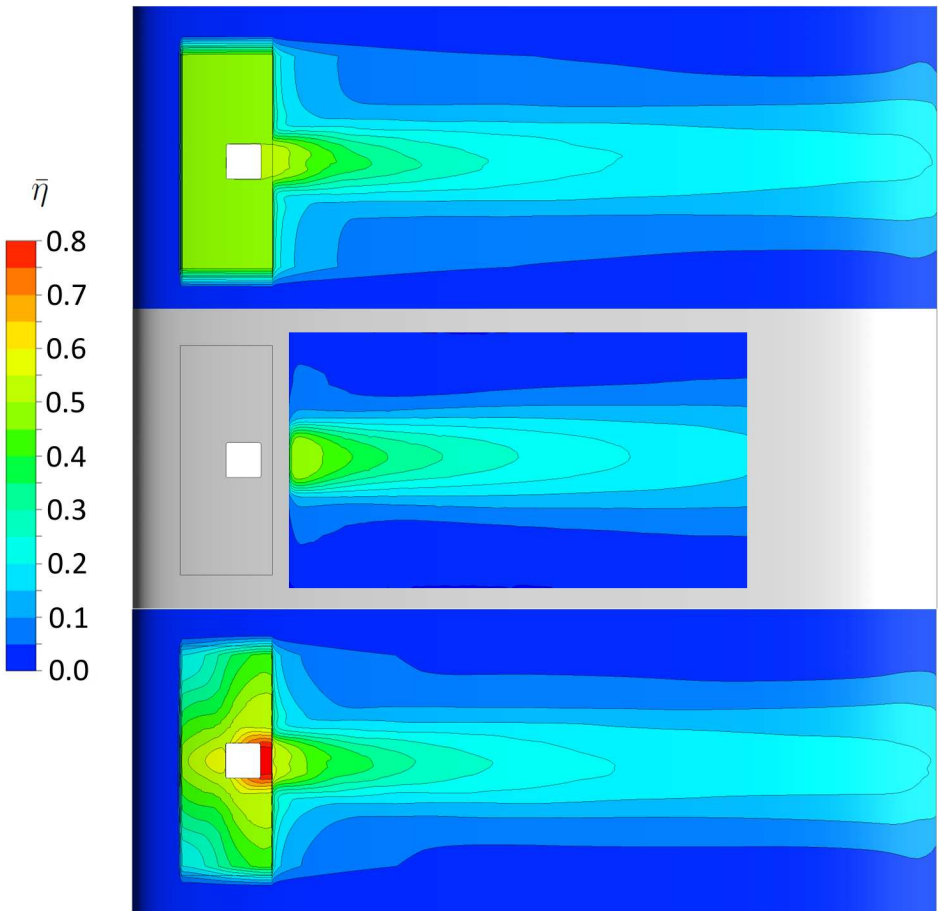

Figure 4.43: SAS calculation with improved thermal boundary conditions: T_1=const. (top) and $T_2 = f(x, y, z)$ (bottom) compared to experiments (middle)

in the near field of the jet, pointing out the importance of heat conduction in the solid and thus the aspect of multiphysics. Differences further away from the symmetry line still persist due to the complex thermal behavior of the mock-up. Even though the second approach predicts a strongly varying temperature field for the ejector plate, the global effect on the surface temperature distribution compared to the first, more pragmatic approach is rather small.

4.6.2 Multiple Ejectors

Despite the fact that many applications consist of multiple jets in cross flow, their simultaneous numerical simulation received up to now little attention due to the complexity of the flow and the associated computational costs. One can argue that for large numbers of aligned jets a single jet with periodic lateral boundary conditions presents a justified simplification. However, for the small number of jets considered here and in order to correctly account for the interaction between neighboring jets in the mid and

Table 4.5: Similarity parameters for the multiple jets in cross flow configuration

C_R	Re_{cf}	Ri_{cf}	$\Delta T/T_{ref,1}$
0.70	$3.69 \; - \; 5.77 \cdot 10^4$	$\ll 1$	0.19

far field the entire flow problem has to be considered.

As satisfying results are obtained for the SAS turbulence model on the single ejector configuration, this approach will be pursued further for the generic configuration equipped with the grid containing multiple ejectors, cf. right hand side of figure 4.2, which is similar to the exhaust of the nacelle anti-icing system. The definition of similarity parameters however is complicated by the fact that the jets have a common plenum and information about the mass flow through the individual orifice is not available. Therefore, the momentum ratio is rather calculated by the known total mass flow. Additionally, due to the different shape the characteristic length has to be estimated for the calculation of the cross flow Reynolds number. Following the square shaped ejector, the length is simply calculated as the square root of the corresponding ejector surface. A set-up is chosen, which resembles the single ejector case in terms of momentum ratio and the corresponding similarity parameters are given in table 4.5. The range of the cross flow Reynolds number corresponds to the values for the smallest and largest ejector. Finally, cross flow Mach number and temperature difference are comparable to the prior configuration, i.e. $Ma_\infty = 0.137$ and $\Delta T = 57$K.

The numerical set-up remains unchanged and the boundary conditions have been adjusted accordingly. The hexahedral mesh already presented in section 4.2 is employed and the baseline numerical time step size $\Delta t = 5 \cdot 10^{-5}$s as well as $\Delta t/2$ are chosen for time advancement. Transient and unsteady flow initialization have been carried out the way described above and inner as well as outer convergence behavior is similar to the ones presented in figures 4.11 and 4.12. A sufficient inner convergence is achieved after 10, respectively 5 iterations and a total number of 7 000 time steps are needed to obtain converged statistical data. In a first step the stationary flow topology is investigated. Streamlines of time-averaged velocity, which are colored by thermal efficiency, are released from the pipe inlets on each side and are presented in figure 4.44. Identically to the single ejector case, the pipe flows impinge on each other and form a recirculation zone inside the plenum. As the jet fluid leaves the plenum, the cross flow momentum forces the jets to bend quickly and to attach to the wall resulting in a strong thermal impact. In contrast to the single ejector case, no recirculation zones behind the orifices are visible. The time-averaged flow field now allows the identification of the individual momentum ratios. The mass flow for every jet as well as its share on the total ejector surface are given in table 4.6. The jets have been numbered from left to right looking in positive X-direction, with ejector number 3 being thus the center jet. It can be seen that the mass flow through the center orifice is larger than

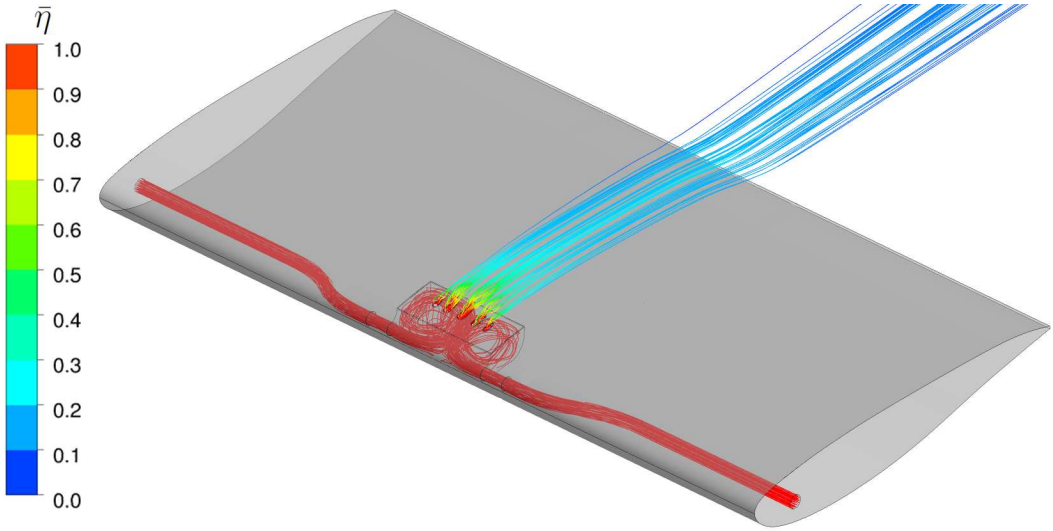

Figure 4.44: Streamlines of time-averaged velocity for multiple ejector configuration

Table 4.6: Mass flow and area distribution for the multiple jets in cross flow configuration

	Ejector 1	Ejector 2	Ejector 3	Ejector 4	Ejector 5	Total
Area	11.9	23.6	29.0	23.6	11.9	100
Mass flow, Δt	10.9	23.2	31.9	22.8	11.2	100
Mass flow, $\Delta t/2$	11.3	22.8	31.6	23.0	11.3	100

its surface quotient, whereas the opposite holds for the exterior ejectors. In contrast to the prior configuration, the recirculation zone inside the plenum has thus an influence on the mass flow distribution. Both calculations show this tendency but a more symmetrical solution is obtained from the simulation with the smaller numerical time step. As mass flow and velocity ratio are proportional, the ratios for the exterior jets are approximately $C_R = 0.08$ and $C_R = 0.16$ respectively; whereas the ratio for the center jet yields $C_R = 0.22$. These values are thus significantly smaller, highlighting an even stronger thermal impact on the wall.

As the distribution of thermal efficiency is of prime interest, numerical data from both simulations are presented and compared to experimental data in figure 4.45. Interestingly, apart from the main lobe in the center, only two side lobes appear in the mid and far field since the two outer jets merge quickly. In the near field, the thermal trace of every ejector is visible with the strongest impact for the outer ejectors, which is in agreement with their very small velocity ratios. Furthermore, the presence of the center jet forces the exterior jets outwards. This effect is also increased by the flow inside the plenum, which has a strong outward lateral component due to its circulation. In general, a satisfying agreement between numerical and experimental data is visible.

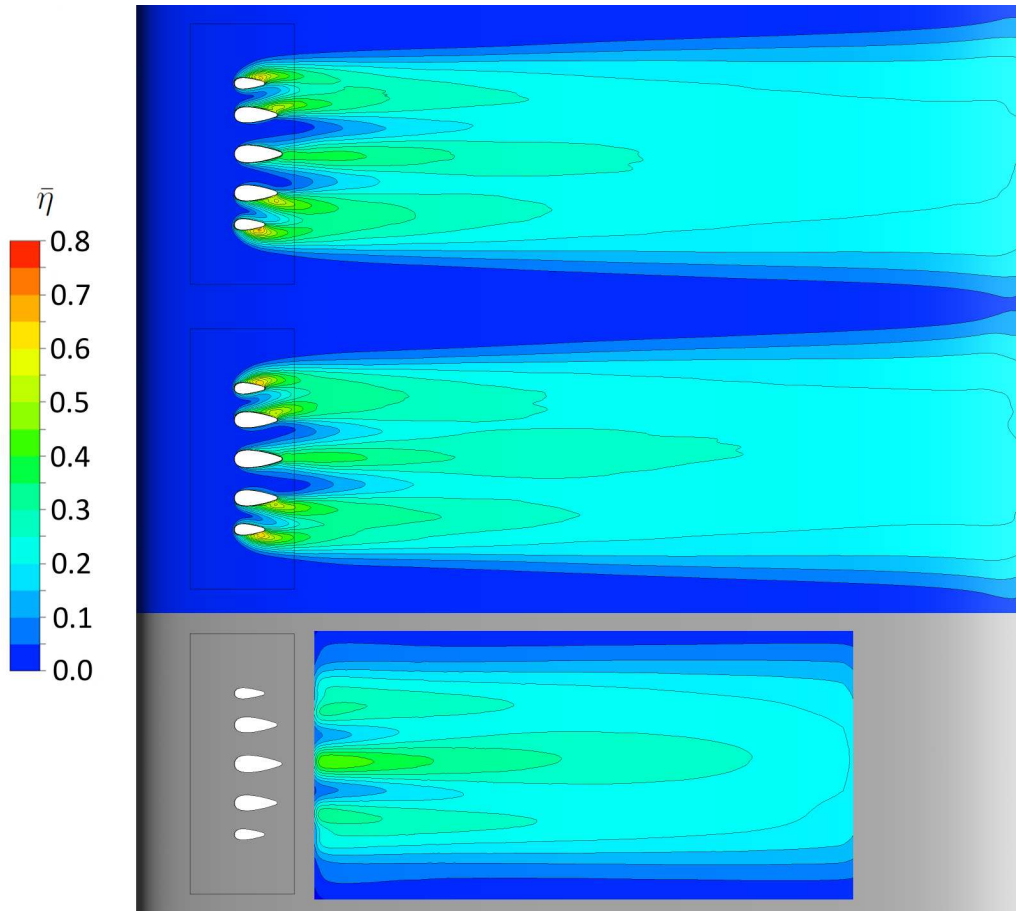

Figure 4.45: Time-averaged thermal efficiency $\bar{\eta}$ obtained from SAS calculations with two different time steps: Δt (top) and $0.5\Delta t$ (middle)

The merging of the outer jets and the prediction of only three lobes is confirmed as well as the overall lateral spreading. The simulation with the smaller time step is closer to experimental data, which is especially observable at the main lobe and its downstream extents. This is due to the fact that the smaller time step allows a better temporal resolution and thus a more accurate mixing prediction as discussed in section 4.4.3. Only the side lobes are slightly overestimated. Modifying the thermal boundary condition as proposed in the previous section would very likely enhance the overall solution. In order to facilitate analysis of thermal mixing phenomena, this was however left undone. Even if only the surface temperature distribution is available for comparison, a sufficient validation level is achieved nonetheless: Firstly, this configuration is based on the single ejector test case. Secondly, temperature is a simple passive scalar, which is transported by the flow field. If thermal efficiency therefore agrees sufficiently, enough confidence is provided that the flow field has been simulated properly as well.

In a second step, the unsteady flow field is regarded in order to investigate the three flow dynamics found to be important for the single ejector configuration, i.e. hairpin vortices, wake meandering and shear layer vortices. As superior results were obtained for the smaller time step, only this case will be considered for the following discussion. The instantaneous isosurfaces of the Q-criterion are plotted in figure 4.46(a). In order to determine the influence of the resolved structures on mixing they are colored by thermal efficiency. The resolution of turbulent fluctuations is clearly visible and each jet develops independently in the very near field. Caused by the low momentum ratio and the ejector shape, archlike vortices develop already at 2/3 of the ejector length in a very frequent manner. Similarly to the single ejector configuration these structure entrain cold cross flow fluid into the jet core and are thus of importance for thermal mixing as shown in section 4.5.2. In the mid and far field a merging of the jet wakes occurs, which leads to a broad field of coherent structures with strong mixing. Additionally, the counter-rotating vortex pair forms at the lateral ejector edges and the horseshoe vortex is visible in front of each orifice. The horseshoe vortices are once again only composed of cold cross flow. An instantaneous temperature distribution is presented in figure 4.46(b). Thermal wakes are visible for all jets and caused by the small velocity ratio, hot jet air impacts the wall in the vicinity of the orifice. Interestingly, these areas are also found on the side or even in front of the ejectors, indicating the strong forces of the cross flow on the exterior jets. The individual thermal traces merge and after 3-4D a "random" temperature field establishes, which is advected downstream.

In order to quantify the dynamical behavior, a closer look is taken at two monitor points located on the local symmetry plane of each ejector. As the symmetrically opposed jets are supposed to exhibit similar characteristics, a total number of only six points needs to be considered here (cf. table B.1). The locations of the first three points $\mathrm{P_{MJICF,1}}$, $\mathrm{P_{MJICF,2}}$ and $\mathrm{P_{MJICF,3}}$ are chosen to be in the upstream shear layer close to the respective ejector edge, which corresponds to $\mathrm{P_{JICF,8}}$ of the single ejector in figure 4.36(a). The locations of the second three points $\mathrm{P_{MJICF,4}}$, $\mathrm{P_{MJICF,5}}$ and $\mathrm{P_{MJICF,6}}$ lie in the jet wake at about 1D above the wall respectively, which corresponds to $\mathrm{P_{JICF,6}}$ of the single ejector in figure 4.35. Estimations of the power spectral density of temperature and X-velocity component for the first three points are presented on the left hand side of figure 4.47. Clearly a high frequency component is dominant in all cases, ranging between $St_D = 0.47$ and $St_D = 0.90$. Even though the values are smaller than for the single ejector case, this behavior corresponds well to the von Kármán vortex street described in section 4.5.3. A correlation of X-velocity component and temperature is visible as well as a shift towards higher Strouhal frequencies as the ejector size increases. The Strouhal number being constructed with the characteristic length of the corresponding ejector, this tendency remains also discernible for the dimensional frequency. On the right hand side of figure 4.47, the estimations of power spectral density for temperature and Z-velocity component are given. A broader spectral peak is visible for all three ejectors with the most dominant frequency between $St_D = 0.4$

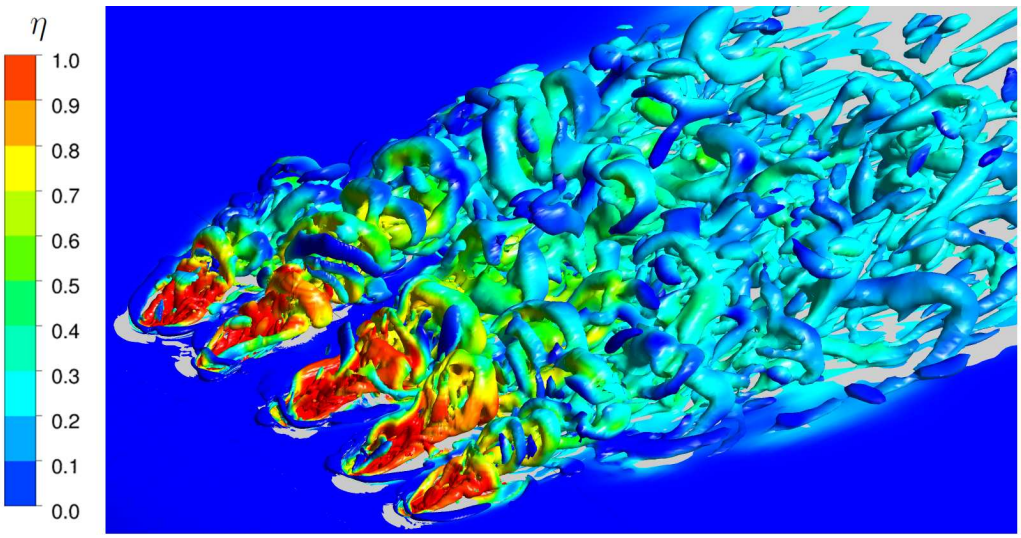

(a) Q-criterion showing coherent structures at $Q^* = 0.5$

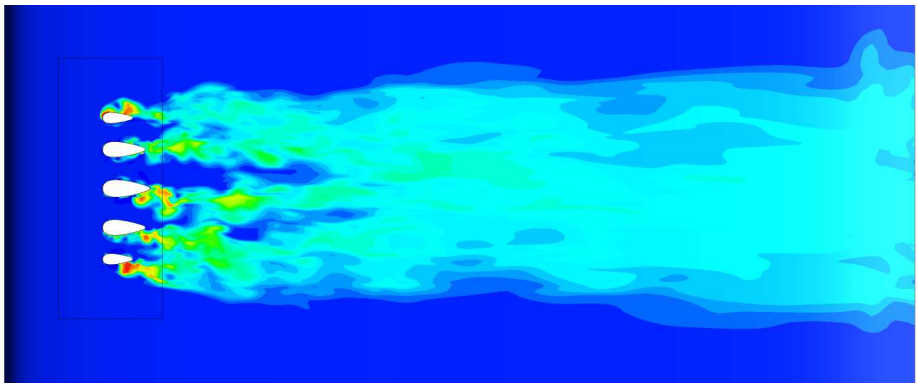

(b) Instantaneous thermal efficiency η

Figure 4.46: SAS showing unsteady flow at exhaust of generic multiple jets in cross flow configuration

and $St_D = 0.6$. These broad peaks correspond to the observation made in figure 4.46(a), where archlike vortices appear but due to the strong dynamics not in a very periodic manner. Once again, velocity component and temperature correlate, showing the impact of hairpin vortices on thermal mixing.

Additionally, as indicated by the individual thermal traces in the near field, cf. figure 4.46(b), the wake meandering shall also be investigated with the help of a spectral analysis of the lateral velocity component. Frequency peaks are indeed observable for monitor points $P_{MJICF,7}$ - $P_{MJICF,12}$ on the center line close to the surface behind each ejector. They are summarized in table 4.7 with the location of the monitor points given in table B.1. For each ejector, the corresponding pair of monitor points shows almost the same Strouhal number ranging from $St_D = 0.30 - 0.50$ based on the characteristic length of the respective jet. Similar to the single ejector case, these lateral velocity

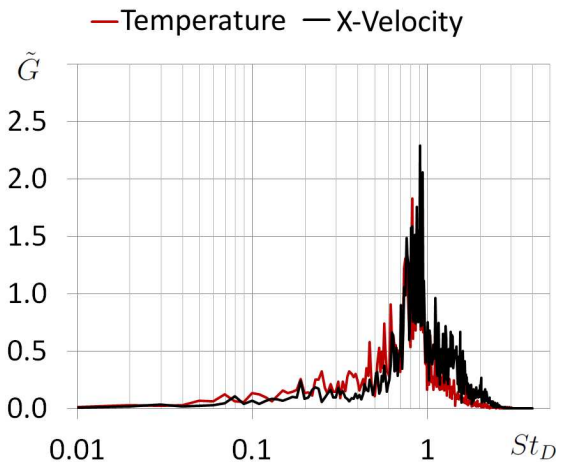

(a) PSD at $P_{MJICF,1}$

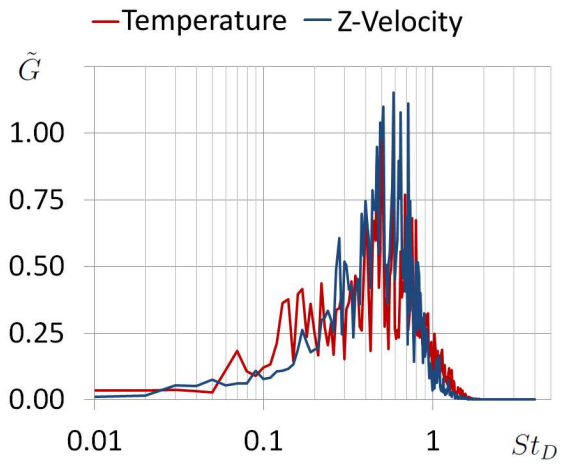

(b) PSD at $P_{MJICF,4}$

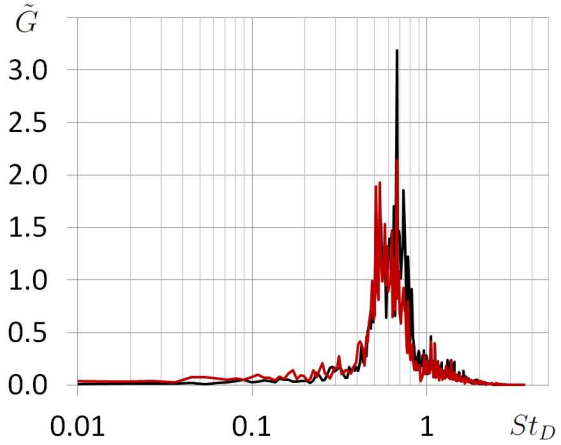

(c) PSD at $P_{MJICF,2}$

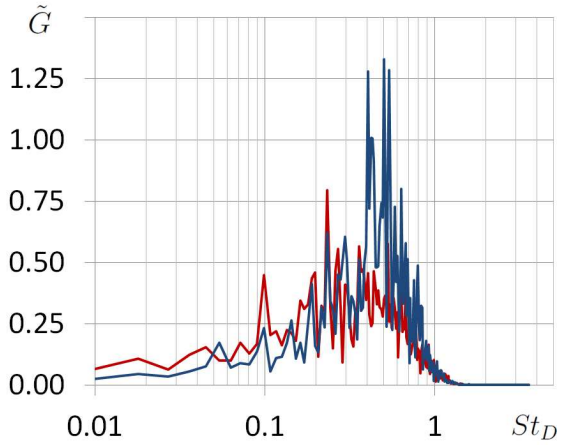

(d) PSD at $P_{MJICF,5}$

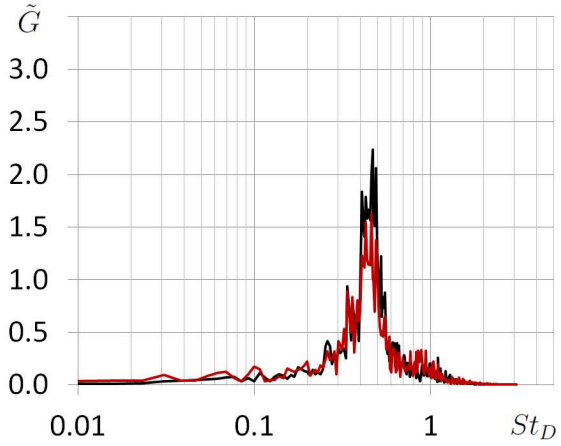

(e) PSD at $P_{MJICF,3}$

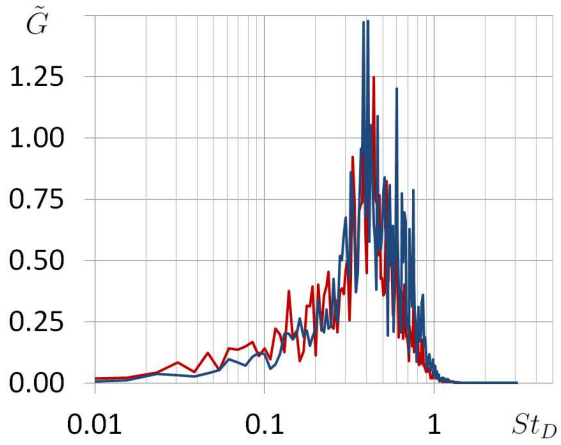

(f) PSD at $P_{MJICF,6}$

Figure 4.47: Power spectral densities for multiple jets in cross flow

Table 4.7: Spectral peaks for lateral velocity component in the jet wake

	$P_{MJICF,7}$	$P_{MJICF,8}$	$P_{MJICF,9}$	$P_{MJICF,10}$	$P_{MJICF,11}$	$P_{MJICF,12}$
Ejector	3	3	2	2	1	1
St_D	0.45	0.45	0.50	0.50	0.33	0.30

fluctuations are a strong evidence of the wake meandering. However, no uniform frequency is present and this behavior is only visible in the near field, where the neighboring jet interaction is weak.

In summary, the multiple ejector configuration shows an individual development of each jet in the near field with similar characteristics as the single jet: A horseshoe vortex as well as a counter-rotating vortex pair form and archlike vortices develop in the wake. Evidence for wake meandering is found and an oscillation in the upstream shear layer show the development of the von Kármán vortex street as well. The characteristic frequencies, either scaled or unscaled, are however significantly different from the single ejector case, which can be explained by the different ejector shape as well as the lateral confinement of the interior jets and the mutual impact on each other. As the wakes grow, the turbulent structures of the five jets start to interact with each other and no coherent large-scale motion is detectable. Instead, a large region of non-coherent vortices of different size and nature appears, which are advected downstream.

Recapitulating this chapter, calculations have been carried out on a generic jet in cross flow configuration in order to validate the different simulation approaches proposed previously. In contrast to the URANS simulation, sufficient resolution of turbulent scales was achieved with the integrated approaches based on SAS, DDES and ELES. As this directly impacts mixing prediction, a good agreement with experimental data became apparent for the latter three strategies. Additional validation of the SAS turbulence model was achieved by investigating hybrid meshing strategies as well as the influence of the numerical time step size and satisfying results in terms of scale-resolution and aerothermal prediction were obtained. Concluding the validation part, the sequential approach based on the SAS turbulence also predicted accurately the surface temperature distribution. Due to a reduction of computational costs by about 50% compared to the integrated SAS approach, the simulation of jet in cross flow applications installed on aircraft now becomes feasible.

The flow analysis revealed important thermal mixing phenomena such as archlike vortices, which develop around the recirculation zone behind the orifice and entrain cold cross flow fluid into the hot core. The counter-rotating vortex pair develops at the lateral ejector edges leading to a pronounced mixing of jet and cross flow fluid. The

well-known horseshoe vortex in front of the jet was identified, which has however no influence on thermal mixing. In order to gain a deeper insight into the dynamics, a Proper Orthogonal Decomposition was carried out, which revealed the wake meandering as an important flow dynamics with great impact on thermal mixing. Assumptions for thermal boundary conditions have been revisited and it was found that heat transfer within the mock-up plays an important role, highlighting the need to account for multiphysics. Finally, the integrated SAS approach was applied to a generic configuration containing multiple jets in cross flow. Scale-resolution was achieved and a satisfying agreement with experimental data was obtained. In the near field, each jet develops individually before a merging of wake structures takes place in the mid and far field.

Chapter 5

Application to Complex Configurations

The promising results obtained on the generic test case encourage the application of Scale-Resolving Simulations to more complex configurations. In this chapter, exhausts of real aircraft air systems are considered, which comprise multiple hot jets in cross flow at small velocity ratios with strong thermal impact on the surface downstream of the ejector grid. The current aerothermal design process relies on wind tunnel testing of simple configurations and empirical models. As standard RANS simulations are known to underestimate the thermal impact of this kind of flow, conclusions drawn from them have to be rather conservative. Recalling the need for a thermal shield as presented in figure 1.1, its dimensions are usually overestimated leading to additional structural weight. More accurate aerothermal predictions would provide access to essential information which is up to now unavailable and which would enable an enhanced design of such exhausts. In order to make Scale-Resolving Simulations accessible to the design process, an adapted sequential approach is presented and subsequently applied to two exhaust types, which constitutes the third main objective of this work. These exhausts stem from the nacelle anti-icing system and the pre-cooling system of the environmental control system. Due to the deeper level of validation for the generic configuration, i.e. influence of time step size and meshing strategy, the SAS turbulence model will be employed. Results for realistic flight conditions are presented and compared to available flight test data for the first application.

5.1 Adapted Sequential Approach

For the reasons already discussed in section 3.4, only the sequential approach is considered here. Additional constraints have to be respected in order to apply the established process to aircraft applications at realistic flight conditions. The original sequential approach would start from a RANS calculation of the entire aircraft including the air

system exhaust and thus the jet in cross flow itself. In an industrial context however, the current process does not offer CFD calculations of the full configuration due to substantial meshing efforts and computational costs. On the other side, numerical grids and RANS simulations of the *clean* configuration, i.e. the aircraft without exhaust geometry, exist or are readily obtainable.

The modified sequential approach is illustrated in figure 5.1. In a first step, a conventional RANS approach is employed on a numerical grid containing the clean geometry, as framed by red lines in the top figure 5.1(a). A global estimation of the flow field can thus be established even if the solution does not take into account the jet in cross flow. The second step remains unchanged and consists in defining the extents of a spatially fixed fluid zone, where a simulation with scale-resolving capabilities shall be applied. The RANS solution is then extracted on the boarders of this region, which are illustrated as dashed black lines in the middle figure 5.1(b). Thirdly, a new computational mesh is generated with the extents of the area of interest but respecting the real exhaust geometry, which is shown as red lines in the bottom figure 5.1(c). Temporally fixed boundary conditions are then provided by the RANS solution for a Scale-Resolving Simulation in the domain of interest. This allows a significant reduction of computational effort while still taking into account local flow topology and installation effects in the vicinity of the exhaust. Basically any of the integrated approaches are applicable in this domain but only the SAS model will be considered due to the increased level of validation.

This methodology leads indeed to an additional error. However, the geometrical difference between the two configurations is locally confined to a small region and, if the inlet boundaries of the SRS domain are located sufficiently far away, the influence of the jet in cross flow on the flow topology vanishes and the uncertainty decreases. Contrary to inlets, the outlet boundary condition does not have a strong influence on the solution if the jet is not taken into account.

5.2 Exhaust of Nacelle Anti-Icing System

The adapted sequential approach will now be applied to simulate the exhaust of the nacelle anti-icing system (NAIS) of a civil aircraft. The actual system is very similar to the one shown in figure 1.1. Bleed air from the engine is used in order to form a recirculating flow inside the air intake with a mass flow $\dot{m}_{rc}$. This hot fluid heats the leading edge of the nacelle and prevents thus the formation of ice during flight. A part of the recirculating mass flow is collected in a plenum and ejected through five droplet shaped ejectors into the main flow, which is shown in figure 5.2.

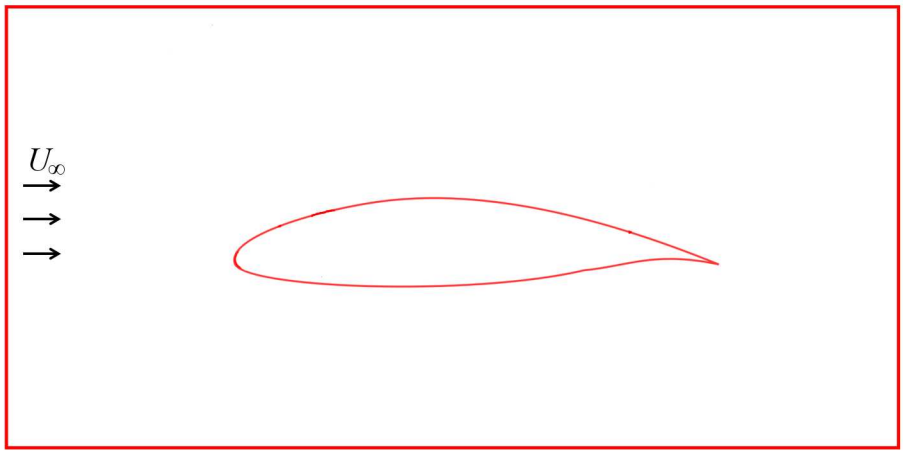

(a) RANS simulation of *clean* configuration

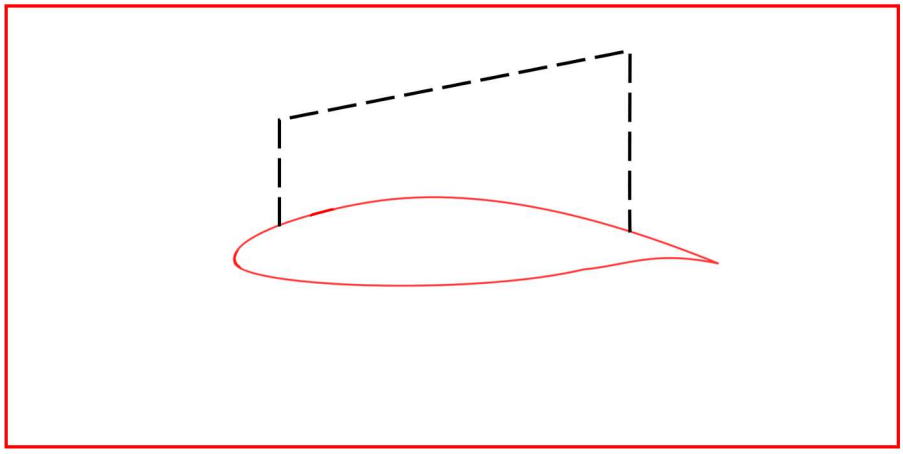

(b) Definition of external part of subdomain and extraction of solution on its boundaries

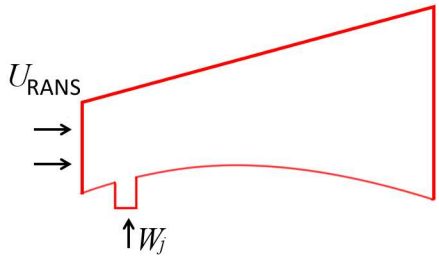

(c) Sacle-Resolving Simulation only in subdomain *including* exhaust geometry

Figure 5.1: The adapted sequential approach for complex configurations, cf. figure 3.5 for original sequential approach

Table 5.1: Similarity parameters for the exhaust of the nacelle anti-icing system

C_R	Re_{cf}	Ri_{cf}	$\Delta T/T_{ref,2}$
0.34	$3.11 - 3.62 \cdot 10^5$	$\ll 1$	0.63

(a) Exhaust position on nacelle

(b) Detail view of ejector grid

Figure 5.2: Multiple jets in cross flow appear at exhaust of nacelle anti-icing system

From available flight test data a stabilized flight phase is chosen that features a small momentum ratio in order to assess thermal impact on nacelle structure. This flight phase corresponds to a holding at $Ma_\infty = 0.5$, an altitude of $H = 10\,000$ft and an aircraft's angle of attack of $\alpha/\alpha_{ref} = 1.0$. The establishing JICF is characterized by the parameters presented in table 5.1. Total momentum ratio and cross flow Reynolds number range are estimated identically as for the generic configuration comprising multiple jets in cross flow. However, both the Reynolds number and the temperature difference are significantly higher. In addition to this, compressibility effects will arise due to the increased free stream Mach number. The momentum ratio is calculated with the classical values for free stream momentum and is thus rather small. However, taking into account installation effects and local flow conditions, the effective momentum ratio is actually increased.

5.2.1 Simulation and Meshing Strategy

Starting point for the simulation is a steady state RANS calculation of the aircraft. As only the clean configuration is required for this computation, neither the interior nor the exhaust grid of the nacelle anti-icing system is included. In order to account for installation effects, the configuration consists of fuselage, wing, pylons as well as

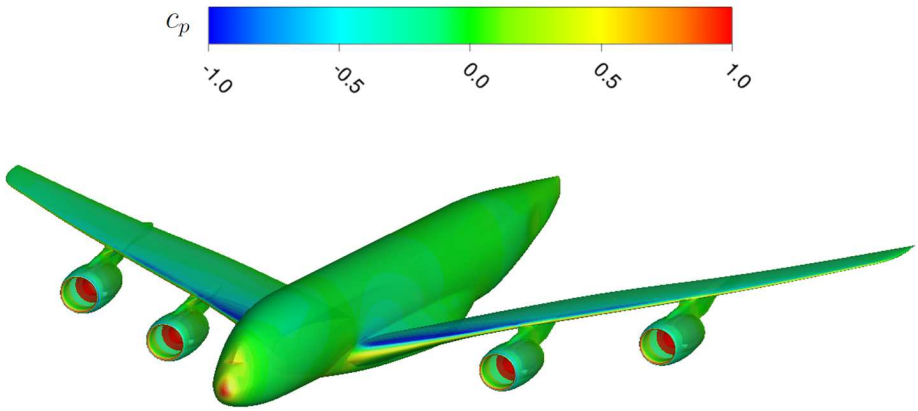

Figure 5.3: Pressure distribution resulting from steady state RANS solution of symmetrized *clean* aircraft configuration

engines and only half of the geometry needs to be taken into account due to symmetry. Numerical boundary conditions are set accordingly to the flight phase given above via a far field approach. Additional conditions have to be applied at the engines according to the power setting, which include inlet conditions for the fan as well as outlet conditions for the core jet, the bypass flow and the ventilation. Using the industrial process, a RANS solution is obtained with the help of the CFD solver elsA [71] on an existing hexahedral mesh. As the SAS turbulence model will be used for Scale-Resolving Simulation, the SST turbulence model is employed for the steady state calculation in order to obtain turbulence boundary conditions in terms of turbulence kinetic energy k and specific dissipation rate ω. The configuration and the resulting pressure distribution are plotted in figure 5.3.

After modifying the clean geometry by including the exhaust grid as well as the interior part of the anti-icing system, the next step consists in defining the domain for scale-resolution. The external part consists of a diverging box with its boundaries having sufficient distance to the exhaust grid. As the flow inside the plenum has a strong effect on the establishing jets in cross flow, a part of the interior of the anti-icing system has to be included as well. The SRS box is constructed only on the interior nacelle of the right wing according to the flight test and figure 5.4(a) illustrates its position and extents. Here it becomes obvious that character of the local flow and installation effects have to be accounted for if representative results are required. The entire domain, including the interior part of the system, is shown in figure 5.4(b). The transparent blue surface represents the skin of the nacelle, whereas the transparent red surfaces show the internal parts of the anti-icing system. The external part of the domain has thus four inflow and one outflow surface.

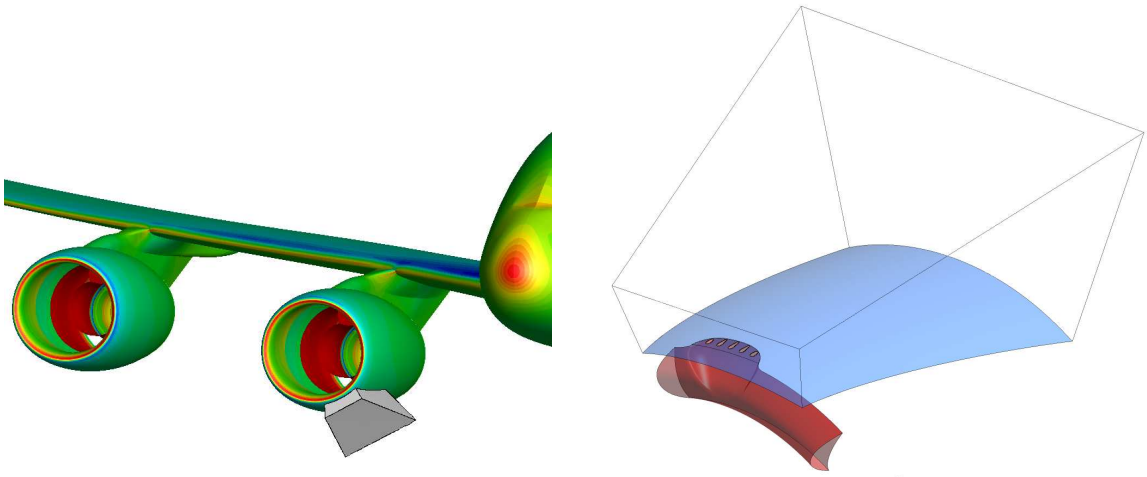

(a) Position and extents of the domain (b) Detail view of domain

Figure 5.4: Computational domain for sequential approach of simulating the exhaust of the nacelle anti-icing system

The relatively simple geometry allows the generation of a hexahedral mesh based on the structured multi-block approach. Due to the large dimensions of nacelle and exhaust grid respectively, this domain was discretized with a total of $36.9 \cdot 10^6$ cells. The same requirements as for the generic configuration have been respected, i.e. sufficient grid refinement in jet and cross flow interaction region and a non-dimensional wall distance y^+ smaller than one. A view of the surface mesh close to the ejectors is presented in figure 5.5, which is very similar to the one utilized for the generic multiple jets in cross flow configuration. A slightly varying blocking topology had to be applied however in order to ensure the mapping of the semi-elliptical ejector plate for the application of appropriate thermal boundary conditions. In order to employ the steady state RANS simulation as fixed boundary conditions for the SRS domain, an interpolation of first order is carried for the external surfaces of the bounding box, where the values for velocity components, pressure, temperature as well as turbulence quantities k and ω are retained. The latter two are of importance since they describe the characteristics of the oncoming boundary layer, which will interact with the jets.

Velocity inlet boundary conditions are then applied for the inflow surfaces of the external part of the domain, where RANS velocity components, temperature and pressure profiles are prescribed as well as the RANS distribution of turbulence kinetic energy and specific dissipation rate. A pressure outlet is employed at the outflow surface, where again the corresponding RANS pressure profile is specified. The definition of internal boundary conditions is not as straightforward. From flight test data, the mass flow of bleed air can be calculated and has thus to be equal to the total jet mass flow $\dot{m}_j$. However, the recirculating mass flow $\dot{m}_{rc}$ is only known approximately. In order

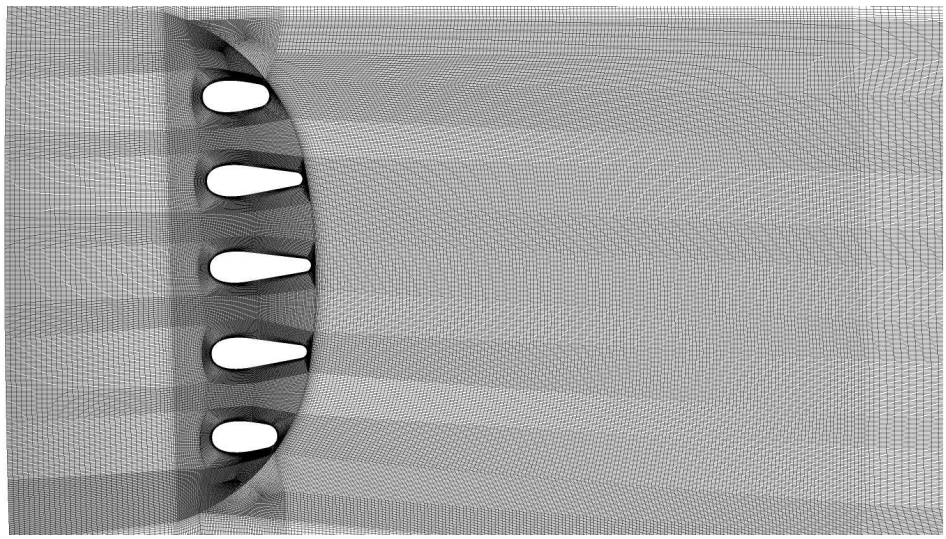

Figure 5.5: Detail of surface mesh for the exhaust of the nacelle anti-icing system

to assess uncertainty, the mass flow ratio $\eta_{\dot{m}} = \dot{m}_{rc}/\dot{m}_j = 4.5$ including an uncertainty of $\Delta\eta_{\dot{m}} \pm 1$ is considered and the influence on thermal efficiency is investigated. Thus according to the ratios $\eta_{\dot{m}} = 3.5$, 4.5 and 5.5, a mass flow of $\dot{m}_{rc}$ is specified at the internal inflow surface. At the internal outflow surface, a constant pressure is applied, which leads to a time-averaged exiting mass flow of $\dot{m}_j\,(\eta_{\dot{m}} - 1)$. Also known from flight test data is the total temperature inside the scoop, which is for simplicity assumed to be constant for the internal fluid and equals thus the jet's total temperature $T_{t,j}$. All walls are treated adiabatically except for the ejector. Following the pragmatic approach presented in section 4.6.1, a constant wall temperature of $T_{isoth} = 1/2\,(T_{t,\infty} + T_{t,j})$ is prescribed in order to account for heat conduction.

The numerical set-up is basically the same as for the generic configuration except for two aspects. Firstly, an ideal gas formulation is assumed as the free stream Mach number yields $Ma_\infty = 0.5$ and compressibility effects are no longer negligible. Secondly, the coupled version of the pressure-based algorithm has to be applied in order to achieve inner convergence. A similar procedure as before is followed for flow initialization, except that additional steady state iterations are needed for obtaining a sufficiently converged solution. Also due to the increased cross flow velocity, the numerical time step size has to be decreased to a value of $\Delta t = 1 \cdot 10^{-5}$s.

5.2.2 Results and Flight Test Comparison

The evolution of the residuals are very similar to the one presented in figure 4.10. The simulation is switched to transient mode after 200 steady state iterations. Within every time step 10 inner iterations are calculated and the residuals decrease by about one to two orders of magnitude. For transient flow initialization 1 000 time steps

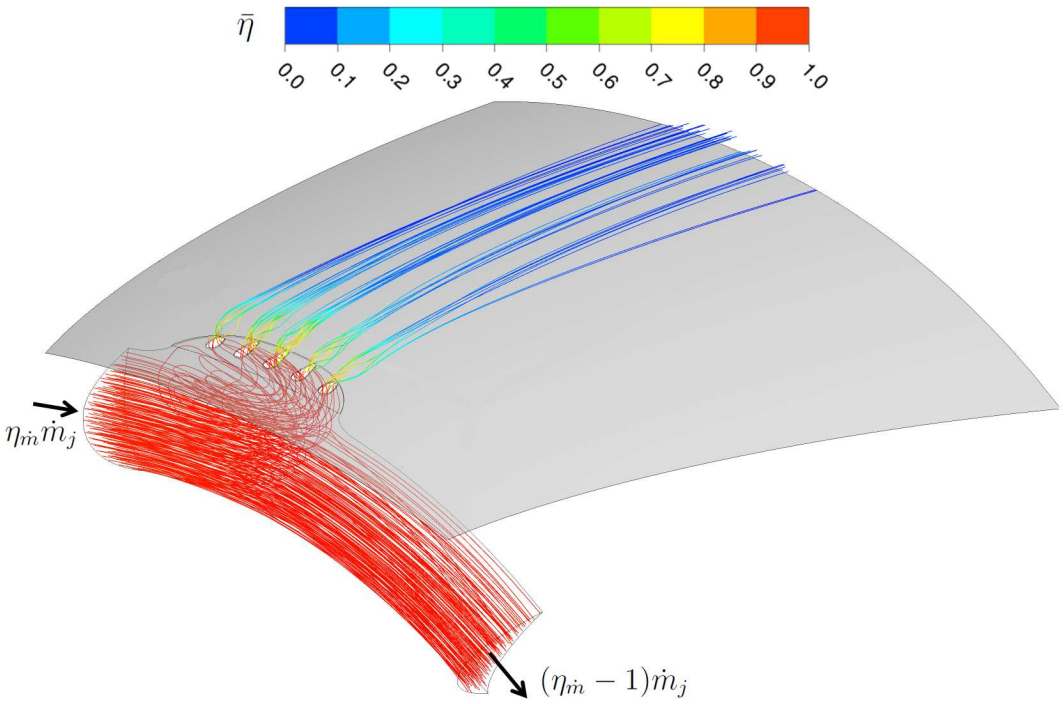

Figure 5.6: Streamlines of time-averaged velocity colored by thermal efficiency

are calculated, which corresponds to the necessary two characteristic convective times based on the length of the area of scale-resolution. A total number of 7 000 time steps are required in order to obtain sufficiently converged time statistics, taking about seven days wall-clock time on 168 cores of the AIRBUS HP POD [97]. Firstly, the stationary flow solution is presented in terms of streamlines of time-averaged velocity colored by thermal efficiency for $\eta_{\dot{m}} = 4.5$ in figure 5.6. As the streamlines are released from the internal inflow surface most of them leave the computational domain through the internal outflow surface. A small part however recirculates inside the plenum and leaves through the five ejectors where they encounter the external flow. The temperature is constant inside the system but once the jets leave the plenum they are cooled rather quickly by the cross flow. Due to the small velocity ratio however, the jets bend abruptly and attach to the nacelle surface leading to a strong thermal impact. Similar to the generic test case, no recirculation zone forms behind the ejectors. Since the other cases with $\eta_{\dot{m}} = 3.5$ and 5.5 respectively exhibit a very similar steady flow topology, they are not shown repeatedly.

The ratio of time-averaged mass flow through each ejector over the total jet mass flow is given in table 5.2 as well as the share of every orifice in the total ejection area. The ejectors being numbered from left to right looking in main flow direction, a strong asymmetry with increasing mass flow towards the right is visible. This stems from the internal design of the system, where the one-sided flow direction leads to a turbulent

Table 5.2: Mass flow and area distribution for the exhaust of nacelle anti-icing system

	Ejector 1	Ejector 2	Ejector 3	Ejector 4	Ejector 5	Total
Area	17.0	21.5	23.0	21.5	17.0	100
Mass flow, $\eta_{\dot{m}} = 3.5$	16.3	20.9	22.6	22.7	17.5	100
Mass flow, $\eta_{\dot{m}} = 4.5$	16.8	20.1	22.0	22.7	18.4	100
Mass flow, $\eta_{\dot{m}} = 5.5$	16.3	19.3	21.6	23.0	19.8	100

recirculation zone inside the plenum, which is most pronounced for the third case. The individual velocity ratios can then be estimated and range approximately between 0.06 and 0.08. Due to the unsteady and compressible flow, the mass flow through each ejector varies in time as well.

Secondly, scale-resolvability is studied with the help of the Q-criterion, which is displayed in figure 5.7(a) for $\eta_{\dot{m}} = 4.5$. Only the second case is presented as unsteady characteristics are identical in a qualitative way. Very similar to the multiple ejector test case presented in section 4.6.2, each jet develops independently of its neighbors in the near field. The counter-rotating vortex pairs are visible as well as the horseshoe vortex in front of every ejector. Clearly, archlike vortices develop periodically in the wake. Once the merging between adjacent jets takes place at about 2-3D downstream of the ejectors, these vortices interact and lose their coherence. Due to the increased mesh refinement in the mid and far field compared to the generic configuration, turbulent fluctuations are resolved over a greater distance leading to an enhanced mixing prediction.

The instantaneous temperature distribution is plotted in figure 5.7(b) and its highly transient and turbulent character becomes obvious. Corresponding to the prior observation, the thermal wake of each jet develops independently in the near field. However, due to the unbalanced mass flow through the ejectors the resulting temperature distributions are not similar. For example, the top jet shows a strong and broad thermal trace indicating a small velocity ratio and thus mass flow, whereas the behavior of the second jet from the bottom indicates the opposite. In the mid and far field, the interaction between the jets is so strong that the temperature distribution appears to be “random” and the influence of the individual wake is not discernible anymore.

The time-averaged values of thermal efficiency are presented in figure 5.8 for all three cases. In contrast to the generic configuration, the two outer traces do not merge as quickly and rather five independent lobes are visible in the near field. Furthermore, they are not symmetric and not aligned with the semi-major axis of the corresponding ejector. This is caused by the local flow characteristics, the curvature of the nacelle and by the unbalanced mass flow through each orifice. In the midfield, at about the second row of sensors, the two upper jets have merged due to their low momentum

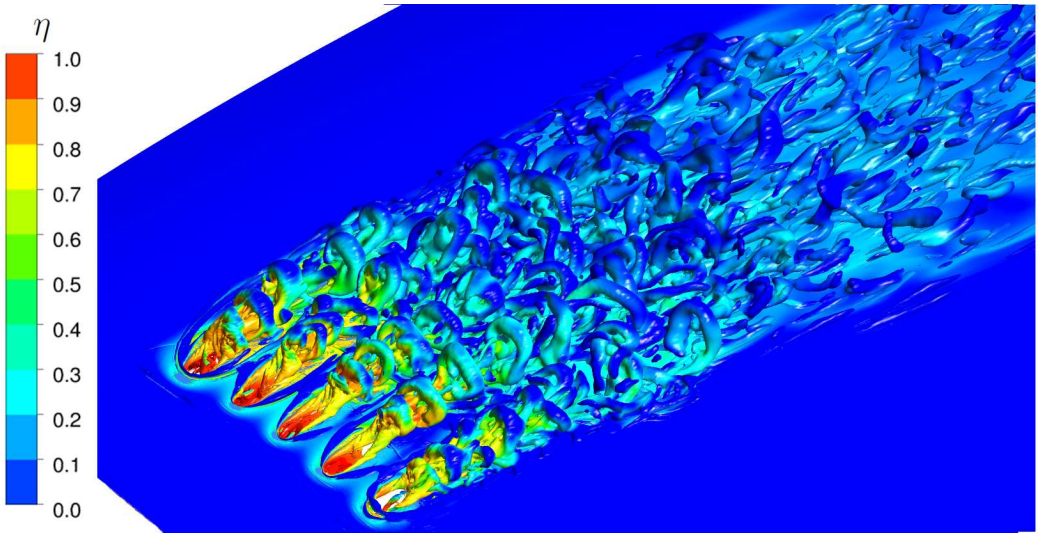

(a) Q-criterion at $Q^* = 0.1$ showing coherent structures at exhaust of nacelle anti-icing system

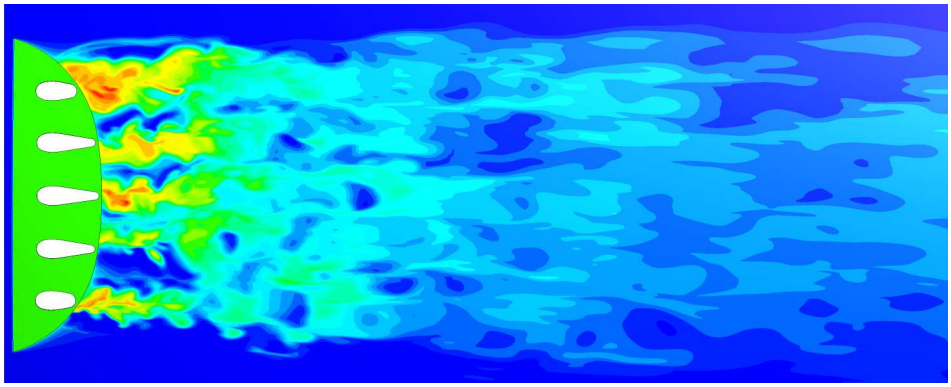

(b) Instantaneous thermal efficiency

Figure 5.7: SAS showing unsteady flow at exhaust of nacelle anti-icing system

ratio and only four lobes are visible. In the far field, the influence of the individual ejectors has vanished and only a broad lobe remains. Comparing all cases with each other, the contour plots qualitatively feature the same topology. Differences are visible in the extent of downstream spreading, which is higher for a smaller value of $\eta_{\dot{m}}$, and in the individual traces in the near field. This is consistent with table 5.2, where the thermal traces of ejectors 4 and 5 are less pronounced for the last case due to the increased individual momentum ratio.

For data collection during flight test, the nacelle surface was equipped with twelve thermal sensors, whose locations T_i are also indicated in figure 5.8. Sampling frequency is however not sufficient for a transient analysis. Instead, a quasi-steady temperature is accessible once a stabilized flight phase is obtained. The computational results for the SAS Case 1 ($\eta_{\dot{m}} = 3.5$), Case 2 ($\eta_{\dot{m}} = 4.5$) and Case 3 ($\eta_{\dot{m}} = 5.5$) as well as flight test data (FTD) are given for the sensor points in table 5.3. For the reference case 2,

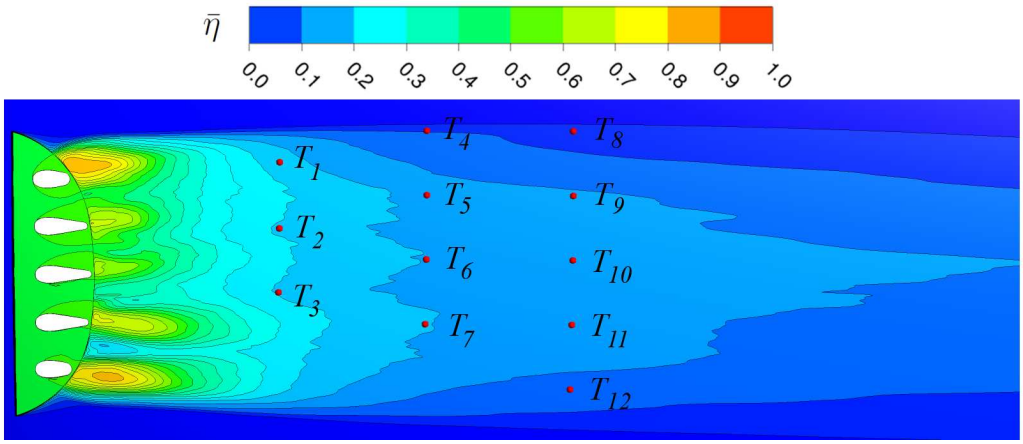

(a) SAS case 1: Time-averaged thermal efficiency for $\eta_{\dot{m}} = 3.5$

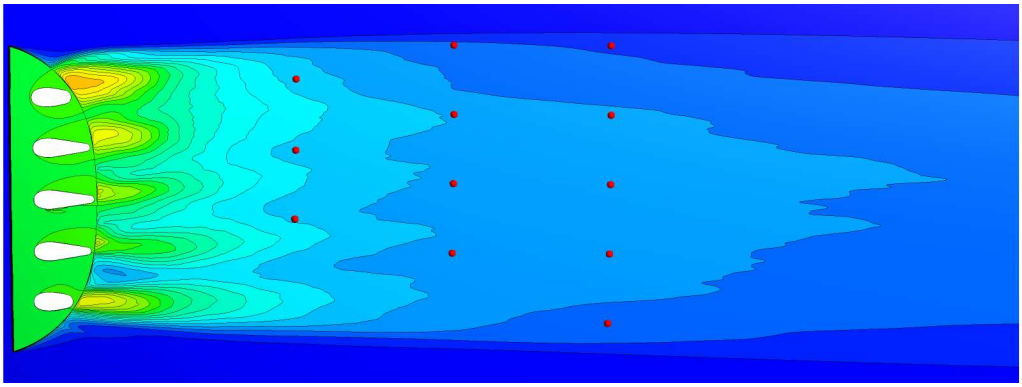

(b) SAS case 2: Time-averaged thermal efficiency for $\eta_{\dot{m}} = 4.5$

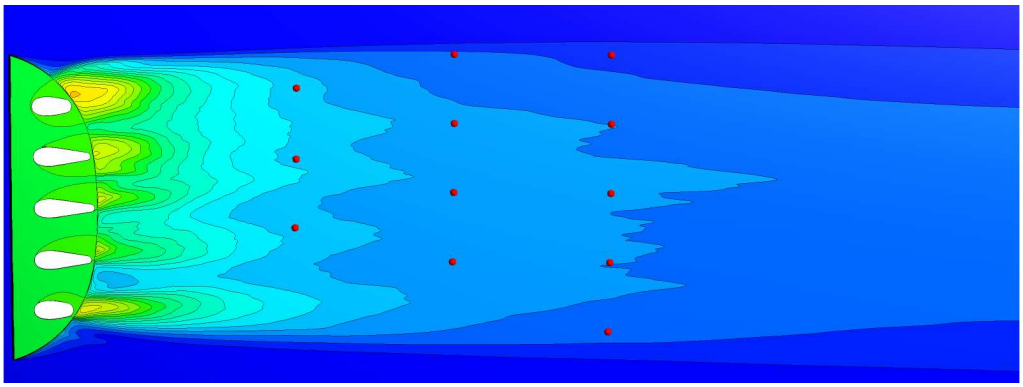

(c) SAS case 3: Time-averaged thermal efficiency for $\eta_{\dot{m}} = 5.5$

Figure 5.8: Thermal impact on surface with location of monitor points T_i

an excellent agreement, i.e. $\Delta\bar{\eta} \leq 0.02$, is achieved for all points except T_7, T_8 and T_{12}. The maximal difference yields $\Delta\bar{\eta} = 0.05$ at T_{12}. As T_7, T_8 and T_{12} are located at the ends of the second and third sensor row, the lateral thermal spreading is slightly underestimated. Numerical data for Case 1 compares very well in the near and far field but underestimates the lateral spreading at the sides. Concerning Case 3, a

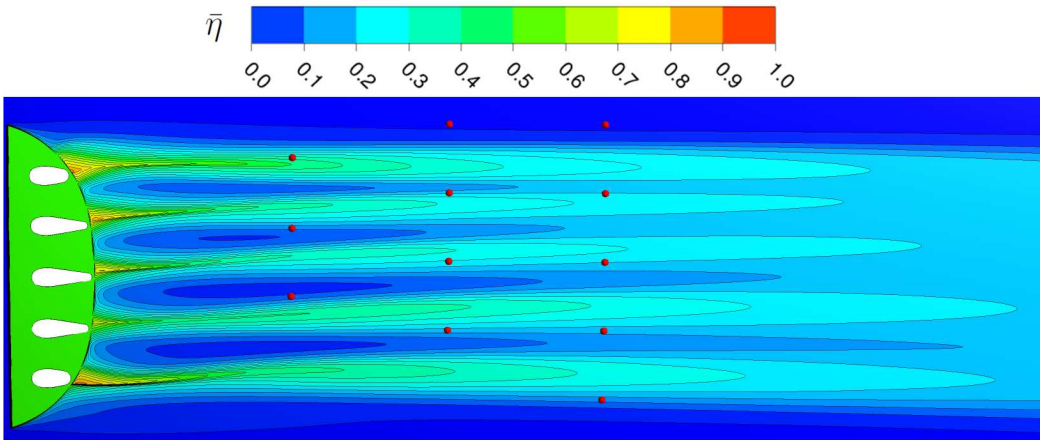

Figure 5.9: RANS case 2: Time-averaged thermal efficiency for $\eta_{\dot{m}} = 4.5$

Table 5.3: Comparison of thermal efficiency $\bar{\eta}$ for exhaust of nacelle anti-icing system

	T_1	T_2	T_3	T_4	T_5	T_6	T_7	T_8	T_9	T_{10}	T_{11}	T_{12}
FTD	0.17	0.21	0.21	0.09	0.16	0.16	0.17	0.07	0.13	0.14	0.14	0.13
SAS 1	0.18	0.19	0.19	0.05	0.14	0.15	0.15	0.03	0.11	0.13	0.12	0.08
SAS 2	0.18	0.19	0.19	0.07	0.15	0.14	0.13	0.04	0.11	0.12	0.12	0.08
SAS 3	0.17	0.19	0.18	0.06	0.13	0.12	0.12	0.04	0.10	0.10	0.10	0.07
RANS 2	0.37	0.10	0.03	0.00	0.18	0.23	0.18	0.00	0.20	0.20	0.17	0.11

slightly larger difference between simulation and flight test data is visible. Even if the uncertainty caused by the recirculating mass flow leads to a maximal difference of $\Delta\bar{\eta} = 0.03$, a very satisfying prediction of the thermal impact is obtained.

For completeness, a steady state RANS computation of the identical flow domain is carried out for the reference case 2, employing the standard $k-\omega$ SST turbulence model. The plot of thermal efficiency is presented in figure 5.9 and the difference in topology is striking. Only very fine thermal traces are visible, which are aligned with the external flow. However, high temperatures are observable far away from the ejectors, which is in contrast to the corresponding SAS computation. Additionally, no noteworthy thermal mixing between neighboring jets is visible, which consequently explains the strong discrepancy between RANS and flight test data revealed in table 5.3. This drastic example points out once again the necessity of scale-resolving simulations for the correct aerothermal prediction of hot jets in cross flow and the capability of the sequential approach in combination with the SAS turbulence model.

A recurring theme throughout this work concerns the uncertainty stemming from thermal boundary conditions, which are even more crucial for this configuration. On

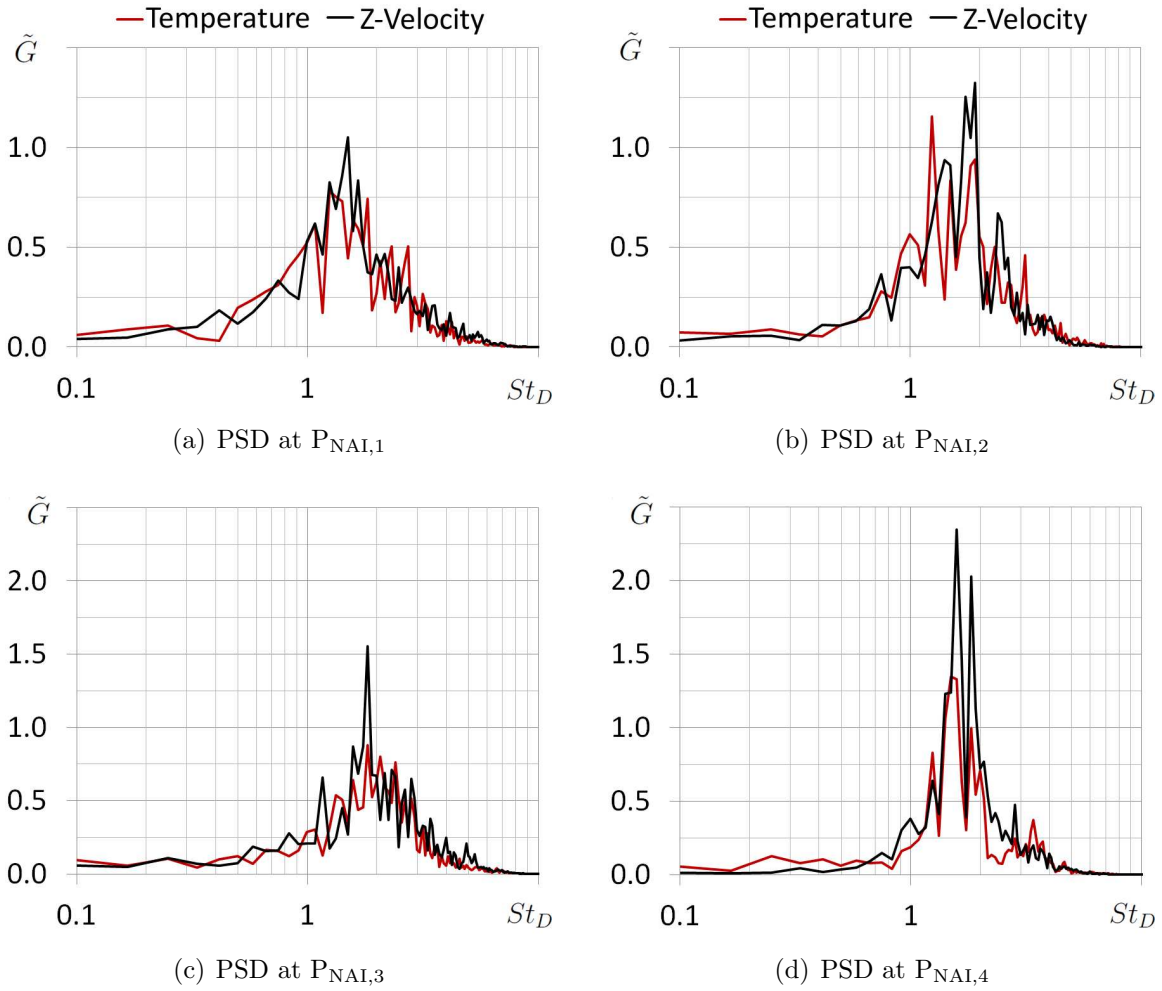

(a) PSD at $P_{NAI,1}$

(b) PSD at $P_{NAI,2}$

(c) PSD at $P_{NAI,3}$

(d) PSD at $P_{NAI,4}$

Figure 5.10: Power spectral densities in the wake showing passage frequency of archlike vortices

the one hand, heat conduction through the ejector plate is reasonably taken into account by applying an isothermal boundary condition. On the other hand, the anti-icing system itself heats of course the leading edge of the nacelle, which will then result in the development of a thermal boundary layer already from the stagnation point. The non-observance of this aspect can thus explain the almost constant offset between numerical and experimental data, i.e. the underestimation of $\Delta\bar{\eta} = 0.02$ for the baseline Case 2. Respecting this circumstance by including the entire system into the simulation set-up would go beyond the scope of this work if it is at all feasible. Nonetheless, the simulation approach presented here allows a very accurate prediction of the exhaust at real flight conditions and is also applicable within an industrial design process.

As this type of simulation methodology provides information about previously inaccessible data, the dynamical behavior of the exhaust flow shall be investigated as well. For this reason monitor points have been placed inside the wake and spectral

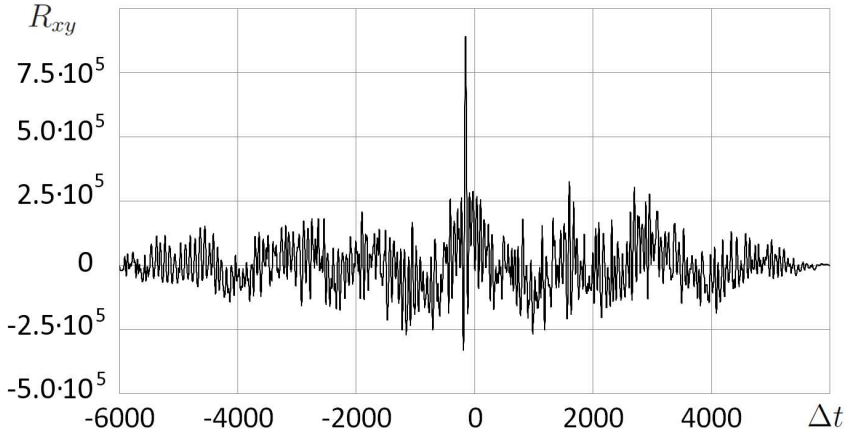

Figure 5.11: Cross correlation of temperature on points $P_{NAI,1}$ and $P_{NAI,5}$

analysis is carried out for velocity components and temperature histories. From the observation of the archlike structures in figure 5.7(a) the frequency associated to the passage of these vortices is of great interest. The power spectra are calculated for the Z-velocity component of the four monitor points $P_{NAI,1}$, $P_{NAI,2}$, $P_{NAI,3}$ and $P_{NAI,4}$, which are shown in figure 5.10. The corresponding locations are given in table B.2 and are illustrated figure B.2(a). They all reveal a high frequency peak with a value of $St_D = 1.4$ for the outer points $P_{NAI,1}$ and $P_{NAI,4}$ and a value of $St_D = 1.9$ for the inner points $P_{NAI,2}$ and $P_{NAI,3}$ respectively. Also included in these plots is the power spectral density of temperature. As they exhibit similar dominant frequencies, the connection of archlike vortices with thermal mixing is confirmed. In order to characterize the convective velocity of these structures, the correlation of temperature is calculated. The two monitor points $P_{NAI,1}$ and $P_{NAI,5}$ are thus regarded, which are located one after another in streamwise direction. The cross correlation R_{xy} presented in figure 5.11 shows a strong peak at $146\Delta t$. Knowing the distance between the monitor points, the convective Mach number can be calculated, yielding $Ma_{\text{conv.}} = 0.49$ which is slightly smaller than the free stream Mach number. The investigation of different monitor points gives similar results, describing a homogeneous convective field in the jet wake. In analogy to the single ejector test case, a synchronous meandering of the five jet wakes could be expected. The coherence of lateral velocity signals obtained from monitor points aligned in spanwise direction, for instance from points $P_{NAI,1}$ and $P_{NAI,4}$, is thus calculated as well but no evidence for such a behavior is found.

5.3 Exhaust of Pre-Cooling System

As the adapted sequential approach has shown its capability to yield satisfying results, it will eventually be applied to the pre-cooling system (PCS) of a civil aircraft, which

Table 5.4: Similarity parameters for the exhaust of the pre-cooling system

C_R	Re_{cf}	Ri_{cf}	$\Delta T/T_{ref,3}$
0.29	$1.90 - 8.29 \cdot 10^5$	$\ll 1$	1.10

is part of its environmental control system. In order to supply fresh air and thermal control for the cabin, bleed and ram air are mixed inside air conditioning packs. However, fluid taken from the engine's compressor stage is too hot and needs to be pre-conditioned. A heat exchanger is therefore employed, in which fan air cools down bleed fluid. The consequently heated fan air is then gathered in a plenum and ejected into the main flow through a ventilation grid situated on the pylon. In contrast to the configurations studied before, the ejector geometry is quite different since it consists of two rows each containing 19 vents. As the vents are aligned in flow direction, the 19 single jets of each row will merge, eventually creating two jets.

Just like for the exhaust of the nacelle anti-icing system, it has to be ensured for safety and certification that at any flight condition the surface temperature downstream of this exhaust remains within the limits allowed. A flight phase is thus chosen, which is critical in terms of exhaust air temperature and momentum ratio. This corresponds to a holding flight at $Ma_\infty = 0.48$, an altitude of $H = 22\,000$ft and an aircraft's angle of attack of $\alpha/\alpha_{ref} = 0.95$. The similarity parameters for this case are summarized in table 5.4. The total momentum ratio is estimated in the same manner as for the other multiple ejector configurations but the cross flow Reynolds number needs special attention. Due to the vent alignment in flow direction, only two jets will form. The first characteristic length scale is again estimated accordingly to the single vent's ejection surface. The second characteristic length is however obtained from the square root of the total ejecting surface of each of the two developing jets. Compared to the previous configuration, the total momentum ratio is even smaller and the temperature difference $\Delta T/T_{t\infty}$ greatly increased. Again, compressibility effects have to be accounted for and the effective momentum ratio is larger due to local flow conditions.

5.3.1 Simulation and Meshing Strategy

In the same manner as for the nacelle anti-icing system, a steady state RANS calculation of the *clean* configuration is required. This means that the pylon contains neither the interior nor the exhaust grid of the pre-cooling system. The standard design configuration consisting of fuselage, wing, pylon, engine and vertical tail plane is used and only half of the geometry needs to be taken into account for symmetry reasons. Numerical boundary conditions are chosen to match the critical flight condition defined above, including inlet and outlet conditions for the engine. Again, the RANS solution is obtained on an existing hexahedral mesh with the help of the CFD solver elsA

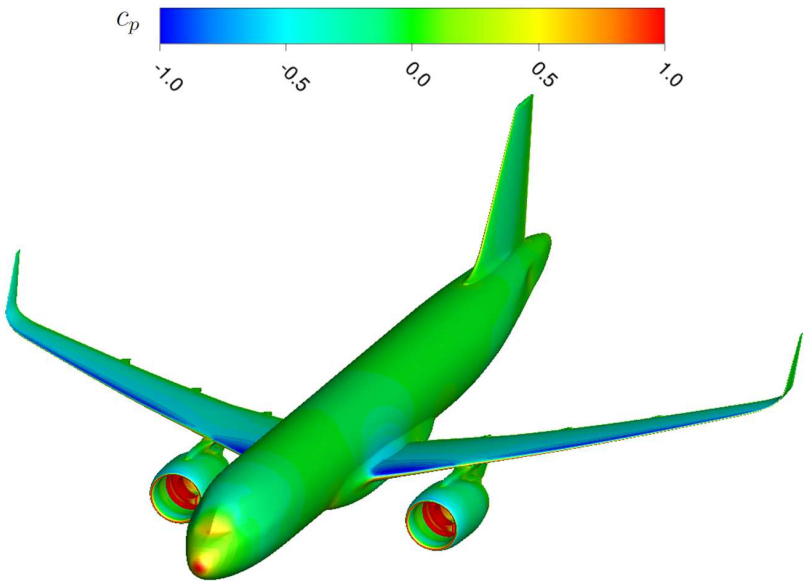

Figure 5.12: Pressure distribution of steady state RANS solution of symmetrized *clean* aircraft configuration

in accordance with the industrial aerodynamic design process. The SST turbulence model is employed as turbulence kinetic energy k and specific dissipation rate ω need to be prescribed for the following SAS calculation. The configuration and the resulting pressure distribution are plotted in figure 5.12.

The clean geometry is then accordingly modified by including the ventilation grid as well as the interior part of the pre-cooling system, which consists in this case of a simple plenum. In contrast to the nacelle anti-icing system, the definition of the scale-resolving domain is not as straightforward. For the considered condition, the jet will impact on the leading edge of the wing and then pass over the suction side, necessitating the divergent box to cover a sufficient part of the upper wing. As the flow below the wing is thus of lesser importance and as complications with the engine's jet shall be avoided, the lower part of the domain is bounded by a surface between nacelle and wing at each side of the pylon. The resulting box, containing four external inflow and three external outflow surfaces, is shown in figure 5.13(a). The evidence of taking into account installation effects for this problem is even more obvious than for the previous example. The entire domain, including the ventilation grid of the system is shown in figure 5.13(b).

Due to the increased complexity of the geometry, especially the numerous ejectors on the ventilation grid, a hybrid tetrahedral mesh with prismatic inflation layers is generated with the support of Airbus. Sufficient spatial refinement is ensured in the jet path as shown in figure 5.14(a), which was estimated by a preliminary simulation, yielding a total number of $46.7 \cdot 10^6$ computational cells. A detailed view of the surface

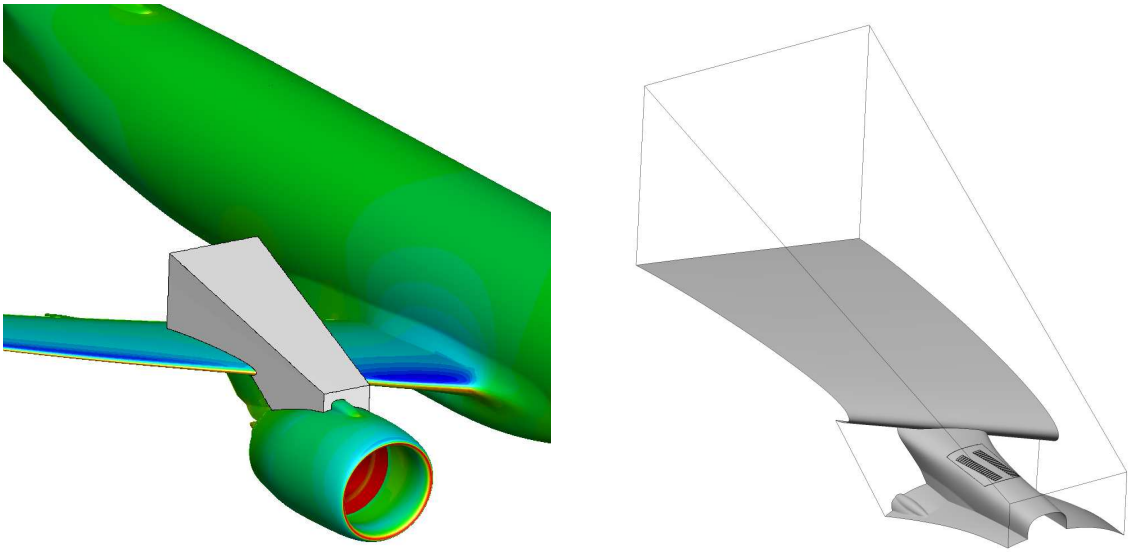

(a) Position and extents of the domain (b) Detail view of domain

Figure 5.13: Computational domain for sequential approach of simulating the exhaust of the pre-cooling system

mesh for the ventilation grid is presented in figure 5.14(b). The proper resolution of the boundary layer requires a y^+ smaller than one and a total of 20 prism layers will be used. Additional volume cells are shown in figure 5.14(c), where the inflation layers around the vents are highlighted in red. As a first order interpolation proved to be sufficient, it will be applied again in order to extract the RANS solution variables, i.e. velocity components, pressure, temperature, turbulence kinetic energy and specific dissipation rate, at the bounding surfaces of the domain.

Velocity inlet boundary conditions and pressure outlet boundary conditions are then applied to the external inflow and outflow surfaces respectively, where the profiles of RANS solution variables are prescribed. The internal boundary condition for this configuration is much simpler, as only one internal inlet has to be defined. Mass flow $\dot{m}_j$ and total jet temperature $T_{t,j}$ are set accordingly to the operating point of the system and turbulent inflow boundary conditions are specified as well. All walls of the configuration are treated adiabatically except the ventilation grid, where a constant wall temperature of $T_{isoth} = 1/2\,(T_{t,\infty} + T_{t,j})$ is prescribed in order to account for heat conduction. The numerical set-up is identical to the one of the nacelle anti-icing system as compressibility effects need to be accounted for and in order to avoid convergence issues. Due to the high free stream Mach number of $Ma_\infty = 0.48$, a small numerical time step size of $\Delta t = 1 \cdot 10^{-5}$s has to be employed.

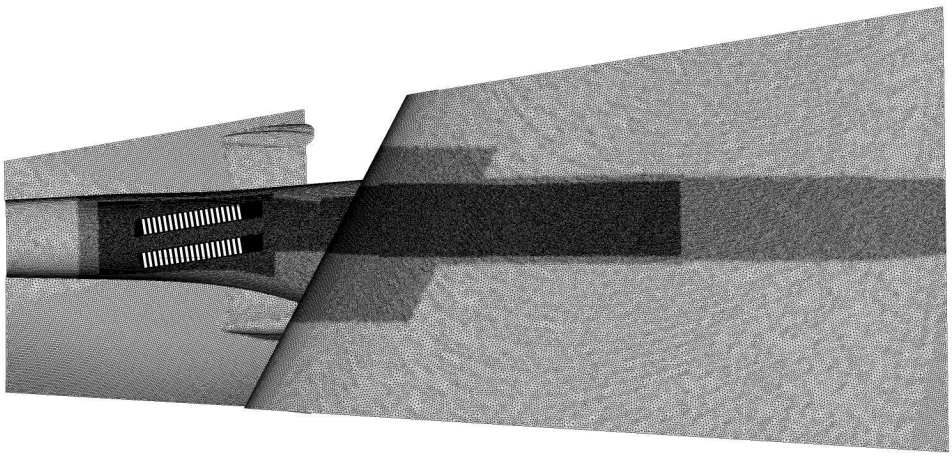

(a) View of the entire surface mesh with spatial refinement in jet path

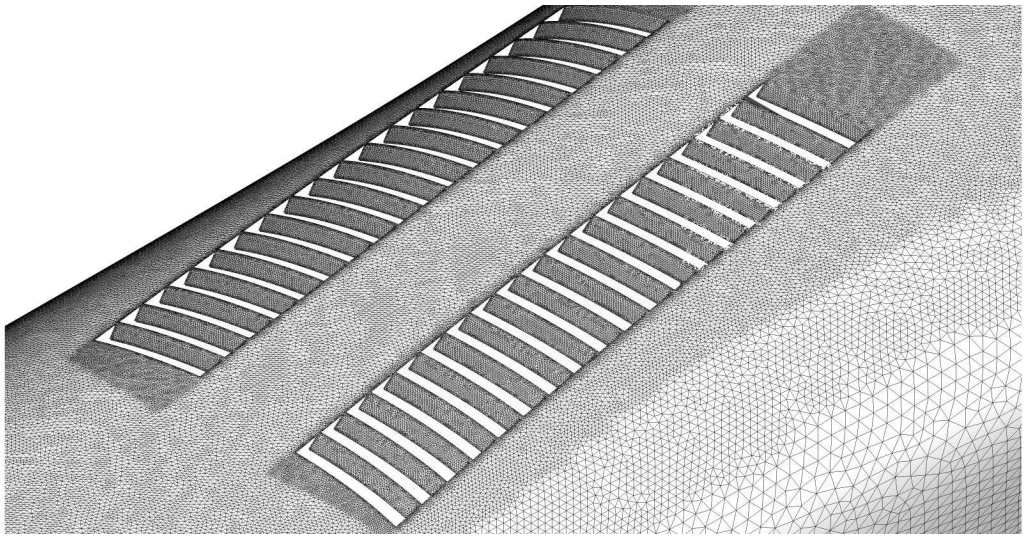

(b) Detail view of the mesh around the ventilation grid

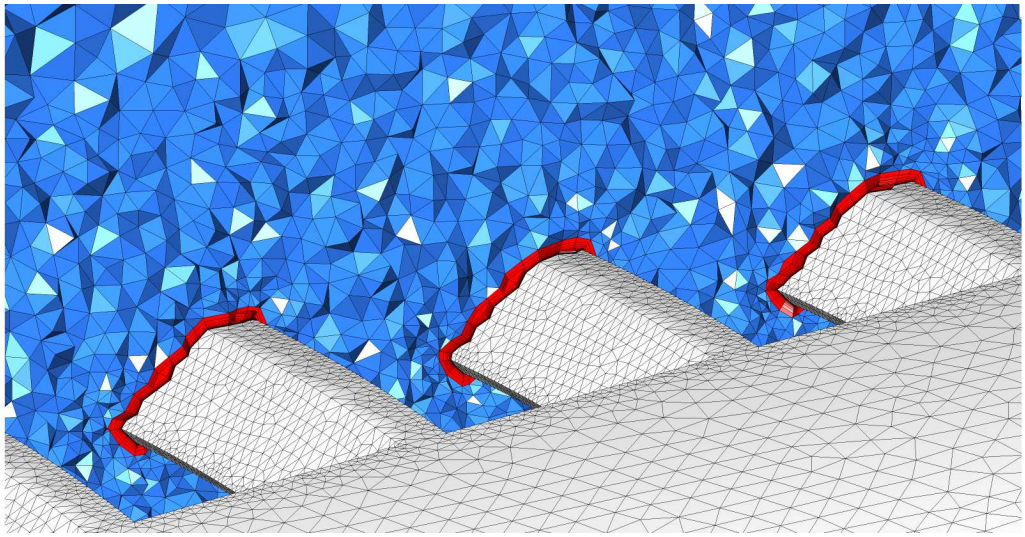

(c) Detail of the volume mesh with prismatic cells highlighted in red

Figure 5.14: Mesh illustration of the exhaust of the pre-cooling system

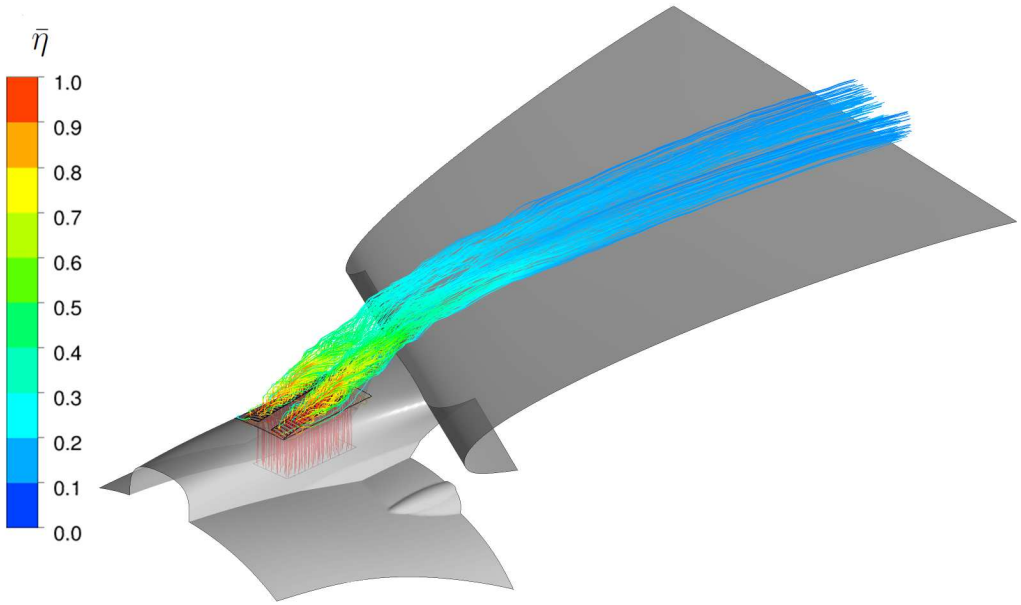

Figure 5.15: Streamlines of time-averaged velocity colored by thermal efficiency

5.3.2 Results

In the same way as for the above simulation a steady flow initialization is carried out but this time over 250 iterations due to the more complex flow field. Following this, the transient calculation is started and due to the large computational domain 2 000 time steps are necessary for transient flow initialization. This corresponds again to about two convective times based on the length of the area of scale-resolution, which is in this case even longer. Within every time step 10 inner iterations are calculated and the residuals decrease about one to two orders of magnitude. A total number of 8 000 time steps are necessary to obtain outer convergence. The total computational time is seven days on 240 cores of the Airbus HP POD [97]. In order to gain a first impression of the flow, streamlines of the time-averaged velocity are calculated from the internal inflow boundary and are shown in figure 5.15. As they pass through the vents, each row forms a single jet and the counter-rotating vortices are clearly visible. Due to the local flow field, these vortices are however inclined and do not attach to the wall. The two jets eventually impinge on the leading edge of the wing and form a strong interaction zone in the vicinity of pylon and wing junction. The remaining jet flow then passes over the suction side of the wing, where it remains close to the surface. A small part of the jet flow however, especially fluid passing through the first upstream vents on the left hand side, does not join the counter-rotating vortex pair but rather stays attached to the left hand side of the pylon and eventually passes under the wing.

Mean thermal efficiency is plotted in figure 5.16(a) on the surfaces in the vicinity of the ejector grid. As imposed by boundary conditions, the surface separating plenum

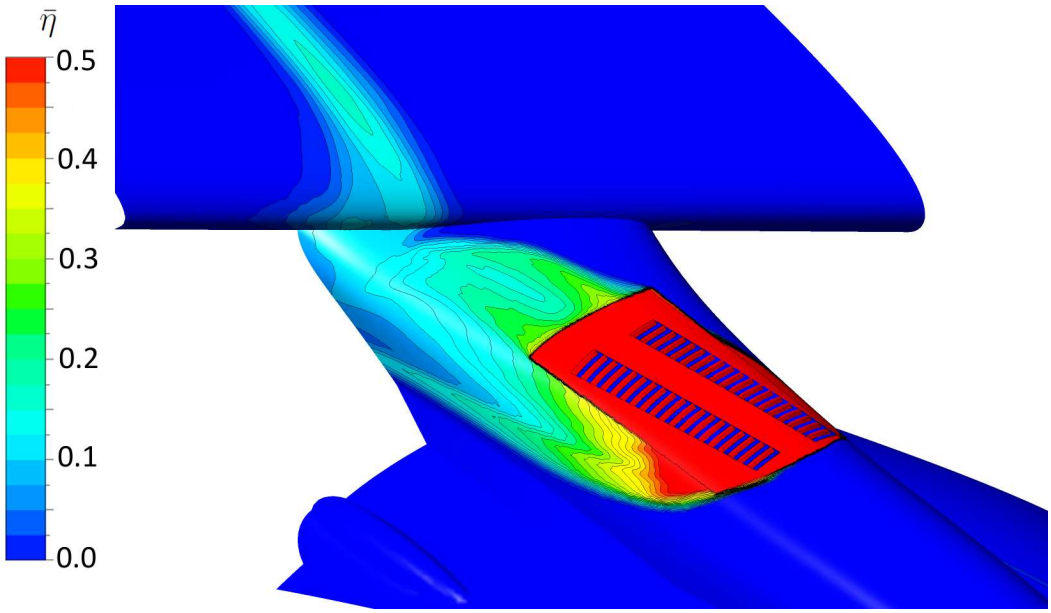

(a) Time-averaged thermal efficiency in the vicinity of ejector

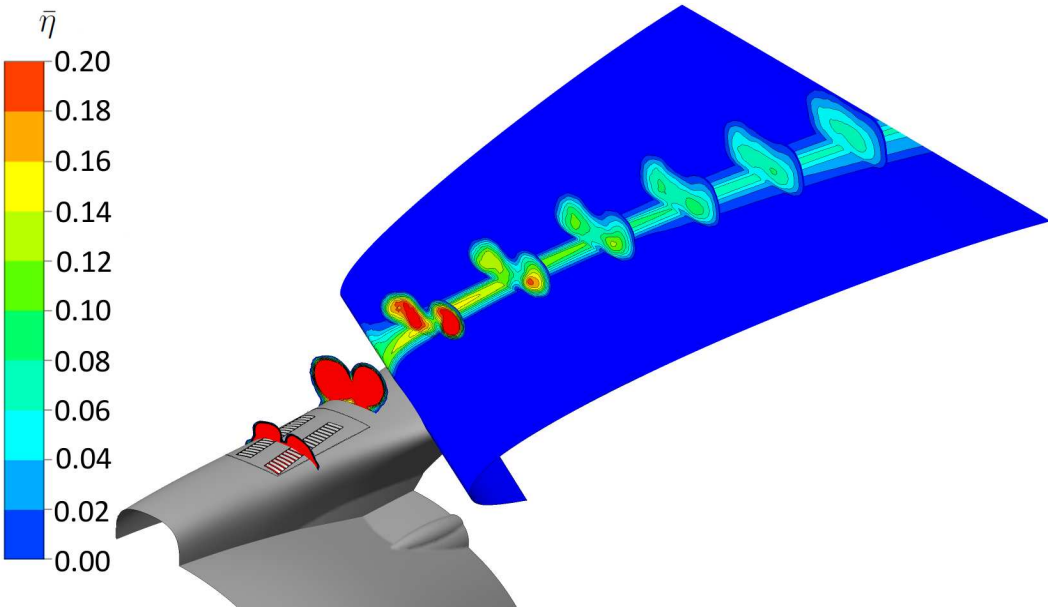

(b) Jet evolution and thermal efficiency on wing

Figure 5.16: Thermal impact of pre-cooler exhaust on pylon and wing

from exterior as well as the vents have a constant efficiency of $\bar{\eta} = 0.5$. In accordance with the development of the jets, two isolated thermal traces appear behind the ventilation grid and extend to the junction of pylon and wing. Due to the local flow however, the thermal trace on the right hand side is forced outboard. In contrast to the other configurations, a strong thermal impact on the outboard side of the pylon is visible as well. This is not only due to the imposed temperature on the plate, which will be discussed in the following paragraph. In addition to this, smaller contour levels

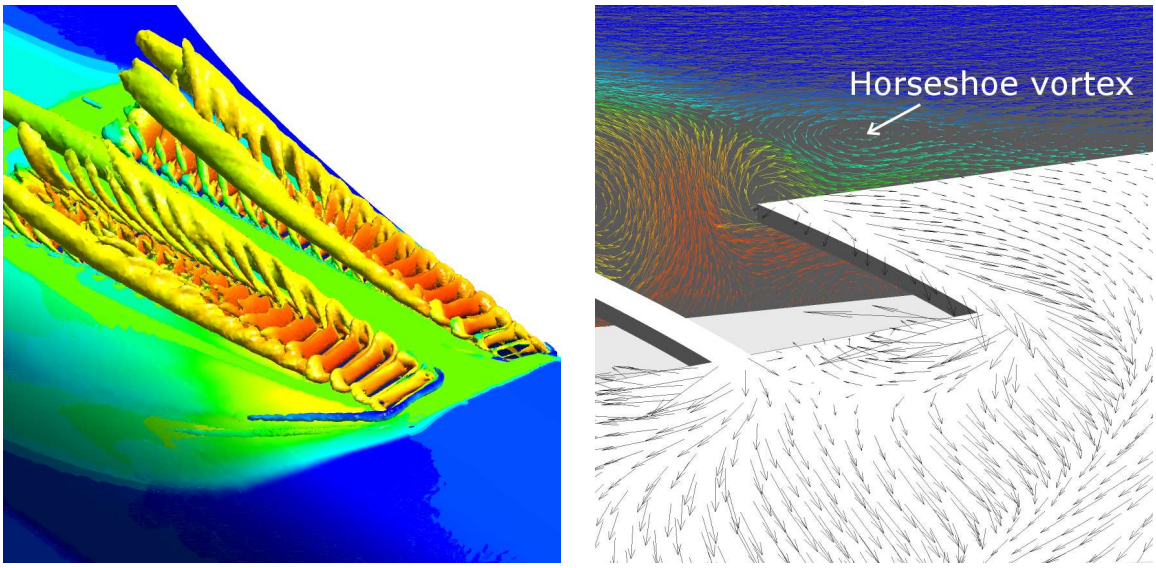

(a) Q-criterion for time-averaged flow field shows counter-rotating vortex pairs and horseshoe vortex for outboard jet

(b) Time-averaged velocity vectors show development of an upstream film of hot fluid located below the horseshoe vortex

Figure 5.17: Details of steady flow topology

of thermal efficiency are presented on the wing and on volume cuts along the jet trajectory in figure 5.16(b). As also visible from the previous illustration, only the jet on the left hand side does impact on the wing surface close to the leading edge. The other jet remains detached from the surface until about 50% of the wing chord included in this simulation. At this point the two thermal cores merge and the trace on the surface enlarges. The non-attachment of the inboard jet is caused by the local flow, which wraps around the right hand side of the pylon and follows the pylon wing junction in outboard direction. It is important to mention that the jet core, in terms of maximal temperature, is not in contact with the wing and only the outer and thus cooler parts of the jet impact on the structure.

The underlying tensor invariant of the Q-criterion can also be computed from the time-averaged velocity field. An isosurface is presented in figure 5.17(a) showing thus the mean vortex topology of the configuration. For each individual vent the counter-rotating pair vortex pair is visible at the lateral edges. They all merge and lead to a single and very strong counter-rotating vortex pair, which is lifted up from the surface. Also clearly visible is the horseshoe vortex for the outboard jet. The temperature contours on this side of the pylon could lead to the assumption that this horseshoe vortex transports hot fluid. Consistently however with the other configurations, this vortex contains mainly cold fluid. In order to find the origin of the thermal side lobe, a time-averaged vector plot is presented in figure 5.17(b), where velocity vectors, colored by temperature, are presented on a plane inside the volume and where vectors of wall shear are shown in black on the surface. Similar to the previous case, where no

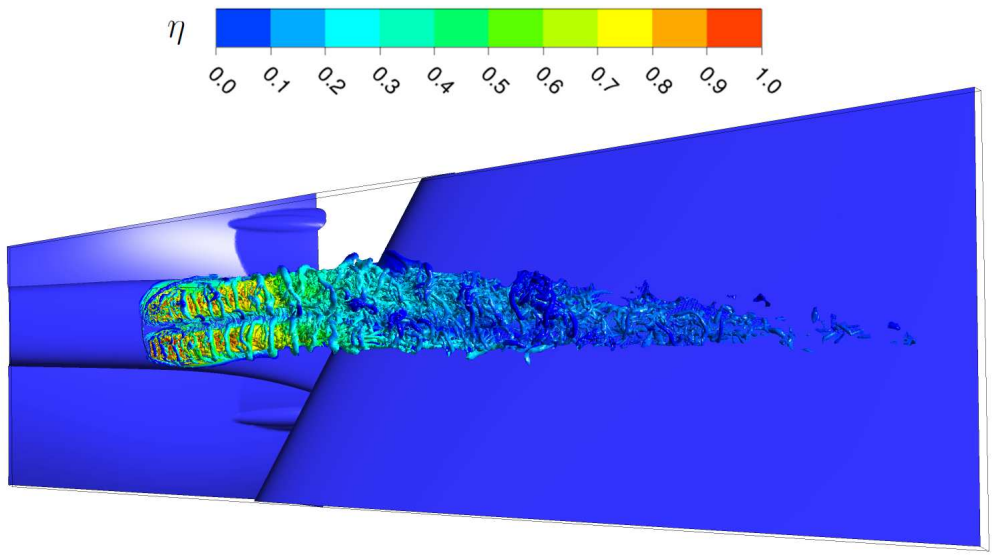

(a) Top view showing alignment with main flow

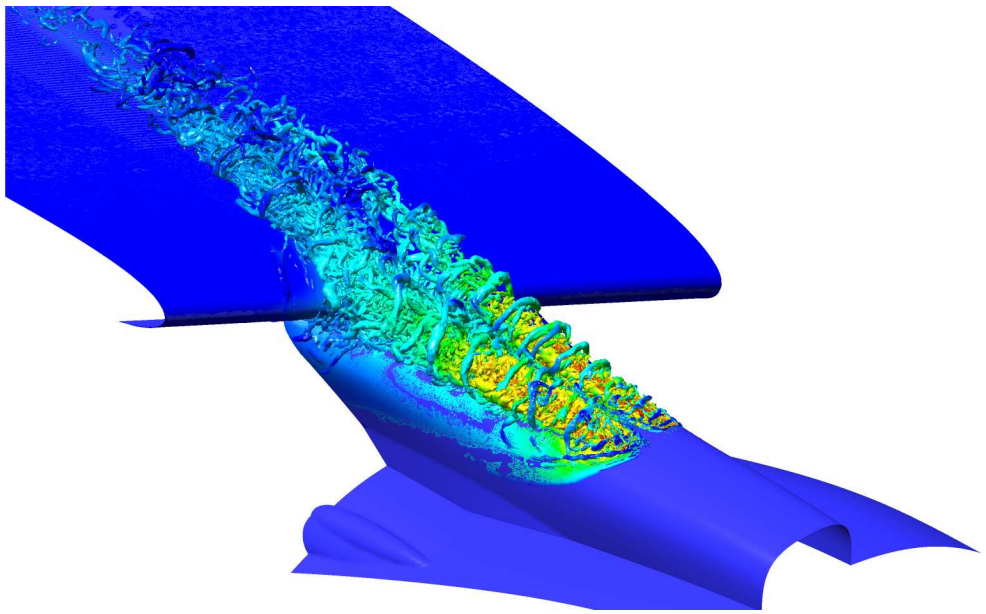

(b) Side view showing jet impact on leading edge of the wing

Figure 5.18: Isosurfaces of Q-criterion at $Q^* = 0.1$

individual supporting flow is provided for the orifices, the mass flow through each vent depends on its location. Especially the first orifices are exposed to the strong cross flow momentum, which forces the jet to wrap also around the *upstream* edge of the first vent. A film of hot fluid is thus present *in front of* the jet with the horseshoe vortex lying above it. This film is then transported to the side and follows the local flow topology as indicated by the wall shear vectors in the same way as the horseshoe vortex. This finally leads to the high temperature distribution on the outboard side of the pylon as visible in figure 5.16(a).

For evaluation of the transient flow, isosurfaces obtained from the Q-criterion are illustrated in figure 5.18(a). In agreement with previous results, the SAS turbulence model allows the resolution of vortices of different size and nature in the jet in cross flow interaction region for this configuration as well. The top view shows the development of two individual jets in alignment with the ventilation grid until the cross flow forces them into the main flow direction. Another view is presented in figure 5.18(b), where the impact of the outboard jet on the leading edge of the wing is clearly visible. From both views the large amount of coherent structures is striking and a flow analysis in terms of turbulent mixing becomes increasingly difficult. From visualization however, two recurring phenomena appear also in this case. Firstly, the already mentioned horseshoe vortex is lying in front of each ventilation row and contains only cross flow fluid. Secondly, archlike vortices develop regularly around both jets already from the upstream edge of the ejector row. In contrast to the other simulations, nearly closed ring vortices form further downstream as the jets do not stay attached to the wall of the pylon. The jets being lifted up, characteristics similar to a free jet become thus more pronounced. The jets develop rather independently even after they impinge on the leading edge. However, a strong zone of interaction can be found below the jet cores at the junction of wing and pylon.

Last but not least attention is turned to the quantification of the transient flow behavior. For this reason ten monitor points, whose locations are given in table B.3 and who are illustrated in figure B.2(b), have been placed inside the jets. Even though the investigation is complicated by the large amount of coherent structures, the passage frequency of the almost ringlike vortices identified in figure 5.18 can be obtained from power spectral densities of the pressure history since vortex cores are associated with local pressure minima. Table 5.5 summarizes the dominant Strouhal numbers, which characterize thus the passage frequency of these structures. There is a noticeable difference between the two jets since the inboard jet exhibits apart from the last point a higher frequency. Furthermore, the outboard jet is characterized by a constant Strouhal number before impacting the leading edge of the wing indicating thus a constant convective velocity. The power spectral densities of points $\mathrm{P_{PC,1}}$ and $\mathrm{P_{PC,2}}$ are additionally plotted in figure 5.19 as they exhibit a different behavior compared to all other points. Clearly, the spectral peak associated to the almost ringlike vortices can be seen at a Strouhal number of $St_D = 0.20$ for the outboard jet and at $St_D = 0.25$ for the inboard jet respectively. In addition, a second high frequency peak at $St_D = 1.17$ for point $\mathrm{P_{PC,1}}$ is striking, which is also obvious for the point $\mathrm{P_{PC,2}}$ even though this amplitude is not as high. Due to its high frequency, this peak has to be attributed to a pressure fluctuation induced by the individual vent.

Returning to the convective Mach number, cross-correlations R_{xy} have been calculated for the Z-velocity components obtained from monitor points that are aligned in streamwise direction. Very similar to the behavior seen in figure 5.11 for the exhaust of the nacelle anti-icing system, global maxima are obtained for all pairs except for the

Table 5.5: Passage frequency of ringlike vortices

Outboard jet	$P_{PC,1}$	$P_{PC,3}$	$P_{PC,5}$	$P_{PC,7}$	$P_{PC,9}$
St_D	0.20	0.20	0.20	0.16	0.22
Inboard jet	$P_{PC,2}$	$P_{PC,4}$	$P_{PC,6}$	$P_{PC,8}$	$P_{PC,10}$
St_D	0.25	0.27	0.22	0.22	0.16

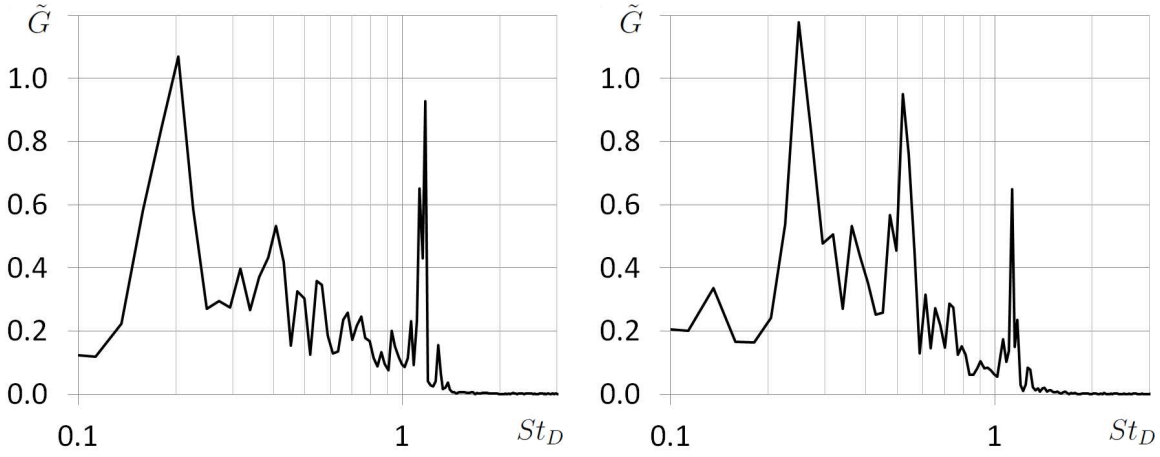

(a) PSD at point $P_{PC,1}$ (b) PSD at point $P_{PC,2}$

Figure 5.19: Power spectral density for pressure history

last one of each jet. Since the last set of points, i.e. $P_{PC,9}$ and $P_{PC,10}$, lie downstream of the impact zone of the jets on the leading edge, the almost ringlike vortices lose their coherent motion. For all other pairs, the convective Mach number can again be obtained with the help of the distance between the monitor points, which is presented in table 5.6. As inferred by the passage frequency, an almost constant convective Mach number for the outboard jet is confirmed. In contrast to this, the convective Mach number for the inboard jet is not homogeneous, which is caused by the local flow topology around the pylon. The non-negligible difference between convective and free stream Mach number highlights once again the need to account for installation effects, which are sufficiently treated with the help of the sequential approach.

Table 5.6: Convective Mach number

Outboard jet	$P_{PC,1} \rightarrow P_{PC,3}$	$P_{PC3} \rightarrow P_{PC,5}$	$P_{PC,5} \rightarrow P_{PC,7}$
$Ma_{\text{conv.}}$	0.36	0.37	0.35
Inboard jet	$P_{PC,2} \rightarrow P_{PC,4}$	$P_{PC,4} \rightarrow P_{PC,6}$	$P_{PC,6} \rightarrow P_{PC,8}$
$Ma_{\text{conv.}}$	0.29	0.40	0.42

In summary, an adapted sequential approach has been introduced enabling the local resolution of turbulence, which is necessary for the correct aerothermal prediction of real aircraft applications comprising multiple hot jets in cross flow. The exhaust of the nacelle anti-icing system, similar to the generic multiple jets in cross flow configuration, has been investigated with the help of the SAS turbulence model and coherent structures have been identified. Even if cross flow Mach number, temperature difference and cross flow Reynolds number are significantly higher for the realistic flight condition considered here, results of the surface temperature distribution behind the orifices compare satisfyingly well with available flight test data. Archlike vortices have been identified as well as their corresponding passage frequency and convective Mach number. No evidence for a global meandering was found but the question arises whether the duration of the numerical simulation is long enough in order to capture such a large-scale and thus low-frequency phenomenon. In a final step, the adapted approach in combination with the SAS turbulence model has been applied to the exhaust of the pre-cooling system. Resolution of turbulent fluctuations is achieved in the jet in cross flow interaction region also for this complex geometry, showing the applicability of the methodology in an industrial design process. The passage frequency of the almost ringlike vortices has been identified at several monitor points as well as their convective Mach number, which highlighted the impact of the local flow topology on the development of the jet. The use of CFD methods provides thus information which was previously inaccessible for this type of flow and which can now complement wind tunnel testing.

Chapter 6

Conclusion and Outlook

Due to the equipment with a wide variety of heat generating systems, the control of the aircraft's thermal environment is crucial for its successful operation. This control is achieved with the help of ventilation, which transports the generated heat outside the aircraft into the external flow. As this introduces hot air exhausts, the problems of additional drag and of heavy-weighted thermal protections arise. The motivation of this work has originated from the deficiency of steady state RANS computations to correctly predict thermal mixing between a hot jet and a cold cross flow, which is frequently encountered at these exhausts. Up to now, the aerothermal design was based only on empirical models deduced from wind tunnel tests of generic configurations. In order to avoid oversizing thermal shields and in order to reduce aerodynamic drag, unsteady CFD techniques in combination with advanced turbulence models were to be investigated for this type of flow.

Numerical strategies were therefore presented which enable the correct aerothermal prediction of flows comprising a single or multiple hot jets in cross flow at high Reynolds numbers. As resolution of turbulent fluctuations is crucial in this context, the capabilities of different Scale-Resolving Simulations were investigated. Due to high cross flow Reynolds numbers, a Direct Numerical Simulation or even a Large Eddy Simulation were out of question. Therefore, the Unsteady RANS simulation based on the SST turbulence model, the Scale-Adaptive Simulation, the Delayed Detached Eddy Simulation and finally the Embedded Large Eddy Simulation were considered. As they are employed in the global domain with the goal to only locally resolve turbulent fluctuations in the jet in cross flow interaction region, they were classified as *integrated* approaches. The first three methodologies offer a *hybrid* approach to resolve turbulence, i.e. no fixed interface between modeled and resolved turbulence exists and transition relies on inherent instabilities of the flow. The latter methodology is characterized as a *zonal* approach with an a priori defined subdomain, where scale-resolution is desired. Contrary to the other simulations, this type of methodology allows the user-specified conversion of modeled turbulence content to resolved structures without the need to rely on inherent instabilities.

Since target applications are exhausts of real air systems on aircraft and since an *integrated* approach would demand excessive computational effort, a *sequential* approach was introduced. This methodology allows coping with the multi-scale problem, i.e. the discrepancy of several orders of magnitude in characteristic length scale of ejector and aircraft (components). It relies on a steady state RANS simulation of the entire domain and a subsequent Scale-Resolving Simulation only inside a small subdomain with fixed boundary conditions obtained from the RANS solution. This still allows taking into account installation effects of the ejector with reduced computational resources compared to the *integrated* approaches, making it well adapted for industrial configurations.

The first main objective consisted in the validation of the proposed turbulence modeling approaches on a generic test case and to investigate the scale-resolvability of the models. This set-up is based on an experimental configuration, which features a hot square jet in cross flow at a high Reynolds number appearing on the suction side of a three-dimensional airfoil. Due to the small momentum ratio, the flow is characterized by an attached jet wake with strong thermal impact on the surface downstream of the orifice. Transient simulations were carried out and results were compared to experimental data. The capability to resolve turbulence fluctuations can be qualified by instantaneous isosurfaces of the Q-criterion. As jets in cross flow are globally unstable for the Reynolds number considered here, the SAS and DDES approach allowed the resolution of turbulent fluctuations in the interaction region as well as the jet wake and very similar coherent structures were resolved in the fluid domain specified for the ELES approach. The deficiency of the URANS simulation was confirmed as only large-scale and non-physical fluctuations were resolved. This directly impacts the resulting surface temperature distribution, which was sufficiently well predicted by SAS, DDES and ELES, whereas the URANS approach yielded a drastically underestimated lateral spreading, highlighting the necessity of proper scale-resolution. Subsequently, first and second order time statistics of the flow field were compared to experimental data with good agreement. Solely the URANS simulation underestimated fluctuating quantities. For the last level of validation, spectral analyses of velocity signals were calculated and results from SAS, DDES and ELES confirmed spectral peaks in the jet wake for a Strouhal number of $St_D = 0.14$. In contrast to this, the URANS approach revealed a dominant frequency in the order of $St_D = 0.095$. The aerothermal prediction of jets in cross flow is thus only possible with a proper scale-resolution, which can, in contrast to the URANS simulation, be achieved by the SAS, DDES and ELES approach.

Subsequently, the influence of the underlying numerical mesh and the choice of the time step size on the SAS computation were evaluated. In addition to the hexahedral mesh, which served for the validation of the different turbulence modeling approaches, a hybrid tetrahedral and a hybrid Cartesian meshing strategy were considered. As sufficient spatial resolution was provided in the jet in cross flow interaction region, turbulent fluctuations were successfully resolved. Validation of the surface temperature

distribution as well as of the flow field pointed out the applicability of these meshing strategies. Due to the better control of transition from cells in the boundary layer to cells in the jet in cross flow region, the hexahedral meshing strategy is favored. With increasing geometrical complexity however, which is encountered for real aircraft applications, the use of hybrid meshing strategies might become inevitable. The impact of the numerical time step size was studied by two additional simulations with double and half the baseline time step. As spatial and temporal resolution correlate, more and finer coherent structures were resolved for decreasing time steps leading to an enhanced aerothermal prediction. This trend persists until the spatial resolution limit of the underlying mesh is reached. For the smallest time step, a slight asymmetry is visible in the surface temperature distribution. This can be attributed to the increased amount of resolved turbulent fluctuations, which necessitates in turn a longer sampling period to obtain better converged time statistics. The last part of the validation study of the generic configuration was devoted to the sequential approach with the SAS turbulence model employed in a subdomain. Boundary conditions for this subdomain were obtained from a steady state computation of the global domain utilizing the SST turbulence model. The subsequent SAS computation carried out in the subdomain exhibited the same scale-resolving capabilities. Differences in surface temperature distribution between integrated and sequential SAS approach were quantified against experimental data, emphasizing the applicability of this methodology.

Due to the achieved depth of validation, the second main objective consisted in the analysis of the steady and transient flow field as well as in the identification of thermal mixing phenomena. The stationary flow topology exhibited a recirculation zone behind the orifice, where hot air accumulated. The well-known horseshoe vortex in front of the jet appeared, being composed however of cold fluid only. Concerning thermal impact, lateral temperature distribution exhibited self-similarity. As the jet posed only a small obstacle to the main flow, archlike vortices developed around the recirculation zone with a characteristic frequency of $St_D = 0.4$. They were advected downstream and had strong influence on thermal mixing as cold cross flow fluid was entrained into the jet core. Shear layer vortices were only predicted by the SAS approach on the upstream side, whereas results from the DDES and the ELES approach showed a quick damping of this phenomenon. Following this, a Proper Orthogonal Decomposition for velocity components and temperature was carried out in a subdomain of the flow. The second mode revealed the existence of a lateral wake meandering behind the orifice with a corresponding characteristic frequency of $St_D = 0.14$, which was already encountered in the validation part. This dynamic had a strong influence on thermal mixing and was non-physically damped in the URANS simulation, leading to the strongly underestimated lateral thermal spreading.

Concerning this generic configuration, two final investigations were carried out. Firstly, the assumptions for thermal boundary conditions were revisited since temperature distribution in the vicinity of the ejector was not entirely satisfying. Due to

the design of the mock-up, the ejector plate separating hot from cold fluid is exposed to internal heat conduction leading to the development of a thermal boundary layer of the cross flow. This fact was taken into account by isothermal boundary conditions with either a constant temperature or a temperature distribution obtained from a steady fluid solid interaction simulation, which greatly enhanced the prediction of the surface temperature in the near field. Even though it would be interesting to investigate the effect of specifying a heat flux, the imposition of a median temperature is a satisfying measure to take heat conduction into account and will be pursued for the complex aircraft configurations. Secondly, the generic configuration was modified by exchanging the ejector grid, thus featuring multiple jets in cross flow (MJICF) and allowing a smooth transition to the industrial configuration. Simulations using the SAS turbulence model were carried out for two different time steps. In the near field each jet developed individually and characteristic coherent structures like the horseshoe vortices and archlike vortices were identified. In the mid field a strong interaction between neighboring jets took place. The satisfying results obtained for the surface temperature distribution emphasizes thus the capability of this model.

The third main objective consisted in the application of the proposed methodology to complex air exhausts on aircraft at realistic flight conditions and eventually in overcoming the difficulties imposed by high Reynolds numbers, increased geometrical complexity and multi-scale problems. Due to the constraints of computational resources and due to the necessity to comply with the current aerodynamic design process, an adapted sequential approach was introduced. Contrary to the original sequential approach, a RANS computation is carried out on the clean aircraft, i.e. neglecting the exhaust geometry, thus allowing the use of existing tools and numerical meshes. The original approach is followed subsequently whereupon the RANS solution is specified as fixed boundary conditions on the external surfaces of the subdomain. As its capability was validated on different meshes as well as on the generic multiple jets in cross flow configuration, only the SAS approach was considered and two complex configurations were investigated.

Firstly, the exhaust of a nacelle anti-icing system (NAIS) on a civil aircraft was regarded since the design of the ejector grid was based on the generic multiple jets in cross flow configuration. A flight phase was chosen which featured a small momentum ratio, a high temperature difference between jet and cross flow as well as a very large cross flow Reynolds number and free stream Mach number compared to the generic configuration. Differences in similarity parameters between real aircraft application and experimental set-up were not avoidable due to the limitations of mock-up and wind tunnel but flight test data was available for validating the proposed simulation strategy also under these conditions. Flow topology and appearing coherent structures were similar to the ones observed for the generic multiple jets in cross flow and numerical and flight test data for mean temperature agreed sufficiently well, which points out the applicability of the adapted sequential approach. The validation of the proposed

methodology now allows incorporating advanced CFD techniques into the aerothermal design process, providing previously inaccessible information and complementing wind tunnel testing. For instance, spectral analysis was carried out in order to quantify the passage frequency and convective Mach number of archlike vortices.

Secondly, the methodology was applied to the exhaust of a pre-cooling system (PCS) of a civil aircraft. Due to the increased complexity of this geometry, a hybrid tetrahedral meshing strategy was employed. An operating condition of the system was chosen, which is critical in terms of temperature difference and momentum ratio. Similar to the previous configuration, a high cross flow Reynolds number and a high free stream Mach number were encountered in this case. Nonetheless, the methodology allowed the resolution of turbulent scales in the jet in cross flow interaction region giving thus confidence on the predicted thermal mixing behavior. In contrast to the other ejector geometries investigated in this work, almost ringlike vortices were observed as the jet is lifted up by the local flow. Due to the strong cross flow forces, a hot fluid film formed in front of the first vent. This film followed the flow topology in the vicinity of the exhaust leading to a strong thermal impact on the side of the pylon. Last but not least, these results were delivered to a new AIRBUS aircraft program, where they serve as a new basis for the aerothermal design process.

Figure 6.1 recapitulates the thesis by illustrating the simulations carried out including their corresponding level of validation and complexity. The successive order of investigations is highlighted once again, which was necessary to cope with such complex configurations as the exhaust of the pre-cooling system by applying advanced computational methods. It became obvious that integrated SRS approaches are capable for small domains comprising one or multiple jets in cross flow. For large domains however, the sequential strategy "from global RANS to local SAS" is more suitable. Due to the satisfying and promising results, new configurations are currently investigated with the help of the proposed methodology, showing the incorporation of advanced CFD techniques into the current industrial process and therefore the impact of this thesis.

In principle, this strategy can be thought applicable to any kind of unsteady flow investigation on aircraft as long as two prerequisites are fulfilled: Firstly, the feedback between the phenomenon to be studied and the preliminary RANS simulation of the aircraft has to be small and secondly, the phenomenon itself has to be inherently unstable. This is indeed the case for most air system outlets. For problems with a strong interaction with the main flow however, the sequential approach will not yield satisfying results anymore as changes in flow topology revealed by unsteady simulations will not be taken into account. Considering for instance the deployment of spoilers, a confined SAS calculation is not the appropriate strategy as the upstream effect of spoilers is rather important. Instead, a global hybrid approach such as SAS or DDES could be applied since transition from modeled to resolved turbulence content is triggered quickly by sharp discontinuities in geometry. For more sensitive problems such

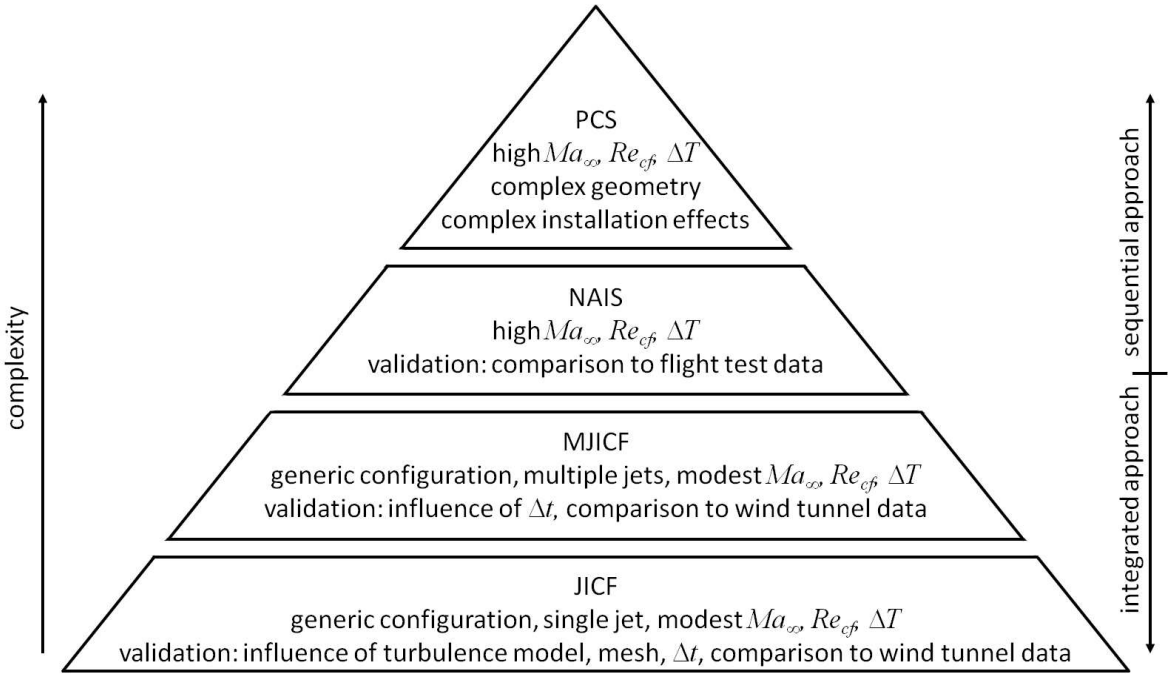

Figure 6.1: Overview of simulations

as flow detachment caused by adverse pressure gradients however, these models are not appropriate as the development of turbulent fluctuations can be insufficient. Zonal approaches like ZDES or ELES should rather be favored, which allow prescribing the resolution of turbulent fluctuations in defined areas. If a global unsteady calculation of the aircraft is inevitable, it would be interesting to investigate the possibility of using two different time steps within a single simulation. On the one hand, a small time step could be employed in the zone of interest in order to allow temporal resolution of turbulent scales. On the other hand, a larger time step could be employed in the rest of the domain in order to save computational costs. The transfer of information between these two zones is however not trivial und would require special attention.

Three aspects should deserve further attention in a future study. The first one concerns the assessment of installation drag that is introduced by every air system outlet but which was left unconsidered in this work. Even though a reciprocal relation between thermal impact on the wall and aerodynamic drag can be expected, additional investigations are needed to quantify this behavior and an optimal relation should be obtained during the aerothermal design process. The second aspect is related to the discrepancy seen in the ELES approach, which showed excellent agreement of the flow field with experimental data but a poor, i.e. overestimated, surface temperature distribution in the near field. This could be associated to the treatment of the boundary layer and especially the conversion of modeled to resolved turbulence content at the

upstream RANS→LES interface needs additional attention. Mesh resolution and time step are only two further impact factors to be studied. The last aspect consists in the investigation of flow dynamics for higher Mach numbers if the entire flight envelope needs to be considered. Local areas of transonic flow can appear in cruise flight and then interact with the jet in cross flow. As of now, the current sequential approach needs modification since it is not capable to handle shock waves across the boundary of the subdomain.

Bibliography

[1] S. Acharya, M. Tyagi, and A. Hoda. Flow and Heat Transfer Predictions for Film Cooling. *Annals of the New York Academy of Science*, 934:110–125, 2001.

[2] S. Acharya, M. Tyagi, A. Hoda, and F. Muldoon. From RANS to DNS: Application to Film Cooling. In *26th National Conference on Fluid Mechanics and Fluid Power*, 1999.

[3] D. Afchain, P. Brousseaud, M. Frugier, and G. Rancarani. La soufflerie F2 du centre du Fauga-Mauzac. Technical Report 1983-139, ONERA, 1983.

[4] L. Albugues. *Analyse éxperimentale et numérique d'un jet débouchant dans un écoulement transverse.* PhD thesis, L'École Nationale Supérieure de l'Aéronautique et de l'Espace, Toulouse, 2005.

[5] J. Andreopoulos. Measurements in a Jet-Pipe Flow Issuing Perpendicularly into a Cross Stream. *Journal of Fluids Engineering*, 104:493–499, 1982.

[6] J. Andreopoulos. Heat Transfer Measurements in a Heated Jet-Pipe Flow Issuing into a Cold Cross Stream. *Physics of Fluid*, 26:3201–3210, 1983.

[7] J. Andreopoulos. On the Structure of Jets in a Crossflow. *Journal of Fluid Mechanics*, 157:163–197, 1985.

[8] J. Andreopoulos and W. Rodi. Experimental Investigation of Jets in a Crossflow. *Journal of Fluid Mechanics*, 138:93–127, 1984.

[9] ANSYS Inc. *ANSYS FLUENT 14.0.* Cannonsburg, PA, 2011.

[10] S. Bagheri, P. Schlatter, P. J. Schmid, and D. S. Henningson. Global Stability of a Jet in Crossflow. *Journal of Fluid Mechanics*, 624:33–44, 2009.

[11] T. J. Barth and D. Jespersen. The Design and Application of Upwind Schemes on Unstructured Meshes. *AIAA Journal*, 1989-0366, 1989.

[12] G. Berkooz, P. Holmes, and J. L. Lumley. The Proper Orthogonal Decomposition in the Analysis of Turbulent Flows. *Annual Review of Fluid Mechanics*, 25:539–575, 1993.

[13] J. N. Blanchard, Y. Brunet, and A. Merlen. Influence of a Counter-Rotating Vortex Pair on the Stability of a Jet in Cross Flow: An Experimental Study by Flow Visualizations. *Experiments in Fluids*, 26:63–74, 1999.

[14] J. E. Broadwell and R. E. Breidenthal. Structure and Mixing of a Transverse Jet in Incompressible Flow. *Journal of Fluid Mechanics*, 148:405–412, 1984.

[15] E. Callaghan and R. Ruggeri. Investigation of the Penetration of an Air Jet Directed Perpendicularly to an Air Stream. Technical Report 1615, National Advisory Committee for Aeronautics, 1948.

[16] E. Callaghan and R. Ruggeri. A General Correlation of Temperature Profiles Downstream of a Heated-Air Jet Directed Perpendicular to an Air Stream. Technical Report 2466, National Advisory Committee for Aeronautics, 1951.

[17] G. M. Carlomagno, F. G. Nese, G. Cardone, and T. Astarita. Thermo-Fluid-Dynamics of a Complex Fluid Flow. *Journal of Infrared Physics and Technology*, 46:31–39, 2004.

[18] S. Coelho and J. Hunt. The Dynamics of the Near Field of Strong Jets in Crossflows. *Journal of Fluid Mechanics*, 200:95–120, 1989.

[19] L. Cortelezzi and A. R. Karagozian. On the Formation of the Counter-Rotating Vortex Pair in Transverse Jets. *Journal of Fluid Mechanics*, 446:347–373, 2001.

[20] Z. Dai, S.-Y. Hsieh, and H. Mongia. Modeling of Jets in Cross Flow with RANS and LES, Part 1: Momentum Transport for Low R w/ RANS. *AIAA Journal*, 2005-0306, 2005.

[21] I. Danaila, J. Dusek, and F. Anselmet. Coherent Structures in a Round, Spatially Evolving, Unforced, Homogeneous Jet at low Reynolds Numbers. *Physics of Fluid*, 9:3323–3342, 1997.

[22] S. Deck. Recent Improvements in the Zonal Detached Eddy Simulation (ZDES) Formulation. *Theoretical and Computational Fluid Dynamics*, 2011.

[23] A. O. Demuren. Numerical Calculations of Steady Three-Dimensional Turbulent Jets in Cross Flow. *Computer Methods in Applied Mechanics and Engineering*, 37:309–328, 1983.

[24] A. O. Demuren. Modeling Turbulent Jets in Crossflow. In *Encyclopedia of Fluid Mechanics, Vol. 2*, pages 430–465. Gulf Publishing Co., 1986.

[25] A. O. Demuren. Characteristics of 3D Turbulent Jets in Crossflow. Technical Report 104337, NASA, 1991.

[26] J. Denev, J. Fröhlich, and H. Bockhorn. Direct Numerical Simulation of a Round Jet into a Crossflow - Analysis and Required Resources. In *High Performance Computing in Science and Engineering '07*. Springer Verlag, 2007.

[27] J. Denev, J. Fröhlich, and H. Bockhorn. Direct Numerical Simulation of a Transitional Jet in Crossflow with Mixing and Chemical Reaction. In R. Friedrich, N. Adams, J. Eaton, J. Humphrey, N. Kasagi, and M. Leschziner, editors, *Proceedings of the 5th Int. Symp. on Turbulence and Shear Flow Phenomena*, pages 1243–1248, 2007.

[28] J. Denev, J. Fröhlich, and H. Bockhorn. Two-Point Correlations of a Round Jet into a Crossflow - Results from a Direct Numerical Simulation. In *High Performance Computing in Science and Engineering '08*. Springer Verlag, 2008.

[29] Y. Egorov, F. Menter, R. Lechner, and D. Cokljat. The Scale-Adaptive Simulation Method for Unsteady Turbulent Flow Predictions. Part 2: Application to Complex Flows. *Flow, Turbulence and Combustion*, 85(1):139–165, 2010.

[30] V. L. Erikson. Film Cooling Effectiveness and Heat Transfer with Injection Through Holes. Technical Report 72991, NASA, 1971.

[31] A. Favre. Equations des gaz turbulents compressibles, part 1: formes générales. *Journal de Mécanique*, 4:361–390, 1965.

[32] A. Favre. Equations des gaz turbulents compressibles, part 2: méthode des vitesses moyennes; methode des vitesses moyennes pondérées par la masse volumique. *Journal de Mécanique*, 4:391–421, 1965.

[33] R. Fearn and R. Weston. Induced velocity field of a jet in a crossflow. Technical Report 1087, NASA, 1978.

[34] T. F. Fric and A. Roshko. Vortical Structure in the Wake of a Transverse Jet. *Journal of Fluid Mechanics*, 279:1–47, 1994.

[35] J. Fröhlich, J. A. Denev, and H. Bockhorn. Large Eddy Simulation of a Jet in Crossflow. In *ECCOMAS 2004 Proceedings*, 2004.

[36] J. Fröhlich and D. von Terzi. Hybrid LES/RANS Methods for the Simulation of Turbulent Flows. *Progress in Aerospace Sciences*, 44:349–347, 2008.

[37] G. H. Golub and C. F. van Loan. *Matrix Computations*. John Hopkins University Press, Baltimore, 3rd edition, 1996.

[38] S. Gopalan, B. Abraham, and J. Katz. The Structure of a Jet in Cross Flow at Low Velocity Ratios. *Physics of Fluids*, 16:2067–2087, 2004.

[39] B. Haven and M. Kurosaka. Kidney and Anti-Kidney Vortices in Crossflow Jets. *Journal of Fluid Mechanics*, 352:27–64, 1997.

[40] A. T. Hsu, G. He, and Y. Guo. Unsteady Simulation of Jet in Crossflow. *International Journal of Computational Fluid Dynamics*, 14:41–53, 2000.

[41] J. Hunt, A. A. Wray, and P. Moin. Eddies, stream, and convergence zones in turbulent flows. Technical Report CTR-S88, Center for Turbulence Research, 1988.

[42] I. Iourokina and S. Lele. Towards Large Eddy Simulation of Film-Cooling Flows on a Model Turbine Blade Leading Edge. *AIAA Journal*, 2005-0670, 2005.

[43] E. M. Ivanova, M. Di Domenico, B. E. Noll, and M. Aigner. Unsteady Simulations of Flow Field and Scalar Mixing in Transverse Jets. In *Proceedings of ASME Turbo Expo 2009: Power for Land, Sea and Air*, volume GT2009-59147, 2009.

[44] E. M. Ivanova, B. E. Noll, and M. Aigner. Unsteady Simulations of Turbulent Mixing in Jet in Crossflow. *AIAA Journal*, 2010-4724, 2010.

[45] E. M. Ivanova, B. E. Noll, and M. Aigner. Computational Modeling of Turbulent Mixing of a Transverse Jet. *Journal of Engineering for Gas Turbines and Power*, 133, 2011.

[46] Jouhaud, J-C. and Gicquel, L. and Enaux, B. and Estève, M-J. Large-Eddy-Simulation Modeling for Aerothermal Predictions Behind a Jet in Crossflow. *AIAA Journal*, 2007-0045, 2007.

[47] E. Kali and S. Benmansour. Large Eddy Simulations of a Rectangular Turbulent Jet in Crossflow. *Journal of Applied Sciences*, 9:3836–3842, 2009.

[48] Y. Kamotani and I. Greber. Experiments on confined turbulent jets in cross flow. Technical Report CR-2392, NASA, 1974.

[49] R. M. Kelso, T. T. Lim, and A. E. Perry. An Experimental Study of Round Jet in Cross-Flows. *Journal of Fluid Mechanics*, 306:111–144, 1995.

[50] R. M. Kelso and A. J. Smits. Horseshoe Vortex System Resulting from the Interaction of a Laminar Boundary Layer and a Transverse Jet. *Physics of Fluid*, 7:153–158, 1995.

[51] W. Kim and S. Menon. A New Dynamic One-Equation Subgrid-Scale Model for Large Eddy Simulations. *AIAA Journal*, 1995-0356, 1995.

[52] D. Knight, G. Zhou, N. Okong'o, and V. Shukla. Compressible Large Eddy Simulation Using Unstructured Grids. *AIAA Journal*, 1998-0535, 1998.

[53] K. Komuro and T. Tsukiji. Study on Vortical Structure of a Transverse Jet Using CFD. In *Proceedings of 10th International Conference on Fluid Control, Measurements, and Visualization*, 2009.

[54] B. P. Leonard. The ULTIMATE Conservative Difference Scheme Applied to Unsteady One-Dimensional Advection. *Computer Methods in Applied Mechanics and Engineering*, 88:17–74, 1991.

[55] Z. Li, S. Murugappan, E. Gutmark, and L. Vallet. Numerical Simulation and Experiments of Jets in Cross Flow. *AIAA Journal*, 2006-0307, 2006.

[56] T. Lim, T. New, and S. Luo. On the Development of Large-Scale Structures of a Jet Normal to a Cross Flow. *Physics of Fluid*, 13:770–775, 2001.

[57] T. Lischer. *Modifikation von statistischen Turbulenzmodellen zur verbesserten Beschreibung des turbulenten Geschwindigkeits- und Mischungsfeldes bei der Querstrahleinmischung*. PhD thesis, Karlsruher Institute für Technologie, Karlsruhe, 2009.

[58] R. J. Margason. Fifty Years of Jet in Cross Flow Research. In *AGARD, Computational and Experimental Assessment of Jets in Cross Flow*, 1993.

[59] Y. Marzouk, A. Ghoniem, and D. Wee. Lagrangian Simulation of a Jet-in-Crossflow at a Finite Reynolds Number. *AIAA Journal*, 2005-0291, 2005.

[60] Y. Marzouk, A. Ghoniem, and D. Wee. Simulations of High Reynolds Number Transverse Jets and Analysis of the Underlying Vortical Structures. *AIAA Journal*, 2005-0308, 2005.

[61] S. Megerian and A. Karagozian. Evolution of Shear Layer Instabilities in the Transverse Jet. *AIAA Journal*, 2005-0142, 2005.

[62] F. Menter. Two-Equation Eddy-Viscosity Turbulence Models for Engineering Applications. *AIAA Journal*, 32(8):1598–1605, 1994.

[63] F. Menter and Y. Egorov. The Scale-Adaptive Simulation Method for Unsteady Turbulent Flow Predictions. Part 1: Theory and Model Description. *Flow, Turbulence and Combustion*, 85(1):113–138, 2010.

[64] F. Menter, P. Galpin, T. Esch, and M. Kuntz. CFD Simulations of Aerodynamic Flows with a Pressure-Based Method. In *Proceedings of 24th International Congress of the Aeronautical Sciences*, 2004.

[65] F. Menter and M. Kuntz. Adaption of Eddy-Viscosity Turbulence Models to Unsteady Separated Flows Behind Vehicles. In *Proceedings of Aerodynamics of Heavy Vehicles: Trucks, Buses, and Trains*, 2004.

[66] F. Menter, M. Kuntz, and R. Langtry. Ten Years of Industrial Experience with the SST Turbulence Model. In *Proceedings of 4th Symposium on Turbulence, Heat And Mass Transfer*, 2003.

[67] B. Morton. The Generation and Decay of Vorticity. *Geophysical and Astrophysical Fluid Dynamics*, 28:277–308, 1984.

[68] S. Muppidi and K. Mahesh. Study of Trajectories of Jets in Crossflow Using Direct Numerical Simulation. *Journal of Fluid Mechanics*, 530:81–100, 2005.

[69] S. Muppidi and K. Mahesh. A Two-Dimensional Model Problem to Explain CVP Formation in a Transverse Jet. *Physics of Fluids*, 18, 2006.

[70] S. Narayanan, P. Barooah, and J. Cohen. Experimental Study of the Coherent Structure Dynamics and Control of an Isolated Jet in Cross Flow. *AIAA Journal*, 2002-0272, 2002.

[71] ONERA DSNA. *elsA*. Châtillon, France, 2011.

[72] U. Piomelli, P. Moin, and J. Ferziger. Model Consistency in Large Eddy Simulation of Turbulent Channel Flows. *Physics of Fluid*, 31:1884–1892, 1988.

[73] S. B. Pope. *Turbulent Flows*. Cambridge University Press, 1st edition, 2000.

[74] B. Pratte and W. Baines. Profiles of the Round Turbulent Jet in a Crossflow. *Journal of the Hydraulics Division,*, 93:53–64, 1967.

[75] J. W. Ramsey and R. Goldstein. Interaction of a Heated Jet With a Deflecting Stream. *Journal of Heat Transfer*, 93:365–372, 1971.

[76] K. Roth, R. Fearn, and S. Thakur. A Numerical Study of the Contrarotating Vortex Pair Associated with a Jet in a Crossflow. *AIAA Journal*, 1989-0448, 1989.

[77] K. Roth, R. Fearn, and S. Thakur. Evaluation of a Navier-Stokes Prediction of a Jet in a Crossflow. *Journal of Aircraft*, 29:185–193, 1992.

[78] J. Rotta. Statistische Theorie nichthomogener Turbulenz. *Zeitschrift für Physik*, 129:547–572, 1951.

[79] J. Rotta. *Turbulente Strömungen*. Teubner Verlag, 1972.

[80] R. Ruggeri, E. Callaghan, and D. Bowden. Penetration of Air Jets Issuing from Circular, Square, and Elliptical Orifices Directed Perpendicular to an Air Stream. Technical Report 2019, National Advisory Committee for Aeronautics, 1950.

[81] D. B. Rusch. *Turbulence Model Validation for Fire Simulation by CFD and Experimental Investigation of a Hot Jet in Crossflow*. PhD thesis, Eidgenössische Technische Hochschule Zürich, Zürich, 2005.

[82] P. Sagaut and S. Deck. Large Eddy Simulation for Aerodynamics: Status and Perspectives. *Philosophical Transactions of the Royal Society A*, 367:2849–2860, 2009.

[83] M. Salewski, D. Stankovic, L. Fuchs, and E. Gutmark. Coherent Structures in Circular and Non-Circular Jets in Crossflow. *AIAA Journal*, 2006-0907, 2006.

[84] A. Sau, T. Sheu, R. Hwang, and W. Yang. Three-Dimensional Simulation of Square Jets in Cross-Flows. *Physical Review E*, 69, 2004.

[85] A. Sau, T. Sheu, S. Tsai, R. Hwang, and T. Chiang. Structural Development of Vortical Flows around a Square Jet in Cross-Flow. *Proceedings of the Royal Society A*, 460:3339–3368, 2004.

[86] J. U. Schlüter and T. Schönfeld. LES of Jets in Cross Flow and its Application to a Gas Turbine Burner. *Flow, Turbulence and Combustion*, 65(2):177–203, 2000.

[87] E. Sergent. *Vers une méthodologie de couplage entre la Simulation des Grandes Échelles et les modèles statistiques*. PhD thesis, L'École Centrale de Lyon, Lyon, 2001.

[88] M. Shur, P. Spalart, M. Strelets, and A. Travin. A Hybrid RANS-LES Approach with Delayed-DES and Wall-Modelled LES Capabilities. *International Journal of Heat and Fluid Flow*, 29:1638–1649, 2008.

[89] J. Smagorinksy. General Circulation Experiments with the Primitive Equations. I. The Basic Experiment. *Monthly Weather Review*, 91:99–164, 1963.

[90] S. H. Smith and M. G. Mungal. Mixing, Structure, and Scaling of the Jet in Crossflow. *Journal of Fluid Mechanics*, 357:83–122, 1998.

[91] P. Spalart. Strategies for Turbulence Modelling and Simulations. *International Journal of Heat and Fluid Flow*, 21:252–263, 2000.

[92] P. Spalart, W.-H. Jou, M. Strelets, and S. Allmaras. Comments on the Feasibility of LES for Wings and on the Hybrid RANS/LES Approach. In *Proceedings of the First AFOSR International Conference on DNS/LES*, 1997.

[93] M. Strelets. Detached Eddy Simulation of Massively Separated Flows. *AIAA Journal*, 2001-0879, 2001.

[94] L. K. Su, D. Han, R. Miraflor, and M. G. Mungal. Measurements of Scalar and Velocity Fields in Turbulent Crossflowing Jets with Low Velocity Ratios. *AIAA Journal*, 2000-0815, 2000.

[95] L. K. Su and M. G. Mungal. Mixing in Crossflowing Jets: Turbulence Quantities. *AIAA Journal*, 2005-0305, 2005.

[96] Y. Sugiyama and Y. Usami. Experiments on the Flow in and Around Jets Directed Normal to a Cross Flow. *Bulletin of The Japan Society of Mechanical Engineers*, 22(174):1736–1745, 1979.

[97] TOP500 Project. Supercomputer Sites. *http://i.top500.org/system/177415*, June 2012.

[98] A. Travin, M. Shur, P. Spalart, and M. Strelets. On URANS solutions with LES-like Behaviour. In *ECCOMAS 2004 Proceedings*, 2004.

[99] M. Tyagi. *Large Eddy Simulations of Complex Turbulent Flows*. PhD thesis, Louisiana State University, 2009.

[100] J. van Doormaal and G. D. Raithby. Enhancements of the SIMPLE Method for Predicting Incompressible Fluid Flows. *Numerical Heat Transfer*, 7:701–707, 1984.

[101] P. Welch. The Use of Fast Fourier Transform for the Estimation of Power Spectra: A Method Based on Time Averaging over Short, Modified Periodograms. *IEEE Transactions on Audio and Electroacoustics*, 15(2):70–73, 1967.

[102] R. Weston and F. Thames. Properties of Aspect Ratio-4.0 Rectangular Jets in a Subsonic Crossflow. *Journal of Aircraft*, 16:701–707, 1978.

[103] W. Wienken, S. J., and A. Keller. A Method to Predict Cavitation Inception Using Large-Eddy Simulation and its Application to the Flow past a Square Cylinder. *Journal of Fluids Engineering*, 128:316–325, 2006.

[104] D. Wilcox. *Turbulence Modeling for CFD*. D C W Industries, 3rd edition, 2006.

[105] J. Williams and N. Wood. Aerodynamic Interference Effects with Jet Lift Schemes on VSTOL Aircraft at Forward Speeds. *AGARD, Aerodynamic of Power Plant Installation*, 1966.

[106] L. L. Yuan, R. L. Street, and J. H. Ferziger. Large-Eddy Simulations of a Round Jet in Crossflow. *Journal of Fluid Mechanics*, 379:71–104, 1999.

[107] J. Ziefle and L. Kleiser. Large-Eddy Simulation of a Round Jet in Crossflow. *AIAA Journal*, 2006-3370, 2006.

Appendix A

Turbulence Model Constants

Constants are given here for the turbulence models employed throughout this work. Recurring constants are not listed repeatedly and are identical to those of the SST model. For all simulations, the turbulent Prandtl number is assumed to have a constant value of

$$Pr_t = 0.85. \tag{A.1}$$

SST Turbulence Model

$$\beta^* = 0.09 \tag{A.2}$$

$$a_1 = 0.31 \tag{A.3}$$

As the SST model is based on a blending of a $k-\varepsilon$ and a $k-\omega$ turbulence model, the model constants α, β, σ_k and σ_ω are blended as well via $\phi = \phi_1 F_1 + \phi_2 (1 - F_1)$.

$$\alpha_1 = \frac{5}{9}, \quad \alpha_2 = 0.44 \tag{A.4}$$

$$\beta_1 = \frac{3}{40}, \quad \beta_2 = 0.0828 \tag{A.5}$$

$$\sigma_{k1} = 0.85, \quad \sigma_{k2} = 1 \tag{A.6}$$

$$\sigma_{\omega 1} = 0.5, \quad \sigma_{\omega 2} = 0.856 \tag{A.7}$$

The blending functions F_1 and F_2 are defined as:

$$F_1 = \tanh\left\{\left\{\min\left[\max\left(\frac{\sqrt{k}}{\beta^*\omega y}, \frac{500\nu}{y^2\omega}\right), \frac{4\sigma_{\omega 2}k}{CD_{k\omega}y^2}\right]\right\}^4\right\} \tag{A.8}$$

$$\text{with } CD_{k\omega} = \max\left(2\rho\sigma_{\omega 2}\frac{1}{\omega}\frac{\partial k}{\partial x_i}\frac{\partial \omega}{\partial x_i}, 10^{-10}\right) \tag{A.9}$$

$$F_2 = \tanh\left[\left[\max\left(\frac{2\sqrt{k}}{\beta^*\omega y}, \frac{500\nu}{y^2\omega}\right)\right]^2\right] \tag{A.10}$$

Scale-Adaptive Simulation

$$\kappa = 0.41 \tag{A.11}$$
$$\sigma_\Phi = \frac{2}{3} \tag{A.12}$$
$$\zeta_2 = 1.47 \tag{A.13}$$
$$C_{SAS} = 2.0 \tag{A.14}$$
$$\tag{A.15}$$

Delayed Detached Eddy Simulation

$$C_{DES} = 0.61 \tag{A.16}$$

The model constant C_k is evaluated dynamically according to [51].

Embedded Large Eddy Simulation

$$A = 25 \tag{A.17}$$
$$C_S = 0.1 \tag{A.18}$$
$$C_w = 0.15 \tag{A.19}$$

Appendix B

Complementing Results

Origin and orientation of coordinate systems are presented in figure B.1. The coordinate system of the generic configuration is identical for both the single and the multiple ejector case. All geometric information is non-dimensional with respect to a characteristic length D of the jet. This length is calculated individually for every case as the square root of the largest ejector surface. Tables B.1, B.2 and B.3 give information about the location of the monitor points used for spectral analysis. As simple coordinates are not as illustrative for the complex configurations, the monitor points are presented in figure B.2 in combination with the Q-criterion in order show their position in the jet wake.

Summarized in table B.5 are the additional contour plots for validation of the generic single ejector test case, which are presented here. Contour plots on the symmetry plane $Y/D = 0$ for mean velocity components $\overline{U}/U_\infty$ and $\overline{W}/U_\infty$ are presented in figures B.3 and B.4. Subsequently, second order time statistics are plotted on the same surface in figures B.5, B.6 and B.7 for the quantities $\sqrt{\overline{u'^2}}/U_\infty$, $\sqrt{\overline{v'^2}}/U_\infty$ and $\sqrt{\overline{w'^2}}/U_\infty$ respectively. Contour plots on a lateral plane at $X/D = 1$ are shown for mean velocity components $\overline{U}/U_\infty$, $\overline{V}/U_\infty$ and $\overline{W}/U_\infty$ in figures B.8, B.9 and B.10, followed by the corresponding fluctuation quantities $\sqrt{\overline{u'^2}}/U_\infty$, $\sqrt{\overline{v'^2}}/U_\infty$ and $\sqrt{\overline{w'^2}}/U_\infty$ in figures B.11, B.12 and B.13. Finally, the mean velocity components $\overline{U}/U_\infty$, $\overline{V}/U_\infty$ and $\overline{W}/U_\infty$ are plotted on a second but one-sided ($Y/D < 0$) lateral plane at $X/D = 7/3$ in figures B.14, B.15 and B.16. The nomenclature corresponds to the one utilized in chapter 4 and is given once again in table B.4.

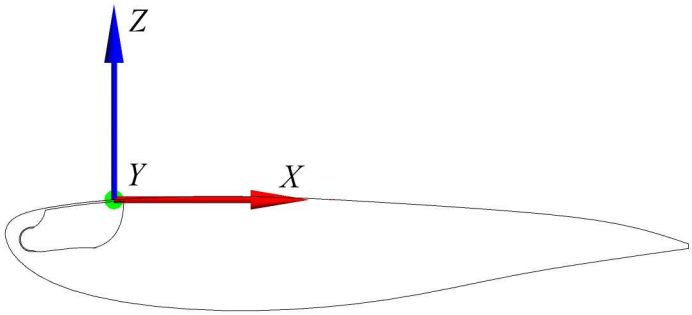

(a) Generic test case

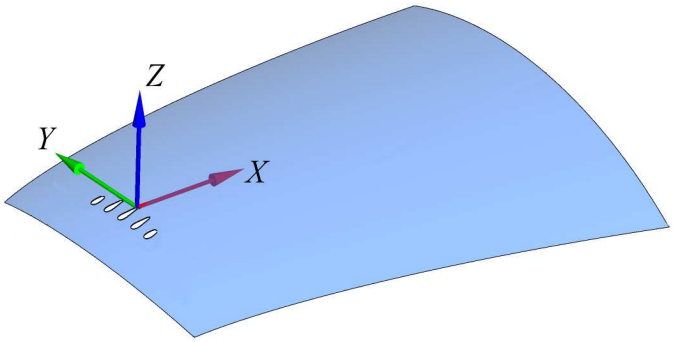

(b) Exhaust of nacelle anti-icing system

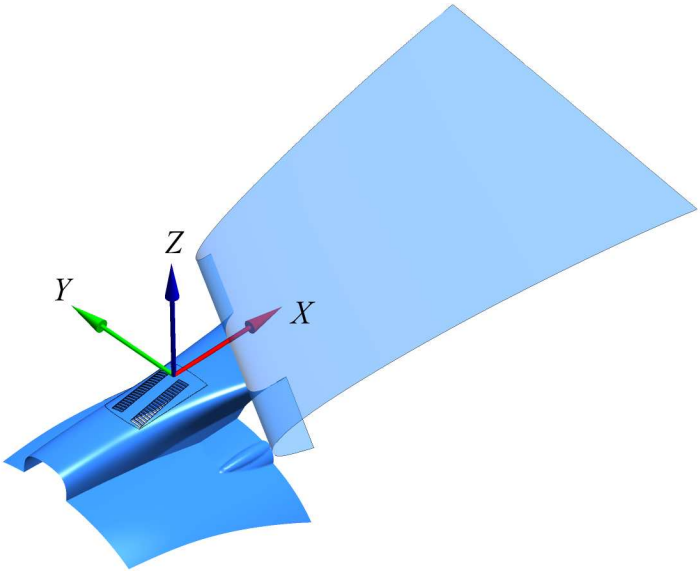

(c) Exhaust of pre-cooling system

Figure B.1: Coordinate systems

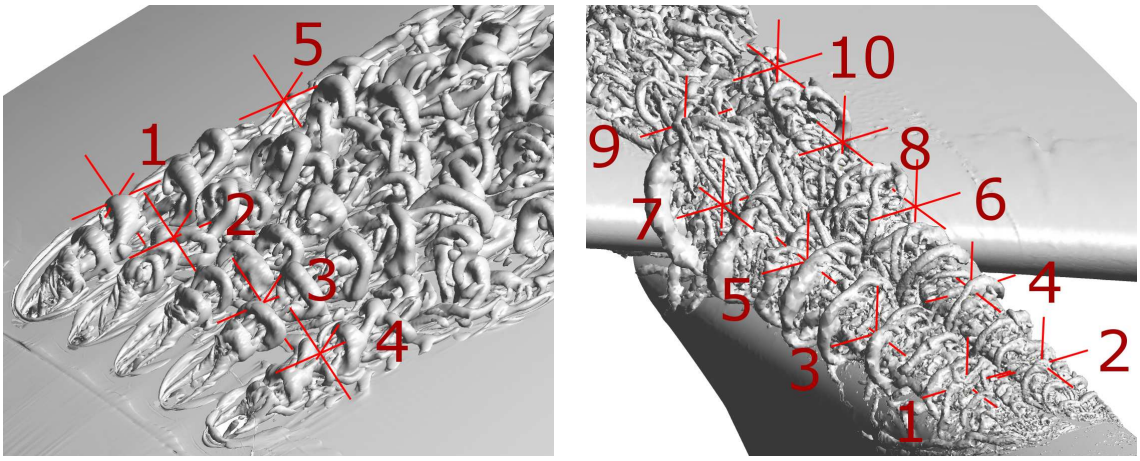

(a) Exhaust of nacelle anti-icing system, points $P_{NAI,*}$

(b) Exhaust of pre-cooling system, points $P_{PC,*}$

Figure B.2: Location of monitor points in jet wake

Table B.1: Location of monitor points for the generic configuration

	X/D	Y/D	Z/D
$P_{JICF,1}$	1.0	0.00	0.50
$P_{JICF,2}$	1.0	0.27	0.50
$P_{JICF,3}$	1.0	0.80	0.50
$P_{JICF,4}$	0.5	0.00	0.13
$P_{JICF,5}$	1.0	0.00	0.16
$P_{JICF,6}$	2.00	0.0	1.10
$P_{JICF,7}$	3.00	0.0	1.10
$P_{JICF,8}$	-0.97	0.0	-0.1
$P_{MJICF,1}$	-1.85	0.00	-0.21
$P_{MJICF,2}$	-1.85	1.60	-0.21
$P_{MJICF,3}$	-1.85	2.90	-0.21
$P_{MJICF,4}$	1.55	0.00	0.96
$P_{MJICF,5}$	1.55	1.60	0.96
$P_{MJICF,6}$	1.55	2.90	0.96
$P_{MJICF,7}$	1.55	0.00	0.16
$P_{MJICF,8}$	1.55	1.60	0.16
$P_{MJICF,9}$	1.55	2.90	0.16
$P_{MJICF,10}$	3.15	0.00	0.22
$P_{MJICF,11}$	3.15	1.60	0.22
$P_{MJICF,12}$	3.15	2.90	0.22

Table B.2: Location of monitor points for the exhaust of nacelle anti-icing system

	X/D	Y/D	Z/D
$P_{NAI,1}$	1.40	4.40	1.05
$P_{NAI,2}$	1.38	2.00	1.18
$P_{NAI,3}$	1.38	-1.57	1.13
$P_{NAI,4}$	1.35	-3.95	0.92
$P_{NAI,5}$	6.85	4.49	1.75

Table B.3: Location of monitor points for the exhaust of pre-cooling system

	X/D	Y/D	Z/D
$P_{PC,1}$	400	166	-18
$P_{PC,2}$	400	161	-18
$P_{PC,3}$	407	169	-17
$P_{PC,4}$	407	162	-16
$P_{PC,5}$	414	169	-15
$P_{PC,6}$	414	161	-14
$P_{PC,7}$	421	171	-14
$P_{PC,8}$	421	162	-12
$P_{PC,9}$	429	162	-10
$P_{PC,10}$	429	169	-12

Table B.4: Nomenclature of the simulations carried out for validation

	Turbulence model	Meshing strategy	Numerical time step
Case 1	SAS	hexahedral	Δt
Case 2	DDES	hexahedral	Δt
Case 3	ELES	hexahedral	Δt
Case 4	URANS	hexahedral	Δt
Case 5	SAS	hybrid tetrahedral	Δt
Case 6	SAS	hybrid Cartesian	Δt
Case 7	SAS	hexahedral	$0.5\Delta t$
Case 8	SAS	hexahedral	$2\Delta t$

Table B.5: Overview of complementing contour plots

Figure	Plane	Quantity
B.3	$Y/D = 0$	$\overline{U}/U_\infty$
B.4	$Y/D = 0$	$\overline{W}/U_\infty$
B.5	$Y/D = 0$	$\sqrt{\overline{u'^2}}/U_\infty$
B.6	$Y/D = 0$	$\sqrt{\overline{v'^2}}/U_\infty$
B.7	$Y/D = 0$	$\sqrt{\overline{w'^2}}/U_\infty$
B.8	$X/D = 1$	$\overline{U}/U_\infty$
B.9	$X/D = 1$	$\overline{V}/U_\infty$
B.10	$X/D = 1$	$\overline{W}/U_\infty$
B.11	$X/D = 1$	$\sqrt{\overline{u'^2}}/U_\infty$
B.12	$X/D = 1$	$\sqrt{\overline{v'^2}}/U_\infty$
B.13	$X/D = 1$	$\sqrt{\overline{w'^2}}/U_\infty$
B.14	$X/D = 7/3$	$\overline{U}/U_\infty$
B.15	$X/D = 7/3$	$\overline{V}/U_\infty$
B.16	$X/D = 7/3$	$\overline{W}/U_\infty$

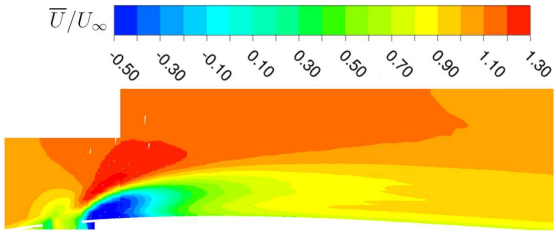

(a) Experiment

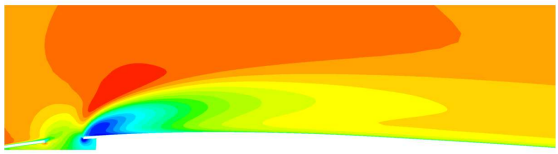

(b) Case 1

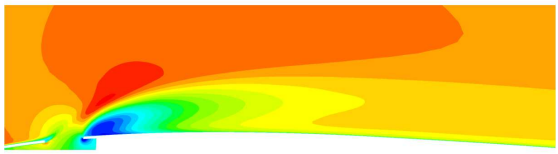

(c) Case 2

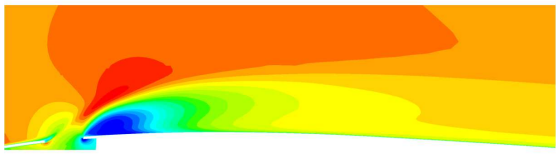

(d) Case 3

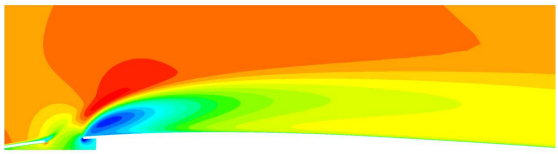

(e) Case 4

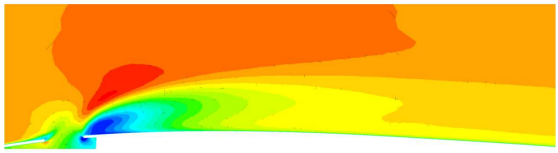

(f) Case 5

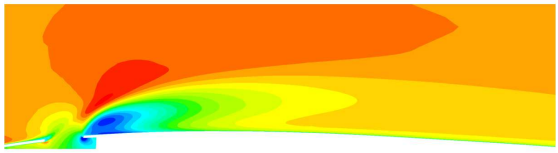

(g) Case 6

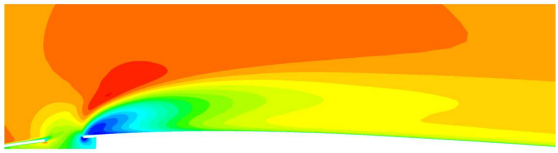

(h) Case 7

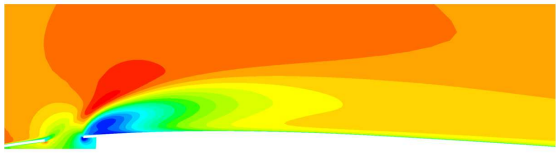

(i) Case 8

Figure B.3: Contours of mean X-velocity component on symmetry plane $Y/D = 0$

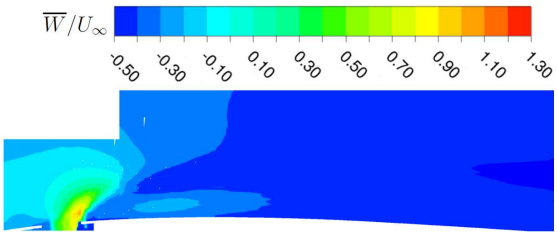

(a) Experiment

(b) Case 1

(c) Case 2

(d) Case 3

(e) Case 4

(f) Case 5

(g) Case 6

(h) Case 7

(i) Case 8

Figure B.4: Contours of mean Z-velocity component on symmetry plane $Y/D = 0$

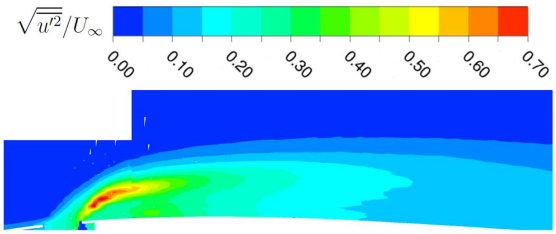

(a) Experiment

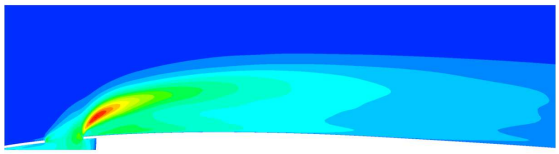

(b) Case 1

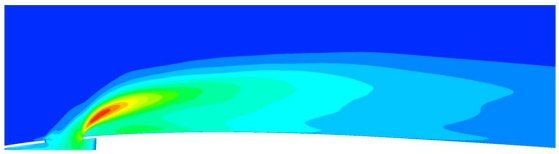

(c) Case 2

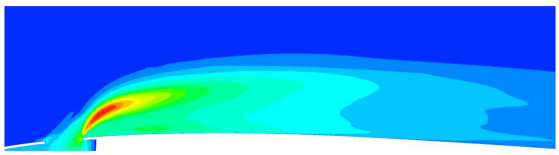

(d) Case 3

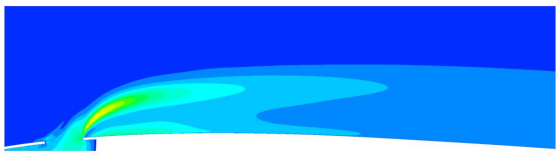

(e) Case 4

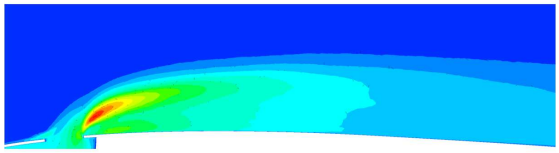

(f) Case 5

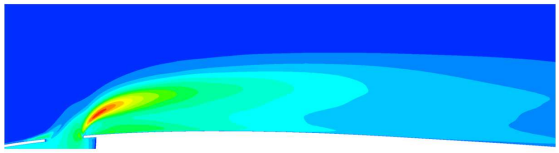

(g) Case 6

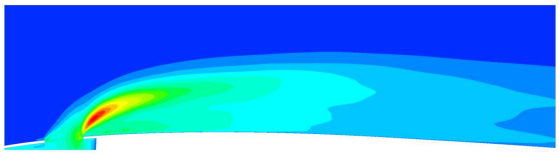

(h) Case 7

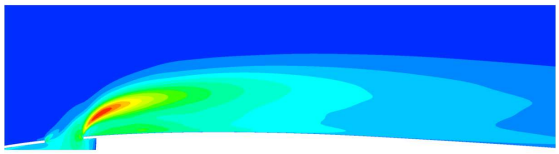

(i) Case 8

Figure B.5: Contours of RMS value for X-velocity component on symmetry plane $Y/D = 0$

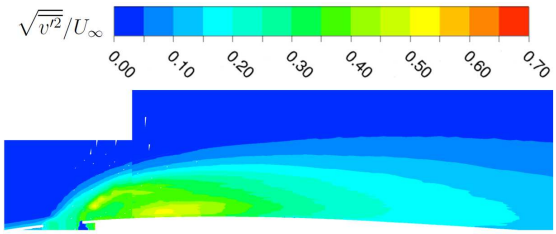

(a) Experiment

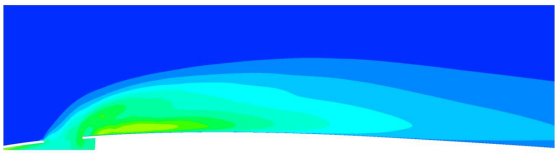

(b) Case 1

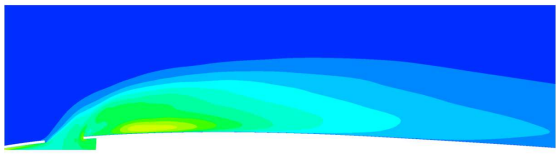

(c) Case 2

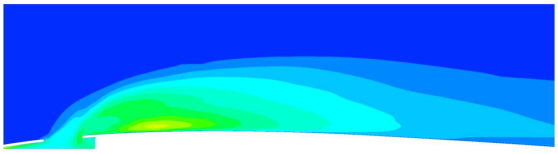

(d) Case 3

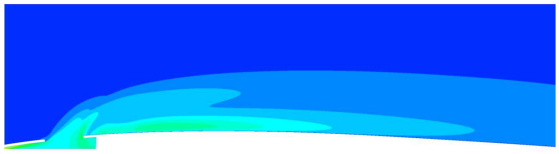

(e) Case 4

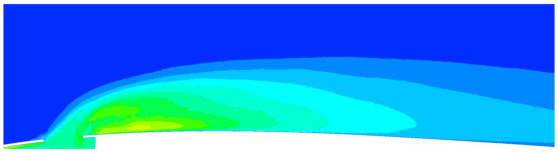

(f) Case 5

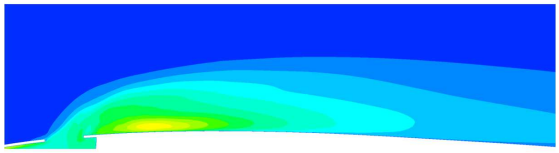

(g) Case 6

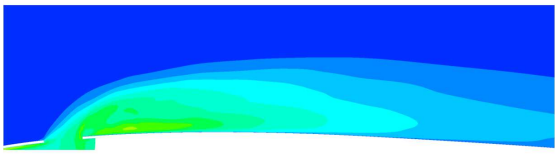

(h) Case 7

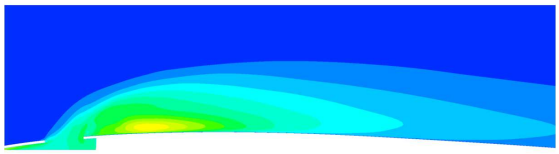

(i) Case 8

Figure B.6: Contours of RMS value for Y-velocity component on symmetry plane $Y/D = 0$

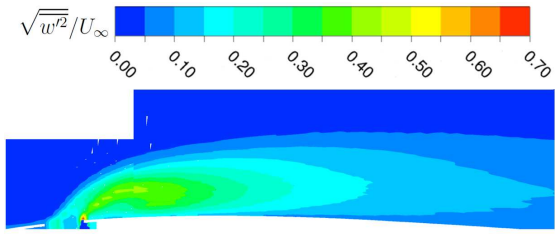

(a) Experiment

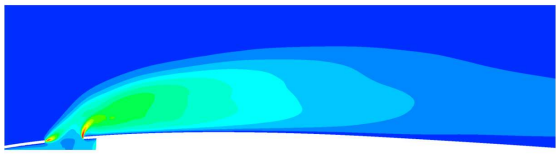

(b) Case 1

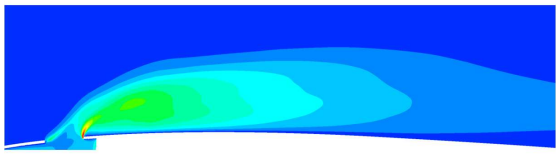

(c) Case 2

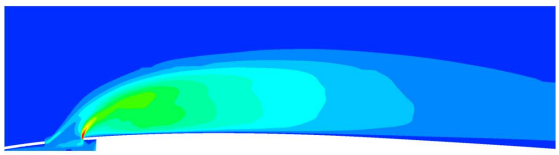

(d) Case 3

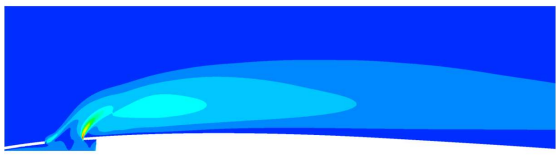

(e) Case 4

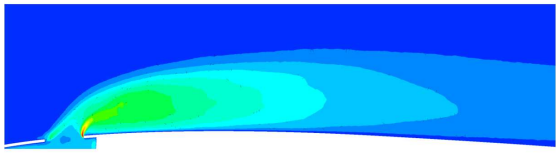

(f) Case 5

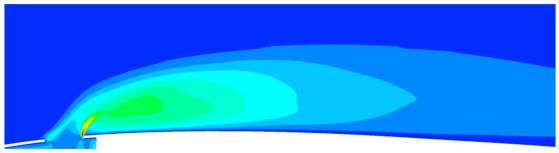

(g) Case 6

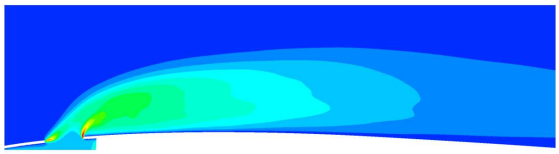

(h) Case 7

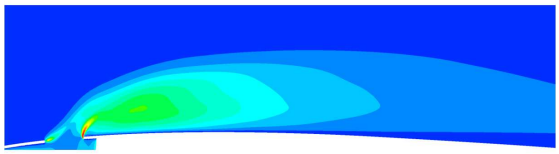

(i) Case 8

Figure B.7: Contours of RMS value for Z-velocity component on symmetry plane $Y/D = 0$

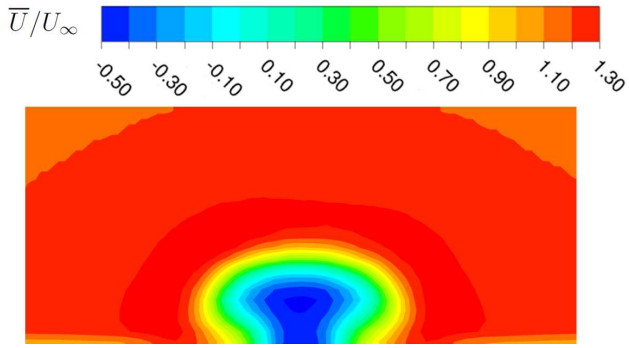

(a) Experiment

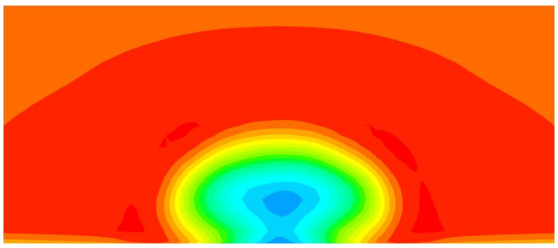

(b) Case 1

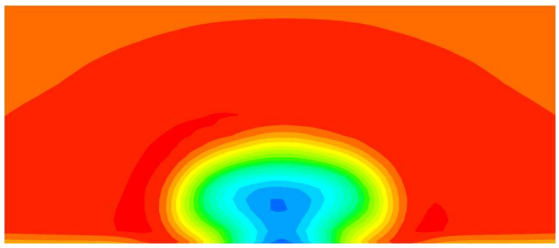

(c) Case 2

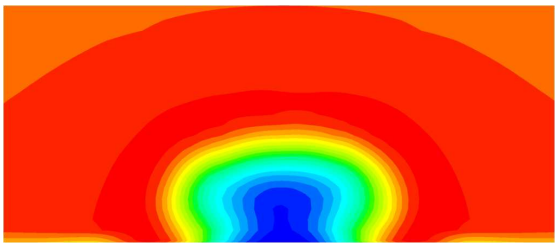

(d) Case 3

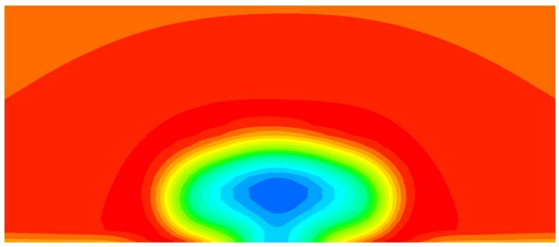

(e) Case 4

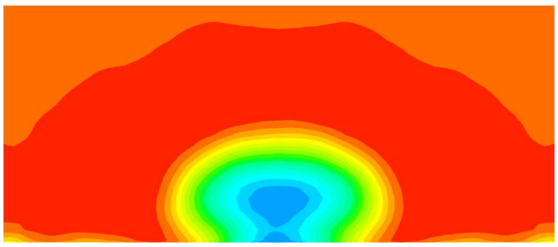

(f) Case 5

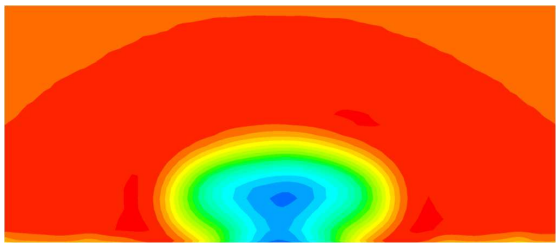

(g) Case 6

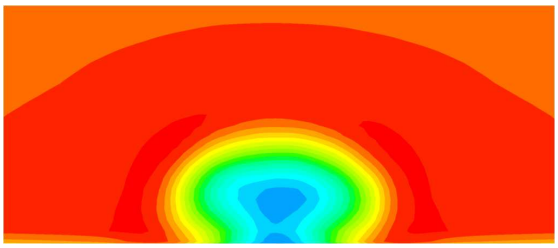

(h) Case 7

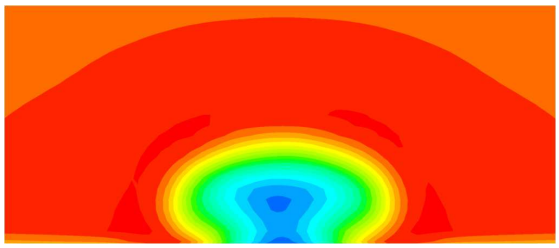

(i) Case 8

Figure B.8: Contours of mean X-velocity component on lateral plane $X/D = 1$

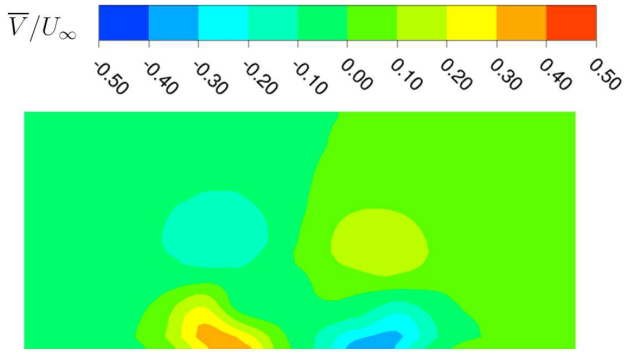

(a) Experiment

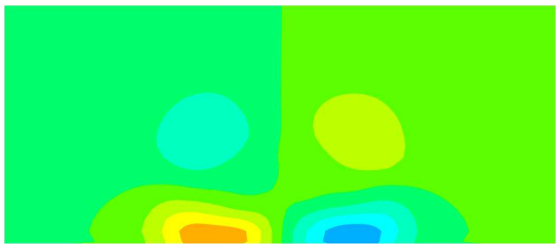

(b) Case 1

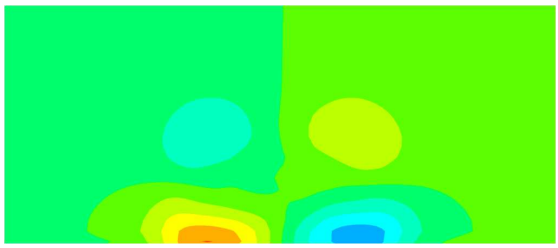

(c) Case 2

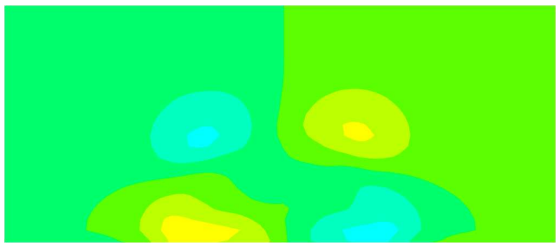

(d) Case 3

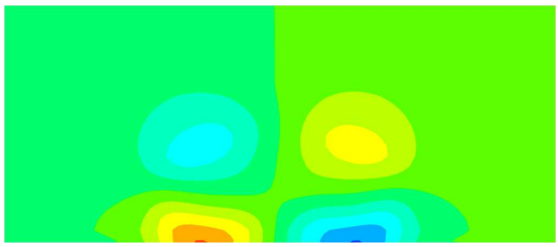

(e) Case 4

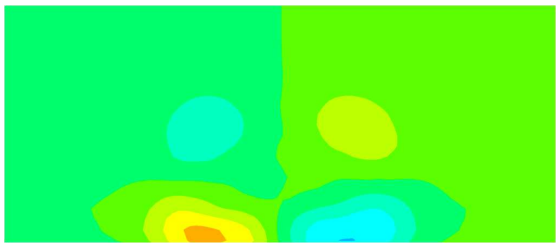

(f) Case 5

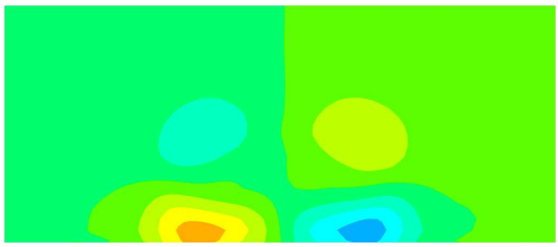

(g) Case 6

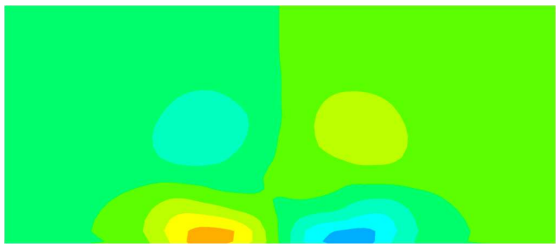

(h) Case 7

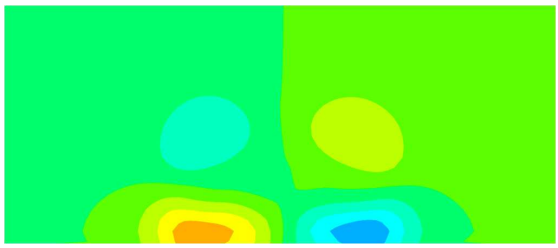

(i) Case 8

Figure B.9: Contours of mean Y-velocity component on lateral plane $X/D = 1$

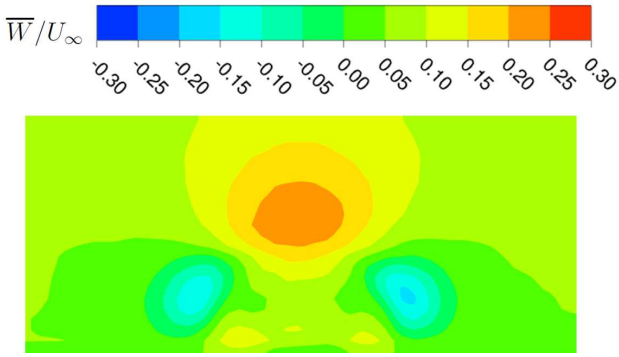

(a) Experiment

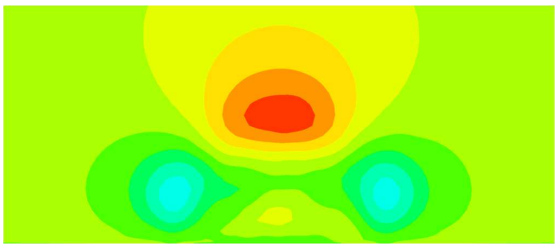

(b) Case 1

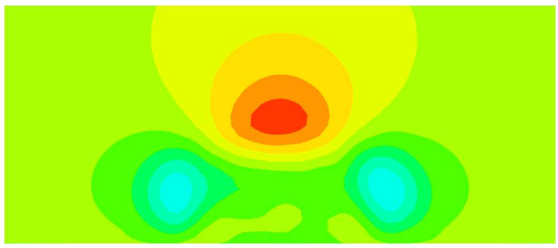

(c) Case 2

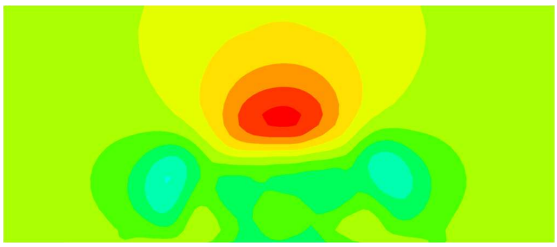

(d) Case 3

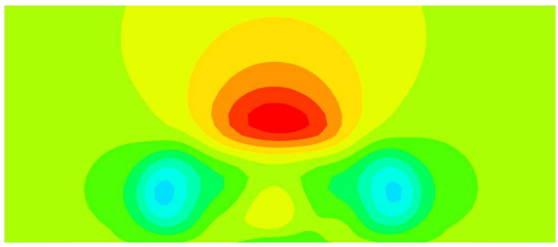

(e) Case 4

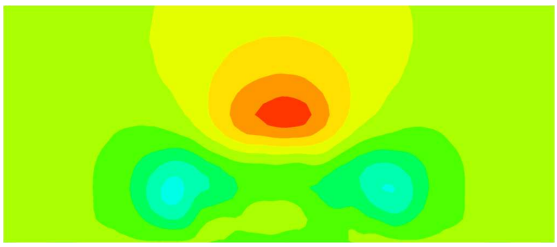

(f) Case 5

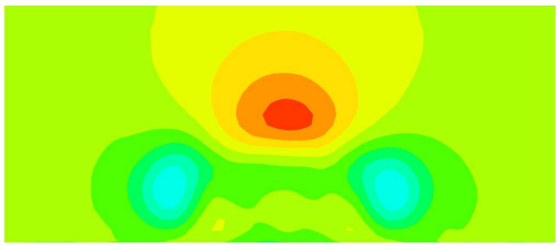

(g) Case 6

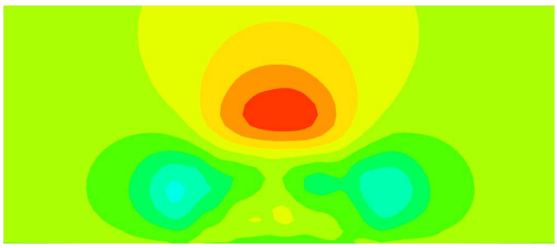

(h) Case 7

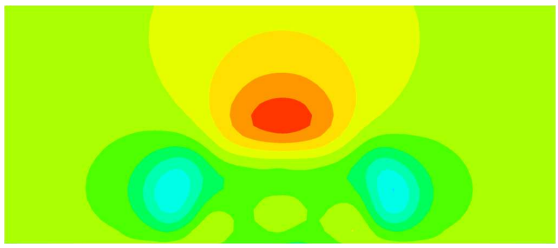

(i) Case 8

Figure B.10: Contours of mean Z-velocity component on lateral plane $X/D = 1$

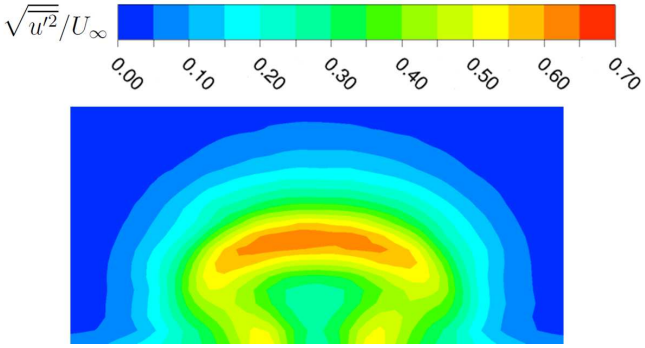

(a) Experiment

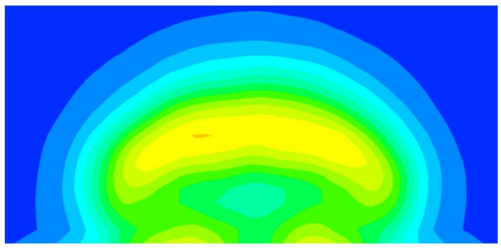

(b) Case 1

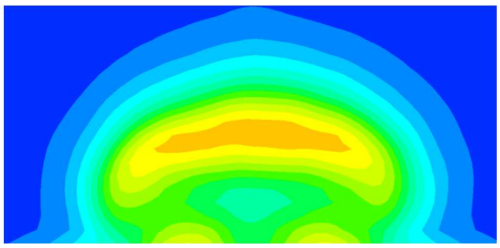

(c) Case 2

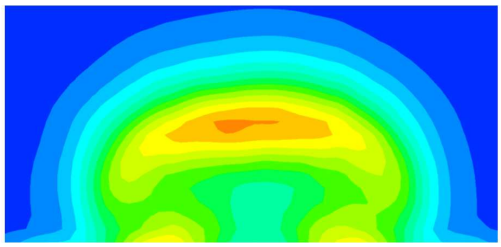

(d) Case 3

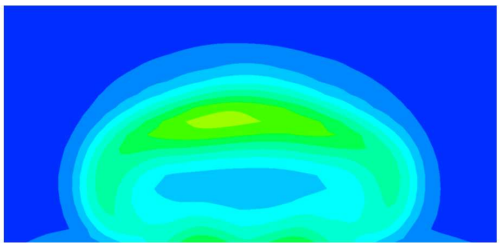

(e) Case 4

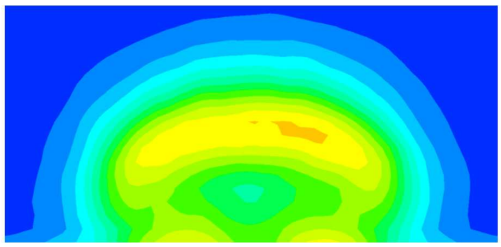

(f) Case 5

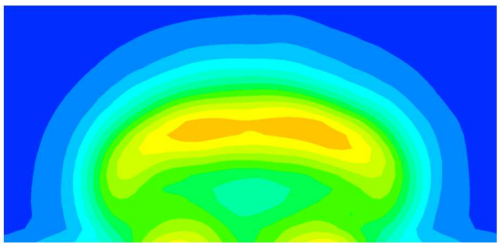

(g) Case 6

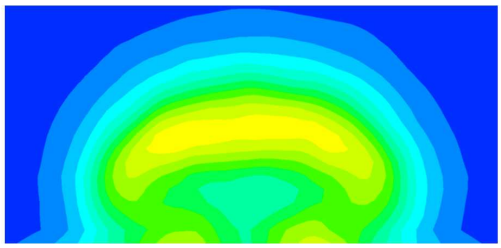

(h) Case 7

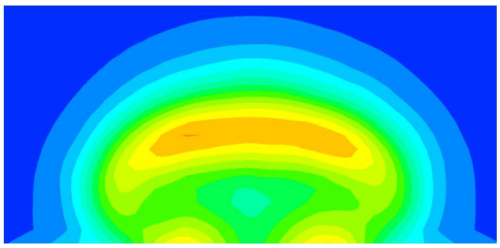

(i) Case 8

Figure B.11: Contours of RMS value for X-velocity component on lateral plane $X/D = 1$

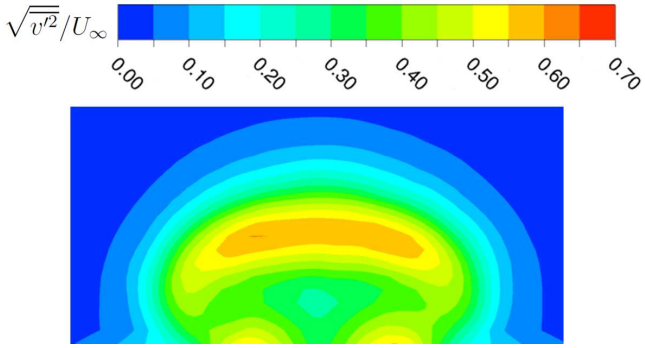

(a) Experiment

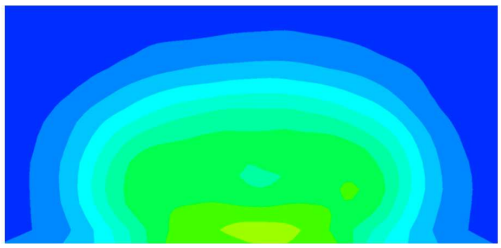

(b) Case 1

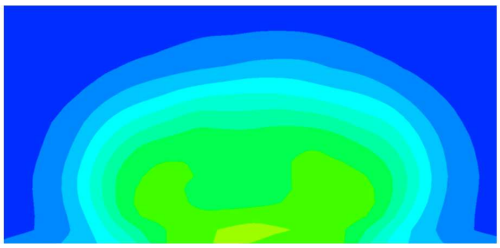

(c) Case 2

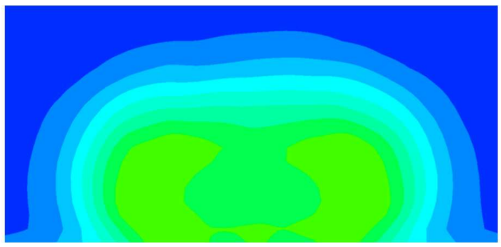

(d) Case 3

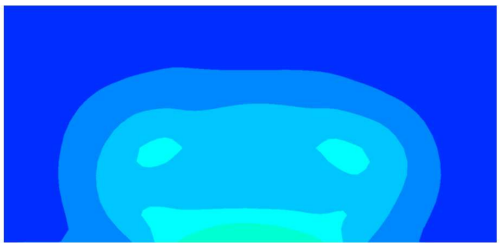

(e) Case 4

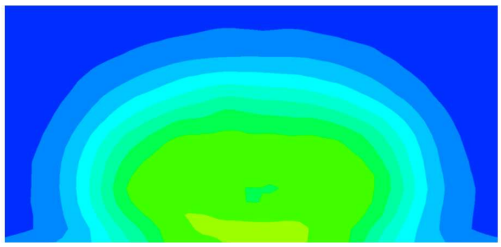

(f) Case 5

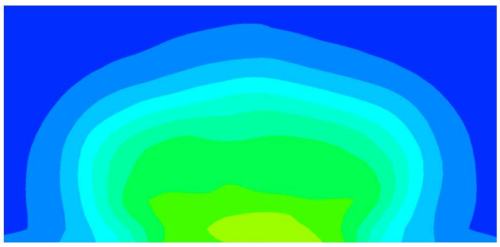

(g) Case 6

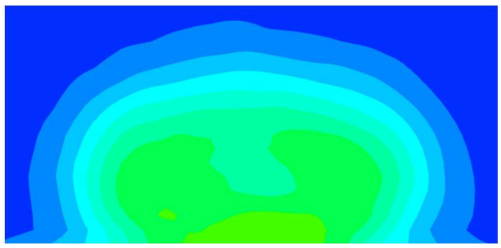

(h) Case 7

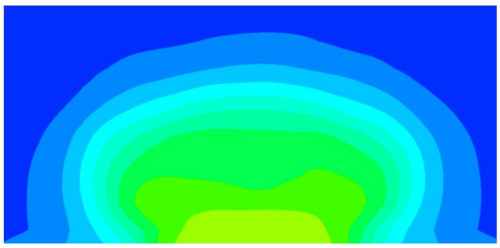

(i) Case 8

Figure B.12: Contours of RMS value for Y-velocity component on lateral plane $X/D = 1$

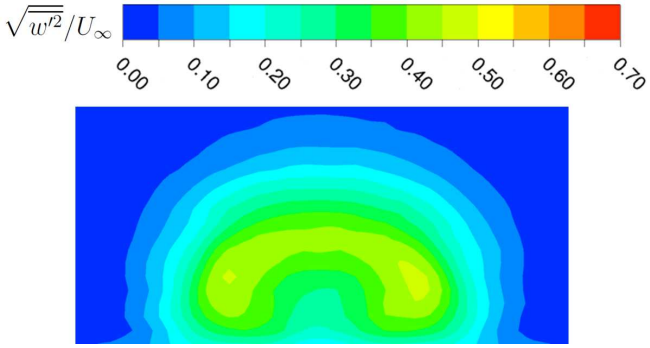

(a) Experiment

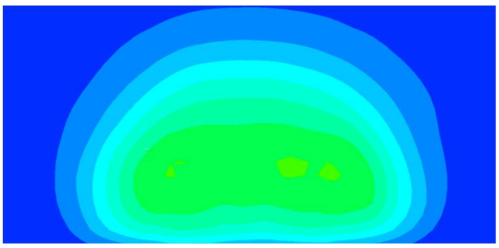

(b) Case 1

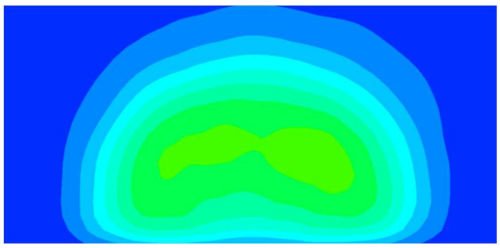

(c) Case 2

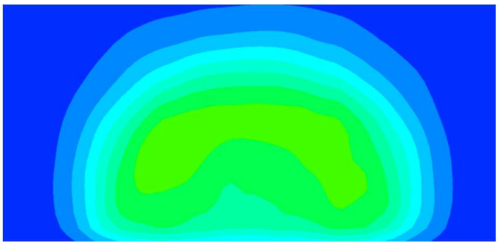

(d) Case 3

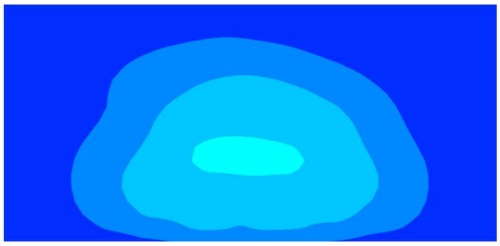

(e) Case 4

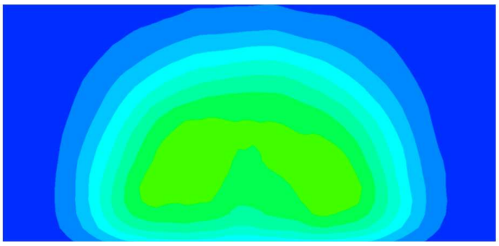

(f) Case 5

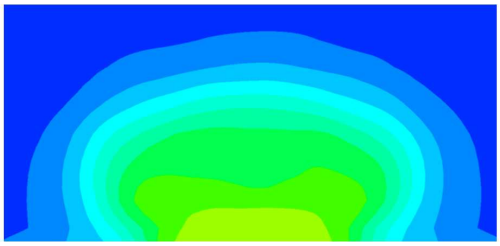

(g) Case 6

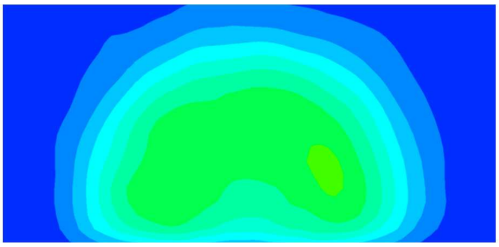

(h) Case 7

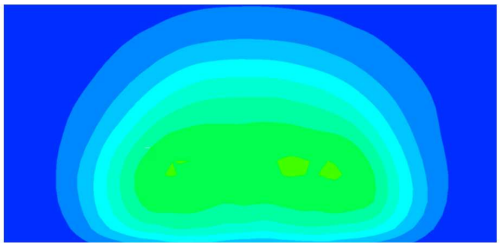

(i) Case 8

Figure B.13: Contours of RMS value for Z-velocity component on lateral plane $X/D = 1$

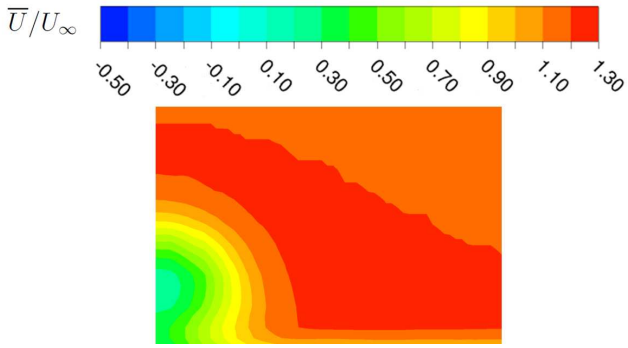

(a) Experiment

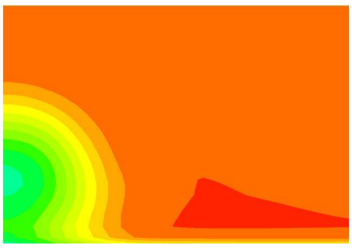

(b) Case 1

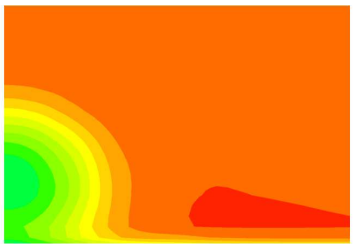

(c) Case 2

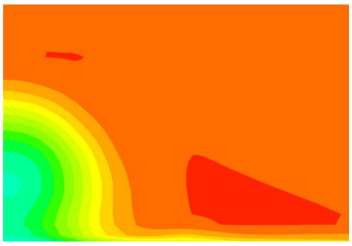

(d) Case 3

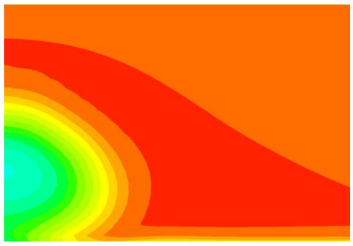

(e) Case 4

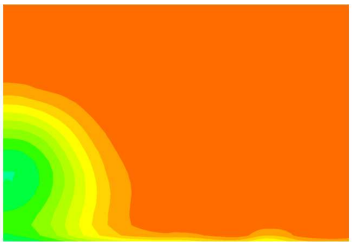

(f) Case 5

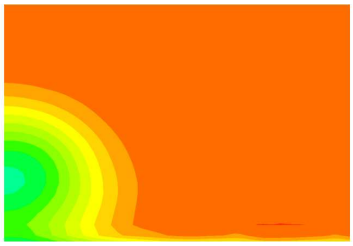

(g) Case 6

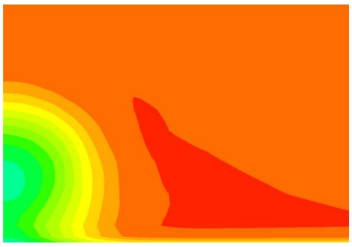

(h) Case 7

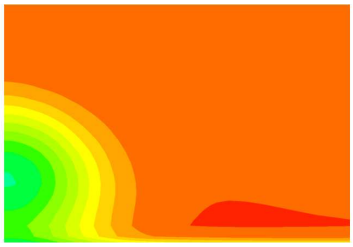

(i) Case 8

Figure B.14: Contours of mean X-velocity component on lateral plane $X/D = 7/3$

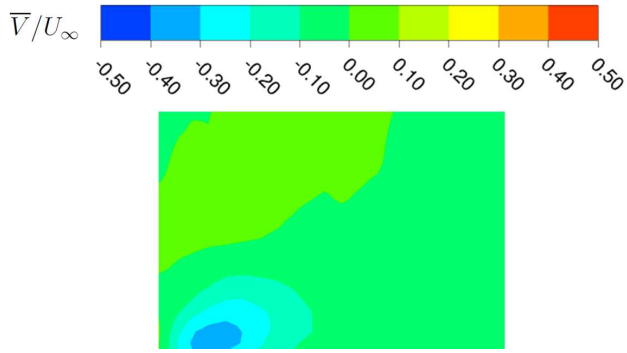

(a) Experiment

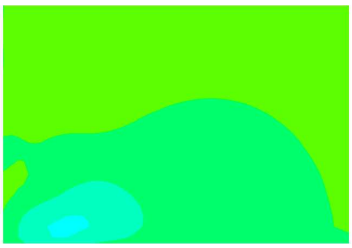

(b) Case 1

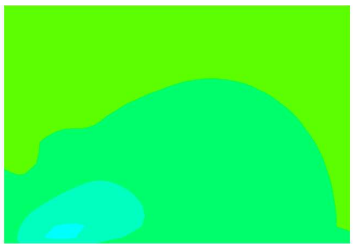

(c) Case 2

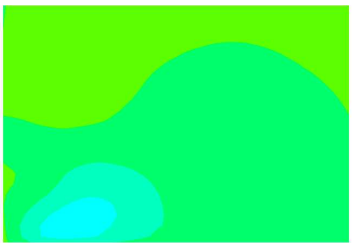

(d) Case 3

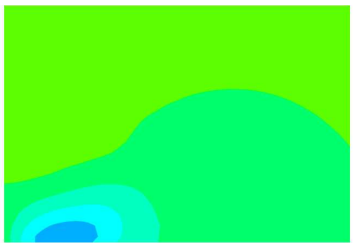

(e) Case 4

(f) Case 5

(g) Case 6

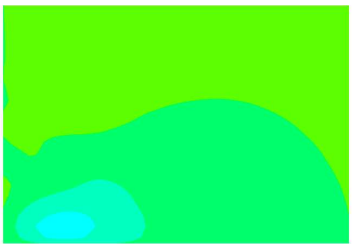

(h) Case 7

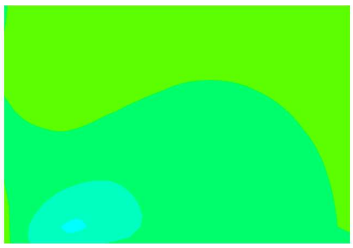

(i) Case 8

Figure B.15: Contours of mean Y-velocity component on lateral plane $X/D = 7/3$

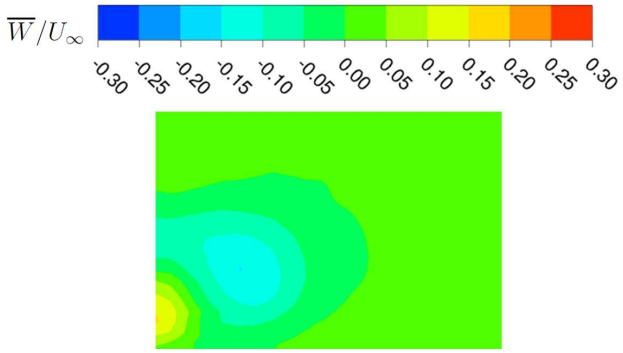

(a) Experiment

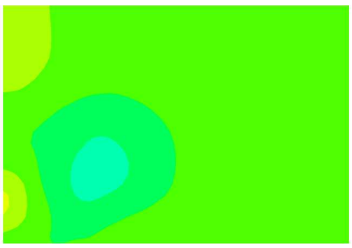

(b) Case 1

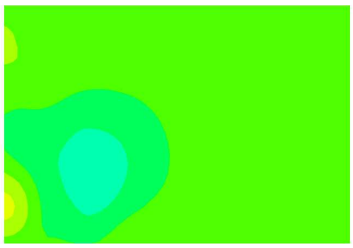

(c) Case 2

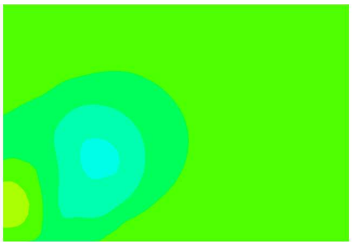

(d) Case 3

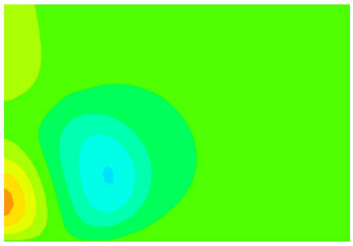

(e) Case 4

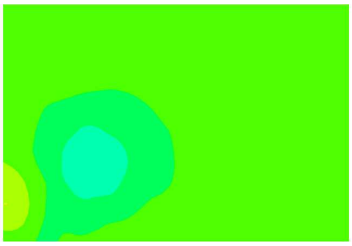

(f) Case 5

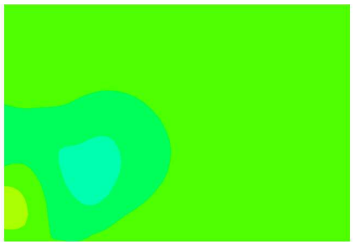

(g) Case 6

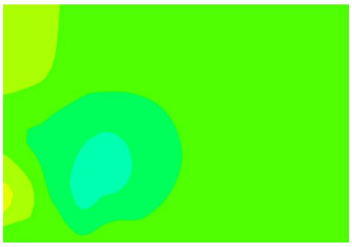

(h) Case 7

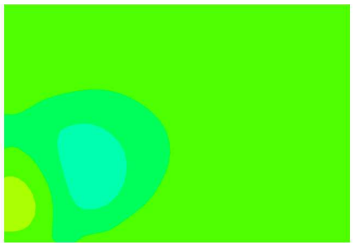

(i) Case 8

Figure B.16: Contours of mean Z-velocity component on lateral plane $X/D = 7/3$

Étude et analyse numérique d'un jet chaud débouchant dans un écoulement transverse en utilisant des simulations aux échelles résolues

Des méthodes numériques sont présentées qui permettent la simulation de jets chauds débouchants dans un écoulement transverse aux grands nombres de Reynolds et aux rapports des vitesses faibles. Différentes approches pour la modélisation de turbulence, c'est-à-dire URANS, SAS, DDES et ELES, sont validées par comparaison à des données expérimentales pour une configuration générique, soulignant la nécessité de résoudre les différentes échelles turbulentes pour une prévision correcte du mélange thermique. L'analyse de la solution instationnaire permet l'identification de processus dynamiques intrinsèques ainsi que des phénomènes de mélange et l'application de l'analyse en composantes principales révèle l'ondulation latérale du sillage de jet. Du fait du caractère multi-échelles qui se manifeste dans la simulation d'un jet débouchant sur une configuration avion, l'approche séquentielle basée sur le modèle SAS est mise en place. Comme les résultats pour la sortie d'un système de dégivrage de nacelle sont en bon accord avec les données d'essai en vol, cette approche est finalement appliquée à la sortie complexe d'un système de pre-cooler, mettant en valeur sa capacité à être appliquée dans un processus industriel.

Mots clés : Jet débouchant dans un écoulement transverse, Modélisation de turbulence avancée, Simulations instationnaires, Aérothermodynamique, Mélange thermique

Numerical Investigations on a Hot Jet in Cross Flow Using Scale-Resolving Simulations

Numerical methods for the simulation of hot jets in cross flow at high Reynolds numbers and small momentum ratios are presented. Different turbulence modeling strategies, i.e. URANS, SAS, DDES and ELES, are validated against experimental data on a generic configuration, highlighting the necessity of scale-resolution for a correct prediction of thermal mixing. The analysis of transient flow simulations allows the identification of inherent flow dynamics as well as mixing phenomena and the application of the Proper Orthogonal Decomposition revealed the lateral wake meandering as being one of them. Due to the multi-scale problem which arises when simulating jets in cross flow on real aircraft configurations, the sequential approach based on the SAS turbulence model is introduced. As results for the exhaust of a nacelle anti-icing system comprising multiple jets in cross flow agree well with flight test data, the approach is applied in a last step to the complex exhaust of a pre-cooling system, emphasizing the capabilities of this methodology in an industrial environment.

Keywords: Jet in Cross Flow, Advanced Turbulence Modeling, Unsteady Simulations, Aerothermodynamics, Thermal Mixing